Shock and Vibration

Advances in Structural Health Management and Composite Structures 2012

Guest Editors: Gyuhae Park, Jung-Ryul Lee, and Chan-Yik Park

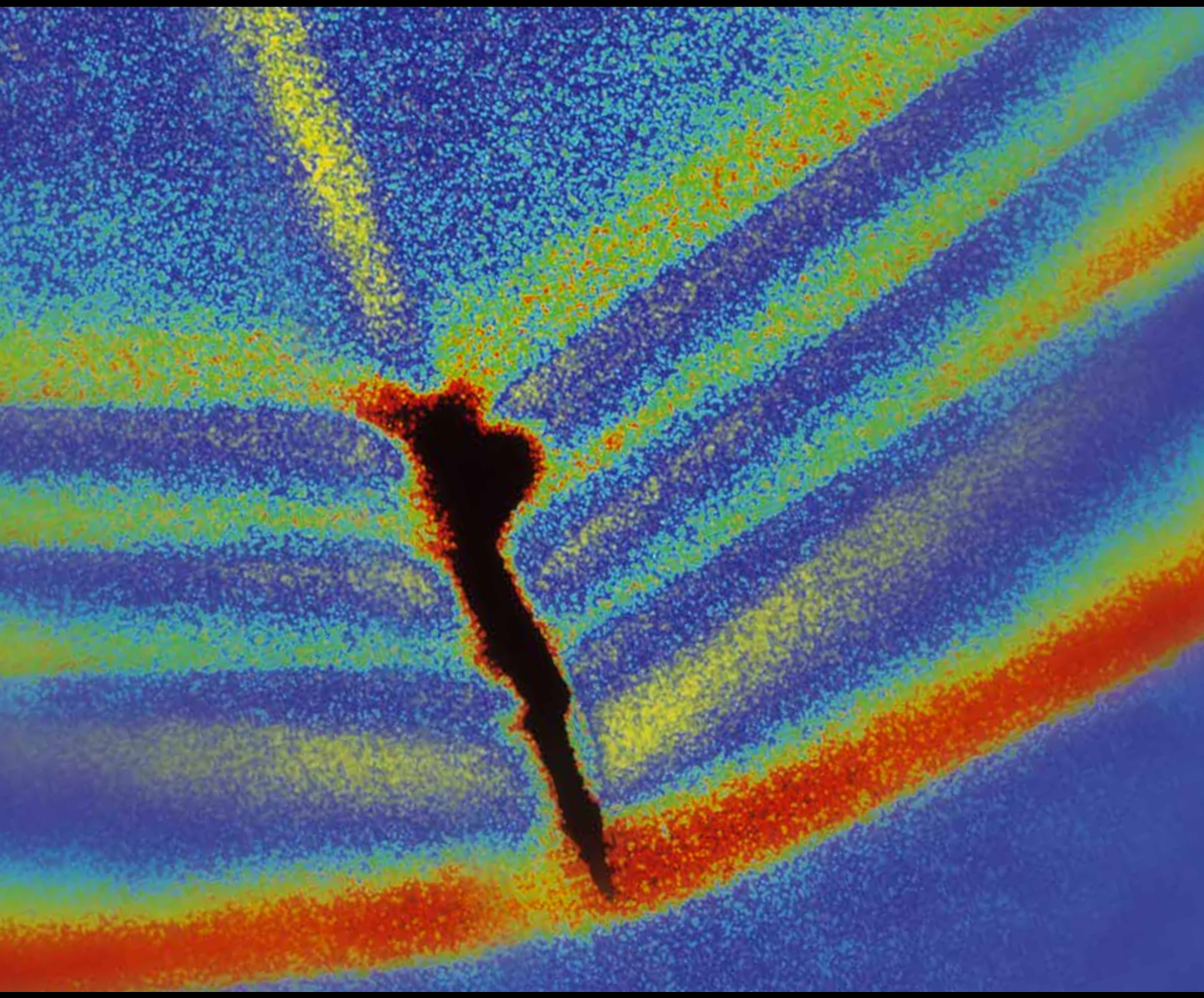

Advances in Structural Health Management and Composite Structures 2012

Shock and Vibration

Advances in Structural Health Management and Composite Structures 2012

Guest Editors: Gyuhae Park, Jung-Ryul Lee,
and Chan-Yik Park

Copyright © 2014 Hindawi Publishing Corporation. All rights reserved.

This is a special issue published in "Shock and Vibration." All articles are open access articles distributed under the Creative Commons Attribution License, which permits unrestricted use, distribution, and reproduction in any medium, provided the original work is properly cited.

Editor-in-Chief

Mehdi Ahmadian, Virginia Polytechnic Institute and State University, USA

Associate Editors

Brij N. Agrawal, USA
Subhamoy Bhattacharya, UK
Dumitru I. Caruntu, USA
Peng Chen, Japan
Longjun Dong, China
Mohammad Elahinia, USA
Anindya Ghoshal, USA
Alicia Gonzalez-Buelga, UK
Hassan Haddadpour, Iran
Hamid Hosseini, Japan
Reza Jazar, Australia
Jeong-Hoi Koo, USA
Mickaël Lallart, France
Kenneth J. Loh, USA
Nuno Maia, Portugal
Tony Murmu, UK
Toshiaki Natsuki, Japan
Miguel M. Neves, Portugal
Gyuhae Park, Republic of Korea
Didier Rémond, France
Rüdiger Schmidt, Germany
Vadim V. Silberschmidt, UK
Kumar V. Singh, USA
Valder Steffen Jr, Brazil
Chao Tao, China
Senthil S. Vel, USA
Gongnan Xie, China
Peijun Xu, USA
Zaili L. Yang, UK
Ahmet S. Yigit, Kuwait
Xinjie Zhang, China
Lei Zuo, USA

Contents

Hindawi Publishing Corporation
Shock and Vibration
Volume 2014, Article ID 109678, 1 page
http://dx.doi.org/10.1155/2014/109678

Editorial

Advances in Structural Health Management and Composite Structures 2012

Gyuhae Park,[1] Jung-Ryul Lee,[2] and Chan-Yik Park[3]

[1] *School of Mechanical Engineering, Chonnam National University, Gwangju, Republic of Korea*
[2] *Department of Aerospace Engineering and Department of Mechatronics Engineering and LANL-CBNU Engineering Institute Korea, Chonbuk National University, Jeonju, Chonbuk, Republic of Korea*
[3] *Aeronautical Technology Directorate (7-2), Aircraft System R&D Institute, Agency for Defense Development, Daejeon, Republic of Korea*

Correspondence should be addressed to Gyuhae Park; gpark@chonnam.ac.kr

Received 20 September 2013; Accepted 22 September 2013; Published 13 May 2014

Copyright © 2014 Gyuhae Park et al. This is an open access article distributed under the Creative Commons Attribution License, which permits unrestricted use, distribution, and reproduction in any medium, provided the original work is properly cited.

The first session of the International Conference on Advances in Structural Health Management and Composite Structures 2012 (ASHMCS 2012) took place in Jeonju, Republic of Korea, on August 29–31, 2012. This conference is organized by Engineering Institute of Korea, an educational and research collaboration between Los Alamos National Laboratory, USA, and Chonbuk National University, Korea. The conference addressed the new development in all aspects of structural health monitoring and composite structures including diagnosis and prognosis, advanced sensors and actuators, modeling and simulation, signal and image processing, pattern recognition and machine learning, and hardware/software integration. Delegates from 14 countries and various academic and industrial communities attended the conference and presented 80 papers. From the conference papers, 10 papers are selected for this special issue after a careful review process. The papers cover a wide spectrum of subjects that include modeling and experimental verification related to damage detection and quantification, pyroshock, and dynamic sensor development. The selected papers reflect the broad range of topics at ASHMCS 2012 and the success of the conference.

Acknowledgments

Acknowledgments are due to the sponsors of ASHMCS 2012, including the Office of Naval Research Global (USA), Asian Office of Aerospace Research and Development (USA), and Foreign Research Recruitment Program of the National Research Foundation of Korea, for their support to the conference. Acknowledgments are also due to all the authors and coauthors of this special issue for their contribution and to the reviewers for their time and collaboration.

Gyuhae Park
Jung-Ryul Lee
Chan-Yik Park

Hindawi Publishing Corporation
Shock and Vibration
Volume 2014, Article ID 929341, 8 pages
http://dx.doi.org/10.1155/2014/929341

Research Article

Magnetic Flux Leakage Sensing-Based Steel Cable NDE Technique

Seunghee Park,[1] Ju-Won Kim,[2] Changgil Lee,[1] and Jong-Jae Lee[3]

[1] *School of Civil, Architectural, and Environmental Engineering, Sungkyunkwan University, Suwon, Gyeonggi 440-746, Republic of Korea*
[2] *Department of u-City Design and Engineering, Sungkyunkwan University, Suwon, Gyeonggi 440-746, Republic of Korea*
[3] *Department of Civil and Environmental Engineering, Sejong University, Seoul 143-747, Republic of Korea*

Correspondence should be addressed to Seunghee Park; shparkpc@skku.edu

Received 11 December 2012; Accepted 13 April 2013; Published 8 May 2014

Academic Editor: Gyuhae Park

Copyright © 2014 Seunghee Park et al. This is an open access article distributed under the Creative Commons Attribution License, which permits unrestricted use, distribution, and reproduction in any medium, provided the original work is properly cited.

Nondestructive evaluation (NDE) of steel cables in long span bridges is necessary to prevent structural failure. Thus, an automated cable monitoring system is proposed that uses a suitable NDE technique and a cable-climbing robot. A magnetic flux leakage-(MFL-) based inspection system was applied to monitor the condition of cables. This inspection system measures magnetic flux to detect the local faults (LF) of steel cable. To verify the feasibility of the proposed damage detection technique, an 8-channel MFL sensor head prototype was designed and fabricated. A steel cable bunch specimen with several types of damage was fabricated and scanned by the MFL sensor head to measure the magnetic flux density of the specimen. To interpret the condition of the steel cable, magnetic flux signals were used to determine the locations of the flaws and the levels of damage. Measured signals from the damaged specimen were compared with thresholds that were set for objective decision-making. In addition, the measured magnetic flux signals were visualized as a 3D MFL map for intuitive cable monitoring. Finally, the results were compared with information on actual inflicted damages, to confirm the accuracy and effectiveness of the proposed cable monitoring method.

1. Introduction

Recently, there have been increasing demands on structural health monitoring (SHM) and nondestructive testing (NDT) in the fields of civil, mechanical, and aerospace engineering. Especially, local monitoring methodologies for specific critical members have been studied to overcome the limitation of global monitoring techniques for whole structures [1–4]. Steel cables in long span bridges are also critical members that suspend almost all of the dead load of the structure. However, cross-sectional damage can occur in a steel cable due to corrosion and fracture, which can lead to stress concentrations. Cross-sectional damage can be a direct cause of structural failure. Therefore, nondestructive evaluation (NDE) is necessary to detect the initial stages of cross-sectional damage in a cable. However, it is difficult to monitor the condition of most cables, as the damage can be invisible and inaccessibly located. To overcome these drawbacks, we propose an automated cable monitoring system, which uses a suitable NDE technique and a cable-climbing robot that can approach the damaged point, which is shown in Figure 1.

Meanwhile, NDE techniques available for incorporation into cable-climbing robots have been widely researched. In this study, a magnetic sensor for the detection of cross-sectional damage was applied. Magnetic sensors are widely used to monitor structures, including aircrafts and ships, due to their excellent reliability and reproducibility. Various kinds of magnetic sensors exist, and optimal magnetic properties can be utilized according to the kind of target structure [5–9].

In this study, an MFL sensor was applied to detect the local fault (LF) damage of steel cables, by capturing the magnetic flux leakage. The magnetic flux leakage method is most suitable for continuous structures that have constant cross-sections, such as cables and pipes, and has been applied for the inspection of steel cables in the mining industry, for ski lifts, elevators, and for other applications [10–15]. However, most MFL devices are fixed systems, which cannot be used for steel cables in bridges. In addition, the measured signals

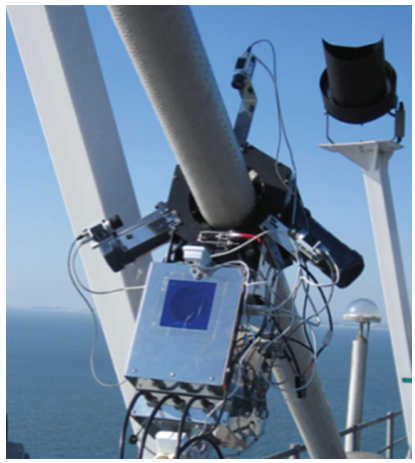

(a)

(b)

Figure 1: The cable-climbing robot with suitable NDE equipment.

from MFL devices require analysis by experts to determine damage. To overcome these limitations, an advanced MFL-based damage detection technique has been developed that utilizes thresholds created from statistical methods used for objective decision-making.

To verify the feasibility of the proposed damage detection technique, an 8-channel MFL sensor prototype was designed and fabricated. A steel cable bunch specimen was also fabricated to perform the experiment, in which cross-sectional damages were formed step-by-step, by making cuts in the cable. The sensor was used to measure magnetic flux at each damage condition. Measured signals from the damaged specimen were compared with the set thresholds. Finally, the measured magnetic flux signal was visualized as a 3D MFL map, for intuitive cable monitoring.

2. Theoretical Backgrounds

2.1. Principle of Magnetic Flux Leakage. A steel specimen that is magnetized has a magnetic field in and around itself, and any place where a magnetic line of force exits or enters the specimen is called a pole. A magnet that is cracked, but not broken completely in two, forms a north and south pole at each edge of the crack, as shown in Figure 2. The magnetic field exits in the north pole and reenters the south pole. The magnetic field spreads out when it encounters the small air gap created by the crack, because the air cannot support as much magnetic field per unit volume as the magnet can. When the field spreads out, it appears to leak out of the material and is thus called a flux leakage field.

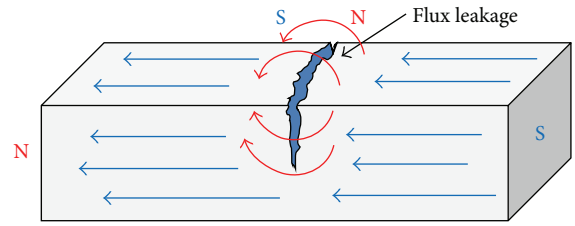

Figure 2: Principle of magnetic flux leakage.

2.2. Magnetic Flux Leakage-Based Local Fault Damage Detection Technique. A strong permanent magnet or an electromagnet is used to establish a magnetic flux in the material to be inspected. When there is no defect, the flux in the metal remains uniform, as illustrated in Figure 3(a). In contrast, Figure 3(b) illustrates the flux leakage that occurs when there is LF damage, due to broken wire or wear. The flux leaks out of the metal near the defect. Sensors that can detect this flux leakage are placed between the poles of the magnet and they generate an electric signal that is proportional to the magnetic flux leakage [16].

In this study, Hall sensors were used to capture the MFL. The Hall sensor operates based on the Hall effect and is illustrated in Figure 4. When a magnetic field is applied to a plate, an electron moving through a magnetic field experiences a force, known as the Lorentz force, that is perpendicular both to the direction of motion and to the direction of the field. It is the response to this force that creates the Hall voltage [17, 18]. This Hall voltage can be measured using a DAQ system and can be used to examine the condition of target structure.

2.3. Establishment of a Threshold Level Using GEV Distribution. After measuring the magnetic flux, it is necessary to determine an appropriate threshold for the measured output voltage that will distinguish between an intact and damaged condition. In this study, a 99.99% confidence level threshold of the intact condition was set, using the generalized extreme value (GEV) distribution. By the extreme value theorem, the GEV distribution is the limit distribution of the properly normalized maxima of a sequence of independent and identically distributed random variables. Because of this, the GEV distribution is used as an approximation, to model the maxima of long (finite) sequences of random variables.

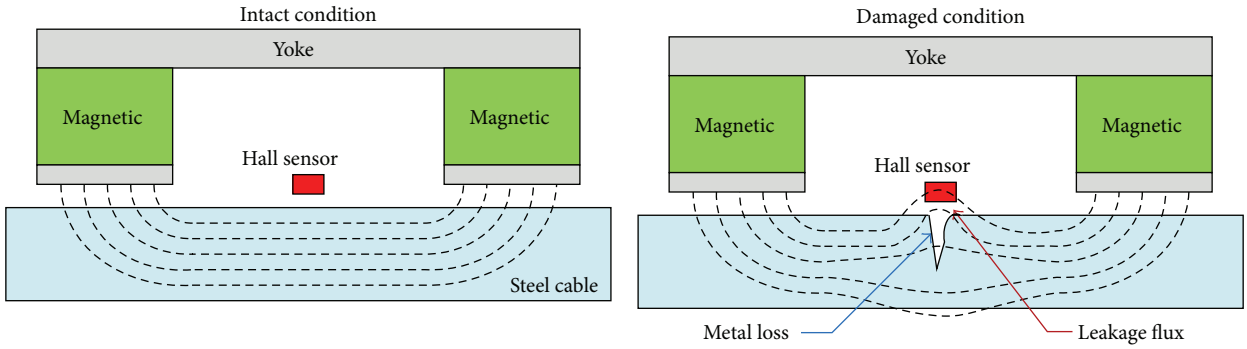

(a) Intact condition (b) Damaged condition

Figure 3: The concept of MFL-based LF damage detection technique.

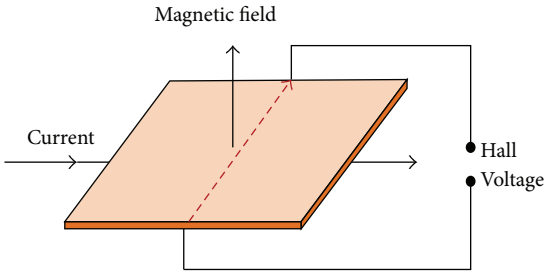

Figure 4: Principle of the Hall effect.

The generalized extreme value distribution has a cumulative distribution function, as shown in

$$F(x;\mu,\sigma,\xi) = \exp\left\{-\left[1+\xi\left(\frac{x-\mu}{\sigma}\right)\right]^{-1/\xi}\right\}, \quad (1)$$

for $1+\xi(x-\mu)/\sigma > 0$, where x is the upper end-point, $\mu \in \mathbb{R}$ the location parameter, $\sigma > 0$ the scale parameter, and $\xi \in \mathbb{R}$ the shape parameter [19].

3. Experimental Study

3.1. Design and Fabrication of MFL Sensor Head Prototype. An MFL sensor head prototype was fabricated, as shown in Figure 5, to perform the experimental study to verify the proposed cable NDE method. The sensor head was composed of a magnetization component and a signal measurement component, which were packed into an aluminum case of 18 cm width, 18 cm height, and 30 cm length. Additionally, the components could be detached conveniently, by making a system that could be readily opened.

First, the magnetization component, which creates the magnetic field for magnetizing a portion of the steel cable specimen, is a pair of yokes, which consist of 2 high strength Nd-Fe-B permanent magnets (neodymium 35) and a plate of carbon steel, as in Figure 6(a). The permanent magnet has the advantage of not requiring any power for operation and allows for a lighter system than if an electromagnetic magnet was to be used.

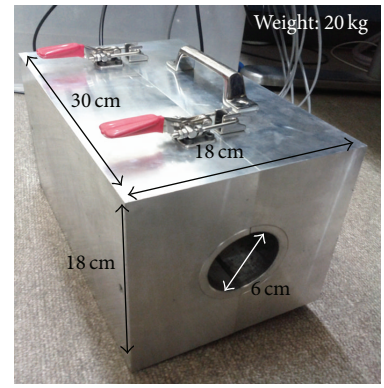

(a)

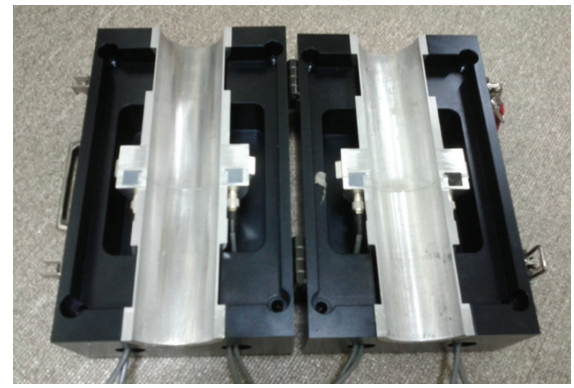

(b)

Figure 5: The fabricated MFL sensor head prototype.

The signal measurement component is composed of 8 channels of Hall sensors, which are circumferentially arranged at regular intervals around a circular configuration as shown in Figure 6(b). Each of the 8 arranged sensors converts the MFL signal to a voltage signal, which is transmitted to a DAQ system. The inner diameter of the sensor head is 60 mm, to accommodate steel cable of the same dimension.

3.2. Experimental Setup and Procedure. A series of experimental studies were carried out to examine the capabilities of the detection technique. A steel cable specimen of 60 mm

Table 1: Scenario of LF damage at specimen.

Intact	Damage number 1	Damage number 2	Damage number 3	Damage number 4
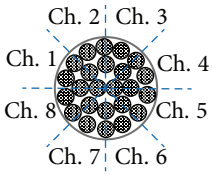	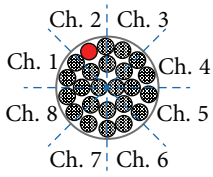	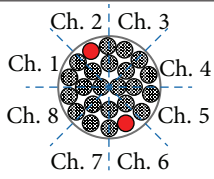	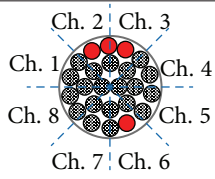	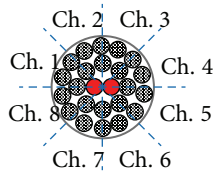
0% loss	4% loss	8% loss	16% loss	8% loss

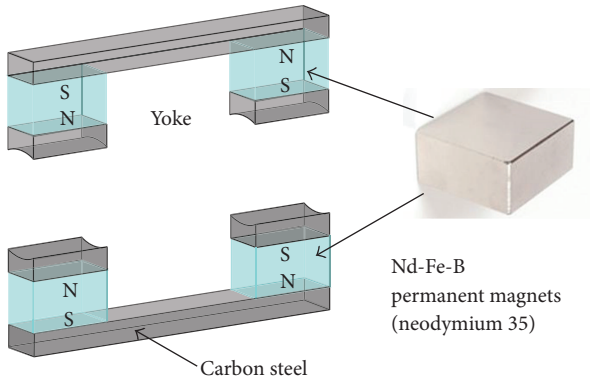

(a) Magnetization part

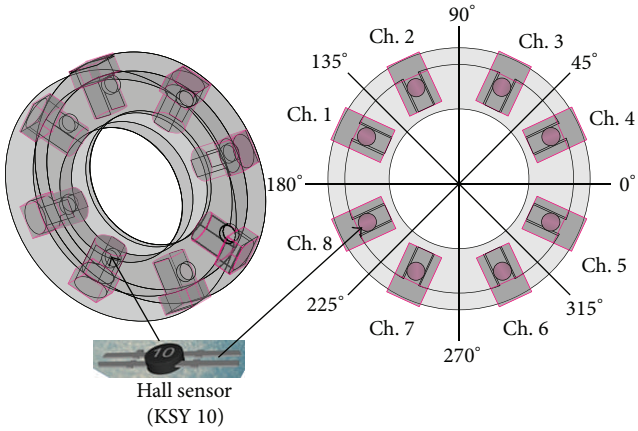

(b) Sensing part

Figure 6: Design of the MFL sensor head.

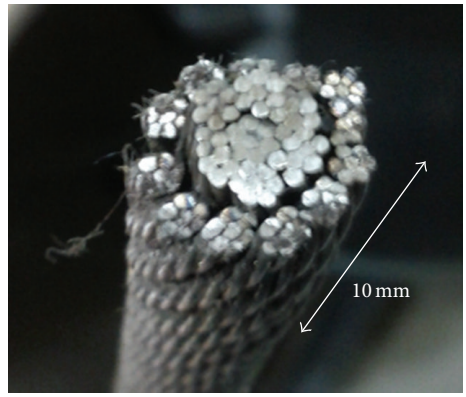

(a)

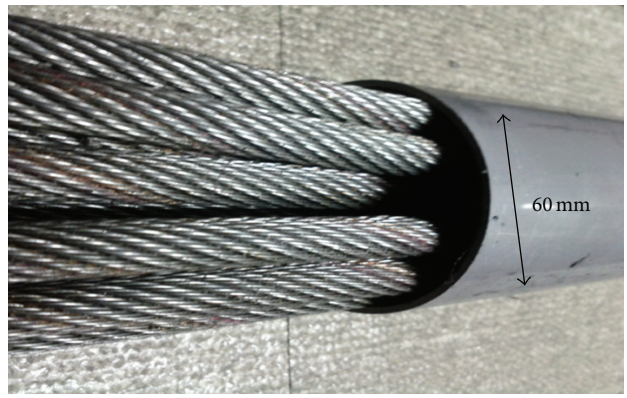

(b)

Figure 7: Specifications of the steel cable specimen.

diameter and 1700 mm length was fabricated for the experiment, by filling 25 strands of steel cable in a pipe of 60 mm external diameter. Each strand of cable was stranded from 7 ∗ 19 element wires and was 10 mm in diameter, as shown in Figure 7.

Thereafter, 4 levels of LF damage were formed step-by-step at the center of the steel cable specimen, as shown in Table 1. In Table 1, a red dot means a fully cut damage of the strand which is specified as a 4% (1/25) cross-sectional loss of cable specimen. First, a cable located near sensing channel 2 was cut (damage level 1). Second, for damage level 2, a cable located in the plane of symmetry with damage level 1 was additionally cut (near sensing channel 6). At level 3, the cut damage was extended by cutting 2 more element cables in a clockwise direction as in Table 1. Finally, at damage level 4, 2 cables located at the center of the cross-section were cut, to form inner damage.

Using the sensor head, MFL signals were measured from only the center 1 m section of the damaged specimen for each damage level condition, as shown in Figure 8. The moving speed of the sensor head was 1 m/sec, and the sampling rate was 1 kHz. Therefore, the displacement resolution of this setup is 1 mm.

Next, a virtual 5 m length of steel cable was rendered, by combining the 5-measurement sections of each damage condition (from intact to damage level number 4), as shown in Figure 9.

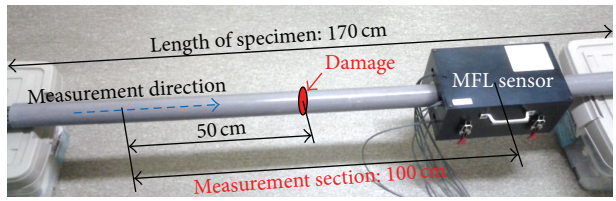

Figure 8: Test setup and measurement.

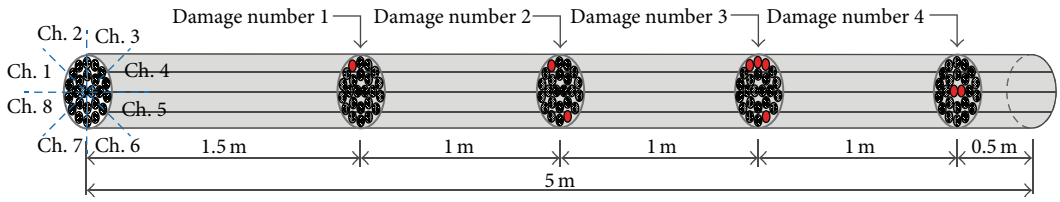

Figure 9: Virtual combined steel cable specimen.

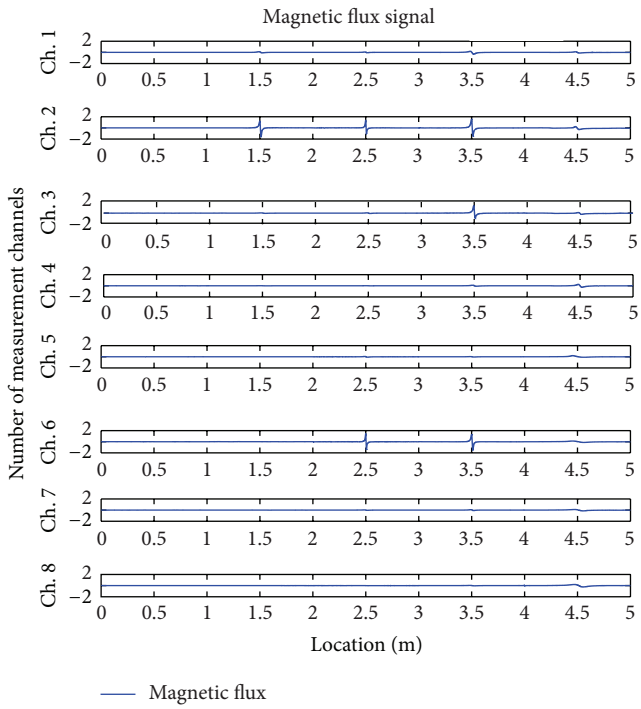

Figure 10: The raw magnetic flux signals from each channel.

Signal processing techniques, such as low-pass filtering and offset correction, were carried out to improve the resolution of the test results.

3.3. Experimental Results

3.3.1. Results of LF Damage Detection Based on MFL Method. The voltage signals that were measured from each channel of Hall sensors are displayed in Figure 10.

This figure shows symmetrical magnetic flux leakage signals measured at sensing channel 2 at the 1.5 m point along the length of the specimen and at channels 2 and 6 at the 2.5 m point. These MFL signals are consistent with the location of the actual local fault damage formed in the specimen. The flux leakage was captured only at sensing channels adjacent to the damages. At the 3.5 m point, the flux leakage signals were measured at sensing channels 2, 3, and 6, and faint flux leakage signals were also measured at sensing channels 1 and 4. This shows that when the damage is greater, flux leakage can be measured in neighboring channels. In addition, small FL signals were captured from every channel at the 4.5 m point (where the cut damages are located at a similar distance from all sensing channels). These facts demonstrate that the MFL sensor method can detect LF damages, and sensing sensitivity is dependent on the distance between the damage and the Hall sensor. Additionally, the circumferential location of the damage can be judged, by arranging the sensors in an array.

A threshold that distinguishes between intact and damaged conditions was set, to determine the damage objectively. Original MFL signals were converted to absolute values so that only magnitudes would be considered in the thresholds. In this study, a 99.99% confidence level threshold of the intact condition was set, using the generalized extreme value (GEV) distribution. The calculated threshold value is 0.1358 V, which is shown with the converted MFL signal in Figure 11.

The converted flux leakage signals exceeded the threshold at sensing channel 2 at the 1.5 m point, channels 2 and 6 at the 2.5 m point, and channels 1, 2, 3, and 6 at the 3.5 m point. At the 4.5 m point, the signals from almost all channels exceeded the threshold by a narrow margin. These measurements coincide with the actual damage locations and show that customized thresholds can be used as criteria to check whether or not damage has occurred.

3.3.2. Visualization of Magnetic Flux. The MFL signal was expressed in a 3-dimensional graph, as shown in Figure 12.

The x-axis is the distance along the specimen, the y-axis is the measurement channel number that represents the position of the sensor in the circumferential direction, and the amplitude of the magnetic flux is displayed on the z-axis and is color coded. Interpolation was performed to overcome the limitations of the limited number of sensing channels

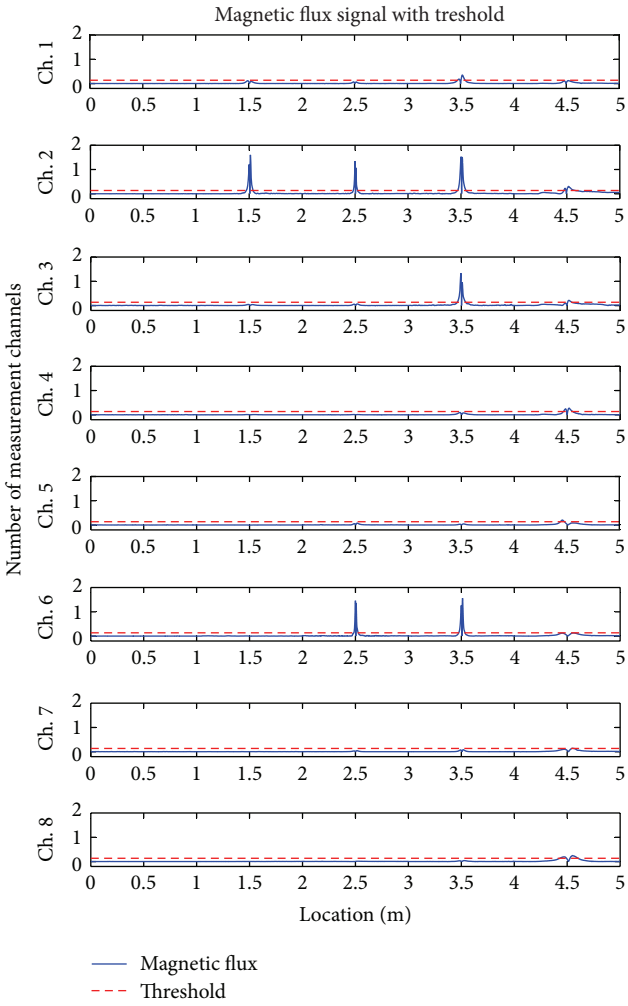

Figure 11: The converted magnetic flux signals with threshold.

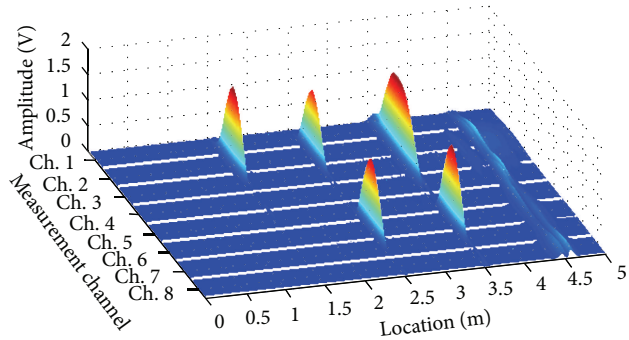

Figure 12: 3D magnetic flux graph.

for the smooth shape of the graph. In this figure, the large peaks that describe the flux leakage are clearly distinguishable from the intact signal, and they lay out the the size and location of the LF damages efficiently. However, small leakage was not distinguishable, due to noise in the signal. Thus, a threshold surface (shown in black) was added on the MFL graph, as shown in Figure 13. This precisely distinguishes the LF damaged areas from noise signals and the intact condition.

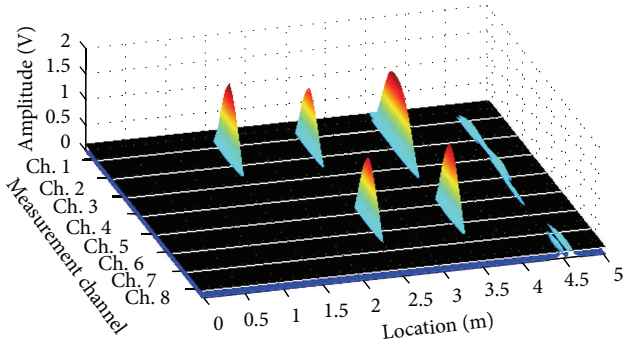

Figure 13: 3D magnetic flux graph with threshold surface.

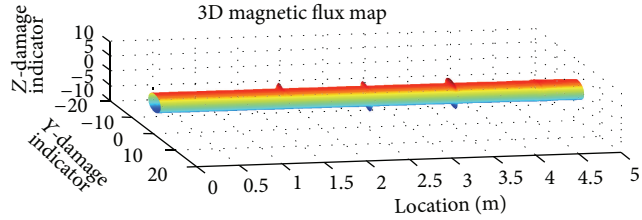

Figure 14: Visualized 3D magnetic flux map.

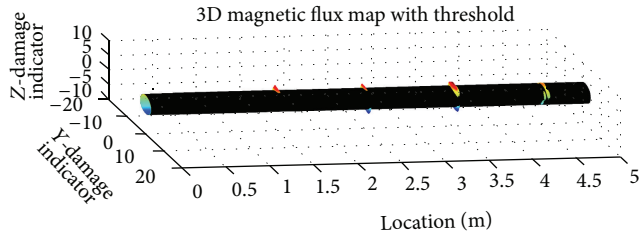

Figure 15: Visualized 3D magnetic flux map with threshold cover.

Finally, the MFL signals were visualized, by mapping onto a shape that is similar to the cable. For visualization, y- and z-dimensional damage indicators were calculated from converted magnetic flux values, using

$$Y_{\mathrm{DI}} = (\mathrm{MF}_c + r) \times \cos\theta,$$
$$Z_{\mathrm{DI}} = (\mathrm{MF}_c + r) \times \sin\theta, \quad (2)$$

where Y_{DI} and Z_{DI} are the y- and z-dimenional damage indicator, MF_c is the magnetic flux of cable, r is a radius for virtual cable visualization, and θ is the circumferential angle of the sensor.

These calculated damage indicators were plotted on a 3D graph with a distance indicator, as shown in Figure 14.

This 3D magnetic flux map represents the damage location information in the longitudinal and circumferential directions and shows the level of damage at a glance, from any angle.

In addition, the 3D magnetic flux map was wrapped with a cylindrical threshold, in a manner similar to Figure 13, as shown in Figure 15.

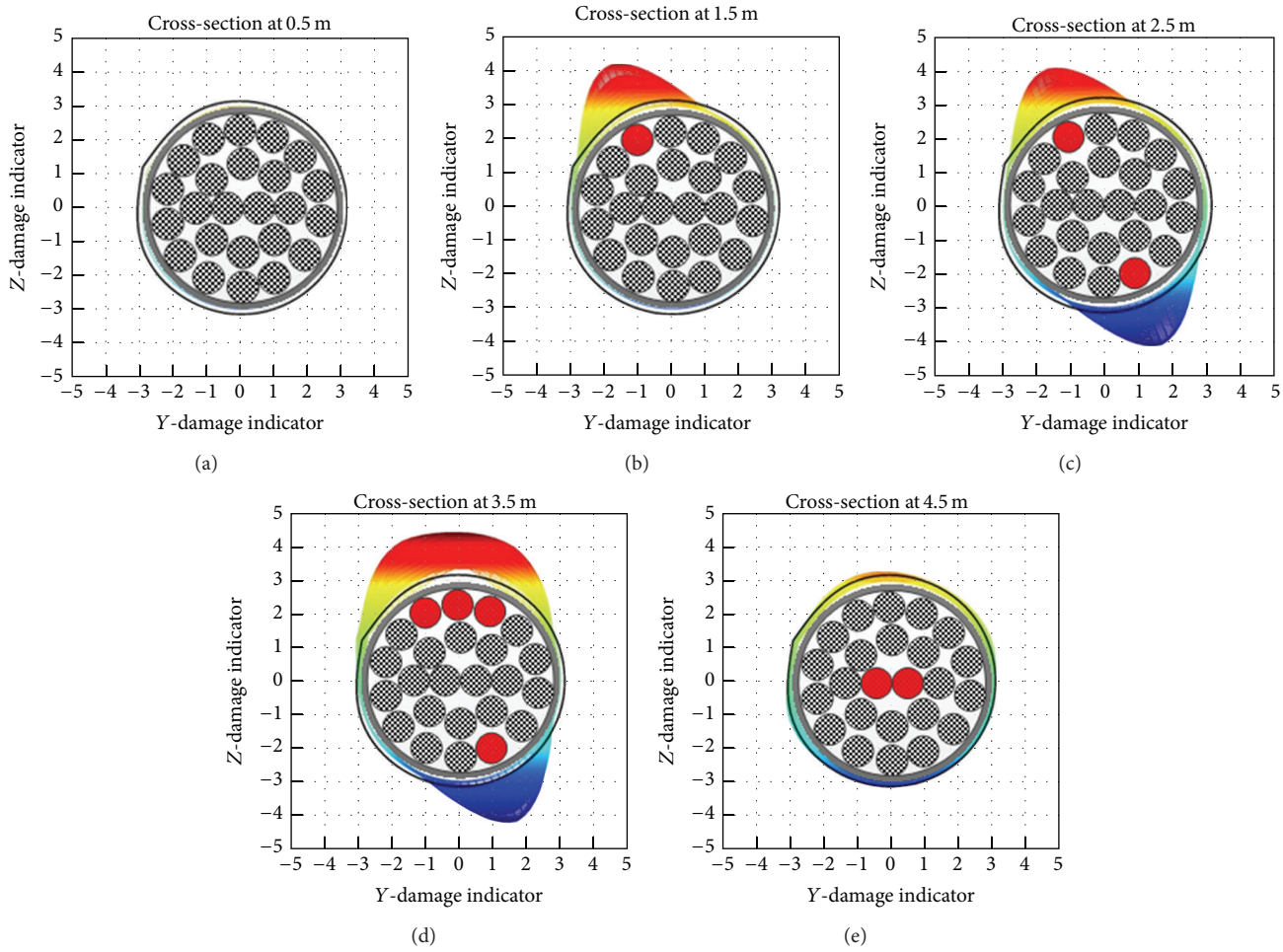

Figure 16: Visualized cross-sections with threshold cover.

This figure shows the damage parts highlighted by the threshold covering process. In addition, the circumferential direction and size of damage can be detected more efficiently by using cross-sections of the 3D MFL map, as shown in Figure 16.

Figure 16 shows visualized cross-sections with a threshold cover. Through this visualization work, it is expected that the damage in a cable can be detected by anyone, even by those with no professional experience with cable NDE.

4. Conclusions

An MFL sensor-based damage detection technique for the health monitoring of steel cables was proposed in this study. Fabrication of an MFL sensor head and a series of experimental studies and damage visualization were performed to verify the feasibility of the proposed technique, which was confirmed via the following observations.

(1) Magnetic flux leakage was detected at the locations of actual LF damage.

(2) The sensing sensitivity is dependent on the distance between the damage and the Hall sensors.

(3) The circumferential location of the damage can be judged by setting the sensors in an array.

(4) Flux leakage signals exceeded the thresholds based on a GEV distribution at the actual damage point.

(5) MFL signals were represented in a 3-dimensional graph that presents the size and location of LF damage at a glance.

(6) The MFL signals were represented with visualizations of the thresholds, by mapping the 3D graph onto a shape similar to the cable shape, which could efficiently provide information about the damage in the cable, from many angles.

Overall, these results demonstrated that the proposed steel cable monitoring technique using MFL sensors can be used to effectively detect local fault damage. In near future, this MFL- based cable NDE technique will be incorporated on cable-climbing robot to configure the automated cable monitoring system. In addition, it is expected that the proposed NDE technique can be utilized as an advanced tool for reliable cable monitoring for smart city infrastructures throughout the convergence with the various ubiquitous technologies.

Conflict of Interests

The authors declare that there is no conflict of interests regarding the publication of this paper.

Acknowledgments

This study was supported by the Basic Science Research Program through the National Research Foundation (NRF) funded by the Ministry of Education, Science and Technology of Korea (no. 2010-0023404) and the Core Research Project of the Super Long Span Bridge R&D Center (08 CTIP-E01) funded by the Korean Ministry of Land, Transport and Maritime Affairs (MLTM). Their complete support is greatly appreciated.

References

[1] S. Park, J. -W. Kim, C. Lee, and S. -K. Park, "Impedance-based wireless debonding condition monitoring of cfrp laminated concrete structures," *NDT & E International*, vol. 44, no. 2, pp. 232–238, 2011.

[2] C. Lee and S. Park, "Damage classification of pipelines under water flow operation using multi-mode actuated sensing technology," *Smart Materials and Structures*, vol. 20, no. 11, Article ID 115002, 9 pages, 2011.

[3] J. Min, S. Park, C. -B. Yun, C. -G. Lee, and C. Lee, "Impedance-based structural health monitoring incorporating neural network technique for identification of damage type and severity," *Engineering Structures*, vol. 39, pp. 210–220, 2012.

[4] C. Lee and S. Park, "De-bonding detection on a CFRP laminated concrete beam using self sensing-based multi-scale actuated sensing with statistical pattern recognition," *Advances in Structural Engineering*, vol. 15, no. 6, pp. 919–927, 2012.

[5] M. L. Wang, G. Wang, and Y. Zhao, *Sensing Issues in Civil Structural Health Monitoring*, Springer, Dordrecht, The Netherlands, 2005.

[6] M. L. Wang, Z. L. Chen, S. S. Koontz, and G. M. Lloyd, "Magnetoelastic permeability measurement for stress monitoring in steel tendons and cables," in *Nondestructive Evaluation of Highways, Utilities, and Pipelines IV*, vol. 3995 of *Proceedings of the SPIE*, pp. 492–500, March 2000.

[7] S. Sumitro, A. Jarosevic, and M. L. Wang, "Elasto-magnetic sensor utilization on steel cable stress measurement," in *Proceedings of the 1st Fib Congress*, pp. 79–86, Osaka, Japan, 2002.

[8] M. Göktepe, "Non-destructive crack detection by capturing local flux leakage field," *Sensors and Actuators A: Physical*, vol. 91, no. 1-2, pp. 70–72, 2001.

[9] C. Mandache, B. Shiari, and L. Clapham, "Defect separation considerations in magnetic flux leakage inspection," *Insight—Non-Destructive Testing and Condition Monitoring*, vol. 47, no. 5, pp. 289–293, 2005.

[10] H. R. Weischedel, "The inspection of wire ropes in service: a critical review," *Materials Evaluation*, vol. 43, no. 13, pp. 1592–1605, 1985.

[11] J. Lee, J. Hwang, J. Jun, and S. Choi, "Nondestructive testing and crack evaluation of ferromagnetic material by using the linearly integrated hall sensor array," *Journal of Mechanical Science and Technology*, vol. 22, no. 12, pp. 2310–2317, 2008.

[12] O. L. Atherton, "Magnetic inspection is key to ensuring safe pipelines," *Oil and Gas Journal*, vol. 87, no. 32, pp. 52–61, 1989.

[13] H. R. Weischedel and C. R. Chaplin, "Inspection of wire ropes for offshore applications," *Materials Evaluation*, vol. 49, no. 3, pp. 362–367, 1991.

[14] K. Mandal, D. Dufour, T. W. Krause, and D. L. Atherton, "Investigations of magnetic flux leakage and magnetic Barkhausen noise signals from pipeline," *Journal of Applied Physics*, vol. 30, no. 6, pp. 962–973, 1997.

[15] K. K. Tandon, "MFL tool hardware for pipeline inspection," *Materials Performance*, vol. 36, no. 2, pp. 75–79, 1997.

[16] K. Mandal and D. L. Atherton, "A study of magnetic flux-leakage signals," *Journal of Physics D*, vol. 31, no. 22, pp. 3211–3217, 1998.

[17] J. E. Lenz, "Review of magnetic sensors," *Proceedings of the IEEE*, vol. 78, no. 6, pp. 973–989, 1990.

[18] E. Ramsden, *Hall-Effect Sensors: Theory and Applications*, Newnes, Oxford, UK, 2006.

[19] S. Coles, *An Introduction to Statistical Modeling of Extreme Values*, Springer, Berlin, Germany, 2001.

Hindawi Publishing Corporation
Shock and Vibration
Volume 2014, Article ID 895693, 8 pages
http://dx.doi.org/10.1155/2014/895693

Research Article

Fully Noncontact Wave Propagation Imaging in an Immersed Metallic Plate with a Crack

Jung-Ryul Lee,[1] Jae-Kyeong Jang,[1] and Cheol-Won Kong[2]

[1] *Department of Aerospace Engineering and LANL-CBNU Engineering Institute Korea, Chonbuk National University, 664-14 Deokjin-dong, Deokjin-gu, Jeonju, Chonbuk 561-756, Republic of Korea*
[2] *Structures and Materials Department, Korea Aerospace Research Institute, Daejeon 305-333, Republic of Korea*

Correspondence should be addressed to Jung-Ryul Lee; leejrr@jbnu.ac.kr

Received 12 February 2013; Accepted 11 June 2013; Published 5 May 2014

Academic Editor: Gyuhae Park

Copyright © 2014 Jung-Ryul Lee et al. This is an open access article distributed under the Creative Commons Attribution License, which permits unrestricted use, distribution, and reproduction in any medium, provided the original work is properly cited.

This study presents a noncontact sensing technique with ultrasonic wave propagation imaging algorithm, for damage visualization of liquid-immersed structures. An aluminum plate specimen (400 mm × 400 mm × 3 mm) with a 12 mm slit was immersed in water and in glycerin. A 532 nm Q-switched continuous wave laser is used at an energy level of 1.2 mJ to scan an area of 100 mm × 100 mm. A laser Doppler vibrometer is used as a noncontact ultrasonic sensor, which measures guided wave displacement at a fixed point. The tests are performed with two different cases of specimen: without water and filled with water and with glycerin. Lamb wave dispersion curves for the respective cases are calculated, to investigate the velocity-frequency relationship of each wave mode. Experimental propagation velocities of Lamb waves for different cases are compared with the theoretical dispersion curves. This study shows that the dispersion and attenuation of the Lamb wave is affected by the surrounding liquid, and the comparative experimental results are presented to verify it. In addition, it is demonstrated that the developed fully noncontact ultrasonic propagation imaging system is capable of damage sizing in submerged structures.

1. Introduction

Lamb waves are useful for the detection of damages in thin sheet materials and tubular properties. Extensive developments in the application of the Lamb wave provide a foundation for the inspection of many products in the aerospace, pipe, pipeline, and transportation industries. Lamb waves are composed of a combination of two fundamental modes: symmetric and antisymmetric. For each of these modes, their velocity (phase or group) of Lamb waves varies with frequency; in other words, they are all dispersive. And, their energy is spread in time and space as it propagates. Hence, as the distance increases, the signal duration increases and the peak amplitude decreases. Also, attenuation is of concern in specimens immersed in liquid, because of leaky Lamb waves. For example, when guided Lamb waves are propagating in a plate that is placed in vacuum or in air, both plate surfaces are considered to be untrammeled. But, if one or both of the surfaces are in contact with liquid, the guided plate waves become leaky Lamb waves, because the energy of the wave leaks to the adjacent liquid.

Ultrasonic waves are increasingly being investigated for nondestructive evaluation (NDE) and structural health management (SHM) of engineering systems, because they can propagate over long distances and cover relatively large areas of thin plates. They can travel comparatively large distances with little attenuation and offer the advantage of exploiting one or more of the phenomena associated with transmission, reflection, scattering, and mode conversion. A few studies have been reported concerning the use of ultrasonic waves for underwater structures.

Na and Kundu [1] investigated the feasibility of flexural cylindrical guided waves for inspecting the mechanical defects of underwater pipes, using a transducer holder and its coupling mechanism. Mijarez et al. [2] developed a system composed of a waterproof transmitter and a seawater-activated battery package, to monitor the tubular cross-beam members used in offshore steel structures. Chen et

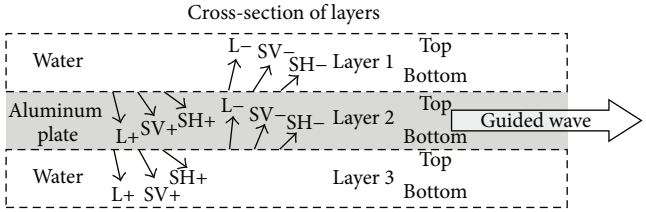

Figure 1: Geometry of a three-layer flat plate system showing the partial waves in each layer (L+−, SV+−, and SH+−) that combine to produce a guided wave [7].

al. [3] proposed a damage identification approach capitalizing on the fundamental asymmetric Lamb wave. Aristégui et al. [4] presented wave propagation characteristics of pipes with fluid loading on both inside and outside of the pipe, which was affected by viscosity of the media. A noncontact approach was also used for the generation and detection of Lamb waves, because of the circumstance of the target to be inspected. Rizzo et al. [5] presented a SHM technique using a hybrid laser/immersion transducer system for the detection of damage in submerged structures. Xu et al. [6] presented a comparison between theoretical predictions and experimental results, to consistently reveal the propagation properties of Lamb waves on a specimen that was in contact with different liquids on both of its surfaces, using laser generation and laser Doppler vibrometer (LDV) sensing.

In this paper, variation of certain mode is analyzed, to evaluate the size and shape of the damage for a test specimen in different boundary conditions: free plate and immersed plate with liquid. A laser ultrasonic propagation imaging (UPI) system capable of fully noncontact inspection of immersed structures is developed, through the modification of the sensor-contact UPI system, based on piezoelectric sensing. In addition, this study visualizes that the Lamb wave propagation characteristics, such as dispersion and attenuation, are affected by liquid and comparative experimental results are presented to verify it.

2. Lamb Waves Propagation in Immersed Thin Plates

2.1. Lamb Waves. A wave mode is defined as the manner of particle movement during wave propagation. In a solid material, particles can oscillate in four primary modes: longitudinal waves, shear transverse waves, surface waves, and plate waves in thin materials. These waves occur as a result of the elastic deformation of material. Lamb waves are complex vibration waves that propagate parallel to the specimen surface. Propagation of Lamb waves depends on the density and the elastic material properties of a component. They are also affected by the test frequency and thickness of structure.

Lamb waves can be generated in a plate with free boundaries, with an infinite number of modes, for both symmetric and antisymmetric displacements within the layer.

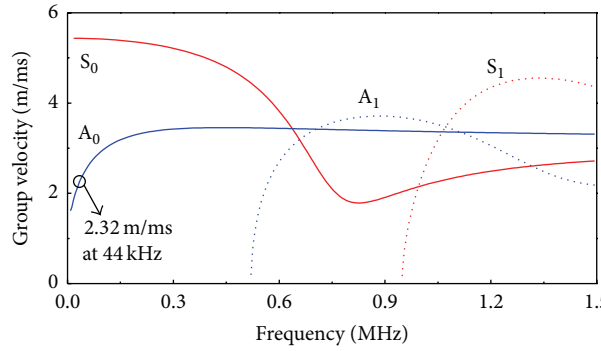

(a)

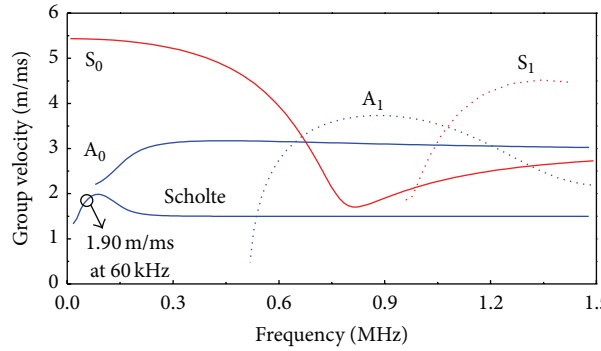

(b)

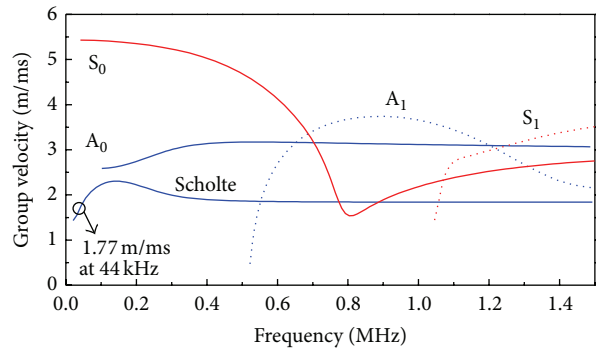

(c)

Figure 2: Group velocity dispersion curves of 3 mm thick aluminum plate: (a) free plate, (b) immersed in water, and (c) immersed in glycerin.

It is stipulated that the symbols S_i and A_i ($i = 0, 1, \ldots$) stand for the symmetric and antisymmetric modes, respectively, and the subscript i implies the order of the mode. Symmetric Lamb waves move in a symmetric fashion about the median plane of the plate. Wave motion in the symmetrical mode is most efficiently produced when the exciting force is parallel to the plate. The antisymmetric Lamb wave mode is often called the "flexural mode" because a large portion of the motion moves in a normal direction to the plate, and a little motion occurs in the direction parallel to the plate. In the laser pulse excitation used in this paper, the magnitude of S_i modes (in-plane motion) is normally smaller than that of A_i modes.

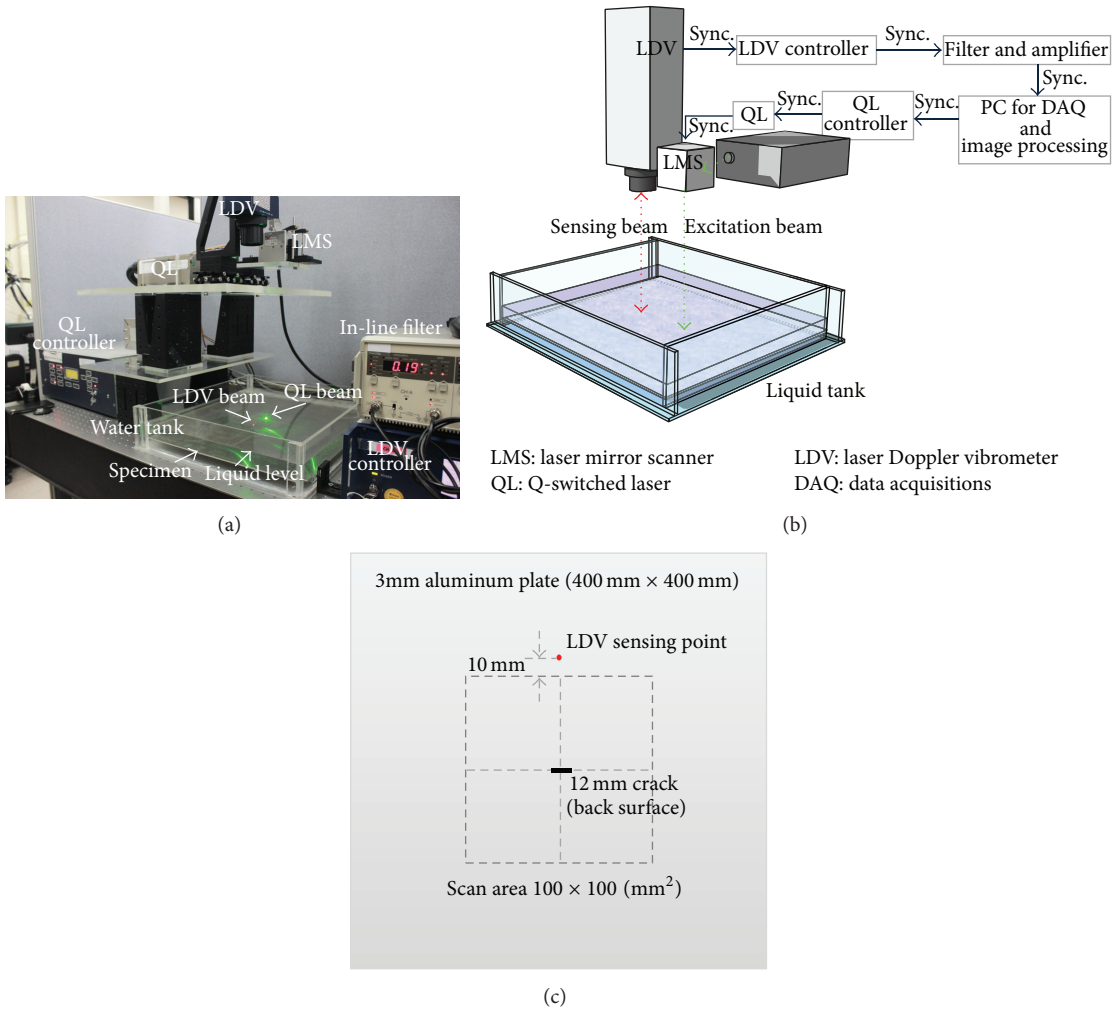

Figure 3: Experimental setup: (a) photo and (b) schematic of the UPI system for submerged structural inspection and (c) specimen with a back surface crack for immersion.

2.2. Wave Propagation with Attenuation in Submerged Plates. When a plate is submerged in an infinite liquid, the Lamb wave propagation energy will be leaked into the liquid. This wave is called a leaky Lamb wave. For example, when a plate is immersed in a liquid, such as water or glycerin, symmetric modes will mostly be retained in the plate, because it is difficult for in-plane particle motion to cross the plate-liquid interface. However, as the antisymmetric modes mostly have out-of-plane displacements, they will leak into the fluid. The leaky Lamb waves behave differently from Lamb waves in free solid. For instance, the dispersion equations associated with the first antisymmetric mode (A_0) show a large discrepancy between the free solid and fluid-coupled solid [8].

In this research, the sample geometry of a three-layer flat and thin plate system was considered, as shown in Figure 1. According to [7], the partial waves are assembled by matching the boundary conditions at each layer. At a certain frequency, wave number, and attenuation combination, these partial waves combine to form a guided Lamb wave, which propagates down to the longitudinal direction. Here, L+−, SV+−, and SH+− stand for longitudinal waves, shear vertical waves, and shear horizontal waves, respectively. In addition, + denotes the downward direction and the − denotes the upward direction of the plate case. We did not consider the SH+− waves, because they were difficult to generate by laser excitation.

2.3. Dispersion Curves in Different Boundary Conditions. If the plate is surrounded by liquid or solid, wave attenuation also occurs due to the leakage of bulk waves into the medium surrounding the waveguide. In this study, to investigate the acoustic properties of the leaky Lamb wave, dispersion curves for a 3 mm thick aluminum plate in three different cases were calculated; free plate and immersed plate in water and in glycerin, as presented in Figure 2. In an aluminum plate immersed in water or glycerin, the A_0 mode disappeared, and its energy was converted to Scholte wave below about 100 kHz. Group velocity of the A_0 mode became slower than that in the free aluminum plate. The Scholte wave is an interface wave between a liquid medium and a solid medium and decreases exponentially away from the surface, into the liquid medium [9].

3. Noncontact Laser Inspection of Immersed Plates

3.1. Ultrasonic Propagation Imaging System for Submerged Structural Inspection. A photo and schematic of the ultrasonic propagation imaging (UPI) system to inspect submerged structures are shown in Figures 3(a) and 3(b). The system was constructed with a laser Doppler vibrometer (LDV), in-line signal conditioner with filters and amplifiers, a personal computer (PC) with a data acquisition and signal processing platform, and a Q-switched solid-state diode pumped laser (QL). The laser pulses were generated by Q-switching technique in QL, at a pulse repetition rate of 200 Hz. The laser beam with a wavelength of 532 nm and energy of 1.2 mJ was directed to a laser mirror system (LMS). The laser beam was reflected toward the target specimen by a pair of laser mirrors in the LMS.

As shown in Figure 3(c), an aluminum plate (400 mm × 400 mm × 3 mm) with a 12 mm long and 2 mm deep artificial crack in the opposite surface was used as the specimen. The scanning area and interval were 100 mm × 100 mm and 0.5 mm, respectively and thus it took 202 seconds to scan the area. The 633 nm sensing laser beam of the LDV was impinged at a point 10 mm above the square scanning area. The typical reflection film was not used on the plate surface.

Ultrasonic sensing using the LDV is based on the detection of the Doppler shift of the laser light. The Doppler shift refers to the frequency shift of the light that is reflected back from the vibrating object to the source. The signal processing platform visualizes the wave propagation in the immersed specimen, using the basic ultrasonic wave propagation imaging (UWPI) algorithm. The UWPI is a visualization technology of propagation for in-plane guided wave or through-the-thickness wave, in the time or frequency domain, based on 3D data processing [10].

In the experiments, when the laser beam impinged the surface of the immersed target specimen, an ultrasonic wave was created at the affected point. The wave was propagated over the specimen and reached the LDV. The time domain ultrasonic wave measured by the LDV was amplified and band-pass filtered between 40 kHz and 140 kHz and then stored in the PC. The experimental case studies were performed with three different cases: free plate and immersed plate in water and in glycerin, as shown in Figure 4.

3.2. Ultrasonic Wave Propagation Imaging in Submerged Plates. The proposed system for submerged structural inspection was able to generate UWPI video clips within 1 s after scanning. Figure 5 shows the freeze-frame at 53.5 μs extracted from the video clip, as the UWPI result in the free plate. On the other hand, Figures 6 and 7 show the freeze-frames at 61 μs and 63 μs extracted from the videos as the UWPI results in the water- and glycerin-immersed plates, respectively. Since the proposed system was designed with both remote excitation and sensing laser beams capable of penetrating the liquid, the UWPI results were successfully obtained. All the freeze-frames in Figures 5–7 were taken at the moments when the maximum ultrasonic amplitudes

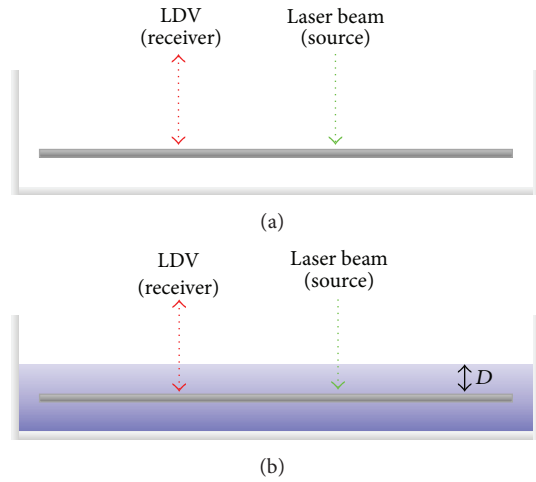

Figure 4: Experimental model in different conditions: (a) free plate in air and (b) immersed plate.

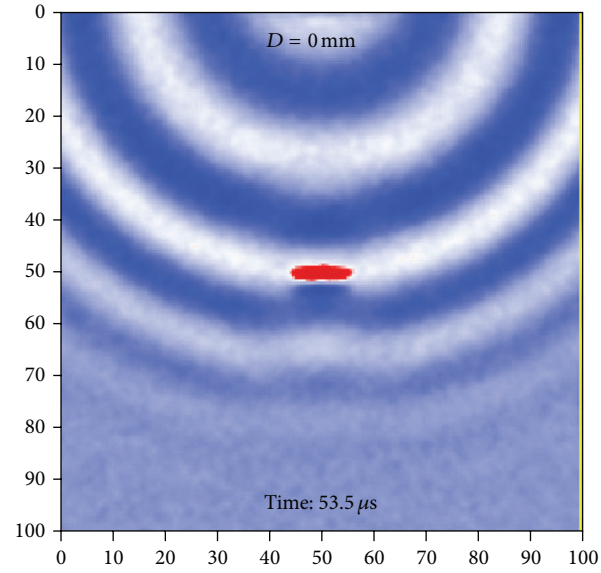

Figure 5: Snapshot at 53.5 μs taken from the ultrasonic wave propagation video clip in the free plate.

at the crack location appeared. As a result, it has been verified that the velocity of wave propagation was reduced in the immersed plates, due to the high densities of the surrounding fluid (air = 1 kg/m^3, water = 1,000 kg/m^3, and glycerin = 1,258 kg/m^3). In addition, as shown in Figures 6 and 7, including the results for different depth (D) of the liquid, such as 10 mm, 40 mm, and 70 mm, the propagation time was not affected by the tested depth of the water. In other words, even 10 mm deep surrounding liquid can be considered as an infinite surrounding medium.

In addition to the successful UWPI in the submerged specimens, the back surface crack that the water- or glycerin-immersed specimen encompasses was visualized in the form of sudden phase change and high peak-to-peak amplitude at the crack location, (50, 50), in the freeze-frames of

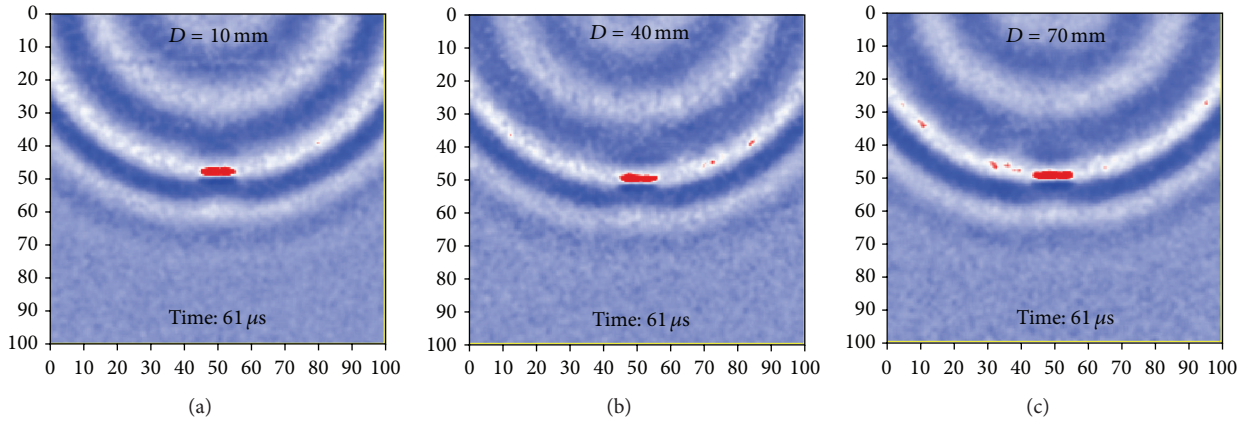

Figure 6: Ultrasonic wave fields at 61 μs in the water-immersed plate according to the water depth: (a) D = 10 mm, (b) 40 mm, and (c) 70 mm (the same color scale for (a) to (c)).

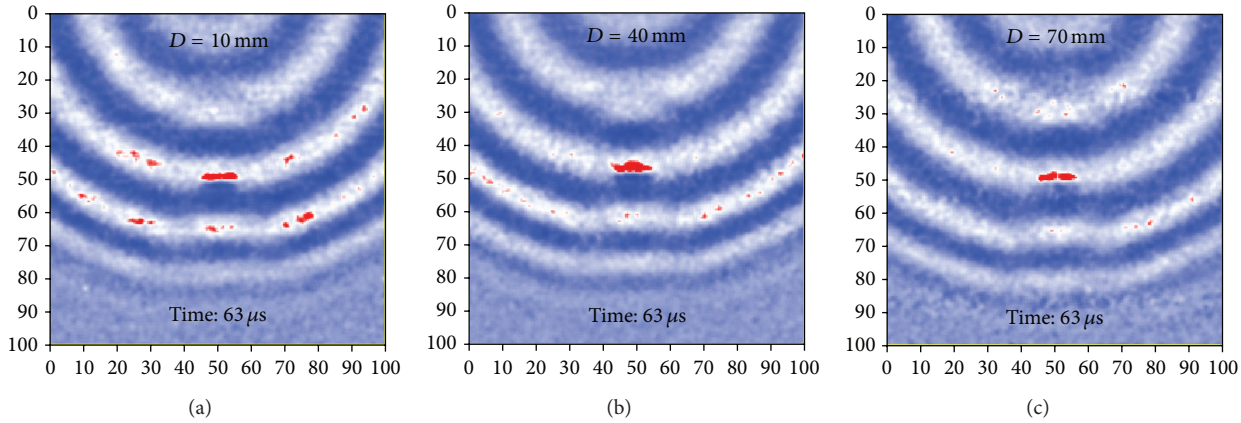

Figure 7: Ultrasonic wave fields at 63 μs in the glycerin-immersed plate according to the glycerin depth: (a) D = 10 mm, (b) 40 mm, and (c) 70 mm (the same color scale for (a) to (c)).

Figures 7 and 8, respectively. However, in contrast to the free plate, a low SNR problem was identified in the immersed conditions, because of the effect of the surrounding liquid. As studied in Section 2.2, the surrounding liquid caused leaky Lamb wave occurrence. As concluded in Figures 6 and 7, the energy losses within the liquid of excitation and the sensing laser beams themselves were negligible, because when the depth of liquid was increased, the SNR did not change considerably. For this reason, repeat scanning technology [11] was implemented in the proposed system for the submerged structural inspection, to increase the SNRs to be similar to the SNR level in the structure in air. The repeat scanning technique can play an important role in real-world submerged structural inspection. In the experiments, the scanning area was repeatedly scanned 10 times. The ten signals obtained at each scanning grid point were averaged, and the averaged waveforms were used as the input data for the UWPI algorithm [12] to generate the ultrasonic wave propagation video clips.

As compared between Figures 6(a) and 8(b) and between Figures 7(a) and 8(c), the respective SNRs under the water- and glycerin-immersed plate conditions were highly improved. The SNR changes before and after the repeat scanning are summarized in Table 1, where the SNR was evaluated in the way presented in Figure 9. On the other hand, the SNR improvement in the free plate by repeat scanning was not considerable, because the original raw signals already had low noise level. As compared between Figures 5, 8(b), and 8(c), the repeat scanning now made the SNRs in the water- and glycerin-immersed plate conditions reach similar levels to that in the free plate.

Figure 10 shows the amplitude distributions along the wavefront (s-axis) at the moments of the maximum ultrasonic amplitude in the crack location, as indicated in Figure 8. And, the s-axis is formed along the same distance from the sensor location. The artificial crack length of 12 mm was estimated at 11.54 mm in the free plate, as shown in Figure 10(a). As also presented in Figures 10(b) and 10(c), the 12 mm long crack was evaluated by the proposed system as 11.29 mm in the water-immersed plate and 10.87 mm in the glycerin-immersed plate. These results were represented by two standard deviations away from the noise mean.

Figure 8 shows the spatial domain freeze-frames of the UWPI videos, while Figure 11 shows the time domain signals

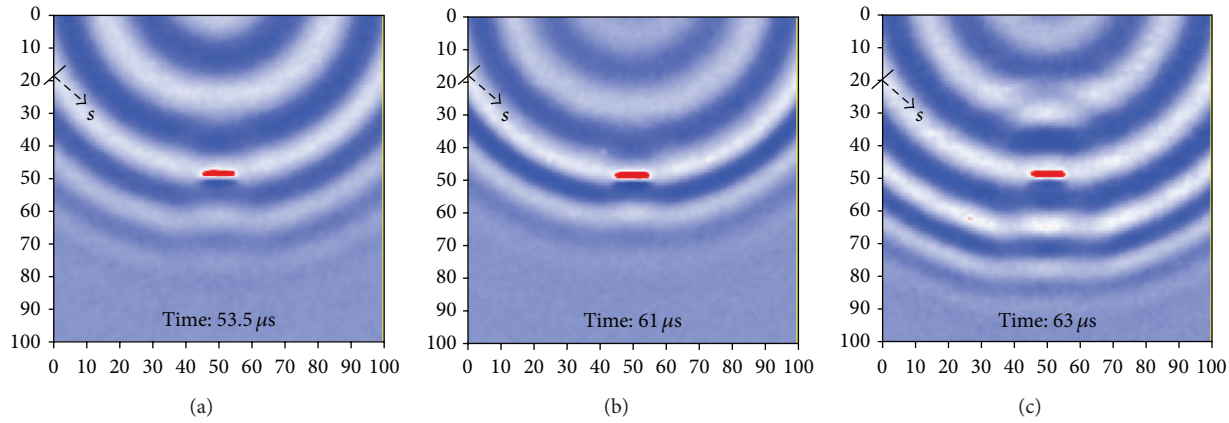

Figure 8: Ultrasonic wave fields obtained by the repeat scanning method (10 times): (a) free plate, (b) immersed plate in water (D = 10 mm), and (c) immersed plate in glycerin (D = 10 mm).

Table 1: SNR comparison related to immersion and repeat scanning.

Number of repeat scanning	Signal-to-noise ratio (dB)		
	Free plate	Water-immersed plate	Glycerin-immersed plate
1	26.01	22.67	20.71
10	28.80	28.23	26.18

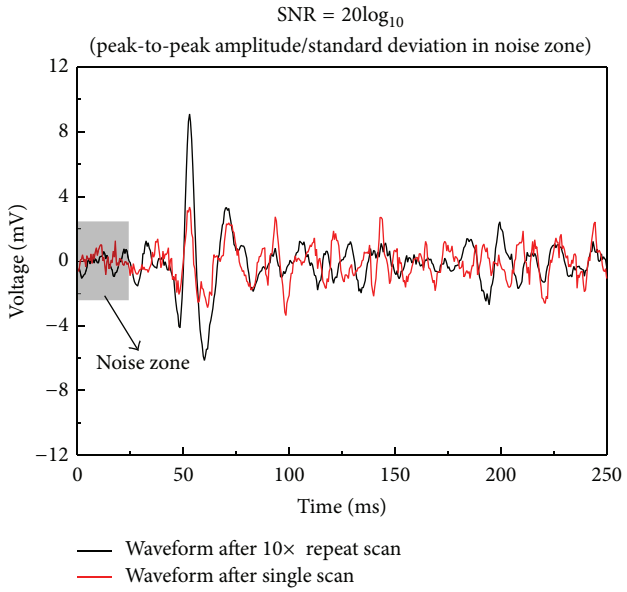

Figure 9: Typical time domain waveforms extracted at (20 and 25) in Figures 6(a) and 8(b) for SNR evaluation (waveform comparison after single scan and 10× repeat scan for water-immersed plate condition) and definition for SNR calculation.

extracted at the impinging point of the center of the crack. The only A_0 or Scolte modes were visible in these time domain signals. The S_0 modes were not observed even in the UWPI videos. In Figure 11(a), the arrival times of the Scolte modes in the water- and glycerin-immersed plates show time delays of 7.5 μs and 9.5 μs, respectively, and the amplitudes of the Scolte modes waves in those conditions show decrease of 4.2 mV and 10.1 mV, respectively, compared with the A_0 mode of the free plate.

Since the UWPI freeze-frames of Figures 5–7 show the moments of the maximum ultrasonic amplitudes at the crack location, the freezing times also imply the relative ultrasonic time-of-flights in the free plate and water- and glycerin-immersed plates, respectively. This information was used to calculate the experimental group velocities for the three different cases, which were determined at 2.35 m/ms, 1.82 m/ms, and 1.72 m/ms, respectively. This result was comparable to the theoretical results in the wave dispersion curves depicted in Figure 2 where the central frequency for each case was estimated based on fast Fourier transform and Hilbert transform as shown in Figure 11(b). The theoretical group velocities at the 44 kHz for the free plate, 60 kHz for the water immersion, and 44 kHz for the glycerin immersion stood at 2.32 m/ms, 1.90 m/ms, and 1.69 m/ms, respectively.

4. Conclusion

In this paper, a noncontact laser UPI system for submerged structural crack visualization was proposed. A 532 nm Q-switched solid-state laser and a 633 nm laser Doppler vibrometer were integrated into the system, for remote excitation and sensing, respectively. The tested specimen was an aluminum plate with dimensions of 400 mm × 400 mm × 3 mm, which encompassed a back surface crack of 12 mm × 1 mm × 2 mm in the middle of the plate. Three cases were studied: free plate, water-immersed plate, and glycerin-immersed plate.

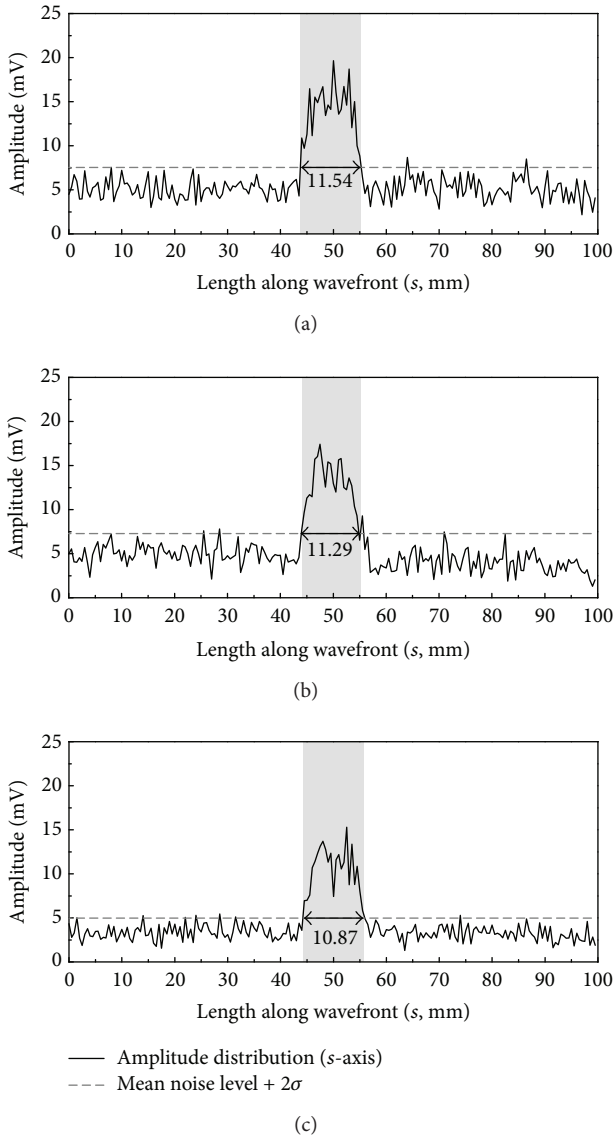

FIGURE 10: Crack length evaluation with the wave fields obtained in (a) the free plate (single scan), (b) the water-immersed plate (10 times scans), and (c) the glycerin-immersed plate (10 times scans).

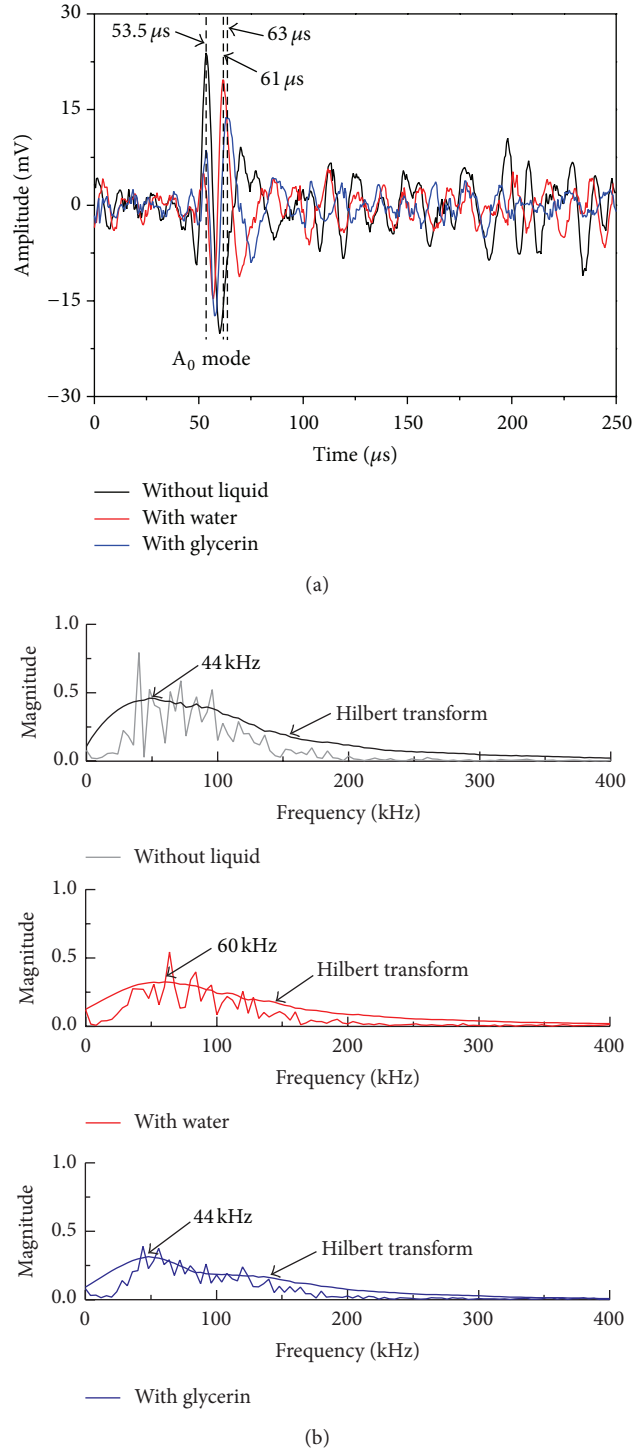

FIGURE 11: Signals extracted at the impinging point of the center of crack: (a) time domain and (b) frequency domain.

First, theoretical wave dispersion curves were plotted, to understand the theoretical difference between the free and immersed plates. Then, wave propagation imaging for the submerged plates was successfully performed by the proposed system, where a laser mirror scanner and LDV were used for excitation laser scanning and noncontact sensing. The detected waves in the immersed plates showed delays in arrival time and reduction in amplitude, compared to the free plate, because of the surrounding liquid. In addition, the SNR was deteriorated in the submerged plates, because of the leaky Lamb wave. Therefore, the repeat scanning technique was incorporated into the system, to increase SNR up to a similar level to the single scan of the free plate and to prepare for real-world application that would involve more complex and thicker immersed structures. Finally, the proposed system successfully visualized the wave propagation and showed damage evaluation capability for the submerged structural back surface crack. The 2 mm deep and 12 mm long back surface crack was evaluated by the proposed system as 11.29 mm in the water-immersed plate and 10.87 mm in the glycerin-immersed plate.

Conflict of Interests

The authors declare that there is no conflict of interests regarding the publication of this paper.

Acknowledgments

This research was supported by the Leading Foreign Research Institute Recruitment Program (2011-0030065) and the Basic Science Research Program (2011-0010489) through the National Research Foundation of Korea, funded by the Ministry of Education, Science and Technology (2011-0030065) and by the university collaboration enhancement project of the Korea Aerospace Research Institute.

References

[1] W.-B. Na and T. Kundu, "Underwater pipeline inspection using guided waves," *Journal of Pressure Vessel Technology*, vol. 124, no. 2, pp. 196–200, 2002.

[2] R. Mijarez, P. Gaydecki, and M. Burdekin, "Flood member detection for real-time structural health monitoring of subsea structures of offshore steel oilrigs," *Smart Materials and Structures*, vol. 16, no. 5, pp. 1857–1869, 2007.

[3] J. Chen, Z. Su, and L. Cheng, "Identification of corrosion damage in submerged structures using fundamental anti-symmetric Lamb waves," *Smart Materials and Structures*, vol. 19, no. 1, Article ID 015004, 12 pages, 2010.

[4] C. Aristégui, M. J. S. Lowe, and P. Cawley, "Guided waves in fluid-filled pipes surrounded by different fluids," *Ultrasonics*, vol. 39, no. 5, pp. 367–375, 2001.

[5] P. Rizzo, J.-G. Han, and X.-L. Ni, "Structural health monitoring of immersed structures by means of guided ultrasonic waves," *Journal of Intelligent Material Systems and Structures*, vol. 21, no. 14, pp. 1397–1407, 2010.

[6] X. Xu, J. Goossens, G. Shkerdin, and C. Glorieux, "Effect of loading a plate with different liquids on the propagation of lamb-like waves studied by laser ultrasonics," *IEEE Transactions on Ultrasonics, Ferroelectrics, and Frequency Control*, vol. 55, no. 3, pp. 675–685, 2008.

[7] B. Pavlakovic and M. Lowe, *DISPERSE: User's Manual Version 2.0.11*, Imperial College, University of London, Non-Destructive Testing Laboratory, 2001.

[8] P. Moilanen, P. H. F. Nicholson, V. Kilappa, S. Cheng, and J. Timonen, "Measuring guided waves in long bones: modeling and experiments in free and immersed plates," *Ultrasound in Medicine & Biology*, vol. 32, no. 5, pp. 709–719, 2006.

[9] F. B. Cegla, *Ultrasonic waveguide sensors for fluid characterisation and remote sensing [Ph.D. thesis]*, University of London, 2006.

[10] J.-R. Lee and C.-Y. Yoon, "Development of an optical system for simultaneous ultrasonic wave propagation imaging at multipoints," *Experimental Mechanics*, vol. 50, no. 7, pp. 1041–1049, 2010.

[11] J. R. Lee, S. Y. Chong, N. Sunuwar, and C. Y. Park, "Repeat scanning technique to improve signal-to-noise ratio for laser ultrasonic propagation inspection for composite structures," *Measurement Science and Technology*, vol. 24, Article ID 085201, 2013.

[12] C. C. Chia, J.-R. Lee, and H.-J. Shin, "Hot target inspection using a welded fibre acoustic wave piezoelectric sensor and a laser-ultrasonic mirror scanner," *Measurement Science and Technology*, vol. 20, no. 12, Article ID 127003, 8 pages, 2009.

Hindawi Publishing Corporation
Shock and Vibration
Volume 2014, Article ID 725030, 14 pages
http://dx.doi.org/10.1155/2014/725030

Research Article

Flaw Imaging Technique for Plate-Like Structures Using Scanning Laser Source Actuation

Changgil Lee and Seunghee Park

Department of Civil and Environmental Engineering, Sungkyunkwan University, Cheoncheon-Dong, Jangan-Gu, Suwon, Gyunggi-do 440-746, Republic of Korea

Correspondence should be addressed to Seunghee Park; shparkpc@skku.edu

Received 6 December 2012; Accepted 14 March 2013; Published 27 April 2014

Academic Editor: Gyuhae Park

Copyright © 2014 C. Lee and S. Park. This is an open access article distributed under the Creative Commons Attribution License, which permits unrestricted use, distribution, and reproduction in any medium, provided the original work is properly cited.

Recently, the longitudinal, shear, and surface waves have been very widely used as ultrasonic wave-based exploration methods to identify internal defects of host structures. In this context, a noncontact nondestructive testing (NDT) method is proposed to detect the damage of plate-like structures and to identify the location of the damage. To achieve this goal, a scanning laser source actuation technique is utilized to generate a guided wave and scans a specific area to find damage location more precisely. The ND:YAG pulsed laser is used to generate Lamb wave and a piezoelectric sensor is installed to measure the structural responses. The measured responses are analyzed using 3-dimensional Fourier transformation (3D FT). The damage-sensitive features are extracted by wavenumber filtering based on the 3D FT. Then, flaw imaging techniques of a plate-like structure are conducted using the damage-sensitive features. Finally, the plates with notches are investigated to verify the effectiveness and the robustness of the proposed NDT approach.

1. Introduction

Recently, there have been increasing demands on structural 2 health monitoring (SHM) and nondestructive testing (NDT) in the fields of civil, mechanical, and aerospace engineering and so on to prevent losses of life and property by continuously monitoring the systems. Especially, local monitoring methodologies have been studied to overcome the limitation of global monitoring techniques [1–4]. Effective SHM/NDT methods must be intuitive so that inspection results can be easily understandable and must have high throughput [5]. To tackle this issue, a lot of researches based on acoustic and ultrasonic technologies have been proposed using laser interferometry, laser vibrometer, pulsed laser, and so on because the ultrasonic waves are sensitive to the mechanical properties of structures, while the wave responses are hardly affected by radiation [5]. Holography based imaging technique, one of the full-field ultrasonic wave imaging techniques, requires highly diffusive target surface. Also, holographic images can be obtained clearly in dark environments, and hence this method is not suitable to remote automatic inspection although this has noncontact inspection capability [6]. Dynamic responses can be collected by laser Doppler vibrometry which measures vibrational velocity of target structures. Although the performance of the laser Doppler vibrometry is improved in terms of scan angles and automatic focusing [7], it has still disadvantage that retroreflective film should be attached on target surfaces to improve signal-to-noise ratio when a scanning head is located far from the target [8–10]. In contrast, laser interferometry, which also senses vibration responses of target structures, works well without the retroreflective film, but its performance has not been proved when the distance between scanning head and target surface is greater than 0.5 m [11, 12]. To overcome these drawbacks, a laser beam pulse can be used to generate ultrasonic waves. The laser beam pulse can provide many advantages including fast wave generation with low pulse energy, high spatial resolution, inspection ability on complex target, and so on [5].

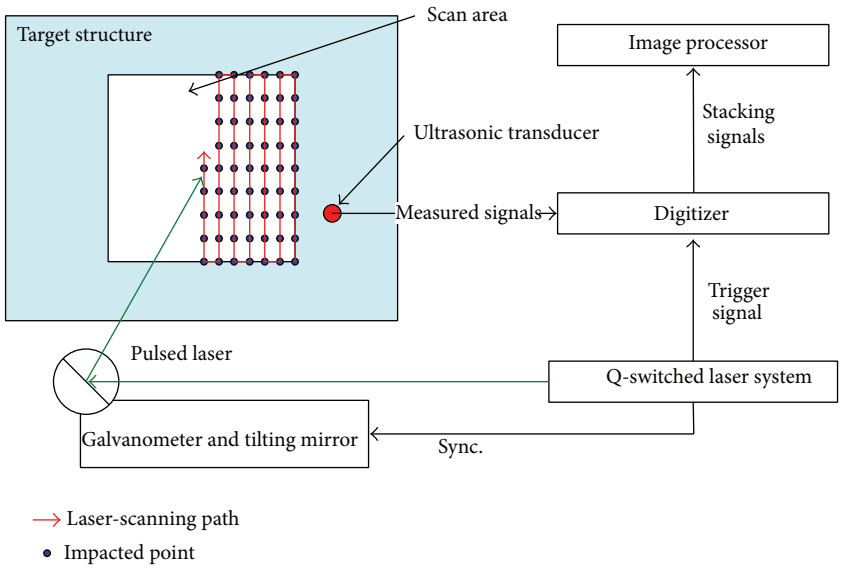

Figure 1: A scheme of an ultrasonic wave propagation imaging system based on a UWPI laser system.

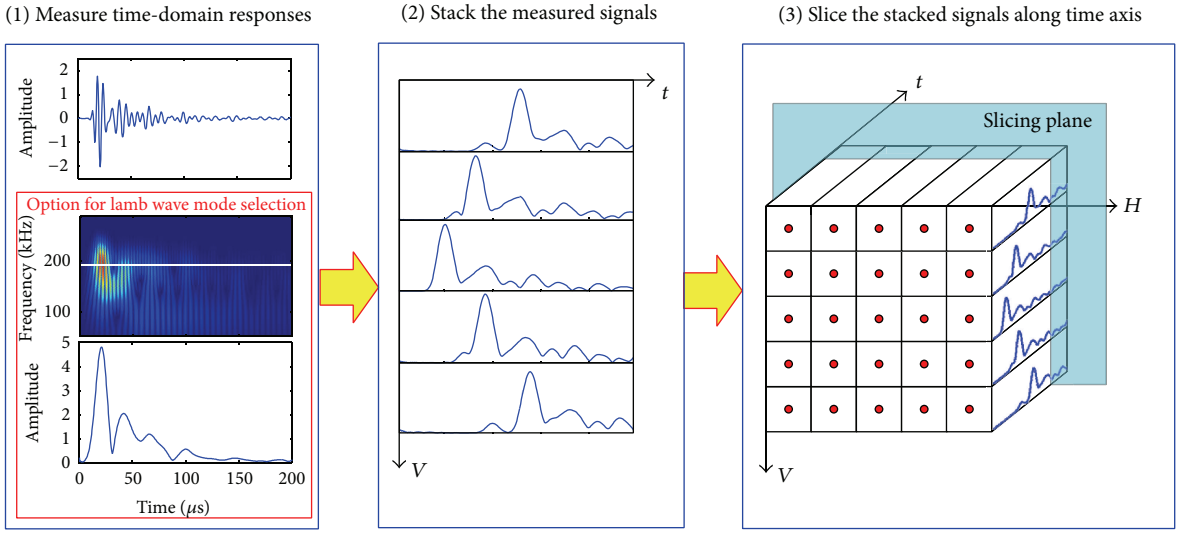

Figure 2: A scheme of an ultrasonic wave propagation imaging algorithm.

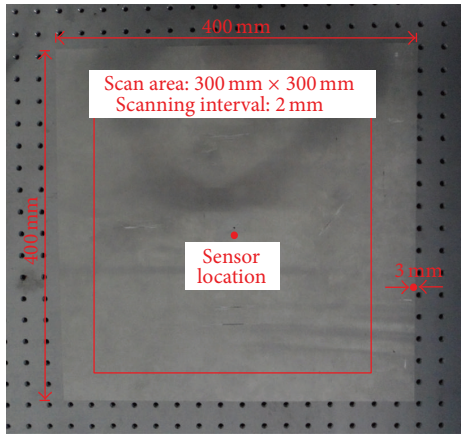

Figure 3: An aluminum plate and scanning information.

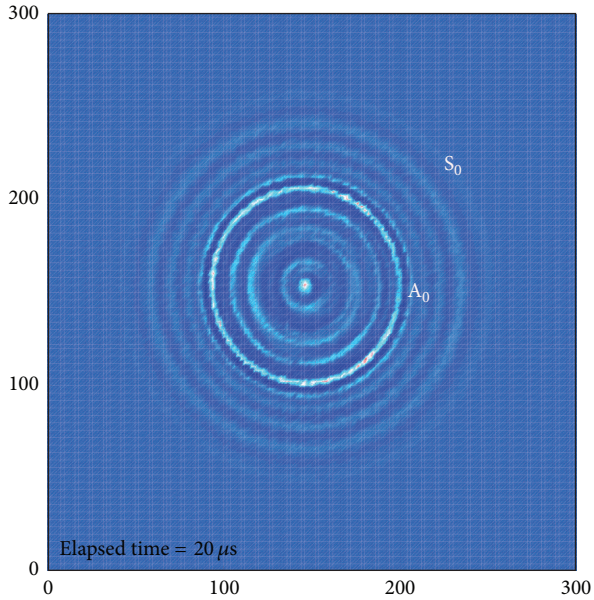

FIGURE 4: UWPI snapshot at 20 μs.

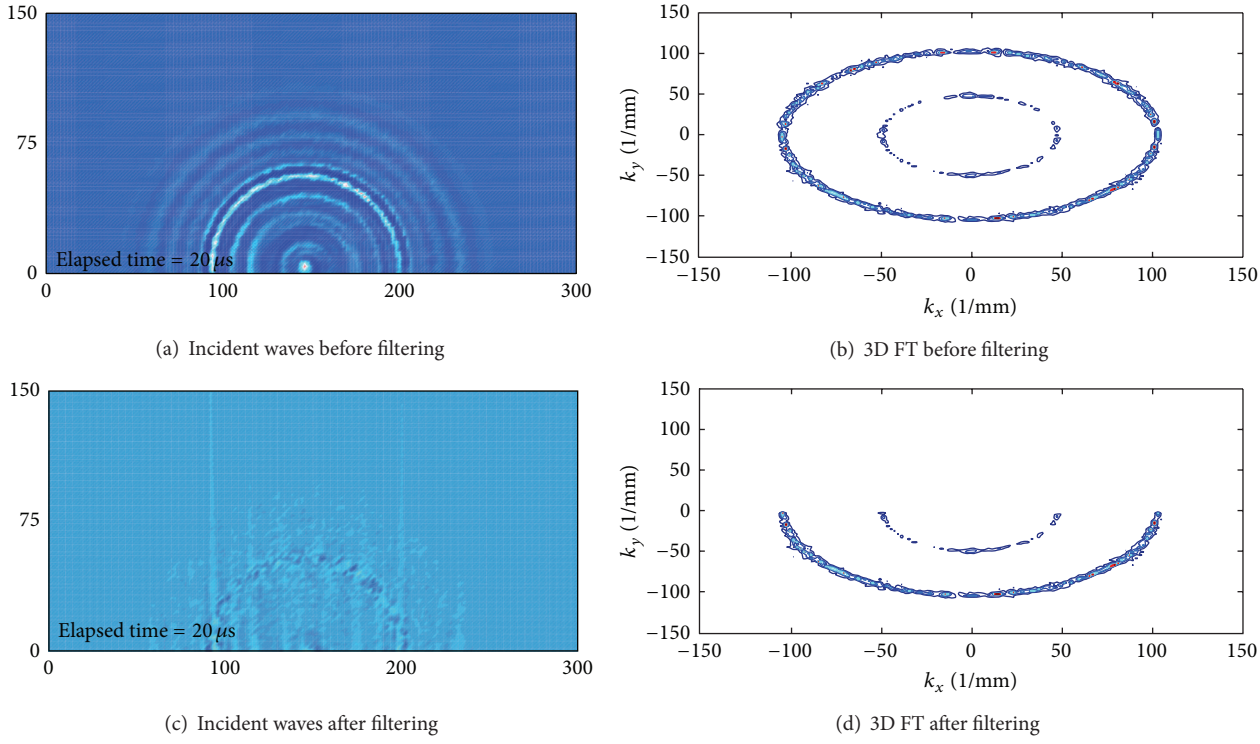

(a) Incident waves before filtering

(b) 3D FT before filtering

(c) Incident waves after filtering

(d) 3D FT after filtering

FIGURE 5: Elimination of upward incident waves by wavenumber filtering.

In this paper, ultrasonic wave propagation is visualized using ND:YAG pulsed laser and a flaw image is constructed based on wavenumber filtering and root mean square (RMS). The ND:YAG pulsed laser is used to generate Lamb wave and a piezoelectric sensor is installed to measure the structural responses. The measured responses are analyzed using 3D FT and then the damage-sensitive features are extracted by wavenumber filtering and RMS [13, 14]. Then, flaw imaging technique of a plate-like structure is conducted using the damage-sensitive features. Finally, the plate with a notch is

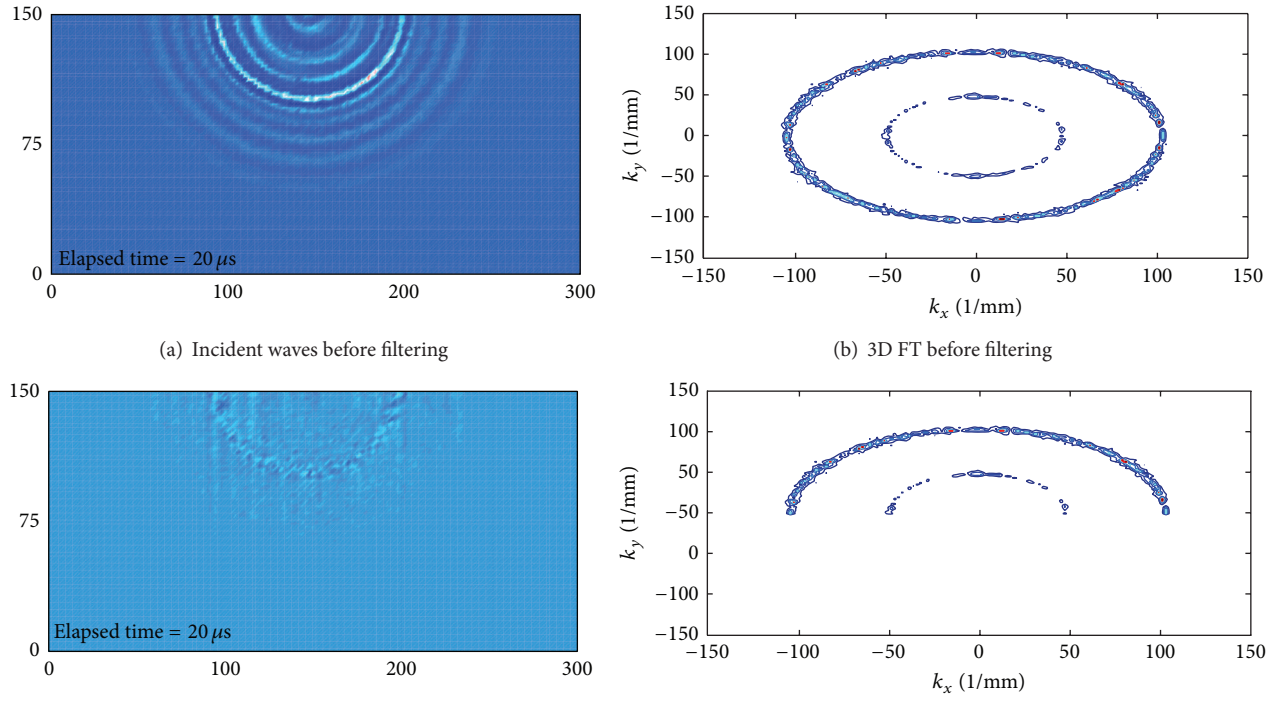

FIGURE 6: Elimination of downward incident waves by wavenumber filtering.

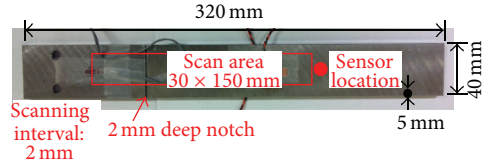

FIGURE 7: Configuration of a specimen with a notch (target to detect).

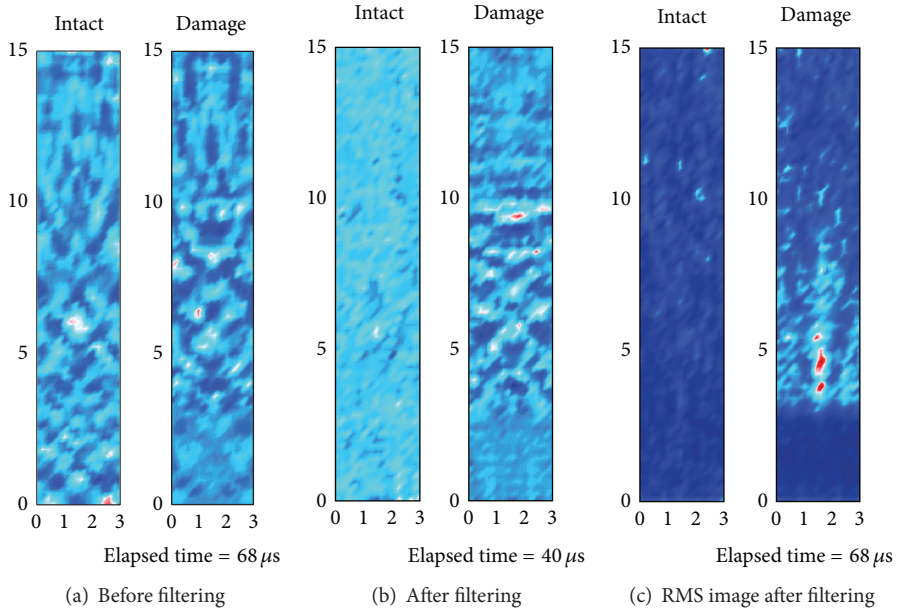

FIGURE 8: Visualization of the guided wave propagation and flaw image.

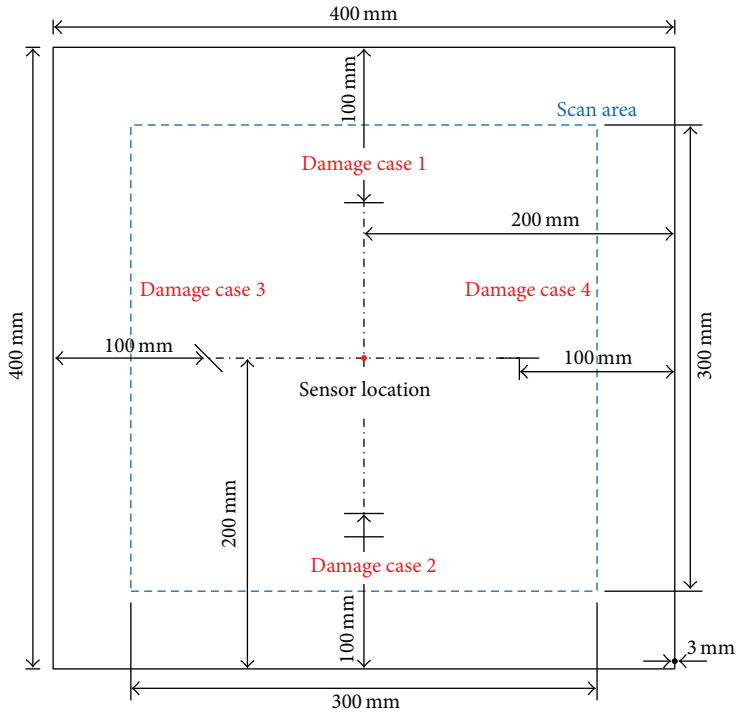

Figure 9: Damage cases: case 1: tangential to wave front, case 2: tangential to wave front (two damages), case 3: an angle of 45 degrees with wave front, and case 4: perpendicular to wave front; dotted line indicates the scan area.

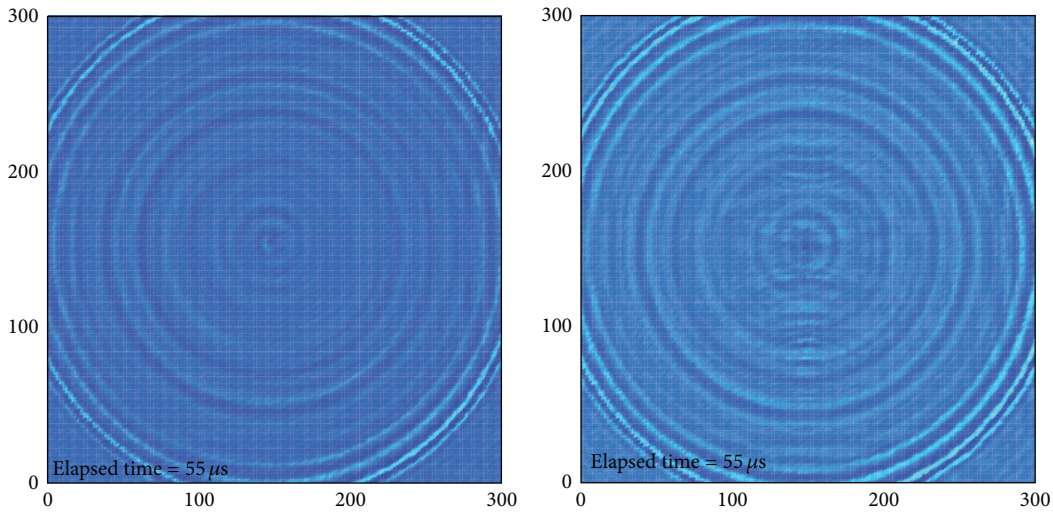

Figure 10: Comparison of UWPI snapshots at 55 μs.

investigated to verify the effectiveness and the robustness of the proposed NDT approach.

2. Ultrasonic Wave Propagation Imaging System

Ultrasonic wave propagation imaging (UWPI) system consists of a Q-switched laser system, a laser mirror scanner based on galvanometer, an ultrasonic sensor, a high-speed digitizer, and an image processor, which was rearranged referring the previous works [5] as shown in Figure 1. Q-switched Nd:YAG diode-pumped solid-state laser is used for the pulsed laser system, which has the wave length of 1064 nm and maximum pulse repetition frequency of 20 Hz [15]. The pulsed laser beam impacts a specific point on a target structure by the laser mirror scanner which is designed so that two galvanometers are operated at the wave length

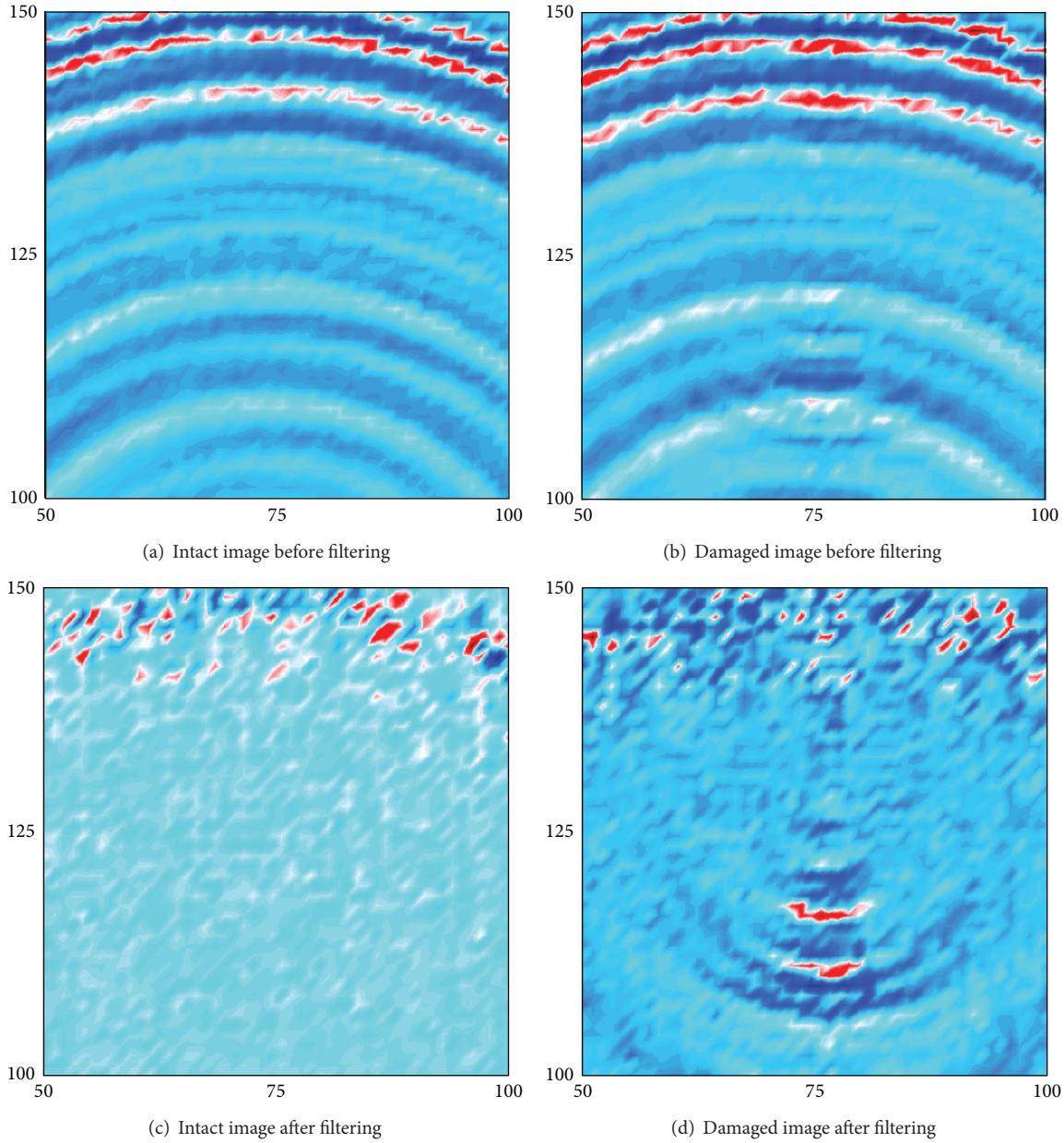

(a) Intact image before filtering

(b) Damaged image before filtering

(c) Intact image after filtering

(d) Damaged image after filtering

Figure 11: Comparison of UWPI snapshots at 48 μs for damage case 1.

of 1064 nm. The operating angles of the galvanometers are orthogonal to each other so that the laser beam can scan 2-dimensional area rapidly. Additionally, maximum angular velocity of the galvanometer is 100 rad/s within ±0.35 rad. The laser beam reflected at the laser mirror scanner is focused on the target structure by a f-theta lens which is installed at the end of the laser mirror scanner. In this study, the f-theta lens is designed so that the distance between the laser mirror scanner and the target structure is 2 m. First, the focused laser beam scans the target structure vertically upward and the laser beam steps horizontally leftward after vertical scanning. Then the laser beam scans vertically downward as shown in Figure 1. Therefore, the scanning laser beams generate a grid of the laser impingement points and the pitch of the grid can be adjusted by the control algorithm of the laser system.

When the pulsed laser beams impact the target structure, ultrasonic waves are generated by thermoelastic mechanism and propagated. The multiple wave responses can be measured by only single PZT attached to the backside or the front side of the structure. The measured time signals are placed at each laser impinging point and the UWPI is obtained as shown in Figure 2. As in Figure 2, wave propagation is visualized with 3 steps. (i) Measuring and filtering signals: to improve signals-to-noise ratio, a pass-band filter is applied. Additionally, specific modes of the ultrasonic waves can be optionally extracted by wavelet transform. In this study,

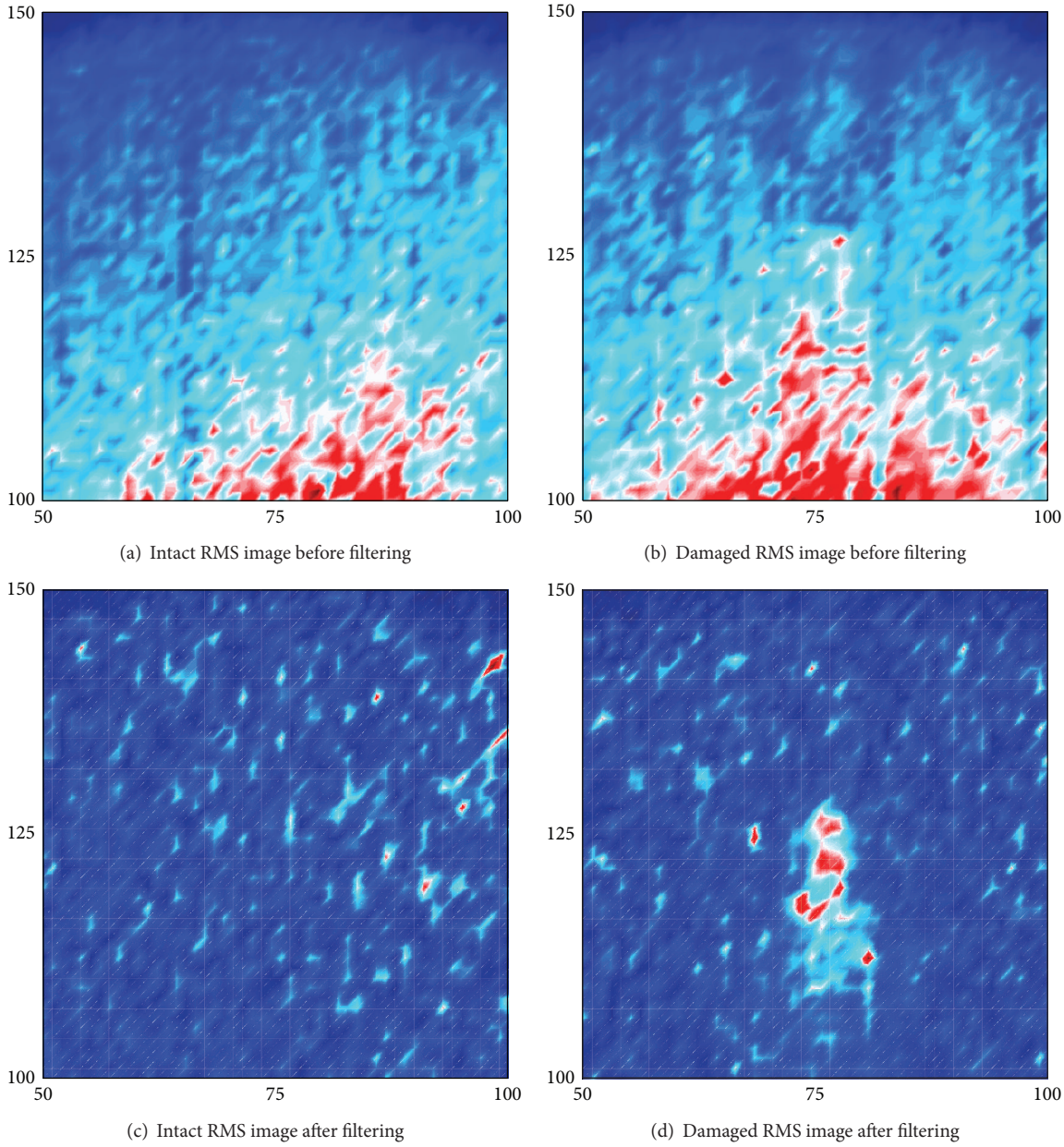

(a) Intact RMS image before filtering

(b) Damaged RMS image before filtering

(c) Intact RMS image after filtering

(d) Damaged RMS image after filtering

FIGURE 12: Comparison of RMS snapshots at 48 μs for damage case 1.

however, wavelet transform is not conducted. (ii) Placing the processed signals to the laser impinging points: the signal group results in a 3D space with respect to horizontal, vertical, and time axes. (iii) Slicing the 3D space along the time axis: finally, the wave propagation image can be obtained by slicing repeatedly within measuring period [5].

3. Flaw Imaging Algorithm

The flaw images can be easily obtained by observing reflected waves from damage after eliminating strong incident waves. To filter out the incident waves, wavenumber filtering concept is applied in this study. First, the wave propagation image is transformed from time/space domain to frequency/wavenumber domain by 3D Fourier transform as described in [13]

$$W\left(k_x, k_y, \omega\right) = \iiint_{-\infty}^{\infty} w\left(x, y, t\right) e^{-(\omega t + k_x x + k_y y)} dx\, dy\, dt, \tag{1}$$

where $w(x, y, t)$ is 2D wave signals in time domain k_x, k_y, and ω are wavenumber with respect to x and y axes and angular frequency, respectively.

The incident waves can be filtered out by eliminating positive or negative side of the frequency/wavenumber domain signals using window function as shown in (2). If a structure contains a flaw, the incident waves are scattered at the damage,

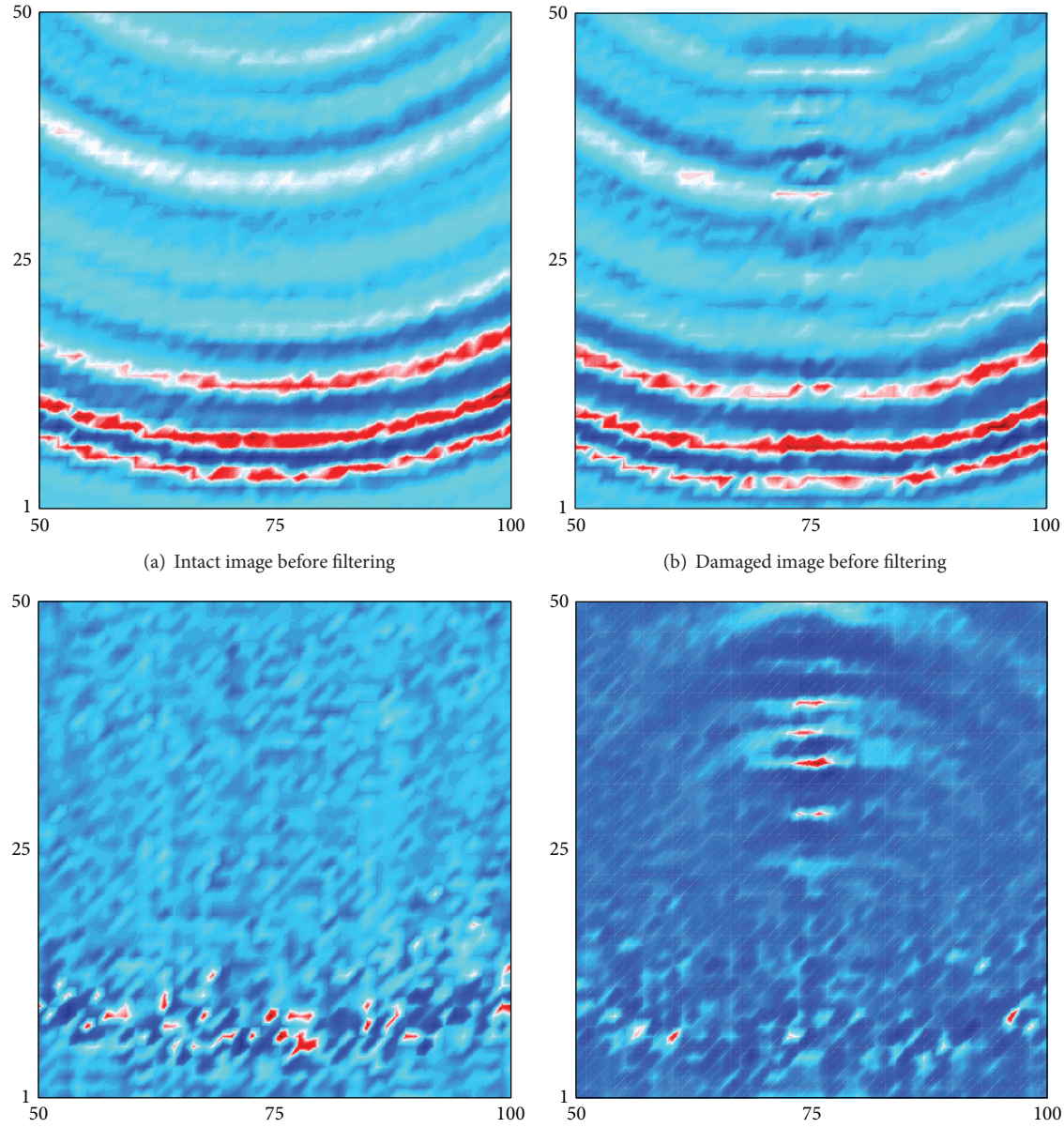

(a) Intact image before filtering

(b) Damaged image before filtering

(c) Intact image after filtering

(d) Damaged image after filtering

Figure 13: Comparison of UWPI snapshots at 48 μs for damage case 2.

and hence the reflections due to only damage can be extracted by the wavenumber filtering:

$$\overline{W}\left(k_x, k_y, \omega\right) = W\left(k_x, k_y, \omega\right) U\left(k_x, k_y, \omega\right), \quad (2)$$

where $\overline{W}(k_x, k_y, \omega)$ is filtered data, $W(k_x, k_y, \omega)$ is UWPI data, and $U(k_x, k_y, \omega)$ is the window function for filtering. In this study, a rectangular function is used for the window function.

The filtered UWPI data is inversely transformed from wavenumber and frequency domain to spatial and time domain. In the next section, this process is described using some figures. Finally, damage can be quantified by calculating root mean square (RMS) values using the filtered signals as shown in [14]

$$w_S^r(x, y) = \left[\frac{1}{T}\int_0^T \left(w^r(x, y, t)\right)^2 dt\right]^{1/2}, \quad (3)$$

where T is the period of the measured signals and $w^r(x, y, t)$ is the reflected signals.

4. Experimental Study

4.1. Preliminary Test Using an Aluminum Plate. First, an intact aluminum plate was scanned to verify the feasibility of the UWPI system. A 6061T aluminum alloy was used

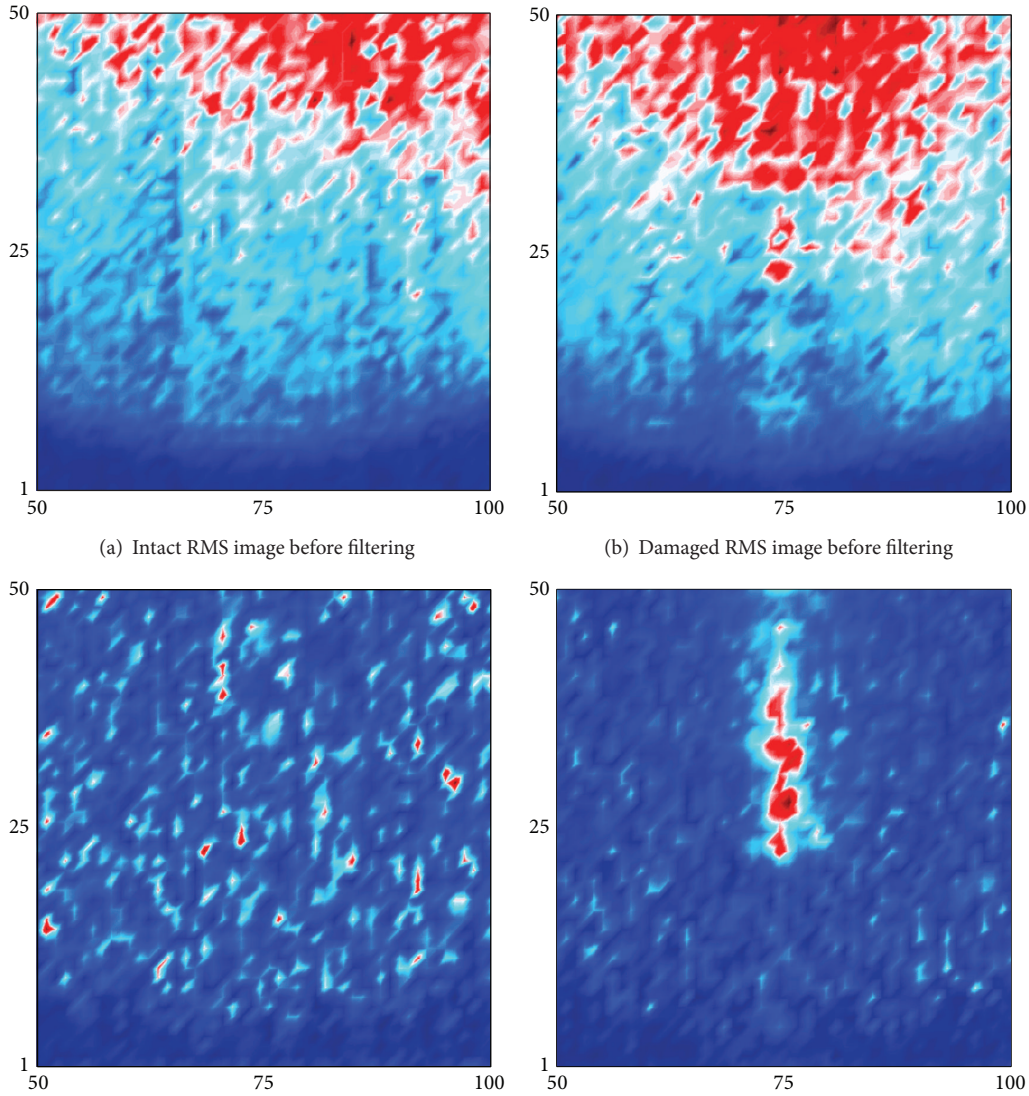

(a) Intact RMS image before filtering

(b) Damaged RMS image before filtering

(c) Intact RMS image after filtering

(d) Damaged RMS image after filtering

Figure 14: Comparison of RMS snapshots at 48 μs for damage case 2.

for the test as shown in Figure 3. The dimension of the plate was 400 mm × 400 mm with the thickness of 3 mm. Scanned area was 300 mm × 300 mm at the center of the plate with the scanning interval of 2 mm, and hence 151 × 151 grid was generated. To measure multiple wave responses, an amplifier-integrated acoustic emission sensor (hereafter, AE sensor) was attached to the backside of the plate to avoid interference of the laser impact. The sensor has a broadband characteristic with lower and higher cutoff frequencies of 100 kHz and 2 MHz, respectively. The resonant frequency of the sensor is 200 kHz ±20% and the maximum sensitivity is 120 ± 3 dB at the resonant frequency. The laser mirror scanner was installed 2 m apart from the plate.

Using the UWPI system, the snapshot of the UWPI at 20 μs is depicted in Figure 4. The amplitude of S_0 mode of the propagating waves is much smaller than that of A_0 mode as show in Figure 4. The group velocities of each mode were about 5.51 km/s for S_0 mode and 3.031 km/s for A_0 mode which were calculated from the UWPI snapshot. The velocities were very close to those from theoretical dispersion curves which were 5.5 km/s for S_0 mode and 3.03 km/s for A_0 mode. Therefore, it can be noted that the UWPI system is well operated.

Next, wavenumber filtering process based on 3D Fourier transform is shown in Figures 5 and 6. The frequency component representing the maximum amplitude of the wave responses was 186 kHz, which is within the range of the resonant frequency of the sensor. Therefore, wavenumber data was obtained at 186 kHz. To eliminate the incident waves, 3D FT data was multiplied by rectangular window as shown

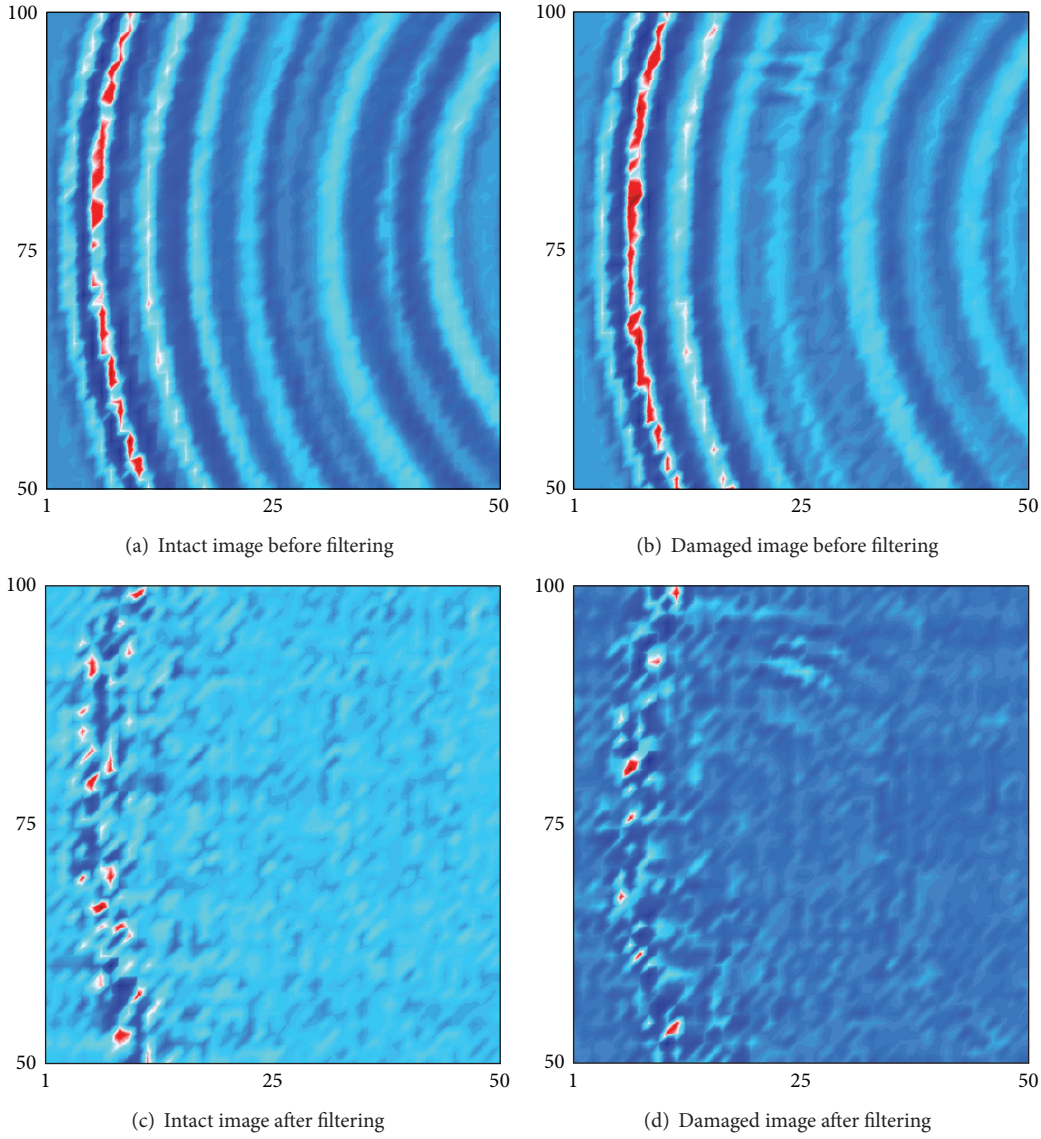

(a) Intact image before filtering

(b) Damaged image before filtering

(c) Intact image after filtering

(d) Damaged image after filtering

Figure 15: Comparison of UWPI snapshots at 46 μs for damage case 3.

in Figures 5(d) and 6(d). After the wavenumber filtering, both upward and downward incident waves were clearly filtered out as in Figures 5(c) and 6(c).

4.2. Damage Detection Using a Steel Coupon. A steel coupon with a notch was used to verify the proposed method as shown in Figure 7. Scan area was 30 mm × 150 mm with the scanning interval of 2 mm. The AE sensor was attached to the backside of the laser impinging point and the sensing point was not in the scan area as shown in Figure 7. The target damage was the 2 mm deep notch which was formed at the same side with the sensor.

The UWPI image is complex before wavenumber filtering due to incident waves, reflections from side boundaries, and the notch as shown in Figure 8(a). Although the shape of the UWPI image is complex, the continuity is marginally observed for the damage case as shown in Figure 8(a). Next, the forward signals were filtered out by the wavenumber filtering and only reflections are more distinguishable than the image obtained from raw data as shown if Figure 8(b). Finally, the discontinuity is dramatically detected from the RMS values of the filtered signals as shown in Figure 8(c) and it can be noted that the notch is successfully detected.

4.3. Damage Detection Using an Aluminum Plate. For next damage detection test, a 6061T aluminum plate was used again, which had same size as in Figure 3. Four types of notches were artificially formed as shown in Figure 9: (i) case 1: one tangential notch to incident wave front, (ii) case 2: two tangential notches to the incident wave front, which were 20 mm apart from each other, (iii) case 3: one diagonal notch to the incident wave front with an angle of 45 degrees, and (iv) case 4: one perpendicular notch to the incident wave front. All of the notches were 2 mm deep, 1 mm wide, and 20 mm

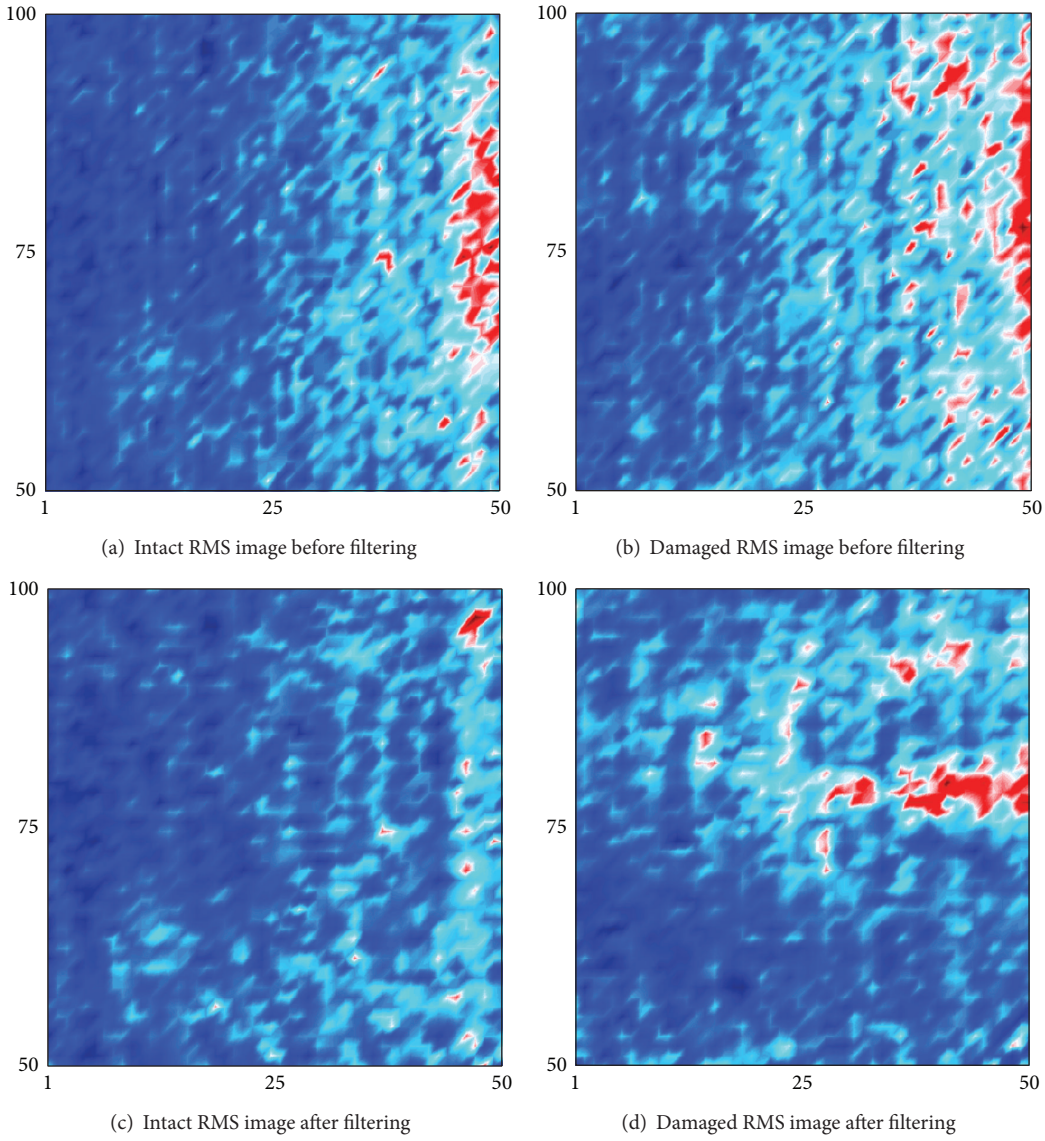

(a) Intact RMS image before filtering

(b) Damaged RMS image before filtering

(c) Intact RMS image after filtering

(d) Damaged RMS image after filtering

Figure 16: Comparison of RMS snapshots at 130 μs for damage case 3.

long. Scan area was same as in Figure 3 and UWPI snapshots at 55 μs are plotted as in Figure 10 so that reflected waves from boundaries cannot be observed. In the damaged plate, reflected waves from the damages are detected and hence the location of the damages can be approximated as show in Figure 10(b).

Next, areas near the damages are zoomed in and flaw imaging process is conducted in those areas. First, intact and damaged images at 48 μs are shown in Figure 11 before and after wavenumber filtering for damage case 1. In Figure 11(b), reflected waves from the damage are distinguishable from incident waves, while only incident waves are observed in Figure 11(a). After the wavenumber filtering, the incident waves were eliminated and hence only reflected waves are plotted in Figure 11(d).

Then, RMS values were calculated at 48 μs using the UWPI images before and after the wavenumber filtering. A flaw is not clearly observed before filtering regardless of damage as shown in Figures 12(a) and 12(b). However, damage is clearly evaluated at point (75, 125) as shown in Figure 12(d) compared to Figure 12(c).

Next, the UWPI and flaw images for damage case 2 are considered. The patterns of the images are similar to damage case 1. In this case, two notches were created and hence the transmitted waves through the first damage were reflected at the second damage. Therefore, the shape of the reflections is more complicated than those from damage case 1 as shown in Figure 13(d).

In Figure 14, RMS images are plotted. The flaw images are not clear before filtering regardless of damage as shown in Figures 14(a) and 14(b). After the wavenumber filtering, the flaw is clearly visualized at the point (75, 25) as shown in Figure 14(d). However, unfortunately, the pattern of the flaw image is the same as the image for the damage case 1

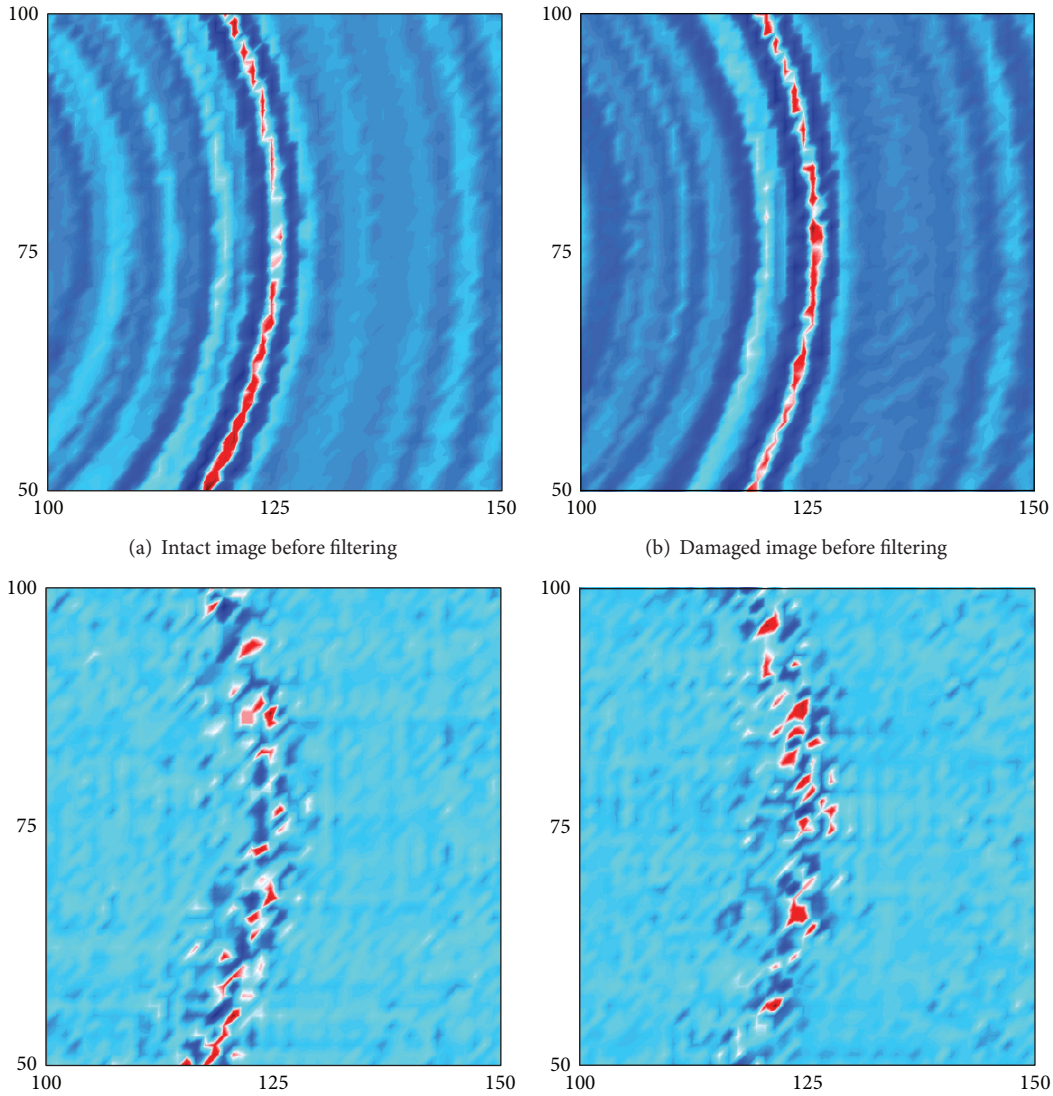

(a) Intact image before filtering

(b) Damaged image before filtering

(c) Intact image after filtering

(d) Damaged image after filtering

Figure 17: Comparison of UWPI snapshots at 35 μs for damage case 4.

and hence two damages can be identified as one damage. This might be because the direction of the transmitted waves through the first damage is same as the direction of the incident waves.

In the case of damage 3, reflected waves from the damage are observed, but the energy level of those is much low because the damage is inclined to the incident wave front as shown in Figure 15.

In this case, RMS images were obtained at relatively longer period than the previous two cases to use reflections from boundary. As results, the damage is visualized as shown in Figure 16(d). Since the damage was inclined to the wave front, the waves were partially reflected. Additionally, the waves were filtered along horizontal axis (or vertical axis) using the wavenumber filtering and hence the damage could not be clearly detected.

The final case is on the perpendicular damage to the incident wave front. In Figure 17(b), the waves are scattered both upward and downward at the damage. In this case, the energy level of the scattered waves is low even after the wavenumber filtering in a similar manner to case 3 because the damage is perpendicular to the incident wave front.

RMS images are also obtained at relatively longer period so that the reflected waves from the corner of the plate can arrive at the damage as show in Figure 18. In this case, also, the damage can be identified if the flaw image is compared to the RMS image from the intact data because of the orientation of the damage.

In this case, the damage could not be also clearly shown in a similar manner with case 3. Additionally, the damage was perpendicular to the wave front, the filter is applied horizontally, and hence the damage could be observed at

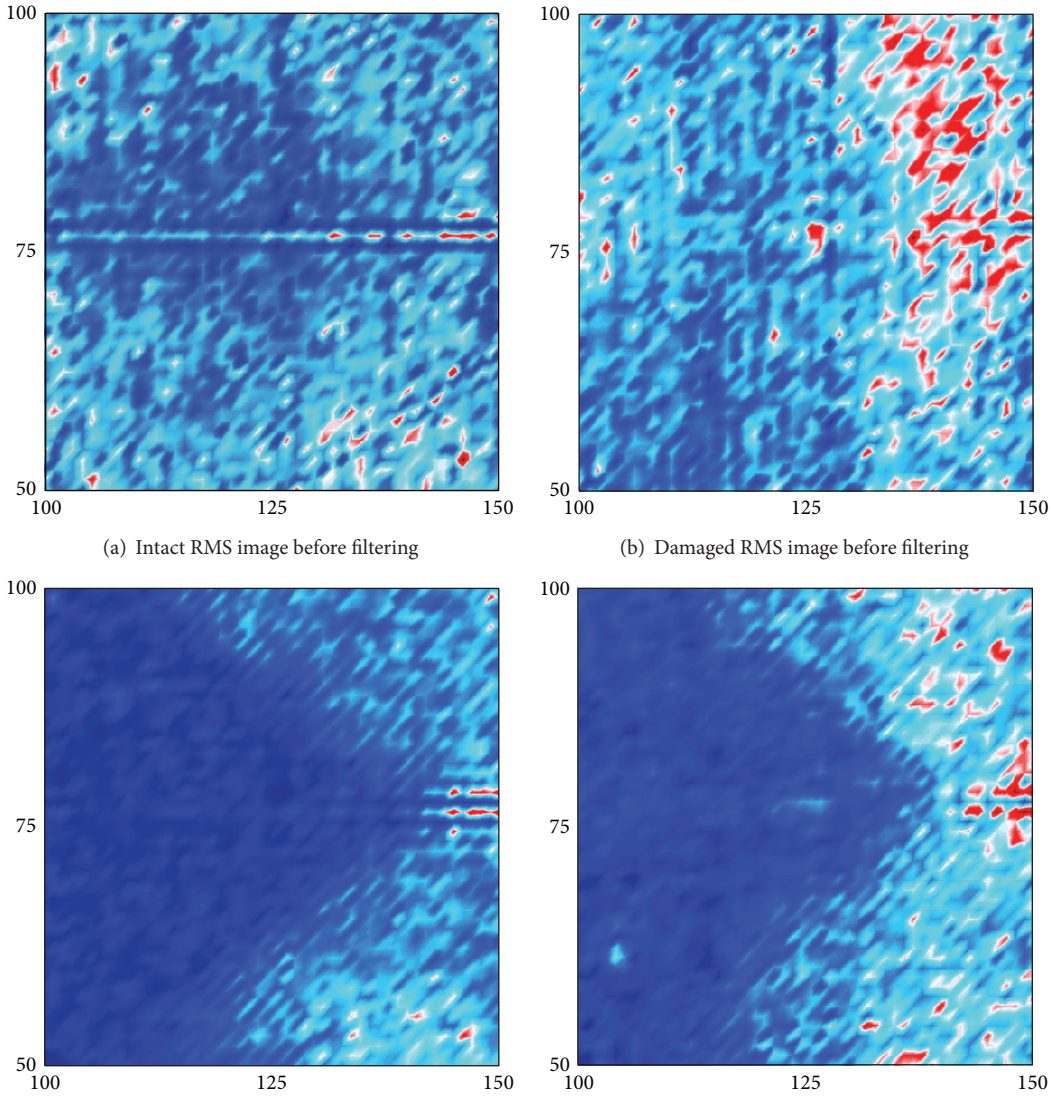

(a) Intact RMS image before filtering

(b) Damaged RMS image before filtering

(c) Intact RMS image after filtering

(d) Damaged RMS image after filtering

Figure 18: Comparison of RMS snapshots at 155 μs for damage case 4.

the longer period of the data to consider the effect of the reflected waves from the boundaries. However, the damage could not be clearly detected because the reflections from the boundaries were attenuated as depicted in Figure 18(d).

5. Conclusion

In this paper, the ultrasonic wave propagation imaging system and flaw imaging technique were proposed based on ND:YAG pulsed laser system and wavenumber filtering. To verify the feasibility of the proposed technique, two steps of damage detection test were conducted. First, a notch in a steel coupon was detected and then various types of damages were identified in an aluminum plate. The notch in the steel coupon was successfully detected by eliminating incident waves and by calculating root mean square, although the shape of the propagating waves was complicated due to the narrow width of the specimen. On the other hand, the damages in the aluminum plate were partially detected. The tangential damages to the incident wave front were successfully identified, while the inclined and perpendicular damages to the incident wave front were visible when the flaw images were compared to the intact images. It could be caused by the sparse scanning grid, the window for the wavenumber filtering, and the filtering direction. Therefore, further research is now ongoing to investigate the detectable size of the flaw and to detect various damages clearly. Additionally, other types of structures will be scanned to verify the applicability of the proposed method.

Conflict of Interests

The authors declare that there is no conflict of interests regarding the publication of this paper.

Acknowledgments

This study was supported by Basic Science Research Program (2010-0023404) through the National Research Foundation (NRF) of Korea, the Nuclear Research & Development of the Korea Institute of Energy Technology Evaluation and Planning (KETEP) Grant funded by the Ministry of Knowledge Economy of Korea government (no. 2011T100200161), the research project Development of Patch/Implant System based on IT Technology for Safe Management of Large Scale-Structure funded by the Ministry of Knowledge Economy of Korea Government. This all-out support is greatly appreciated.

References

[1] S. Park, J.-W. Kim, C. Lee, and S.-K. Park, "Impedance-based wireless debonding condition monitoring of cfrp laminated concrete structures," *NDT & E International*, vol. 44, no. 2, pp. 232–238, 2011.

[2] C. Lee and S. Park, "Damage classification of pipelines under water flow operation using multi-mode actuated sensing technology," *Smart Materials and Structures*, vol. 20, no. 11, Article ID 115002, 9 pages, 2011.

[3] J. Min, S. Park, C.-B. Yun, C.-G. Lee, and C. Lee, "Impedance-based structural health monitoring incorporating neural network technique for identification of damage type and severity," *Engineering Structures*, vol. 39, pp. 210–220, 2012.

[4] C. Lee and S. Park, "De-bonding detection on a CFRP laminated concrete beam using self sensing-based multi-scale actuated sensing with statistical pattern recognition," *Advances in Structural Engineering*, vol. 15, no. 6, pp. 919–927, 2012.

[5] J. R. Lee, C. C. Chia, H. Jin Shin, C. Y. Park, and D. Jin Yoon, "Laser ultrasonic propagation imaging method in the frequency domain based on wavelet transformation," *Optics and Lasers in Engineering*, vol. 49, no. 1, pp. 167–175, 2011.

[6] R. E. Green Jr., "Non-contact ultrasonic techniques," *Ultrasonics*, vol. 42, no. 1–9, pp. 9–16, 2004.

[7] http://www.polytec.com/fileadmin/user_uploads/Products/Vibrometers/PSV-500/documents/OM_DS_PSV-500_2012_09_3000_E.pdf.

[8] B. Köhler, "Dispersion relations in plate structures studied with a scanning laser vibrometer," in *Proceedings of the 9th European Congress on Non-Destructive Testing (ECNDT '06)*, Paper no. 2.1.4, pp. 1–11, 2004.

[9] N. S. B. Muhammad, T. Hayashi, M. Murase, and S. Kamiya, "Analysis of guided wave propagation by visualizing in-plane and out-of-plane modes," in *AIP Conference Proceedings*, vol. 1096, pp. 774–781, 2008.

[10] P. Castellini, M. Martarelli, and E. P. Tomasini, "Laser Doppler Vibrometry: development of advanced solutions answering to technology's needs," *Mechanical Systems and Signal Processing*, vol. 20, no. 6, pp. 1265–1285, 2006.

[11] B. Pouet, S. Breugnot, and P. Clémenceau, "An innovative interferometer for industrial laser ultrasonic inspection," in *AIP Conference Proceedings*, vol. 760, pp. 273–280, 2005.

[12] T. Blum, B. Pouet, S. Breugnot, and P. Clémenceau, "Non-destructive testing using multi-channel random-quadrature interferometer," in *AIP Conference Proceedings*, vol. 975, pp. 239–246, 2008.

[13] M. Ruzzene, "Frequency-wavenumber domain filtering for improved damage visualization," *Smart Materials and Structures*, vol. 16, no. 6, pp. 2116–2129, 2007.

[14] M. Radzieński, L. Doliński, M. Krawczuk, A. Zak, and W. Ostachowicz, "Application of RMS for damage detection by guided elastic waves," *Journal of Physics: Conference Series*, vol. 305, no. 1, Article ID 012085, pp. 1–11, 2011.

[15] http://www.quantel-laser.com/tl_files/client/MY%20QUANTEL%20SPACE/Sales%20Literature/CFR_Specs_EN_072012.pdf.

Hindawi Publishing Corporation
Shock and Vibration
Volume 2014, Article ID 430854, 9 pages
http://dx.doi.org/10.1155/2014/430854

Research Article

Damage Identification of Wind Turbine Blades Using Piezoelectric Transducers

Seong-Won Choi,[1] Kevin M. Farinholt,[2] Stuart G. Taylor,[2] Abraham Light-Marquez,[2] and Gyuhae Park[1,2]

[1] *School of Mechanical Systems Engineering, Chonnam National University, Gwangju 500-757, Republic of Korea*
[2] *Engineering Institute, MS T001, Los Alamos National Laboratory, Los Alamos, NM 87545, USA*

Correspondence should be addressed to Gyuhae Park; gpark@chonnam.ac.kr

Received 14 February 2013; Accepted 14 June 2013; Published 7 April 2014

Academic Editor: Jung-Ryul Lee

Copyright © 2014 Seong-Won Choi et al. This is an open access article distributed under the Creative Commons Attribution License, which permits unrestricted use, distribution, and reproduction in any medium, provided the original work is properly cited.

This paper presents the experimental results of active-sensing structural health monitoring (SHM) techniques, which utilize piezoelectric transducers as sensors and actuators, for determining the structural integrity of wind turbine blades. Specifically, Lamb wave propagations and frequency response functions at high frequency ranges are used to estimate the condition of wind turbine blades. For experiments, a 1 m section of a CX-100 blade is used. The goal of this study is to assess and compare the performance of each method in identifying incipient damage with a consideration given to field deployability. Overall, these methods yielded a sufficient damage detection capability to warrant further investigation. This paper also summarizes the SHM results of a full-scale fatigue test of a 9 m CX-100 blade using piezoelectric active sensors. This paper outlines considerations needed to design such SHM systems, experimental procedures and results, and additional issues that can be used as guidelines for future investigations.

1. Introduction

Wind turbines are becoming a larger source of renewable energy in the world. The US government projects that 20% of the US electrical supply could be produced via wind power by 2030 [1]. To achieve this goal, the turbine manufacturers have been increasing the size of the turbine blades, often made of composite materials, to maximize power output. As a result of severe wind loadings and the material level flaws in composite structures, blade failure has been a more common occurrence in the wind industry. Monitoring the structural health of the turbine blades is particularly important as they account for 15–20% of the total turbine cost. In addition, blade damage is the most expensive type of damage to repair and can cause serious secondary damage to the wind turbine system due to rotating imbalance created during blade failure. Therefore, it is imperative that a structural health monitoring (SHM) system be incorporated into the design of the wind turbines in order to monitor flaws before they lead to a catastrophic failure.

There has been a considerable research effort focused on applying SHM techniques on wind turbine blades [2, 3]. However, most of these studies focus on a single technique for damage detection; consequently very little work has been done to compare the results of multiple active-sensing techniques. Thus, the goal of this study is to assess the relative performance of high-frequency SHM techniques, namely, Lamb wave propagation and frequency response functions (FRFs), as a way to nondestructively monitor the health of a wind turbine blade with piezoelectric active sensors. In conjunction, consideration is given to employing multiple techniques together as a means of increasing the effectiveness of SHM for detecting and locating damage. This combination method is possible because of the multifunctional nature of the piezoelectric active sensors. In this paper, an array of piezoelectric sensors on a 1 m section of a 9 m CX-100 blade is used for simulated damage detection under the laboratory setting. Once the damage detection performance was characterized, the piezoelectric active-sensing techniques are applied to SHM of a full-scale 9 m CX-100 blade, where the

blade was dynamically loaded in a fatigue test until reaching catastrophic failure.

2. SHM Using Piezoelectric Active Sensors

Piezoelectric transducers have been widely used in SHM applications because they provide both sensing and actuation capabilities within a local area of the structure. These transducers could easily provide high-frequency excitations, and the subsequent structural responses could be captured by the same excitation sources. Two active and local sensing techniques, including Lamb wave propagations and FRF at high frequency ranges, are briefly summarized in this section.

2.1. Lamb Wave Propagations. Since the 1960s, the ultrasonic research community has studied Lamb waves for the nondestructive evaluation of plates [4]. Lamb waves are mechanical waves corresponding to vibration modes of plates with a thickness in the same order of magnitude as their wavelength. The advances in sensor and hardware technologies for efficient generation and detection of Lamb waves and the need to detect subsurface damage in laminate composite structures have led to a significant increase in the use of Lamb waves for detecting defects in structures.

The dispersive nature of Lamb waves means that the different frequency components of the Lamb waves travel at different speeds and that the shape of the wave packet changes as it propagates through solid media. There are two types of modes that form in a plate when excited with Lamb waves: asymmetric (A) and symmetric (S). The asymmetrical modes are analogous to shear waves (equivalent to S waves in earthquake engineering), while symmetrical modes are analogous to compression waves (equivalent to P waves in earthquake engineering). The selection of the excitation frequency for Lamb waves must be made so as to excite a structure at a certain mode (S_0 or A_0) and to avoid any higher modes that might also be present. Lamb wave propagation methods look for the possibility of damage by tracking changes in transmission velocity and wave attenuation/reflections. Several methods have been proposed to enhance the interpretation of the measured Lamb wave signals to detect and locate structural damage. They are based on changes in wave attenuations using wavelets [5], time-frequency analysis [6], wave reflections [7], and time of flight information [8]. A more complete description on the Lamb wave propagation technique can be found in [9].

3. Frequency Response Functions

The basic concept of high-frequency response functions is to use high frequency vibrations to monitor local regions of a structure for changes in the structure's parameters. It is a well-known fact that FRFs represent a unique dynamic characteristic of a structure. From the standpoint of SHM, damage will alter the stiffness, mass, or energy dissipation properties of a system, which, in turn, results in the changes in the FRF of the system [10]. Several investigations have been made to utilize the measured FRF for detecting damage in structures [11–13]. In addition, the piezoelectric impedance-based method [14] is also in line with those based on FRF, because it indirectly measures the mechanical impedance of a structure over select frequency ranges. By utilizing piezoelectric active sensors, the FRF could be measured up to hundreds of kHz ranges, which allows the method to be sensitive to small defects in the structure and not sensitive to operational or boundary condition changes, which occurs at relatively low frequency ranges.

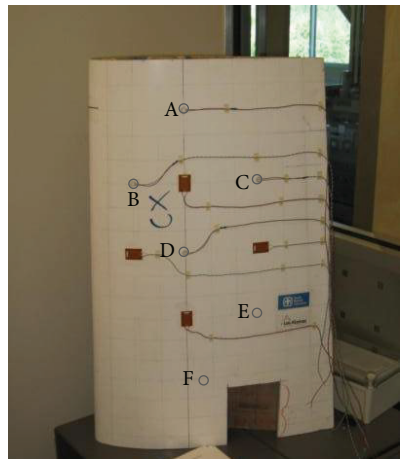

Figure 1: Turbine blade section.

4. Experimental Procedure and Results

The experimental setup under a laboratory setting consisted of a 1 m long × 0.55 m wide section of a CX-100 wind turbine blade with a thickness that varies from 0.3 cm (trailing edge) to 10 cm (spar cap) instrumented with six piezoelectric patches, labeled A–F, as shown in Figure 1. Figure 1 also shows 4 rectangular macrofiber composite (MFC) sensors attached to the turbine blade; these sensors were not used in this study. The patches E and F are boned inside the blade. The CX-100 is a carbon reinforced composite 9 m turbine blade designed by Sandia National Laboratory (SNL) [15]. The piezoelectric patches are 13 mm in diameter and are attached to the surface of the turbine blade using cyanoacrylate adhesive. The use of 6 piezoelectric patches results in 15 possible wave propagation paths, labeled with the actuator patch first and the sensor patch second. The length of AF is measured at 600 mm as the longest path, and EF is the shortest distance at 220 mm. The vertical paths (AD and AE) are located directly on the center support spar of the blade, as seen in the cross section picture in Figure 2. The patches were connected to a National Instruments (NI) PXI data acquisition system for data acquisition.

4.1. Lamb Wave Propagations. The Lamb wave propagation experiments utilize the pitch-catch approach, where one of the piezoelectric patches is used as an actuator and another as a sensor. The actuator transmits a signal that travels, along the surface of the structure, to the sensor where it is recorded.

Figure 2: Cross section view of CX-100.

To maximize the effectiveness of the Lamb wave technique the excitation frequency needs to be carefully selected. In order for damage detection to be possible the amplitude of the response must have a higher signal to noise ratio, and the response must be separated by a sufficient amount from the electromagnetic interference (EMI) to allow for proper identification of the arrival waveform. Due to the complexity of the blade section, traditional methods of predicting the ideal excitation frequency for homogeneous material [16] are not applicable and the ideal frequency was determined experimentally.

Overall, most of the paths showed desirable responses with an input frequency of 25 kHz: three paths (AD, BD, and DF) gave more advantageous responses with an input frequency of 200 kHz and three paths (AE, AF, and BE) did not provide an acceptable response at any frequency leaving the 12 paths. It also has identified that the travel distance of the waves is about 50 cm; thus for monitoring of the blade using Lamb wave propagations, one may need to either deploy a large number of traditional sensors or design an ultrasonic transducer to more effectively excite and sense a certain frequency range for SHM.

After the excitation frequency has been determined, multiple baselines for the undamaged structure were recorded. These baselines contain variations in the boundary conditions to attempt to simulate potential real world variability, including mass loading and manually induced vibrations to the structure. Damage was then introduced by applying a piece of industrial putty to the surface of the turbine blade in the path of propagation of the Lamb waves. The putty serves to change the damping properties of the structure in a localized area, similar to the effects of a delamination. The putty was approximately 5 cm × 5 cm, with 0.5 cm thickness. An example of recorded signal is shown in Figure 3. The responses (path BC) are recorded in the direct path before and after the simulate damage was applied. One can clearly see the attenuation of the first arrival wave caused by the simulated damage.

The signal processing technique used was based on monitoring the changes in the energy content of the propagated waves. First, the arrival signals were captured in time to avoid interference with boundary reflected waves. This captured signal was then converted into the frequency domain using a discrete Fourier transform. These frequency domain data were integrated, using the trapezoidal approximation method in an attempt to determine the energy content of the recorded response. A damage index was then created, which is defined as the percent difference between the true baseline and each of the other recorded values. To incorporate all of the baseline readings into a single value, all of the damage indices for the baseline cases were averaged and then compared with the correlation coefficient for the damaged case. The result of the induced damage (shown in Figure 3) is illustrated in Figure 4. Ten baselines were first measured to construct the baseline database under different boundary conditions. The average of all the baselines is taken as an undamaged value and compared against the damage index for the damaged case.

The result shows that path BC indicates very clear signs of damage. In addition, pathes AC and CE is also affected by this damage. Therefore, it is possible to get the approximate location of damage based on the paths. AC and CD both have very similar magnitude damage indices which would suggest that the damage is located about the same distance from those 2 paths, which also agrees with the indication that the damage was on or near the BC path. Based on the fact that the AB and BD paths are not indicating damage, it is likely that the damage is closer to the C piezoelectric patch. This process could approximately locate induced structural damage.

In most cases, this method could detect the simulated damage in the test, but only when damage was introduced close to the sensor-actuator paths. This low spatial detectability results from the relatively high damping present in composite structures, which limits the distance the Lamb wave can travel. This suggests that a large number of sensors would be needed to monitor the entire turbine blade. Furthermore, with the presence of the spar inside of the blade, the selection of the wave frequency is not always straightforward; piezoelectric transducers should be installed in such a way that they can avoid wave scattering caused by the spar.

4.2. High-Frequency FRF. Initially, the testing was conducted using an input frequency bandwidth of 30–80 kHz on each sensor-actuator combination. The experimental results, where the same damage as in the previous section in Figure 4 was introduced, are shown in Figure 5. The high-frequency response displays the changes in shape due to the simulated damage condition. The top portion of the figure is the real part, while the bottom portion is the imaginary part of FRF. As can be seen in the figure, the real portion of the response shows more variability due to baseline changes, while the imaginary portion is very stable, which is the ideal behavior. Changes due to boundary conditions are slight shifts in the magnitude of the FRF at the resonance and antiresonance peaks. The changes caused by damage result in a complete change in the frequency response function.

Damage index was obtained using a correlation function between baselines and a new set of data. The correlation coefficient determines the linear relationship between the two data sets:

$$\rho = \frac{1}{n-1} \times \frac{\sum_{i=1}^{n} \left(\mathrm{Im}\left(Z_{i,1}\right) - \mathrm{Im}\left(\bar{Z}_1\right)\right)\left(\mathrm{Im}\left(Z_{i,2}\right) - \mathrm{Im}\left(\bar{Z}_2\right)\right)}{\sigma_{z_1}\sigma_{z_2}}, \quad (1)$$

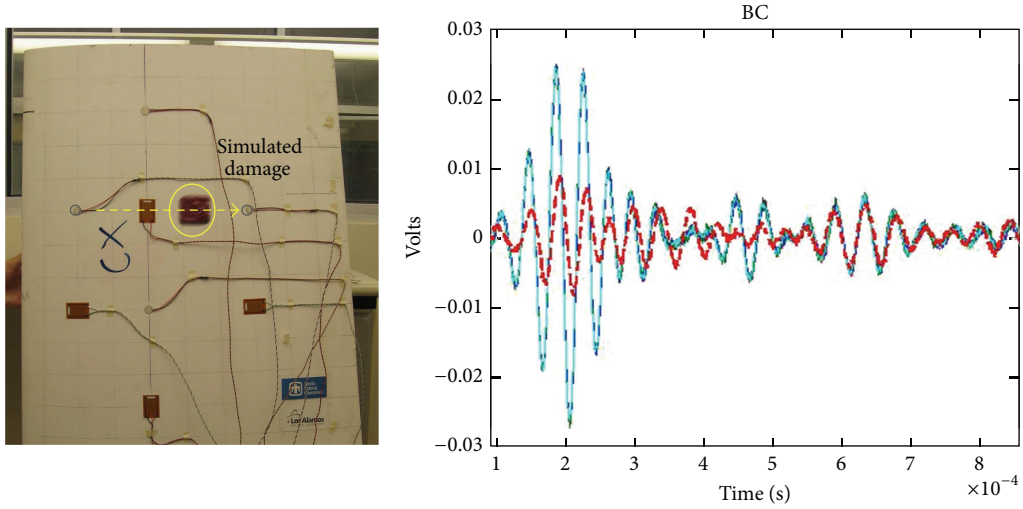

Figure 3: Turbine blade section with simulated damage and ten recorded baseline signals and damaged signal for path BC.

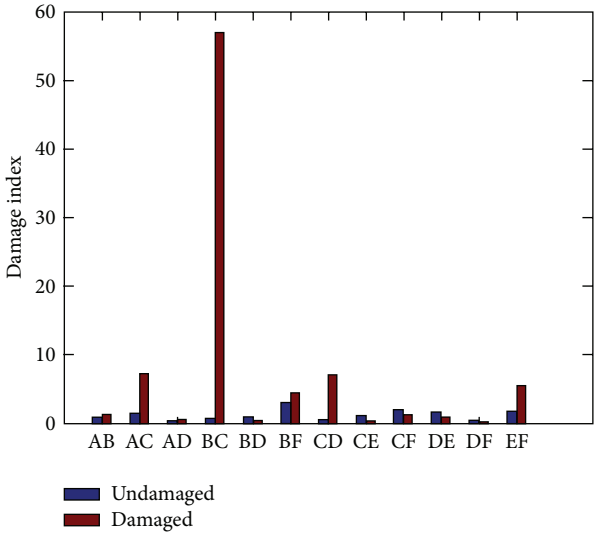

Figure 4: Damage index values for undamaged and damaged blade.

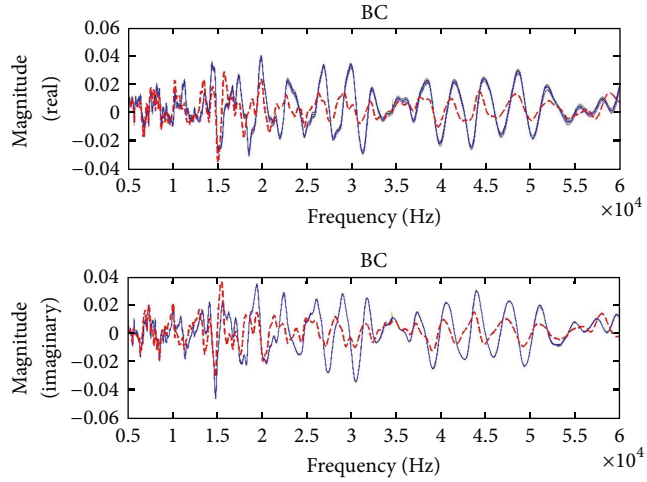

Figure 5: 15 recorded baseline signals and damaged signal for path BC.

where ρ is the correlation coefficient, $Z_{i,1}$ is the baseline FRF data and $Z_{i,2}$ is the compared FRF data at frequency i, $\bar{Z}_1$ and $\bar{Z}_2$ are the means of the signals, and the σ terms are the standard deviations. For convenience, the feature examined in this study is $(1 - \rho)$, in order to ensure that, with increasing damage or change in structural integrity, the metric values also increase. A greater damage metric value means that a certain degree of dissimilarity, with respect to a baseline measurement, is present in a particular measurement. The goal here is to show that this dissimilarity is directly related to the amount of damage present.

A correlation-based damage metric chart is illustrated in Figure 6. The figure shows that almost every path is indicating the presence of damage on the structure. The only exception is the EF path, which is the farthest path from the damage location. Paths BC and AE have the largest damage indices (as a reminder the AE path did not provide an acceptable response for the Lamb wave method). This indicates that the damage is located on or very near to both of these paths.

Although extensive averaging was required to enhance SNR, this method could detect any damaged condition imposed into the blade. With the high-frequency range interrogated and relative high damping present in the structure, the damage localization was also observed; that is, more pronounced response changes if damage was introduced close to the transducers.

For the frequency response function method, the longer propagation paths were capable of producing an acceptable recorded response for damage detection compared to Lamb wave propagation. This suggests that it might be possible to limit the number of sensors required to cover the entire turbine blade. This is further aided by the fact that the FRF method was determined to have global damage detection

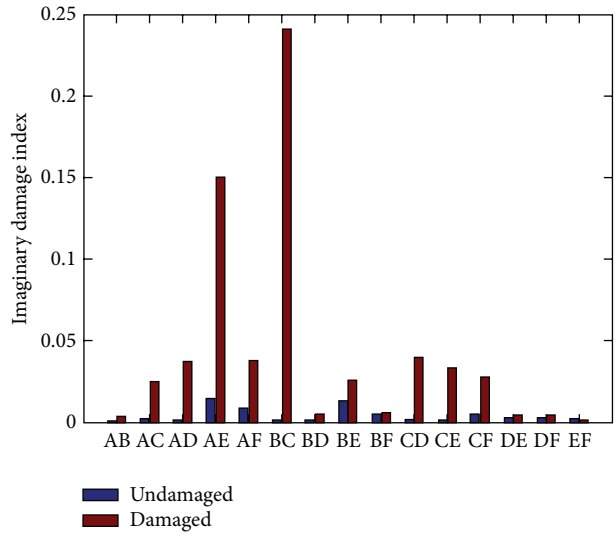

Figure 6: Damage index values using FRFs.

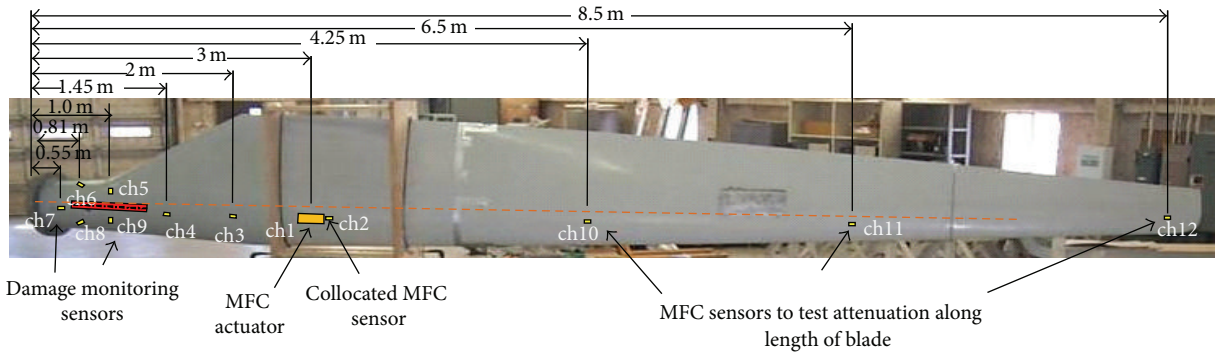

Figure 7: Overview of the fatigue test setup. A single MFC actuator in Ch1 is used to excite the blade, and 11 MFC sensors are used to measure the signal.

capability. In addition, it was discovered that the magnitude of the damage index is directly related to the proximity of the propagation path to the damage location. This feature can be utilized to determine the location of the damage with an acceptable degree of accuracy. Similar results were obtained for damage placed at multiple locations on the turbine blade. To summarize, the FRF method is an acceptable structural health monitoring technique for reliably detecting and locating damage in wind turbine blades and has the potential for limiting the number of sensors required to cover the entire structure.

4.3. Comparison of the Two Methods. The performances of two methods for SHM of wind turbine blades were investigated in this section. It was found that both methods were capable of detecting damage, which was simulated by placing a piece of industrial putty on the surface of the 1 m CX-100 blade section. Lamb wave techniques offer the ability to detect damage on or near the path of the propagating wave and can be used to approximately locate the damage. However, long paths (longer than 50 cm) were incapable of transmitting a waveform along the entire path, due to the high damping properties of composite turbine blades. The frequency response method showed a greater ability to detect damage on a global scale and the proximity of the damage location to the magnitude of the damage index allowed for the location of the damage to be determined. The frequency response method was also capable of transmitting a meaningful signal for all the propagation paths, including the longer distances. Consequently, the FRF method would require fewer sensors mounted on the structure in order to detect the presence of damage. Additionally, the FRF method utilizes a random excitation over a given bandwidth for all the propagation paths, eliminating the need to find the ideal excitation frequency, as is required for the Lamb wave method. However, as this method uses standing waves, the performance in localization of the damage is poorer than the wave propagation approach.

5. CX-100 Full-Scale Fatigue Testing

A full-scale fatigue test of a CX-100 wind turbine blade was also performed by SNL at the National Renewable Energy Laboratory (NREL). An overview photograph of the

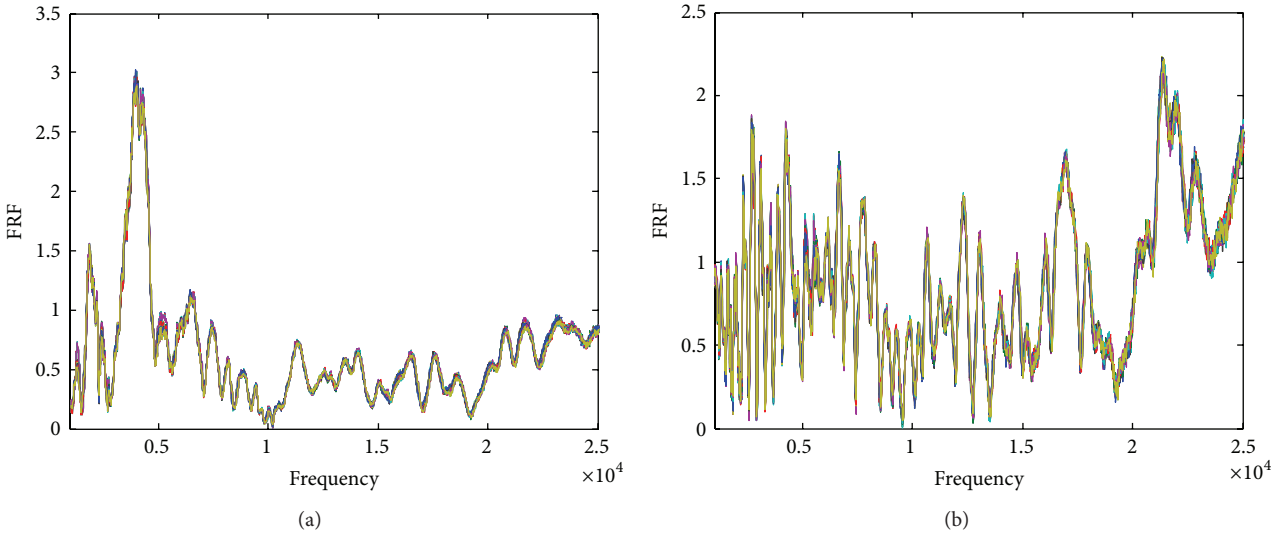

Figure 8: Identified FRFs. (a) Ch3, (b) Ch4. 20 measurements (from 260 k to 506 k cycles) are overlapped in the figure.

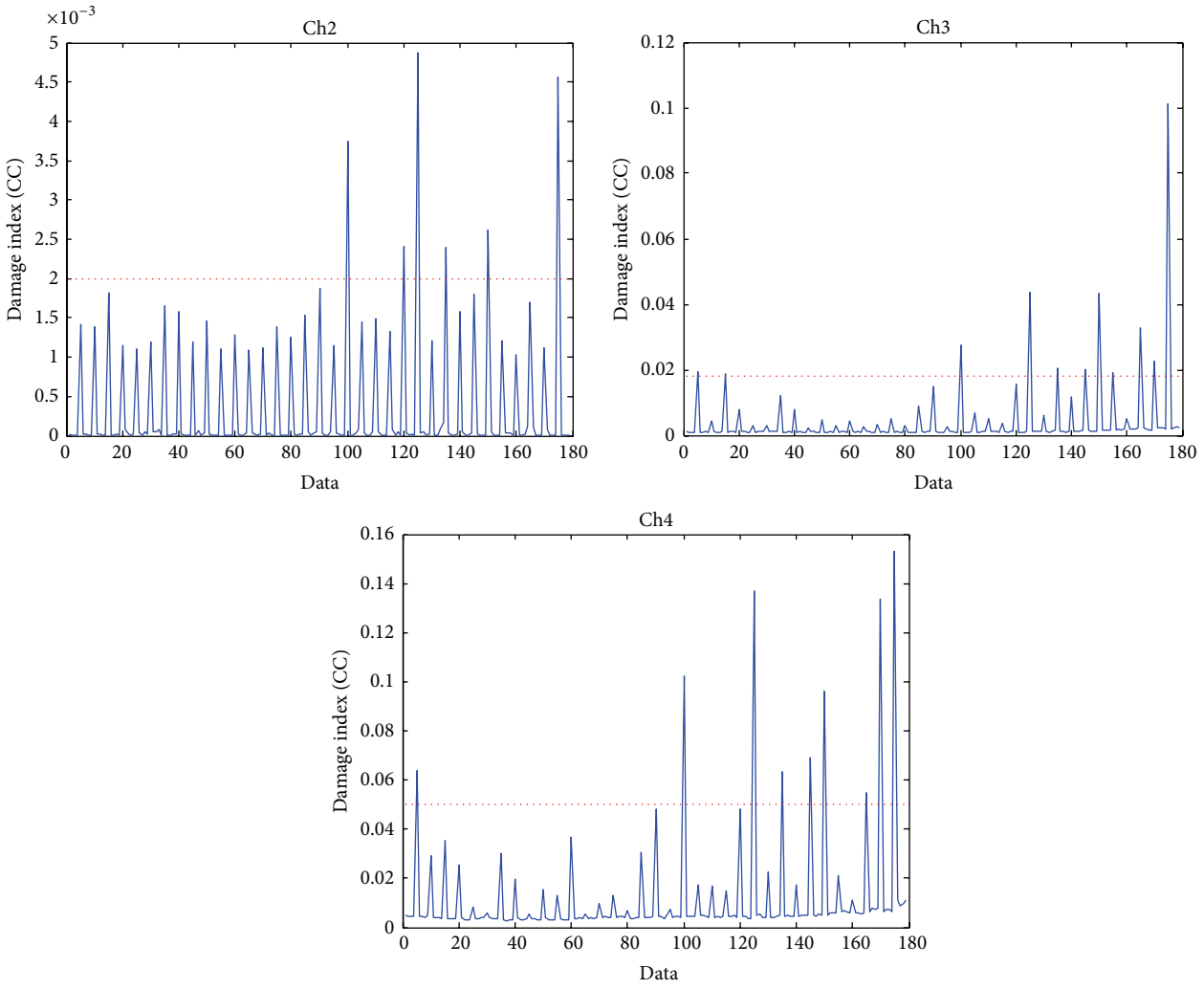

Figure 9: FRF-based DI values for Ch2–4. DI is measured between the current measurement and the previous reading.

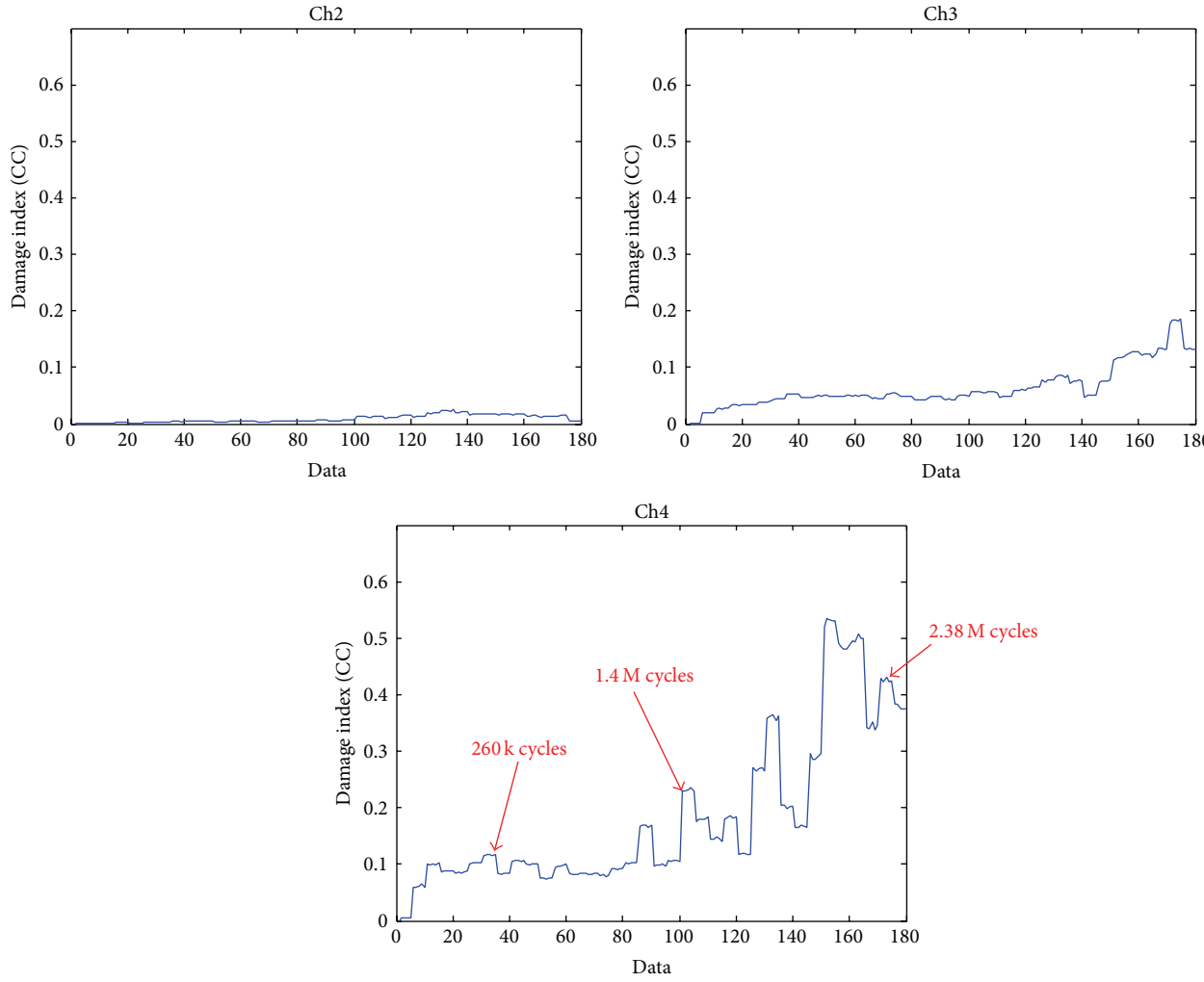

FIGURE 10: FRF-based DI values which are compared to a baseline for Ch2–4. DI is obtained between the current measurement and the baselines.

test setup is shown in Figure 7. The 9 meter blade was instrumented with eleven 2.5 × 3.75 cm MFC sensors and one 5 × 10 cm MFC actuator. The location of the sensors and the actuator in relation to the blade geometry is also shown in Figure 7. The blade underwent fatigue excitation at 2 Hz for defined intervals, and active-sensing data were collected between sessions while the fatigue excitation source was shut down. These data were collected from the eleven sensing channels at a sampling rate of 60 kHz, producing 32768 time points for each channel. A 7.5 RMS random excitation signal amplified by a factor of 30 was provided to the actuator. During the test, the fatigue damage was visually identified in the root area after 2.3 million cycles.

The collected data were converted to the frequency domain using FFT for the start of the fatigue cycling and at each cessation thereafter. The FRF obtained from the blade in the pristine condition was used to predict the system response from data collected at testing interval. FRF measurements of channels 3 and 4 are shown in Figure 8, for the frequency range of 1–25 kHz. Although extensive averaging was required to enhance the signal to noise ratio, the identified FRFs are repeatable and represent the dynamic characteristic of the local area of the structure.

The correlation coefficient between the current measurement and the previous reading was used as a feature to track the progression of structural change over the course of the fatigue test. In this way, the effect of fatigue loading given within the measurement interval could be estimated. The values of the correlation coefficients calculated at periodic intervals throughout the course of the test are shown in Figure 9. Note that plots are not in the same scale.

Right after starting the fatigue load, Ch3 and Ch4 showed some "settling" effects, which exhibit increases in DI values. All three results indicate that there is a large increase in data measured at data 100. This corresponds to the measurement made right after 1.43 million cycles. Although we did not have any reference data to compare against, the results indicate that there was likely a notable change in the blades integrity on the test just before this measurement was taken. In addition, the measurement made at 125 shows another substantial increase,

which was made after 1.8 million cycles. Another change was observed in the data 150, which was measured at 2.11 million cycles. Finally, the measurements taken on the final day (175 at 2.53 million cycles), all three measurements showed a large increase in the damage metrics, which indicates the on-set of structural damage on the blade. It is also interesting to note that the Ch4 (close to the damaged area) already showed certain increase in the DI value (170 : 2.38 million cycles) just before the final test, which may indicate the imminent damage.

Figure 10 depicts another FRF-based DI value. In this case, the measurements were compared to the baseline, which was measured on the first day of the test. The changes in FRF indicate changes in the structural parameters, which in turn indicate the presence of damage. By comparing the measurements made on the first day, these figures give relative changes in structural integrity. It can be seen that the values in Ch4 are substantially higher than Ch3 and Ch2, which indicates the damage is located close to this sensor.

The active-sensing technique at this fatigue test provides relatively repeatable responses, could detect damage, has localized sensing capability, and is less sensitive to operational variations. The method and analysis are relatively straightforward and do not require significant memory and power usage of the system, and the whole process can be embedded in the turbine blades with the appropriate development of hardware. It must be noted, however, that more than four sensors were broken during the test, as the adhesive was not ideal for a fatigue test. In addition, the hardware connectors did not function multiple occasions during the test. The sensor diagnostic procedure, which confirms the operational status of piezoelectric transducers [17, 18], should be implemented for fatigue test. Also, with the reduced number of sensors and a shorter traveling distance, the wave propagation technique was not considered in this test. These issues will be addressed for future tests.

6. Summary

This study investigated two piezoelectric active-sensing SHM techniques, including Lamb wave propagations and frequency responses, for wind turbine blade monitoring. With these techniques, the condition of the turbine blade can be qualitatively assessed with the presence and location of damage successfully identified using each method. In addition, the use of higher excitation frequencies enabled each method to be sensitive to small defects in the structure, while remaining insensitive to the effects of boundary and ambient condition changes on the response. This method can provide real-time health monitoring because the hardware and signal processing requirements can be significantly relaxed, especially in the case of FRF-based methods. This paper also summarizes the SHM results of a full-scale fatigue test of a 9 m CX-100 blade using piezoelectric active sensors, which confirms the localization capability of the active-sensing technique. The fatigue test also points out the importance of ensuring the robustness of sensing equipment and the reliability of the SHM system for field deployment under harsh operational conditions. This subject is currently being investigated by the authors.

Conflict of Interests

The authors declare that there is no conflict of interests regarding the publication of this paper.

Acknowledgments

This work was funded by the Department of Energy through the Laboratory Directed Research and Development Program at Los Alamos National Laboratory. This research was also partially supported by the Leading Foreign Research Institute Recruitment Program through the National Research Foundation of Korea funded by the Ministry of Education, Science and Technology (2011-0030065). G. Park acknowledges the partial support of the "Leaders Industry-University Cooperation" Project, supported by the Ministry of Education, Science and Technology (MEST), Republic of Korea. The authors also would like to acknowledge Mark Rumsey and Jon White from Sandia National Laboratory for their support and guidance on this study.

References

[1] U.S. Department of Energy, 20% Wind Energy by 2030: Increasing Wind Energy's Contribution to U.S. Electricity Supply, Wind & Hydropower Technologies Program, 2008, http://www1.eere.energy.gov/windandhydro/pdfs/41869.pdf.

[2] C. C. Ciang, J. R. Lee, and H. J. Bang, "Structural health monitoring for a wind turbine system: a review of damage detection methods," *Measurement Science and Technology*, vol. 19, no. 12, Article ID 122001, 2008.

[3] B. Lu, Y. Li, X. Wu, and Z. Yang, "A review of recent advances in wind turbine condition monitoring and fault diagnosis," in *Proceedings of the IEEE Power Electronics and Machines in Wind Applications (PEMWA '09)*, pp. 1–7, Lincoln, Neb, USA, June 2009.

[4] N. Bourasseau, E. Moulin, C. Delebarre, and P. Bonniau, "Radome health monitoring with Lamb waves: experimental approach," *NDT and E International*, vol. 33, no. 6, pp. 393–400, 2000.

[5] S. S. Kessler, S. M. Spearing, and C. Soutis, "Damage detection in composite materials using Lamb wave methods," *Smart Materials and Structures*, vol. 11, no. 2, pp. 269–278, 2002.

[6] J. B. Ihn and F. K. Chang, "Detection and monitoring of hidden fatigue crack growth using a built-in piezoelectric sensor/actuator network: II. Validation using riveted joints and repair patches," *Smart Materials and Structures*, vol. 13, no. 3, pp. 621–630, 2004.

[7] V. Giurgiutiu, A. Zagrai, and J. J. Bao, "Piezoelectric wafer embedded active sensors for aging aircraft structural health monitoring," *Structural Health Monitoring*, vol. 1, no. 1, pp. 41–61, 2002.

[8] M. Lemistre and D. Balageas, "Structural health monitoring system based on diffracted Lamb wave analysis by multiresolution processing," *Smart Materials and Structures*, vol. 10, no. 3, pp. 504–511, 2001.

[9] A. Raghavan and C. E. S. Cesnik, "Review of guided-wave structural health monitoring," *Shock and Vibration Digest*, vol. 39, no. 2, pp. 91–114, 2007.

[10] G. Park, A. C. Rutherford, J. R. Wait, B. Nadler, C. R. Farrar, and T. N. Claytor, "High-frequency response functions for composite plate monitoring with ultrasonic validation," *AIAA Journal*, vol. 43, no. 11, pp. 2431–2437, 2005.

[11] S. H. Diaz Valdes and C. Soutis, "Delamination detection in composite laminates from variations of their modal characteristics," *Journal of Sound and Vibration*, vol. 228, no. 1, pp. 1–9, 1999.

[12] H. Zhang, M. J. Schulz, A. Naser, F. Ferguson, and P. F. Pai, "Structural health monitoring using transmittance functions," *Mechanical Systems and Signal Processing*, vol. 13, no. 5, pp. 765–787, 1999.

[13] J. P. Dunne, D. M. Pitt, K. J. Kilian, and D. A. Sofge, "Recent advances in active damage interrogation," in *Proceedings of the 42nd AIAA/ASME/ASCE/AHS/ASC Structures, Structural Dynamics, and Materials Conference and Exhibit Technical Papers*, pp. 1937–1945, Seattle, Wash, USA, April 2001.

[14] G. Park, H. Sohn, C. R. Farrar, and D. J. Inman, "Overview of piezoelectric impedance-based health monitoring and path forward," *Shock and Vibration Digest*, vol. 35, no. 6, pp. 451–463, 2003.

[15] D. Berry, *Design of 9-Meter Carbon-Fiberglass Prototype Blades: CX-100 and TX-100, NM SAND2007-0201*, Sandia National Laboratories, Albuquerque, NM, USA, 2007.

[16] V. Giurgiutiu, "Tuned Lamb wave excitation and detection with piezoelectric wafer active sensors for structural health monitoring," *Journal of Intelligent Material Systems and Structures*, vol. 16, no. 4, pp. 291–305, 2005.

[17] G. Park, C. R. Farrar, A. C. Rutherford, and A. N. Robertson, "Piezoelectric active sensor self-diagnostics using electrical admittance measurements," *Journal of Vibration and Acoustics*, vol. 128, no. 4, pp. 469–476, 2006.

[18] G. Park, C. R. Farrar, F. L. di Scalea, and S. Coccia, "Performance assessment and validation of piezoelectric active-sensors in structural health monitoring," *Smart Materials and Structures*, vol. 15, no. 6, pp. 1673–1683, 2006.

Hindawi Publishing Corporation
Shock and Vibration
Volume 2014, Article ID 318380, 5 pages
http://dx.doi.org/10.1155/2014/318380

Research Article

Electromagnetic Wave Absorbing Composites with a Square Patterned Conducting Polymer Layer for Wideband Characteristics

Won-Jun Lee[1] and Chun-Gon Kim[2]

[1] *The 7th R&D Institute-2, Agency for Defense Development, P.O. Box 35-7, Yeseong-gu, Daejeon 305-600, Republic of Korea*
[2] *Department of Aerospace Engineering, School of Mechanical, Aerospace & System Engineering, KAIST, 373-1 Guseong-dong, Yuseong-gu, Daejeon 305-701, Republic of Korea*

Correspondence should be addressed to Won-Jun Lee; lwj@add.re.kr

Received 11 January 2013; Accepted 19 September 2013; Published 6 April 2014

Academic Editor: Gyuhae Park

Copyright © 2014 W.-J. Lee and C.-G. Kim. This is an open access article distributed under the Creative Commons Attribution License, which permits unrestricted use, distribution, and reproduction in any medium, provided the original work is properly cited.

The applications of electromagnetic- (EM-) wave-absorbers are being expanded for commercial and military purposes. For military applications in particular, EM-wave-absorbers (EMWAs) could minimize Radar Cross Section (RCS) of structures, which could reduce the possibility of detection by radar. In this study, EMWA composite structure containing a square periodic patterned layer is presented. It was found that control of the pattern geometry and surface resistance induced EMWA characteristics which can create multiresonance for wideband absorption in composite structures.

1. Introduction

1.1. Periodic Patterns for Radar Absorbing Structures (RAS). An electrically conductive medium is used as an EM-wave reflector and shielding structure. When the conductive surface is engraved, DC can always be conducted, but in the case of AC, there is a specific region where the EM wave cannot be transmitted or reflected. In the frequency range of interest, periodic patterns such as EM wave filters are considered frequency selective surfaces.

There are various methods and equations to verify the characteristics of the pattern layer; however, a computer simulation using FEM was assumed to be an effective tool to verify the accuracy of the equations. When the square array pattern is located in free space, the approximate equation for the resonance characteristics is as follows [1]:

$$Y_{\text{ind}} = (-j)\left(\nu - \frac{1}{\nu}\right)\frac{\left[A/C + (1/2)\,(A/\lambda)^2\right]}{\ln \csc\left((\pi/2)\,(\delta/A)\right)}, \nu = \left(1 - 0.41\frac{\delta}{A}\right)\left(\frac{\lambda}{A}\right), \quad \delta = \frac{A-C}{2}. \tag{1}$$

Total transmission occurs at

$$\frac{\lambda}{A} = 1 - 0.41\frac{\delta}{A}. \tag{2}$$

A and C mean the size of unit cell and λ is the wavelength. From the Babinet principle, the grid type and patch type have the same resonance point, with opposite filter characteristics. The equation assumes the medium of frequency selective surface (FSS) is a metallic material like perfect electric conductor (PEC) of an infinitely thin film. When we design the periodic pattern for a radome, this equation is useful. but the equation assumes a free-space boundary. When a dielectric slab is added to the FSS layer, the real characteristics of the periodic pattern are changed. In general, the degree of change depends on the dielectric properties and the resonance frequency moves to the low frequency range [2].

The high impedance surface is different from the lossy surface; the periodic pattern is usually made by metal. The pattern controls only the reactive part of the impedance, and the layer is assumed to be thicker than the skin depth. As a result, control of the pattern thickness cannot affect the EM characteristics of the filter.

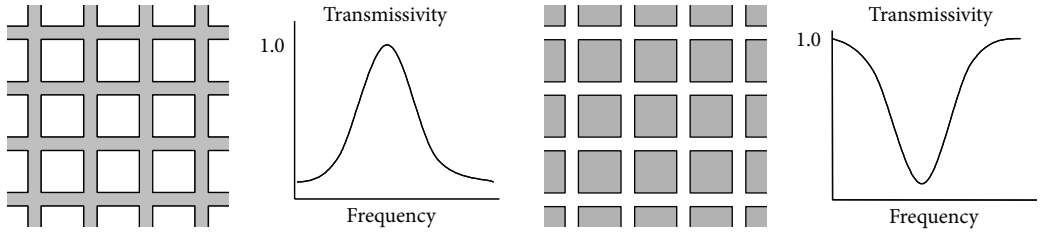

Figure 1: Inductive and capacitive screen.

1.2. Advantage of Periodic-Pattern-Layered RAS (PPRAS). One of the basic models for RAS is the Salisbury absorber, which uses a specific resistive sheet with a low dielectric spacer. The resonance peak can be controlled by the thickness of the spacer. As the thick spacer in the Salisbury absorber is its main demerit, many efforts have been made to reduce the thickness. The principle of impedance-matching with $\lambda/4$ thickness is that the maximum electric field is located at that point, and the resistive screen dissipates the energy of the electric field. Since the resistive sheet should not reflect the entire incident EM wave, it should have a free-space impedance of 377 Ω/sq. and be located at distance $\lambda/4$ from the PEC back-layer. This means that the Salisbury absorber has to be of minimum thickness and the resistivity of the screen should have a constant value.

The attempt to broaden the bandwidth of the Salisbury absorber involved multilayers of resistive screen, and the effort to minimize its thickness involved the study of highly dielectric materials [3]. However, such materials generally reduce the mechanical properties of the RAS and are costly to synthesize. Even if these kinds of materials do reduce the thickness, the bandwidth remains relatively narrow.

Another way to reduce the thickness is by application of a periodic pattern layer. Based on the $\lambda/4$ resonance, the engraved periodic patterns on the screen could reduce the total thickness of the RAS. In other words, this can move the resonance peak to a lower frequency range. The advantages of using such a pattern layer are reduction of thickness and the peak tuning of the RAS. Additionally, the loss control of the pattern is capable of changing the EM wave absorbing characteristics of the RAS. Because the pattern layer contains inductance (L) and capacitance (C) in the single layer, the filter characteristics of L and C are totally different. From the equivalent circuit theory, the combination of L and C could make a simple RF filter. As the number of elements increases, the order increases and the system shows good filter characteristics. These characteristics may be demerits of the RF circuit but, fortunately, these same characteristics are merits for the EM-wave-absorber. For example, a fractal pattern array with unit cells of various scales can be assumed to be a high-order system in filter design. The essence is that these high-order characteristics can be generated by the single layer pattern, not by the multilayered RAS.

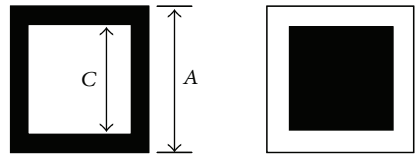

Figure 2: Unit cell of infinite array (inductive grid, capacitive patch).

2. PPRAS Design and Fabrication

2.1. Design of the Composite Substrate. The target frequency of the RAS designed in this research was X-band. Based on the target frequency, the Ku-band was included for ultrawide-band RAS. A RAS which could cover both bands is useful for air-stealth technology. In the first step, the RAS for X-band was designed with a thin substrate to verify the thickness reduction effect. The design of the substrate thickness was the main concern, because the thickness determines the target frequency range. For the Salisbury absorber in X-band, the thickness of the air spacer ($\varepsilon_r = 1.0 - j0.0$) is 7.5 mm, and glass/epoxy ($\varepsilon_r = 4.2 - j0.002$) is about 3.5 mm.

2.2. Design of the Periodic Pattern Layer. Through previous research on various patterns, the characteristics of each type could be verified. In this research, the square unit cell was adopted because of the simplicity of design and analysis to the various incidence angles. The square cell is divided into inductive (grid type) and capacitive (patch type) surfaces (Figure 1).

Basically, the dielectric substrate with PEC back plate has inductive characteristic and the capacitive pattern layer is effective for the RAS. According to the above consideration, square patch was used as unit cell, and the capacitance can be calculated by the following equation [4]:

$$Z_p = \frac{1}{j\omega C_p}, \quad C_p = \frac{(\varepsilon + 1)\,\varepsilon_0 D}{\pi} \log\left(\frac{2D}{\pi g}\right), \tag{3}$$

where D = array period and d = gap between patches.

The size of unit cell, the gap between patches, and the thickness and permittivity of the dielectric substrate mainly control the inductance and capacitance of the pattern

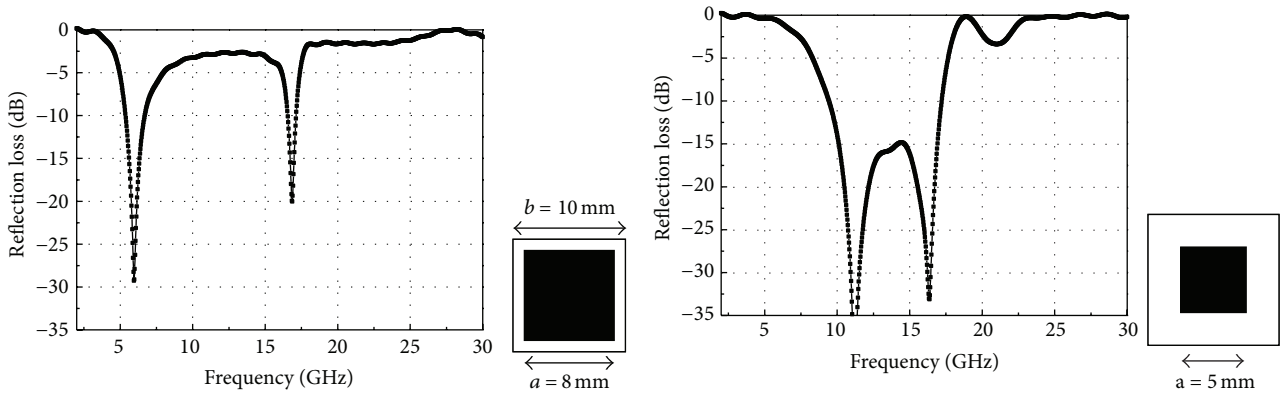

(a) Width = 8 (b) Width = 5

Figure 3: Peak control: AMC absorber with Salisbury absorber.

layer, and the resonance frequency can be estimated from the variables (Figure 2). The resonance occurs when the imaginary part of impedance becomes zero.

From $Z = R + jX = R + j\omega L + 1/j\omega C$

$$X = \omega L - \frac{1}{\omega C} = 2\pi f L - \frac{1}{2\pi f C} = 0. \quad (4)$$

Resonance frequency $= 1/2\pi\sqrt{LC}$:

$$f_{\text{resonance}} = \frac{1}{2\pi\sqrt{\mu_0 h \cdot \varepsilon_0 D\left(\varepsilon_r + 1\right)/\pi \cdot \log\left(2D/\pi d\right)}}. \quad (5)$$

The approximate resonance point can be calculated from the above equation, and the more exact resonance frequency was deduced from computer simulation. Within reasonable boundary conditions, parameter sweep and optimization were performed. The approximate equation assumes the thickness of the conductive square patch is enough to generate L and C, and the target resonance frequency was set to 10.3 GHz.

2.3. Expansion of Bandwidth. The maximum electric conductivity of the synthesized conducting polymer (CP) was set and the surface resistance was controlled by varying the coating thickness. In the case of the CP, the thickness for a Salisbury resistive screen was 2 μm, and sheet resistance was 377 Ω/sq. When the coating layer exceeds this thickness, surface resistance decreases and conductivity increases. When the pattern layer is applied, the effective surface resistance should be considered. The unit cell with a 6 mm square pattern should have a 6 μm coating thickness to achieve the Salisbury resistive effect, as there was a 2 mm null-grid region. When the thickness exceeded 6 μm, L and C resonance was initiated, and the artificial magnetic conductor (AMC) characteristic was as if the thickness was more than 12 μm. In other words, the 6~12 μm range would be the transition thickness for the AMC absorber, and at 12 μm thickness, the increased conductivity of the patterns could generate L and C on the surface of the periodic layer. As a result, there was a combination of Salisbury and AMC absorption in the transition range of the coating thickness.

When we design the periodic pattern layer with coating thickness control, the resonance peaks from these two EM-wave-absorber effects can be tuned effectively. That is the essence of wideband RAS with peak control in the X- and Ku-bands.

As the effective surface resistance was applied to maintain 377 Ω/sq., the pattern shape was functionless when the thickness was less than specified, whether the pattern existed or not. Clearly then, for the evaluation of the critical thickness, the transition thickness is important to be considered in the pattern design and conductivity of the coating material. When the unit cell has enough thickness to generate current using incident EM wave energy, the AMC characteristics are generated. If the pattern shape is effective in generating large amounts of L and C, the AMC resonance peak moves into the lower frequency range, and this means that the AMC peak location can be controlled. When the peaks of the Salisbury screen and the AMC are properly arranged for the specific frequency range, the combined dual peak can make the wideband absorption region within the single-layered PPRAS.

For the square pattern used in this research, as the size of a square increases, the capacitance also increases. As a result, the AMC peak moves to the lower frequency range, whereas the Salisbury peak remains in the original frequency region. When the size of a square decreases, the AMC peak moves to the higher frequency range located near the Salisbury resonance peak.

Figure 3 shows the location and movement of the AMC peak with variation of square size. In the first graph, the square size is large and the capacitance is also relatively large. The location of the AMC peak is near 6 GHz and Salisbury peak is at 17 GHz. In the second graph, the square size is smaller. The AMC peak moved to the right, but the Salisbury peak location remained fixed. As a result, the AMC peak and

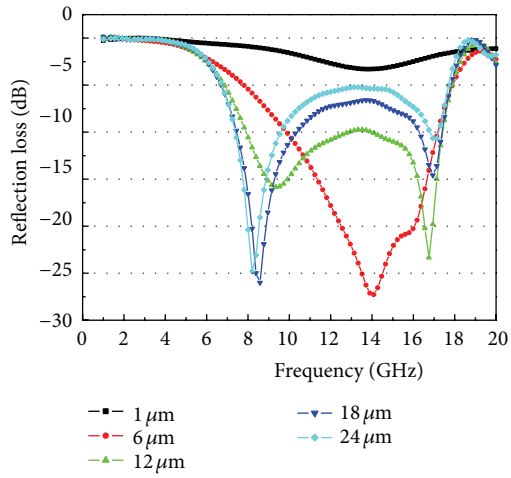

Figure 4: Simulation model: reflection loss change with different CP thickness.

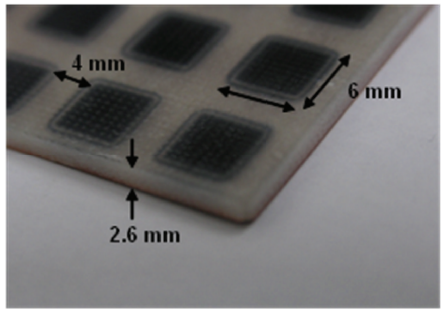

Figure 5: PPRAS composite.

Salisbury peak are combined in a specific frequency range. Generally, this kind of dual-peak control was achieved by control of the thickness of the multilayered RAS. The result of this multiple-peak control is expansion of the EM wave absorption bandwidth in the single-layered PPRAS.

The simulation model was designed for measurement of the S-parameter. The boundary condition was the TEM-mode plane wave. The back plate of the PPRAS was covered by PEC, and its transmission and reflection characteristics were simulated. The design was conducted with parameter sweep and optimization with CST-MWS. Based on the simulation result, we prepared an effective PPRAS model. The thickness of the substrate was 2.6 mm and the unit cell size was 6 mm with a 4 mm gap (Figure 5).

Figure 4 shows variation in the reflection loss with change in the thickness of the CP layer, while the other variables are fixed. Up to 6 μm, the AMC peak did not appear at the target frequency (left peak). When the thickness approached 12 μm, the single peak split into two peaks. When the thickness increased more than 12 μm, two clear peaks were present.

The coating thickness needed to establish this critical transition point is determined by the conductivity of the coating materials, and the CP paste synthesized in this study

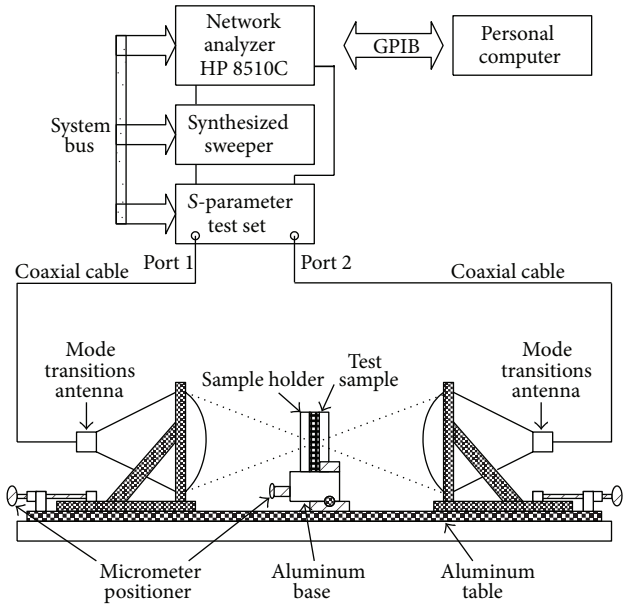

Figure 6: Free-space measurement system.

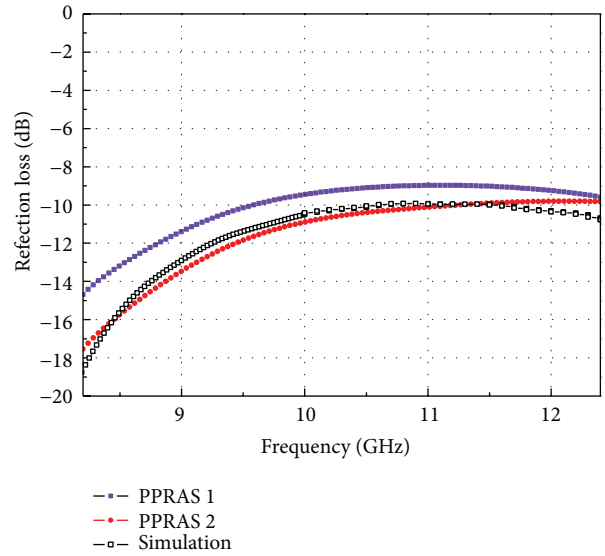

Figure 7: Reflection loss of the PPRA in X-band.

had the desired transition characteristics with a coating of 6–12 μm. If the thickness increased more than 12 μm, the peaks were totally separated.

3. Results and Conclusion

The reflection loss of the PPRAS plate was measured in X-band. The free-space measurement system was used. In the experiment and simulation, transmission was prevented by a metal back plate. The relation between the incidence wave and reflection wave verified the absorption characteristics.

The measurement system is illustrated in Figure 6. Two spot-focusing horn antennas for X-band were located on a

square aluminum plate (1.83 m × 1.83 m). The sample was located at the midpoint between the antennas. The specimen was a square plate (150 mm × 150 mm) and the antenna was connected to a network analyzer (HP 8510C). The designed PPRAS had 9.5 GHz bandwidth under −10 dB, and its X-band properties were measured. The S-parameters are shown in Figure 7.

The absorbers had about −10 dB absorption characteristics in the X-band, as designed. PPRAS 1 and 2 show similar traces as the simulation result and the result follows the initial design target. From the graph, we can expect that the first peak is located in the lower frequency range, and the second peak is located in the higher frequency range. As the S-parameter was measured only in X-band, we cannot confirm the exact location of the peaks. PPRAS 1 and 2 were two similar specimens, which were fabricated considering fabrication error. The disagreement of the graphs of the two specimens was caused by measurement errors, coating resolution, pattern uniformity, and various fabrication errors.

In this study, we designed PPRAS using a composite material. The PPRAS had a dual resonance peak in the layer with a single pattern, and the peak could be effectively designed and controlled to cover the X- and Ku-bands. As a result, we realized a thin, wideband RAS using PPRAS.

Conflict of Interests

The authors declare that there is no conflict of interests regarding the publication of this paper.

References

[1] S. W. Lee, G. Zarrillo, and C. L. Law, "Simple formulas for transmission through metal periodic grids or plates," *IEEE Transactions on Antennas and Propagation*, vol. 30, no. 5, pp. 904–909, 1982.

[2] B. A. Munk, *Frequency Selective Surfaces: Theory and Design*, Wiley-Interscience, 2000.

[3] S.-S. Kim, Y.-C. Yoon, and K.-H. Kim, "Electromagnetic wave absorbing properties of high-permittivity ferroelectrics coated with ITO thin films of 377 Ω," *Journal of Electroceramics*, vol. 10, no. 2, pp. 95–101, 2003.

[4] S. A. Tretyakov and C. R. Simovski, "Dynamic model of artificial reactive impedance surfaces," *Journal of Electromagnetic Waves and Applications*, vol. 17, no. 1, pp. 131–145, 2003.

Hindawi Publishing Corporation
Shock and Vibration
Volume 2014, Article ID 695836, 14 pages
http://dx.doi.org/10.1155/2014/695836

Research Article

Shock Response Spectra Reconstruction of Pointwise Explosive-Induced Pyroshock Based on Signal Processing of Laser Shocks

S. Y. Chong,[1] J. R. Lee,[1,2,3] and C. W. Kong[2]

[1] *Department of Aerospace Engineering and LANL-CBNU Engineering Institute Korea, Chonbuk National University, 567 Baekje-daero, Deokjin-gu, Jeonbuk, Jeonju 561-756, Republic of Korea*
[2] *Structures and Materials Department, Korea Aerospace Research Institute, Daejeon 305-333, Republic of Korea*
[3] *X-NDT Inc., #304, Building of Engineering Institute Korea, 567 Baekje-daero, Deokjin-gu, Jeonbuk, Jeonju 561-756, Republic of Korea*

Correspondence should be addressed to J. R. Lee; leejrr@jbnu.ac.kr

Received 6 December 2012; Accepted 14 March 2013; Published 3 April 2014

Academic Editor: Gyuhae Park

Copyright © 2014 S. Y. Chong et al. This is an open access article distributed under the Creative Commons Attribution License, which permits unrestricted use, distribution, and reproduction in any medium, provided the original work is properly cited.

Pyroshock has been an issue of great concern for aerospace and defense industrial applications. When pyroshock devices are detonated, they can easily cause failures in electronic, optical, relay, and magnetic components generally in mid- and far-fields which is not avoidable at the design level. Thus, many numerical and experimental pyroshock simulations have been widely studied to predict explosive-induced pyroshock effect quantitatively, especially the shock response spectrum (SRS). In this study, a laser shock-based pyroshock reconstruction method is proposed to simulate a pointwise explosive-induced pyroshock signal. The signal processing algorithm for the laser shock-based pyroshock reconstruction is developed in a LabVIEW platform and consists of subbands decomposition, SRS matching in decomposed bands, and wave synthesizing. Then, two experimental setups are configured to obtain pyroshock signals and laser shock signals at four points in an aluminum plate. The reconstructed pyroshock signals synthesized according to the signal processing of the laser shocks demonstrate high similarity to the real pyroshock signals, where the similarity is evaluated by the mean acceleration difference between the SRS curves. The optimized settings of the subband decomposition were obtained and can be in the future used in a pyroshock simulator based on laser shock for pyroshock simulation at any arbitrary point.

1. Introduction

Pyrotechnic shock or pyroshock has been an issue of great concern for aerospace and defense industrial applications. Pyroshock is the transient oscillatory response of a structure to loading (high frequency and high magnitude stress waves) induced by the detonation of pyrotechnic devices using pointwise or linear explosives [1], incorporated into or attached to the structure. As a result, its high frequency energy can easily cause failures in electronic, optical, relay, and magnetic components, especially in aerospace applications during the separation of structural subsystems, the deployment of appendages, and the activation or deactivation of subsystems [2].

Various pyroshock simulation methods, which are generally classified as experimental and numerical simulations, have been studied to predict pyroshock effects quantitatively on the intended pyroshock environments. These pyroshock environments can be classified as near-, mid-, and far-field environments [1, 3]. Then, a shock response spectrum (SRS) is used as a tool to analyze and quantify a pyroshock. The SRS is a graphical representation of maximum response regarding a single response for a single degree of freedom (SDOF) system as a function of the natural frequency of the SDOF [2]. Various experimental test simulations have been introduced, and these include ordnance test, scaled test, electrodynamic shaker tests, and tuned or tunable resonant fixtures, resulting in realistic pyroshock data with high amplitude and high frequency [1]. Generally, the preparation of the specimens and sensors is often problematic and the experimental repeatability is poor. In addition, the experimental methods are of high cost because many sample structures or realistic

models are used in pyroshock study. In numerical simulation methods, they are used to complement experimental simulation and shorten the overall design process, and they include finite element method (FEM), statistical energy analysis (SEA), hybrid methods, and hyrocode methods [1]. However, numerical methods show inefficiency in pyroshock wave analysis when insufficient elements are used [4].

From the past decades, laser excitation has been used for various applications such as material property measurements and structural nondestructive testing and evaluation and for the simulation of elastic waves [5]. Recently, Lee et al. [1] have shown the feasibility of a laser excitation for pyroshock simulation. In that study, it was reported that the laser excitation was able to be manipulated to be similar to the mechanical shock with a peak-to-peak acceleration of 7000 g and a central frequency of 70 kHz.

Many signal processing techniques have been introduced in the field of pyroshock. Recently, Brake [6] developed a method to reconstruct a time-domain wave from the SRS when only SRS is available. This method used three theoretical basic functions to reconstruct a time history that corresponds to a given SRS: an impulse function, a sine function/damped sine function, and a modified Morlet wavelet. However, a high fidelity representation of the SRS was needed, and it required significantly more time to obtain accuracy in matching the target SRS when the genetic algorithm approach was used. Hale and Adhami [7] researched for synthesis of SRS using the time-frequency analysis. Besides the techniques introduced in pyroshock, signal decomposition and synthesis methods [8–10] have been widely used. Particularly, the subbands decomposition method based on filter bank has been used not only for data compression [9] but also for feature extraction [8]. The work principle is that a filter bank contains a set of analysis filters which decompose the bandwidth of the input signal into subband signals with uniform frequency bands. Then, processing can be performed on the subbands according to a specific application [8].

In regard to the prior studies, the laser excitation, which has nondestructive property, can provide better solutions than the conventional experimental techniques, where the laser excitation will not damage the real structures or will not alter the properties of the target structure. Thus, the simulator based on laser excitations can be applied even to the flight-ready structures. Moreover, the laser excitation is also able to obtain real stress wave from the real target structure for pyroshock simulation. With these advancements of laser excitation, a reconstruction method of shock response spectra (SRSs) for pointwise explosive-induced pyroshock based on the signal process of laser shocks is first proposed in this paper. In addition, the finding of this work is to determine the optimized parameter settings of the proposed signal processing algorithm. Then, the settings will be further used for a new pyroshock simulator development. The simulator will be incorporated with the proposed signal processing algorithm, which can simulate a pyroshock signal using a laser shock signal at any arbitrary point with no requirement of any real pyroshock signal. Two experimental setups are configured to obtain the pyroshock signal and the laser shock signal. In addition, the signal processing algorithm is developed and realized in a LabVIEW platform with two main functions, subbands decomposition and SRS matching synthesis. In subbands decomposition, both pyroshock and laser shock signals are decomposed into the subbands using a set of hieratical bandpass filters. Then, the decomposed signals are inputted into the synthesis process with the SRS matching function to reconstruct the SRS of the pyroshock signal based on the laser shock signal. The laser shock signal matched by the proposed algorithm is considered as a reconstructed pyroshock signal. Then, the similarity of a reconstructed pyroshock is analyzed by minimizing the acceleration difference with the SRS of the real pyroshock.

2. Pyroshock Shock Response Spectrum Reconstruction Algorithm Using Laser Shock

Figure 1 shows the schematic diagram of the signal processing algorithm developed to reconstruct a pointwise explosive-induced pyroshock using a laser shock. In order to realize this algorithm, first we assumed that pyroshock signals obey the wave superposition principle [11]. As shown in Figure 1, the overall algorithm consisted of two main functions, subbands decomposition and synthesis with the SRS matching function. In the subbands decomposition, the Butterworth infinite-impulse-response (IIR) bandpass filter was used to decompose both pyroshock and laser shock signals into a set of time-domain signals with different frequency bands. Commonly, SRS curve is plotted on a log-log graph where the log-scale x-axis is representing the natural frequency of a pyroshock and each cycle of the logarithmic scale covers a range of values spanning one factor of 10. It also meant that the next cycle covers a range 10 times larger. In addition, a pyroshock is normally analyzed at the broad natural frequency range, for example, from 100 Hz to 100 kHz. For that, the appropriate selection of the number of subband filters used is a must in order to achieve narrow band in each subband signal. For example, 100-subband filters are selected to decompose the pyroshock signal (100 Hz to 100 kHz), and each subband signal has equal bandwidth of 999 Hz, respectively. With this decomposition bandwidth, it is difficult to obtain good analysis results in the lower natural frequency range of a pyroshock. Thus, to increase higher number of subband filters to obtain higher frequency resolution is not an appropriate way because it will cause the increase of processing time. In regard to this point, two levels of the subbands decomposition process were employed and denoted as Level 1 (L1) and Level 2 (L2). L1 was used to decompose the pyroshock signal with wider frequency bands accordingly to the natural frequency ranges set in each log-scale cycle, respectively, and L2 was further used to decompose each subband signal of L1 with narrow frequency bands, respectively. Then, the SRS matching synthesis extracted features for SRS matching from the decomposed pyroshock and laser shock signals and synthesized the decomposed signals to obtain a reconstructed pyroshock signal.

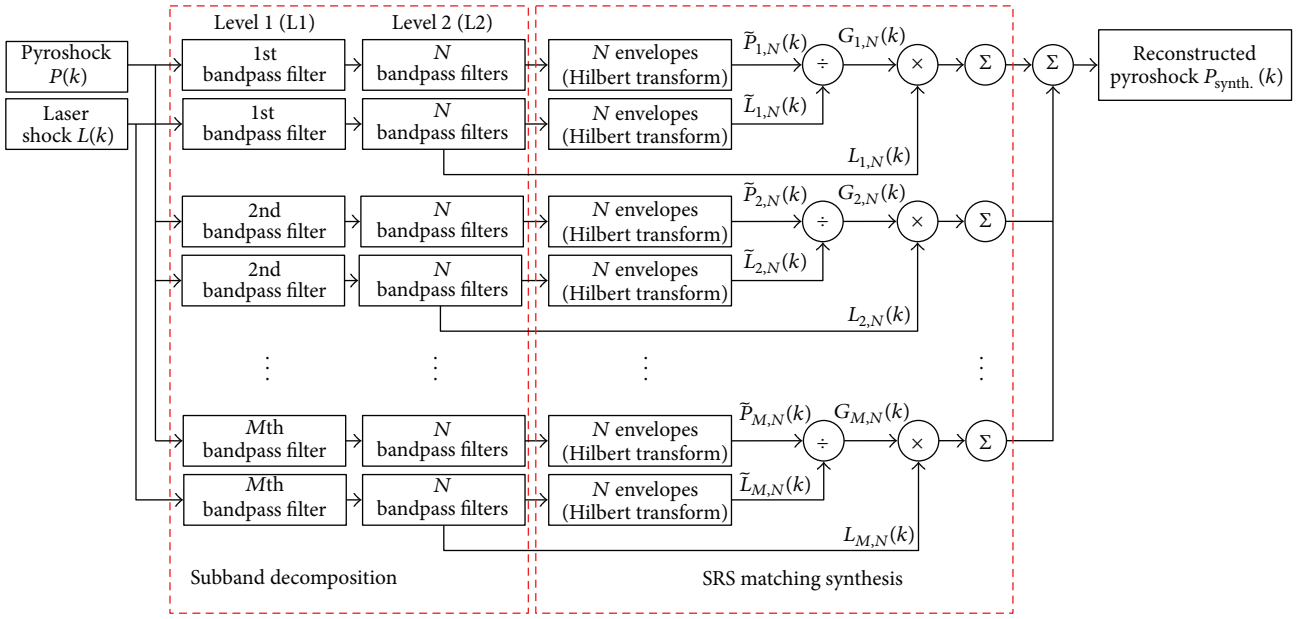

FIGURE 1: Schematic diagram of the signal processing algorithm to reconstruct a pyroshock signal using a laser shock signal.

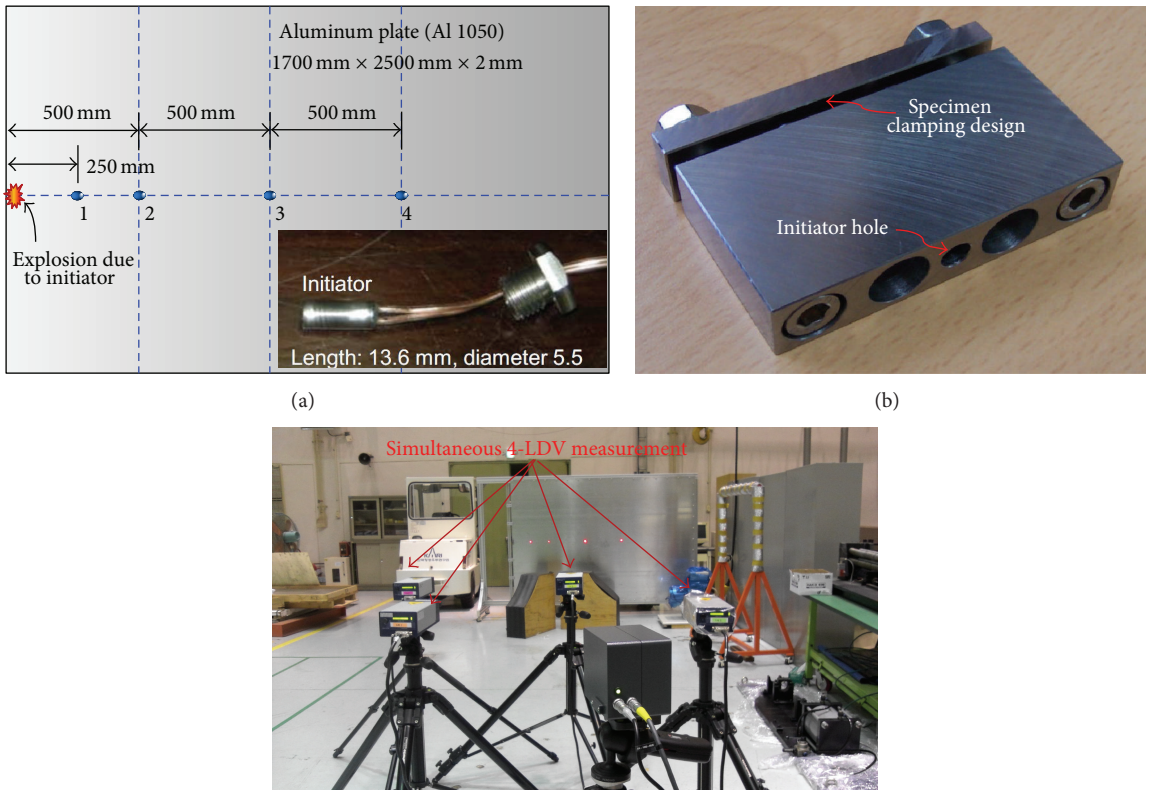

FIGURE 2: Experimental setup for pyroshock measurement: (a) 2 mm thick aluminum plate (Al 1050), (b) initiator mount, and (c) four laser Doppler vibrometers setup configuration.

Table 1: Examples of M and N bandpass filter matrix setting in Level 1 and Level 2.

	Level 1 (L1) N bandpass filters			
	1	3		
	100–100 kHz	100–1 kHz	1 kHz–10 kHz	10 kHz–100 kHz
Level 2 (L2) M bandpass filters				
1	99.9 kHz	900 Hz	9.0 kHz	90.0 kHz
5	—	180 Hz	1.8 kHz	18.0 kHz
10	—	90 Hz	900 Hz	9.0 kHz
20	—	45 Hz	450 Hz	4.5 kHz

Table 2: Mean acceleration differences (%) in the pyroshock SRS repeatability test over the four points.

Case	Mean acceleration difference (%)			
	Pt1	Pt2	Pt3	Pt4
Ref-1	15.0	11.5	29.5	34.8
Ref-2	10.9	8.0	25.3	27.2
Ref-3	10.3	8.0	26.5	28.1
Average	12.1	9.2	27.1	30.0
Average Pt1~Pt4	**19.6%**			

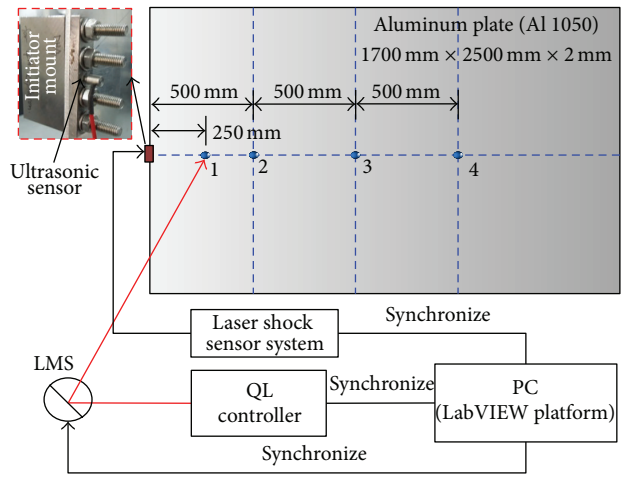

LMS: laser mirror scanner
QL: Q-switched continuous wave laser

Figure 3: Experiment setup for laser shock measurement in the same specimen in the pyroshock measurement.

As for the details of the proposed algorithm, a pyroshock signal and a laser shock signal, which are measured at the same local point, are inputted into the subbands decomposition. The pyroshock signal, denoted by $P(k)$, is used as a reference for the laser shock signal, denoted by $L(k)$, to convert the laser shock into a reconstructed pyroshock signal. Then, the notation of k is the index of the discrete-time instants of the signal. In L1, $P(k)$ is decomposed into different frequency bands by M bandpass filters, as shown in Figure 1. At the same time, the decomposition process of $L(k)$ is also the same as the decomposition process of $P(k)$, and the decomposed signals of $L(k)$ and $P(k)$ are defined as $L_i(k)$ and $P_i(k)$, respectively, where the index is $i = 1, 2, \ldots, M$.

Once the L1 decomposition process is completed, both $P_i(k)$ and $L_i(k)$ are further processed in L2. The respective ith decomposed signals of $P_i(k)$ and $L_i(k)$ are decomposed again into N signals with equal bandwidths by N bandpass filters, respectively. For example, as shown in Figure 1, $P_1(k)$ is decomposed into N signals and $P_2(k)$ is decomposed into another N signals with N bandpass filters, respectively. This process is also performed the same for $L_1(k)$. Then, the resultants of the two-level subbands decomposition process are defined as $P_{i,j}(k)$ and $L_{i,j}(k)$ for the pyroshock and laser shock signals, respectively, where the index is $j = 1, 2, \ldots, N$.

After the decomposition, the SRS matching and synthesis process with $P_{i,j}(k)$ and $L_{i,j}(k)$ follows. In this process, the signal envelope extraction function based on the Hilbert transform is used, and the function can be expressed as [12]

$$E(t) = \sqrt{x(t)^2 + H[x(t)]^2},$$
$$H[x(t)] = \frac{1}{\pi} \int_{-\infty}^{\infty} \frac{x(\tau)}{\tau - 1} d\tau, \quad (1)$$

where $E(t)$ is the enveloped signal of an input signal $x(t)$ and $H[x(t)]$ is the Hilbert transform of the input signal $x(t)$. Hence, based on (1), the total enveloped signals of $M \times N$ for each $P_{i,j}(k)$ and $L_{i,j}(k)$ are extracted and defined as $\widetilde{P}_{i,j}(k)$ and $\widetilde{L}_{i,j}(k)$, respectively, as shown in Figure 1. Once the enveloped

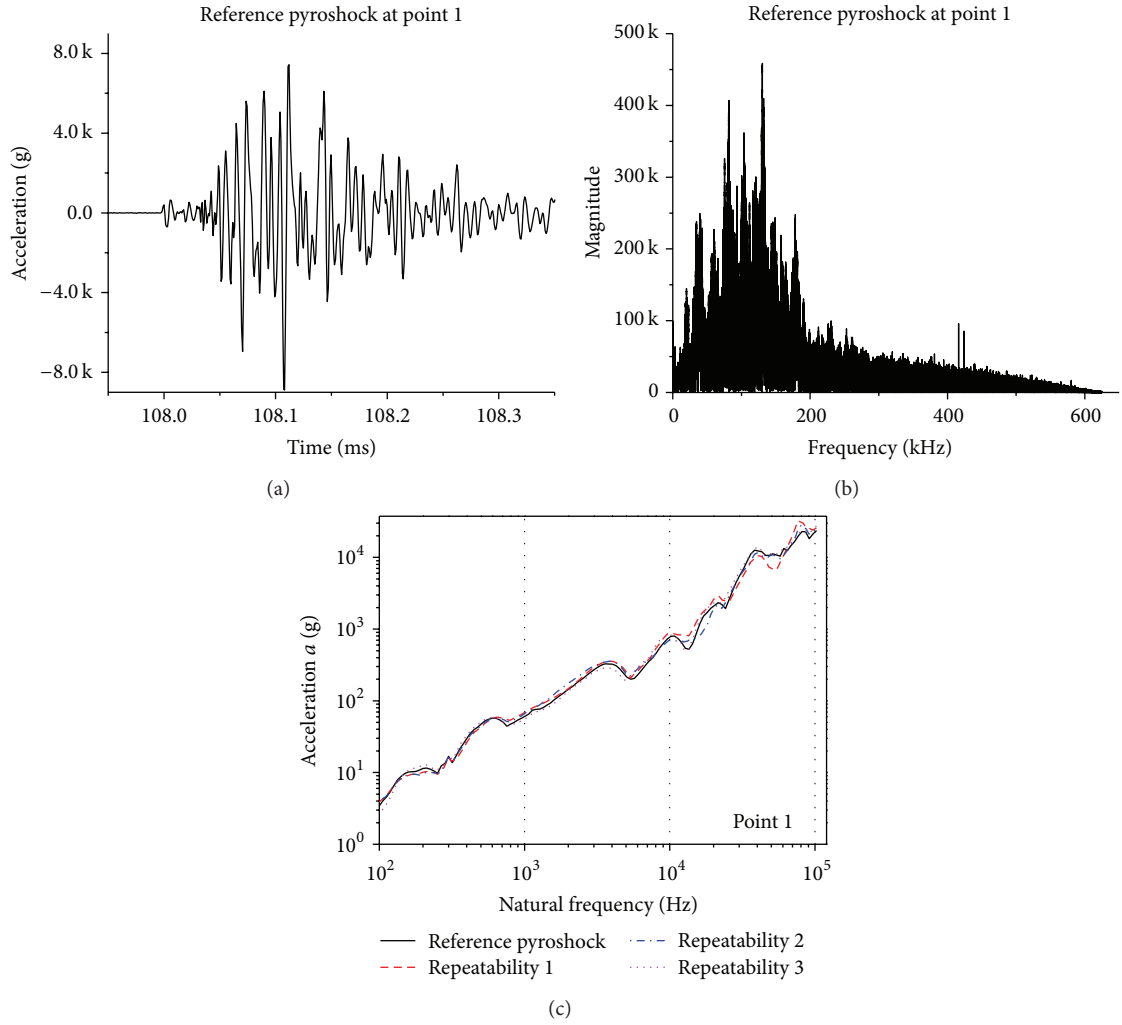

Figure 4: Reference pyroshock signal at Pt1: (a) time-domain, (b) frequency-domain, and (c) SRS response of the reference pyroshock signal and the SRS repeatability.

signals are determined, a reconstructed pyroshock signal can be determined as follows:

$$P_{\text{recon.}}(k) = \sum_{i=1}^{M}\sum_{j=1}^{N} G_{i,j}(k)\, L_{i,j}(k), \tag{2}$$

$$G_{i,j}(k) = \frac{\widetilde{P}_{i,j}(k)}{\widetilde{L}_{i,j}(k)}. \tag{3}$$

Equation (2) shows that the reconstructed pyroshock signal can be obtained by multiplying a gain $G_{i,j}(k)$ by the decomposed laser shock signal $L_{i,j}(k)$, respectively, and the gain $G_{i,j}(k)$ is the ratio of $\widetilde{P}_{i,j}(k)$ to $\widetilde{L}_{i,j}(k)$.

The code for this algorithm was developed in a LabVIEW platform.

3. Experimental Setups

In this section, two experimental setups for pyroshock measurement and laser shock measurement from a specimen are first introduced. The specimen used in these experiments was a 2 mm thick aluminum plate (Al 1050) and Figure 2(a) presents the schematic of the aluminum plate specimen with a size of $1700 \times 2500 \times 2\ \text{mm}^3$. Then, the settings and operation of the signal processing algorithm are presented too.

3.1. Pointwise Explosive Pyroshock Measurement. For the pyroshock measurement, an initiator as the pointwise explosive was used as a pyroshock source as shown in the inset of Figure 2(a). Figure 2(b) illustrates an initiator mount which was made of a stainless steel material. The initiator mount was used to mount the initiator and clapped at the left end of the specimen plate, as illustrated in Figure 2(a). Once the initiator was detonated, a pyroshock wave was generated and the wave propagated away from the source into the aluminum plate. In this paper, four reference pyroshock signals were considered for the implementation of the signal processing algorithm. Hence, four LDVs (OFV-5000, Polytech) were set up at approximately 3 m stand-off distance, as shown in Figure 2(c), to simultaneously measure four pyroshock

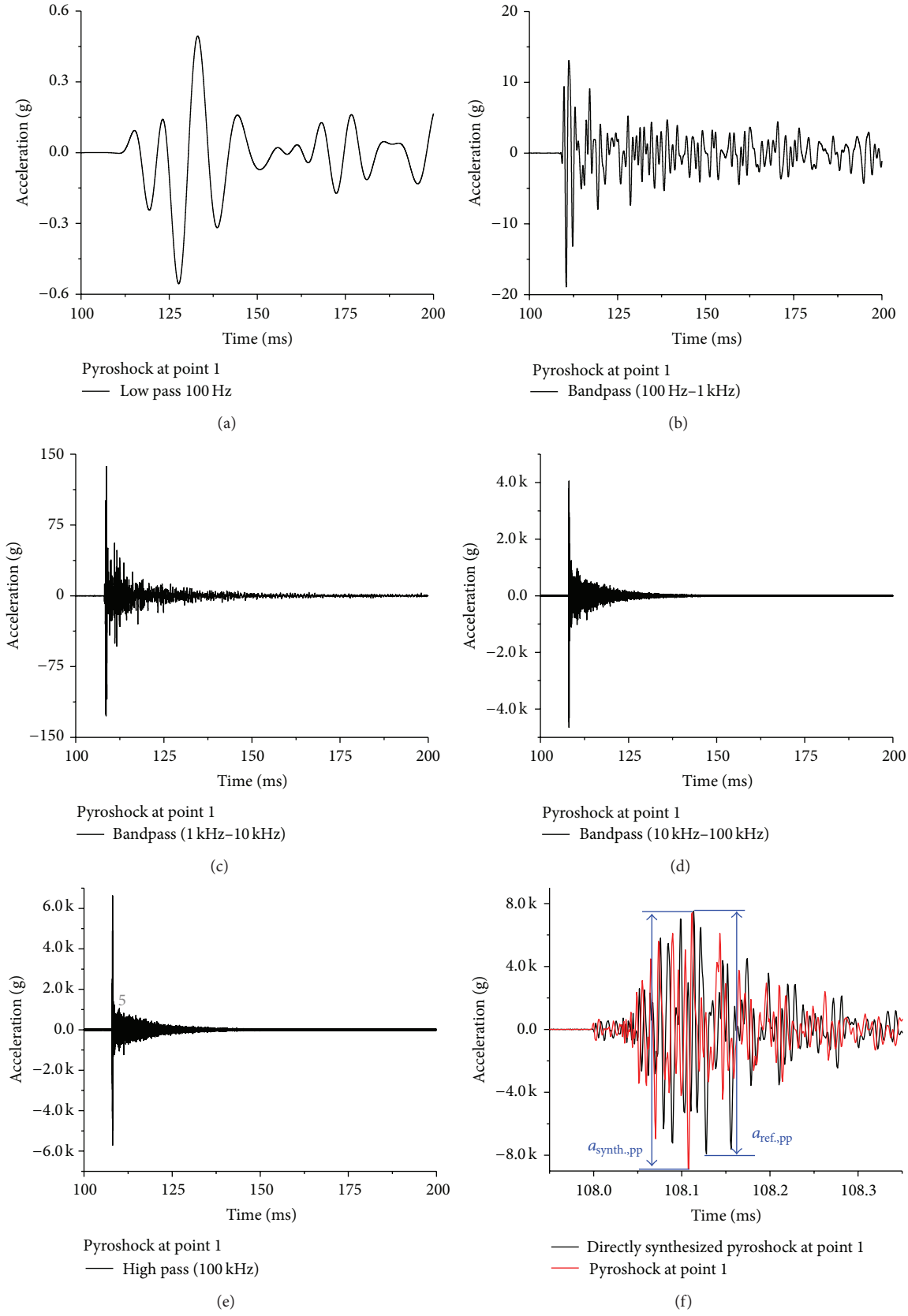

FIGURE 5: Decomposition of the reference pyroshock signal at Pt1 with the bandwidths of (a) 0 to 100 Hz, (b) 100 Hz to 1 kHz, (c) 1 kHz to 10 kHz, (d) 10 kHz to 100 kHz, and (e) 100 kHz to 625 kHz and (f) direct synthesizing of the decomposed signals ($a_{ref.,pp}$ and $a_{synth.,pp}$ are the peak-to-peak accelerations of pyroshock and direct synthesized pyroshock at point 1).

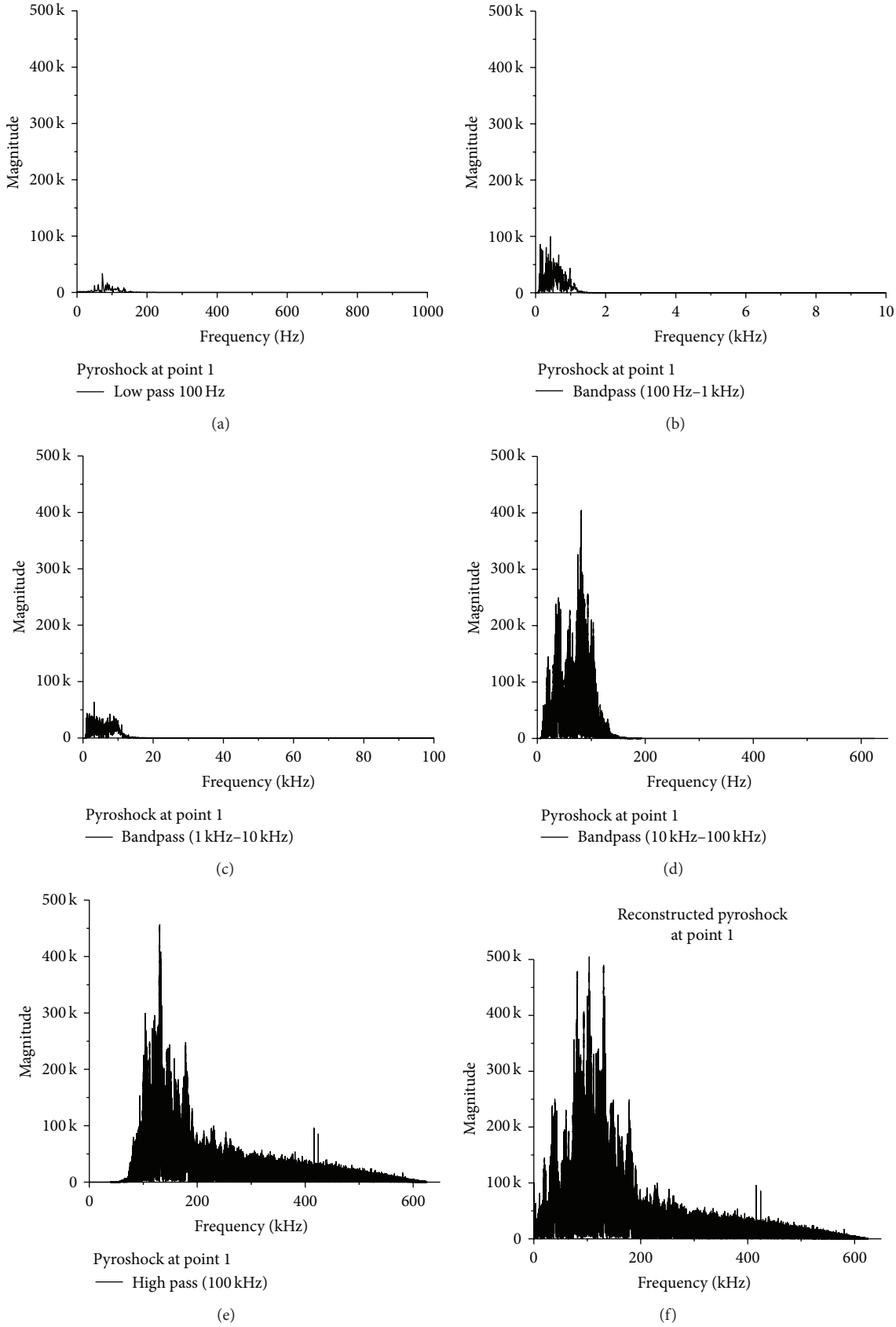

Figure 6: Frequency components of the reference pyroshock signal at Pt1 with respect to the bandwidths of (a) 0 to 100 Hz, (b) 100 Hz to 1 kHz, (c) 1 kHz to 10 kHz, (d) 10 kHz to 100 kHz, and (e) 100 kHz to 625 kHz. (f) Frequency components of the reconstructed pyroshock signal at Pt1.

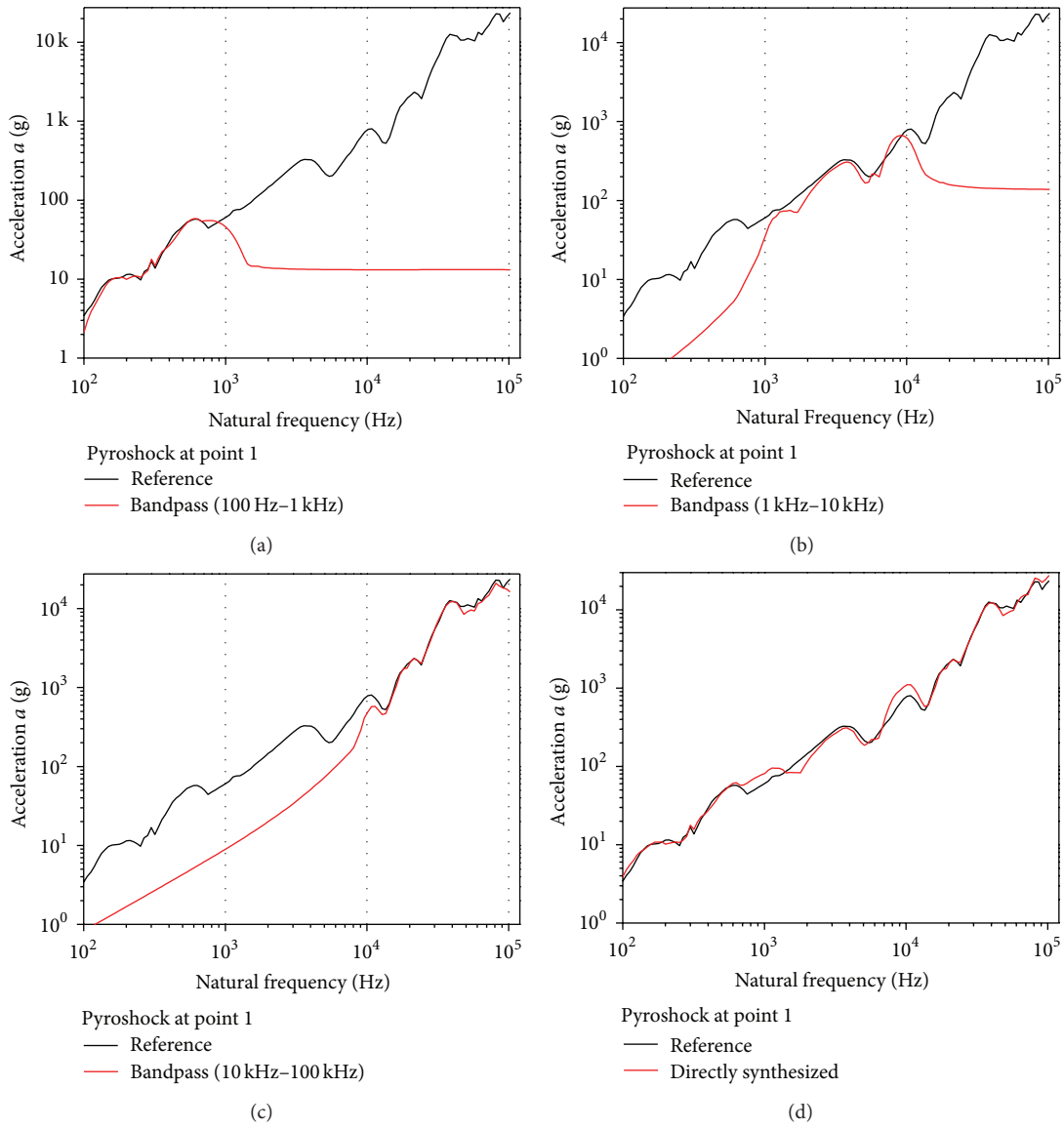

Figure 7: Comparison between the reference SRS curve and the pyroshock SRS curve decomposed in the frequency band of (a) 100 Hz to 1 kHz, (b) 1 kHz to 10 kHz, and (c) 10 kHz to 100 kHz and (d) comparison between the reference SRS curve and the SRS curve superposed with the decomposed three pyroshock signals.

Table 3: Mean acceleration difference (%) in SRS between the reconstructed pyroshock signals and reference pyroshock signals.

Level 1 (L1) *M* bandpass filters	Level 2 (L2) *N* bandpass filters	Mean acceleration difference (%)				
		Pt1	Pt2	Pt3	Pt4	Average Pt1~PT4
1	1	533.7	458.9	477.4	418.6	472.15
3	1	121.5	161.3	172.7	120.1	143.90
3	5	35.2	60.5	82.1	37.4	53.80
3	10	24.5	24.2	23.6	25.9	24.55
3	20	24.5	21.0	17.6	19.6	20.68
3	**23**	**23.6**	**19.1**	**18.8**	**17.9**	**19.85**
3	25	25.0	21.4	20.6	16.9	20.98
3	30	25.5	20.6	18.6	17.1	20.45
3	40	28.0	22.0	20.2	23.9	23.53

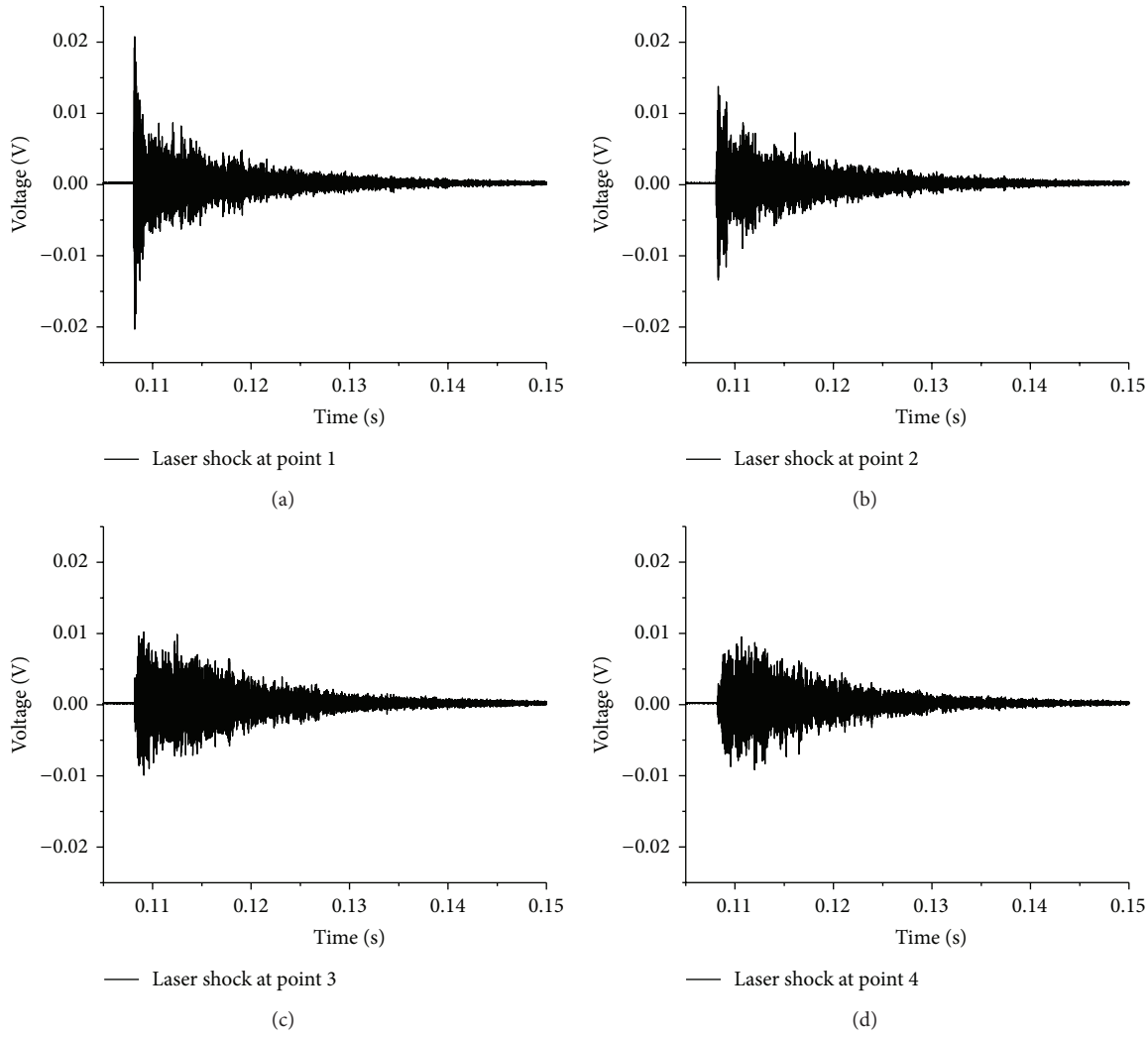

Figure 8: Laser shock signals at (a) Pt1, (b) Pt2, (c) Pt3, and (d) Pt4.

signals. As shown in Figure 2(a), the four sensing points (Pt1–Pt4) were located along a line with the distances of 250 mm, 500 mm, 1000 mm, and 1500 mm from the initiator mount. During the measurement, retroreflective films were used to minimize the speckle noise to improve the signal-to-noise ratio (SNR) of the sensing signal. Thus, they were attached on the local sensing points (Pt1–Pt4), respectively. The band of interest for the pyroshock signal in this paper was 100 Hz to 100 kHz. Therefore, the four pyroshock signals were measured with a low pass of 100 kHz in the respective controllers of the LDVs. Afterwards, the signals were acquired and digitized through the four channels of an 8-channel high-speed digitizer (NI PCI-5105) at a sampling time interval of $T = 0.8\,\mu$s and a signal length of $k = 900{,}000$ samples in a LabVIEW platform. In the measurement, high sampling frequency was selected in order to preserve the acquired pyroshock signal without aliasing, as well as the waveform shape for time-domain analysis. After the acquisition, four pyroshock signals were stored in a computer for later implementation of the signal processing algorithm.

3.2. Laser Shock Measurement. Figure 3 demonstrates the experimental setup for the laser shock measurement on the aluminum plate used in the pyroshock measurement. As illustrated in Figure 3, the experimental setup was configured with a Q-switched Nd:YAG diode pumped solid state laser (QL) with 1064 nm wavelength, a QL controller, a galvanometric laser mirror scanner (LMS), a laser shock sensor system, and a computer with a LabVIEW platform for data acquisition and synchronization control.

The QL was used as a laser shock source and controlled by the QL controller. The LMS has two mirrors with 1064 nm reflective coating, where each mirror is mounted on a galvanometer. Hence, the LMS was used to maneuver the laser pulse to the sensing point. In the laser shock sensor system, an in-line bandpass filter was used during the laser shock signal acquisition. Then, an omnidirectional amplifier-integrated accelerometer (PZT transducer) was selected for the system to measure a laser shock signal. It has broadband frequency characteristics with the cutoff frequency of 2 MHz and the sensitivity of up to 316 V/mm/s. In regard to its high

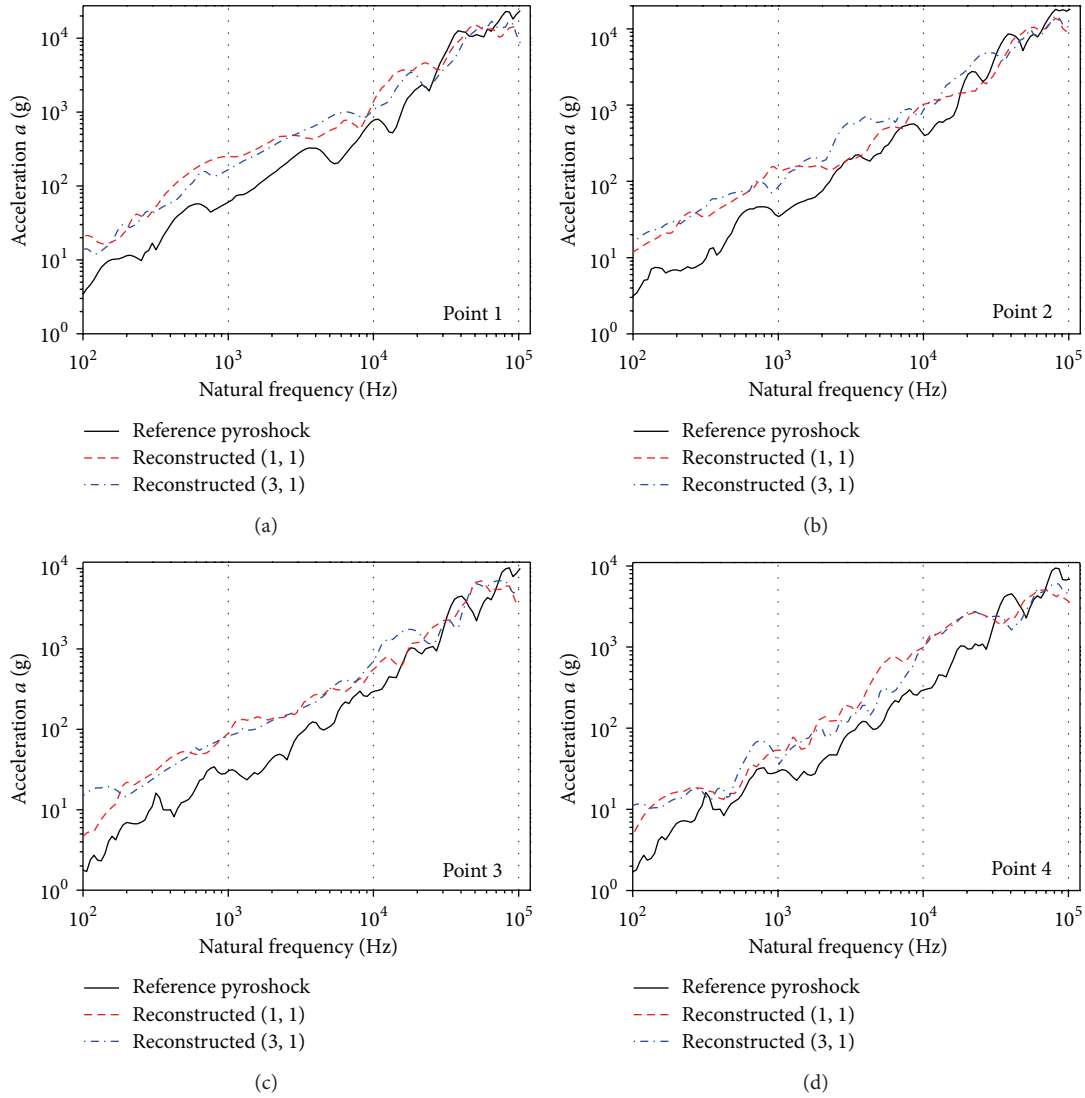

Figure 9: SRS curve comparison between the reference and reconstructed pyroshock signals at (a) Pt1, (b) Pt2, (c) Pt3, and (d) Pt4 in the decomposition cases of (1, 1) and (3, 1).

sensitivity in comparison to LDV (0.2 V/mm/s), the sensor was more suitable to be used in the laser shock measurement. As shown in the inset of Figure 3, the accelerometer was bonded on the surface of the initiator mount (Figure 2(b)) using a cyanoacrylate adhesive. Lastly, a computer was used to synchronize the laser shock generation and measurement events and stored the laser shock signal for later processing.

The LMS maneuvered the laser pulse set at laser energy of 2.5 mJ towards the sensing point as shown in Figure 3. The four laser shock signals were acquired one point by one point. When the laser pulse impinged on the surface of the specimen, the laser shock was generated based on a thermoelastic regime. Then, the laser shock wave propagated away from the impingement point to the accelerometer. Using the reciprocity of wave propagation time, the laser shock wave was regarded as a wave generated at the excitation point and received from the laser impingement point. After that, the laser shock signal was filtered in the in-line bandpass filter with the cuton of 100 Hz and cutoff of 100 kHz simply because the frequency band to be analyzed in terms of SRS was the frequency band of 100 Hz to 100 kHz. Subsequently, the signal was acquired into the high-speed digitizer (NI PCI-5105) at the same sampling time interval and signal length as in the pyroshock measurement, $T = 0.8\,\mu$s, $k = 900{,}000$ samples in the LabVIEW platform.

3.3. Signal Processing Algorithm Setting and Operation. After the pyroshock and laser shock measurements, the pyroshock and laser shock signals were stored into the computer. Before these signals were processed by the proposed algorithm, the two settings of the algorithm were considered and set, as shown in Table 1.

One bandpass filter ($M = N = 1$) was chosen in L1 and L2, respectively. Both high and low cutoff frequencies were set to 100 Hz to 100 kHz. In the second case, three bandpass

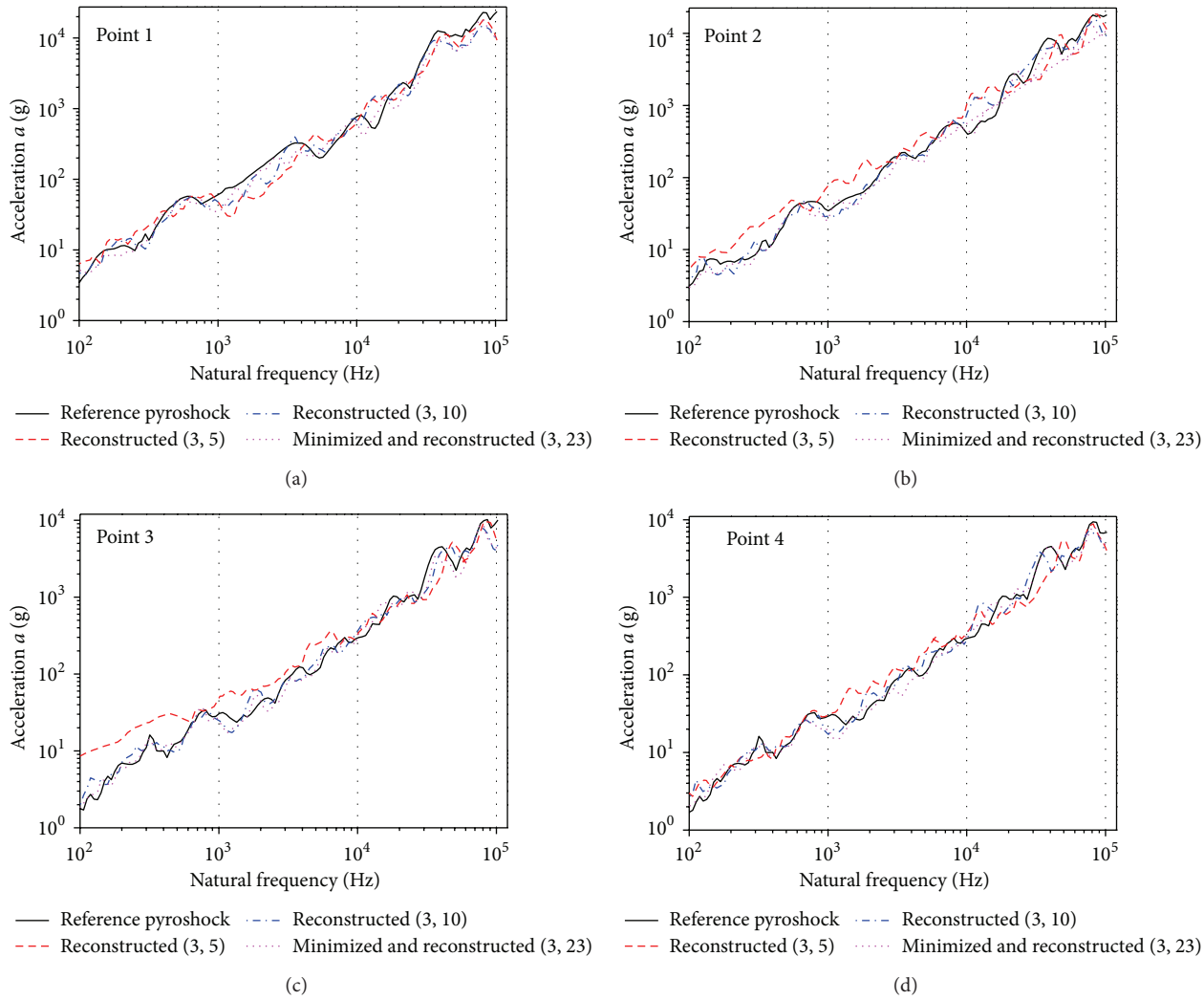

FIGURE 10: SRS curve comparison between the reference pyroshock signal and the pyroshock signals reconstructed with hieratical subband decomposition and MAD minimization at (a) Pt1, (b) Pt2, (c) Pt3, and (d) Pt4 in cases of three different N bandpass filters in Level 2 ((3, N) cases).

filters ($M = 3$, $N = 1$) were chosen and the respective high and low cutoff frequencies were set to 100 Hz to 1 kHz, 1 kHz to 10 kHz, and 10 kHz to 100 kHz. This set of high and low cutoff frequencies was chosen because the midfield is between 10 kHz and 100 kHz and the far-field is below 10 kHz [13] and also the frequency scale of an SRS curve is plotted on the 3-cycle log-scale x-axis in a log-log graph. As shown in Table 1, four different N bandpass filters in L2 were chosen. Each decomposed signal after L1 was decomposed again with the N bandpass filters with equal bandwidths, respectively. First, one bandpass filter was set in L2 for processing, and then the processing is followed by 5, 10, and 20 bandpass filters in the second case.

After the parameter setting, the reference pyroshock signal and the laser signal, which were measured at Pt1, were inputted into the subbands decomposition (Figure 1). After the decomposition, $P_{M,N}(k)$ and $L_{M,N}(k)$ were obtained. Then, in the wave matching, the enveloped signals $\widetilde{P}_{M,N}(k)$ and $\widetilde{L}_{M,N}(k)$ were extracted from the decomposed signals. Subsequently, the gain $G_{M,N}(k)$ based on (3) was determined, and the synthesized pyroshock signal at Pt1 could be determined through (2). After the processing of Pt1, the processing was repeated to obtain the synthesized pyroshock signals at Pt2, Pt3, and Pt4, respectively. Also, after the processing in case 1 was completed, the processing was repeated for case 2 with the same manner, where four synthesized pyroshock signals were generated with respect to $N = 1$ in L2, and then followed by 5, 10, and 20.

After all these synthesized pyroshock signals were obtained, the similarity between the SRS curves of the synthesized pyroshock signal and the reference pyroshock signal was evaluated based on the mean acceleration difference (MAD, %) as follows:

$$\text{MAD}\,(\%) = \left(\frac{1}{Z} \sum_{i=0}^{Z-1} \left| \frac{a_P - a_{\text{recon.}}}{a_P} \right| \right) \times 100\%, \tag{4}$$

where Z is the total number of acceleration values in the SRS curve, a_P is the acceleration in the SRS curve of a reference pyroshock signal, and $a_{\text{recon.}}$ is the acceleration of the SRS curve for a reconstructed pyroshock signal.

4. Results and Discussion

4.1. Pyroshock Characteristics Study. Before the implementation of the proposed signal processing algorithm, the characteristics of pyroshock signals were investigated. As mentioned in Section 2, for the algorithm to construct a pyroshock signal based on a laser shock signal, the assumption that the pyroshock signal is governed by the principle of wave superposition was also verified. For that, the reference pyroshock signal at Pt1 was used to verify the agreement of the superposition principle.

Figure 4(a) shows the reference pyroshock signal plotted in the time domain. The peak-to-peak amplitude in acceleration of the pyroshock $a_{\text{ref.,pp}}$ was 16,322.5 g. Figure 4(b) shows the frequency components of the pyroshock obtained by the fast Fourier transform (FFT) with a frequency range of up to 625 kHz. The area under the curve is equal to the energy of the signal. As shown in Figure 4(b), the energy of the pyroshock was concentrated below the frequency of 130.3 kHz. In addition, the frequencies of 81.5 kHz, 103.7 kHz, and 130.3 kHz had higher energy among the other frequency components. Figure 4(c) shows the SRS response of the pyroshock signal from 100 Hz to 100 kHz. The corresponding acceleration range with respect to the natural frequency was approximately from 3.8 g to 27,676.4 g. Then, Figure 4(c) also includes the SRS curves with respect to the other three repeated pyroshock measurements. As summarized in Table 2, the average of the MADs over the four points calculated using (4) in the pointwise explosive tests was 19.6%.

To verify if the pyroshock signal is governed by the principle of superposition, the pyroshock signal at Pt1 was first decomposed into five different subbands with the bandwidths of 0 to 100 Hz, 100 Hz to 1 kHz, 1 kHz to 10 kHz, 10 kHz to 100 kHz, and 100 kHz to 625 kHz, respectively. Figures 5(a)–5(e) show the decomposed signals in the five subbands. The subbands with higher frequencies included the decomposed pyroshock signals with higher amplitudes. Even if the reference pyroshock signal was acquired with the 100 kHz low-pass filter built in the LDV, the amplitude of the decomposed signal with the 100 kHz numerical high-pass filter, as illustrated in Figure 5(e), had higher peak-to-peak acceleration in comparison to the other decomposed signals. To reconstruct the pyroshock signal, all of the decomposed pyroshock signals were just simply summed up, and the reconstructed pyroshock signal was obtained as shown in Figure 5(f). As shown in Figure 5(f), the reconstructed pyroshock signal exhibited the peak-to-peak acceleration $a_{\text{recon.,pp}}$ obtained at 15,446.55 g, and it has only 5.4% difference from the peak-to-peak acceleration, $a_{\text{ref.,pp}}$, of the reference pyroshock signal at Pt1. The difference was suspected due to some data distorted during the signal decomposition and synthesis processes.

Next, the frequency components of the decomposed signals were obtained by using FFT as shown in Figures 6(a)–6(e), respectively. The energy of the decomposed pyroshock signals increased as the corresponding frequency bandwidth increased. Within them, the frequency components from 10 kHz to 625 kHz possessed the most energy in the reference pyroshock signal. In addition, the frequencies of 81.5 kHz, 103.7 kHz, and 130.3 kHz had higher energy among the other frequency components. This has reflected that the peak-to-peak acceleration of the signal for Figure 5(e) stood at the highest amplitude value. Then, the shape of the frequency components for the reconstructed pyroshock signal was also similar to the reference pyroshock signal at Pt1 as shown in Figure 6(f).

Figures 7(a)–7(c) demonstrate the SRS curves between 100 Hz and 100 kHz of the decomposed pyroshock signals, respectively. Frequency range is important because it is considered as the far- and midfield frequency components in the SRS analysis of the pyroshock. As shown in Figure 7(a), the SRS curve of the pyroshock signal decomposed from 100 Hz to 1 kHz showed a good match to that of the reference pyroshock signal at Pt1 in the frequency range of 100 Hz to 1 kHz. Then, as shown in Figures 7(b) and 7(c), the respective SRS curves of the decomposed pyroshock signals also showed good agreement with those of the reference pyroshock signals in the respective decomposed frequency zones. As presented in Figure 7(d), the SRS curve of the pyroshock signal superposed with the decomposed three time-domain signals also showed good agreement with the SRS curve of the reference pyroshock signal at Pt1. Consequently, as proven in Figure 7(d), the pyroshock signal can be analyzed with the wave superposition principle.

4.2. Pyroshock SRS Generation Using a Laser Shock. With the validated assumption, the signal processing algorithm proposed to reconstruct a pyroshock signal using a laser shock signal was verified in this section. The generation mechanisms of the pyroshock and laser shock are different from each other; the origin of both resulting waves is commonly stress waves. On the other hand, their frequency components and amplitude are different.

Figures 8(a)–8(d) show the laser shock signals at Pt1, Pt2, Pt3, and Pt4, respectively. Each laser shock signal was measured at the submillivolt level. Each laser shock signal was inputted into the laser shock-based pyroshock reconstruction algorithm presented in Section 2, together with the reference pyroshock signal at the corresponding measurement point. Both signals were decomposed in the way listed in Table 1 and their SRSs were matched and synthesized. Moreover, the same processing was performed for the other three points.

Figures 9 and 10 show the SRS curves at Pt1, Pt2, Pt3, and Pt4, respectively, which were generated by the laser shock-based pyroshock SRS reconstruction algorithm. Table 3 summarizes the MAD of the SRS curves between the reconstructed pyroshock signals and the reference pyroshock signals, which was calculated using (4).

For the single band and nonhieratical decomposition cases, $(M, N) = (1, 1)$ and $(1, 3)$, the SRS curves of both

simulated pyroshock signals showed very low similarity to the reference pyroshock signals as shown in Figure 9. The MAD was also very high as presented in Table 3. For the cases using the hieratical method and more bands, (3, 5) and (3, 10), the MADs in the SRS curves of the reconstructed pyroshock signals were improved and demonstrated better similarity as the N increased from 5 to 10 subbands. Therefore, the simple bisection method was used to find N minimizing the average MAD over the four points in SRSs between the reconstructed and reference pyroshocks, where the boundary values for N were 20 and 40. The iteration converged into $N = 23$ and the average of the resulted MADs over the four points was 19.85%, which is an acceptable value for the prediction of the SRSs of real pyroshocks because the ballistic pyroshock measurement experiments using the actual explosives showed only 19.6% in the average of MAD as reported in Section 4.1.

Table 3 indicates that some cases show better results at point 3 or point 4. These results have shown that the similarity of the reconstructed SRS is dependent on the number of bandpass filters set. A pyroshock signal was decomposed by a number of bandpass filters to allow the respective decomposed laser signals to match with the decomposed pyroshock signals. However, during the filtering process, some of the dominant frequency components of the decomposed pyroshock signals, which have the dominant energy to reconstruct an SRS curve, might be filtered out from the passband of the bandpass filters. Then, with both decomposed signals, the SRS matching synthesis process, as shown in Figure 1, could not accurately reconstruct the acceleration amplitude of the pyroshock and eventually caused the low similarity between the acceleration amplitudes of the reconstructed SRS and the reference SRS.

As mentioned in Section 1, the signal processing algorithm can be further developed to reconstruct a pyroshock signal at any arbitrary point at a target specimen. Thus, the settings of the algorithm have to be statistically considered and acted as a common setting for a pyroshock simulator. Thus, the cases with $M = 3$ and $N = 23$ were the best settings to be employed in the signal processing algorithm that will be incorporated with the pyroshock simulator for the SRS reconstruction based on 2 mm aluminum plate at any arbitrary point. As for the signal processing time of the case (3, 23), it took 1.75 min using a 64-bit PC (Intel i7 CPU at 2.67 GHz) with 4 GByte RAM. These results have proven that the SRS curves of a pointwise explosive pyroshock can be estimated and reconstructed at multiple points in a structure using a laser shock with much lower amplitude and wider frequency range and the proposed laser shock-based pyroshock SRS reconstruction algorithm.

5. Conclusion

The laser shock-based pyroshock SRS reconstruction algorithm was proposed for the case of a pointwise explosive-induced pyroshock. The algorithm was based on the new idea that the generation mechanisms of the pyroshock and laser shock are different but the origin of both resulting waves is commonly the stress wave even if their frequency components and amplitude are different. The SRS is an important tool to analyze and quantify a pyroshock. The near-field pyroshock is avoided in the pyrotechnic design level but the mid- and far-field pyroshocks can easily cause failures in electronic and optical components sensitive to high frequency energy below 100 kHz and failures in relay and magnetic components sensitive to low frequency ranges from 2 kHz to 4 kHz. Therefore, in this study, the proposed algorithm was concentrated on the frequency range between 100 Hz and 100 kHz to reconstruct the pyroshock with the laser shock. As for the experiments, the laser shock was measured using the four-point excitation by the Q-switched laser and the single accelerometer in the aluminum plate and the pyroshock measurement was carried out using the single initiator (pointwise explosive) and four LDVs in the same plate. For signal processing, it was verified that the measured pyroshock waves are governed by the wave superposition principle. The proposed signal processing method consisted of the hieratical subband decomposition and the SRS matching synthesis. Two levels of subband decomposition were chosen and a Butterworth IIR bandpass filter was used for subbands decomposition. Then, in the SRS matching synthesis, all the envelopes of the decomposed signals were extracted and the gain was determined. Finally, the gained decomposed laser shock signals were synthesized to reconstruct the SRS of the pyroshock signal. The same process was done for the different points in the specimen, Pt1–Pt4. The similarities between the SRS curves of the reference and reconstructed pyroshocks were evaluated by using MAD (%). Through the minimization of the MAD in SRS between the reconstructed and reference pyroshocks, 19.85% was achieved in terms of the average of the MADs over the four points, which was a satisfiable value because the ballistic pyroshock measurement experiments using the actual explosives showed to be 19.6% in the average of MADs over the four points. The results showed also that the similarity between the reconstructed and reference SRS curves was dependent on the passband bandwidth being set in the bandpass filters as used in the subband decomposition process. For that, the proposed signal processing algorithm can be improved in the future by including a feature where the passband bandwidth of the bandpass filters can be set based on the dominant frequency energy of a reference pyroshock, so that the signal processing algorithm can reconstruct an SRS curve with the better similarity level. Lastly, since the SRS curves of the pyroshock can be predicted with the proposed laser shock-based pyroshock SRS reconstruction method, expensive, laborious, and time-consuming pyroshock experiments which are also dangerous to both the structure itself and testers can be minimized in the development of pyrotechnical devices.

Conflict of Interests

The authors declare that there is no conflict of interests regarding the publication of this paper.

Acknowledgments

This research was supported by Space Core Technology Development Program (2013042548) and the Basic Science Research Program (2011-0010489) and through the National Research Foundation of Korea funded by the Ministry of Education, Science and Technology. This study was also supported by the University Collaboration Enhancement Project of the Korea Aerospace Research Institute.

References

[1] J.-R. Lee, C. C. Chia, and C.-W. Kong, "Review of pyroshock wave measurement and simulation for space systems," *Measurement*, vol. 45, no. 4, pp. 631–642, 2012.

[2] E. Fillippi, H. Attouoman, and C. Conti, "Pyroshock simulation using the alcatel etca test facility," in *Launch Vehicle Vibrations, 1st European Conference*, CNES, Toulouse, France, 1999.

[3] M. G. Ryschkewitsch, "Pyroshock test criteria," NASA Technical Standard NASA-STD-7003, NASA, Washington, DC, USA, 2011.

[4] M. Gherlone, D. Lomario, M. Mattone, and R. Ruotolo, "Application of wave propagation to pyroshock analysis," *Shock and Vibration*, vol. 11, no. 3-4, pp. 145–156, 2004.

[5] J.-R. Lee, H. Jeong, and C.-W. Kong, "Wave propagation visualization in an experimental model for a control rod drive mechanism assembly," *Nuclear Engineering and Design*, vol. 241, no. 9, pp. 3761–3767, 2011.

[6] M. R. Brake, "An inverse shock response spectrum," *Mechanical Systems and Signal Processing*, vol. 25, no. 7, pp. 2654–2672, 2011.

[7] M. T. Hale and R. Adhami, "Time-frequency analysis of shock data with application to shock response spectrum waveform synthesis," in *Proceedings of the IEEE Southeastcon*, vol. 1, pp. 213–217, Williamsburg, VA, USA, April 1991.

[8] V. X. Afonso, W. J. Tompkins, T. Q. Nguyen, and S. Luo, "ECG beat detection using filter banks," *IEEE Transactions on Biomedical Engineering*, vol. 46, no. 2, pp. 192–202, 1999.

[9] A. N. Akansu and R. A. Haddad, *Multiresolution Signal Decomposition: Transforms, Subbandss, and Waveletsd*, Academic Press, San Diego, Calif, USA, 2nd edition, 2001.

[10] J. Liu and W. Cao, "Fast algorithms of slight signal decomposition and reconstruction," in *Proceedings of the 3rd International Conference on Computational Electromagnetics and its Applications (ICCEA '04)*, pp. 115–117, November 2004.

[11] L. M. A. Augilar, C. Robledo-Sanchez, M. L. A. Carrasco, and M. M. M. Otero, "The principle of superposition for waves: the amplitude and phase modulation phenomena," *Applied Mathematics & Information Science*, vol. 6, no. 2, pp. 307–315, 2012.

[12] S. Choi and Z. Jiang, "Comparison of envelope extraction algorithms for cardiac sound signal segmentation," *Expert Systems with Applications*, vol. 34, no. 2, pp. 1056–1069, 2008.

[13] D. R. Mulville, "Pyroshock test criteria," NASA Technical Standard NASA-STD-7003, NASA, Washington, DC, USA, 1999.

Hindawi Publishing Corporation
Shock and Vibration
Volume 2014, Article ID 436156, 10 pages
http://dx.doi.org/10.1155/2014/436156

Research Article

Development of a Numerical Model for an Expanding Tube with Linear Explosive Using AUTODYN

Mijin Choi,[1,2] Jung-Ryul Lee,[1,2,3] and Cheol-Won Kong[4]

[1] *Department of Aerospace Engineering, Chonbuk National University, 567 Baeje-daero, Deokjin-gu, Jeonju 561-756, Republic of Korea*
[2] *LANL-CBNU Engineering Institute Korea, Chonbuk National University, 567 Baeje-daero, Deokjin-gu, Jeonju 561-756, Republic of Korea*
[3] *Department of Mechatronics Engineering, Chonbuk National University, 567 Baeje-daero, Deokjin-gu, Jeonju 561-756, Republic of Korea*
[4] *Structures and Material Department, Korea Aerospace Research Institute, Daejeon 305-333, Republic of Korea*

Correspondence should be addressed to Jung-Ryul Lee; leejrr@jbnu.ac.kr

Received 24 October 2012; Accepted 14 March 2013; Published 24 March 2014

Academic Editor: Gyuhae Park

Copyright © 2014 Mijin Choi et al. This is an open access article distributed under the Creative Commons Attribution License, which permits unrestricted use, distribution, and reproduction in any medium, provided the original work is properly cited.

Pyrotechnic devices have been employed in satellite launch vehicle missions, generally for the separation of structural subsystems such as stage and satellite separation. Expanding tubes are linear explosives enclosed by an oval steel tube and have been widely used for pyrotechnic joint separation systems. A numerical model is proposed for the prediction of the proper load of an expanding tube using a nonlinear dynamic analysis code, AUTODYN 2D and 3D. To compute a proper core load, numerical models of the open-ended steel tube and mild detonating tube encasing a high explosive were developed and compared with experimental results. 2D and 3D computational results showed good correlation with ballistic test results. The model will provide more flexibility in expanding tube design, leading to economic benefits in the overall expanding tube development procedure.

1. Introduction

Pyrotechnic devices are widely used in many space applications. They are used to perform releasing, cutting, pressurization, ignition, switching, and other mechanical work to initiate flight sequences during space missions, such as the separation of subsystems, boosters, fairings, stages, or payload satellites. Such explosive separation devices generate a shock environment that could have a destructive effect on the structure and hardware, especially on electromechanical and optical equipment. The environment is very complex, and studies have revealed that little information is available describing the basic mechanism of shock transmission and predicting shock response. Therefore, improved guidelines for pyrotechnic design, development, and qualification are clearly needed [1–3].

Pyrotechnic devices may generally be divided into point sources and line sources. Typical point sources include explosive bolts, separation nuts, pin pullers and pushers, and certain combinations of point sources for low explosive actuation. Typical linear sources include flexible linearly shaped charges, mild detonating fuses, and Super∗Zip for high explosive actuation [4, 5].

An example of line sources is shown in Figure 1. The pyrotechnic device shown is a high-load-carrying separation system that must act without contamination of the payload and is called an expanding tube in this study. The device is one of the greatest shock producers in aerospace separation systems. The detailed components of the expanding tube are also represented in Figure 1, consisting of an MDF (mild detonating fuse), support, and a flattened steel tube. The MDF is a small diameter extruded tube containing a single strand of explosive cord. It is manufactured by filling a tube with explosive material and extruding the tube using a conventional, multiple-die, cold extrusion process [6–9]. Structure separation is accomplished when the MDF is ignited. When an MDF is initiated, the detonation is propagated along

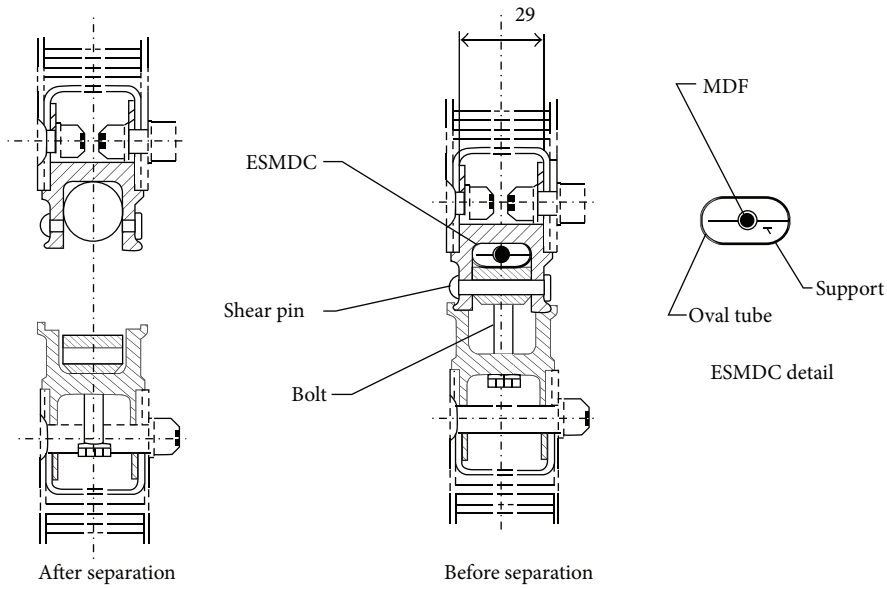

Figure 1: A pyro-separation system [9].

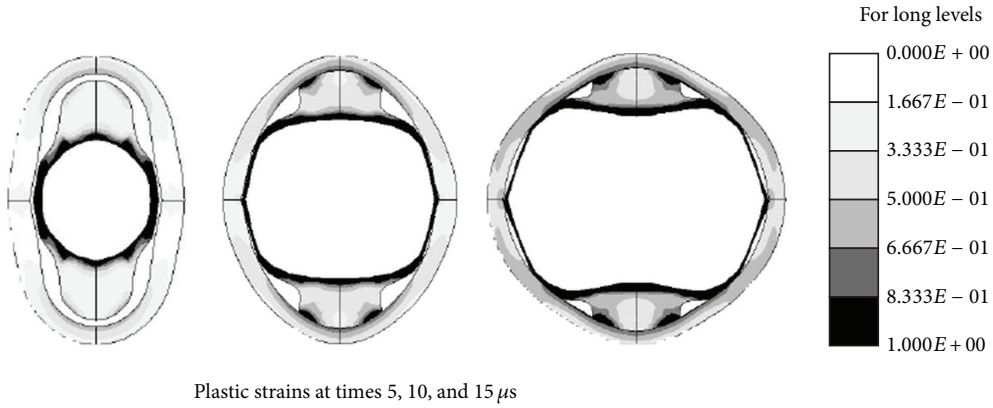

Figure 2: Numerical simulation of expanding tube free expansion [10].

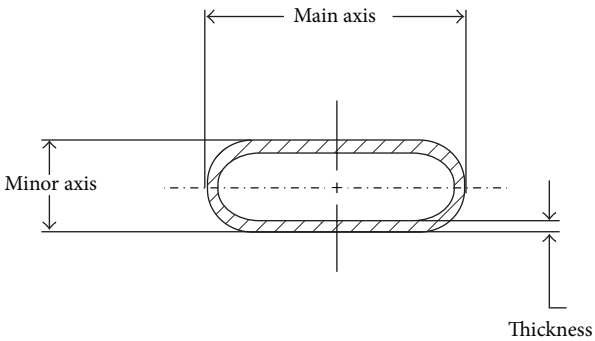

Figure 3: Geometry of expanding tube.

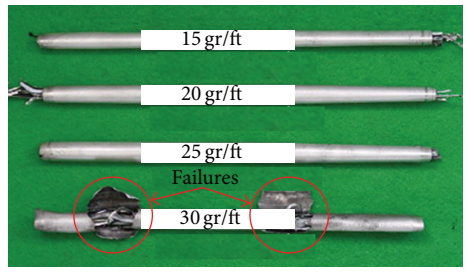

Figure 4: Experimental results of expanding tube.

the entire length of the linear explosive at a VOD (velocity of detonation) between 6.0 and 7.5 km/s, with very high shock energy. This chemical reaction acts as mechanical loading, which allows the elliptical steel tube to expand mainly in the minor-axis direction and fractures pin joints. Consequently, the expanded tube can separate structures according to its design, without contamination [8]. Since the performance of expanding tubes is mainly related to the explosive load, investigation of the proper explosive load against expanding tube failure and structural damage is important to its design.

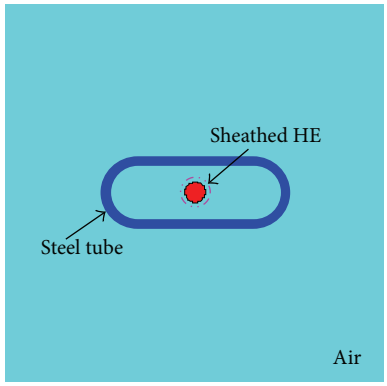

Figure 5: Material location of two-dimensional expanding tube.

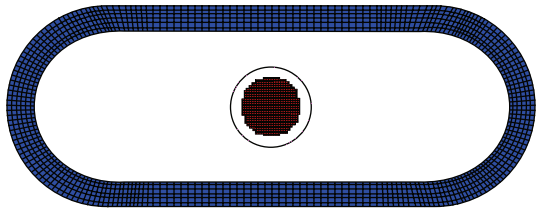

Figure 6: Two-dimensional expanding tube numerical model.

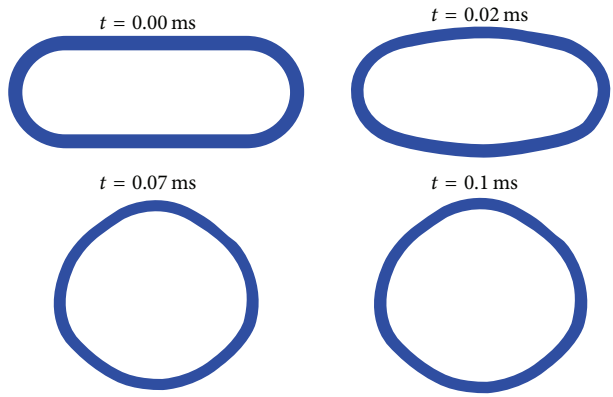

Figure 7: Expanding tube distortions (explosive load 15 gr/ft).

Even if the expanding tube design has to be verified in ballistic tests, adding a numerical simulation step between the expanding tube sample fabrication and its ballistic test can be a more effective approach for proper explosive load determination. The numerical model can explain the full physics of the phenomena by solving the governing equations that describe the behavior of the system under consideration.

In spite of the advantages of numerical simulation, only a few numerical and experimental investigations on pyrotechnic devices can be found in the literature. Quidot [10] adopted LSDYNA to simulate a pyrotechnic separation system. A line source comprised an expanding tube with a 1 mm thick stainless steel case, internal synthetic material, and a lead-RDX cord with a 2 g/m RDX charge. Numerical simulations were performed for this device, as shown in Figure 2. However, the proper explosive load, which is the most important factor for real-world applications of expanding tube design, was not addressed under consideration of the detonation wave propagation, the fracture mechanism, and experimental validation.

In this study, two- and three-dimensional numerical analyses of expanding tube were performed in order to develop a numerical model with high accuracy. The explicit dynamic code AUTODYN is adopted to simulate expansion of the tube and compute a proper core load. AUTODYN is a hydrocode program that is especially suited to solve the interaction problems of different systems of structure, liquid, and gas together, as found in many studies of high explosive simulation [11–15]. To verify the accuracy of the developed model, the numerical results were compared to experimental ballistic test results for different explosive load conditions.

2. Ballistic Tests of Expanding Tubes

Experiments were performed to properly design a pyrotechnic device. Explosive tests were carried out for different core loads of 15, 20, 25, and 30 gr/ft. The expanding tube is an open-ended cylinder, in which an MDF filled with hexanitrostilbene (HNS) explosive is set along the central axis of the cylinder. All MDF cords were manufactured with 3 mm diameters regardless of the respective explosive loads, and the wall thickness of the sheath was 0.1 mm. Figure 3 represents a section view of an expanding tube with a major axis of 20 mm, a minor axis of 8 mm, and a thickness of 1 mm, regardless of the core load. The tests were carried out 4 or 5 times for each core case, and the deformed shape and failure were investigated. Figure 4 shows the results of ballistic tests with explosive core loads of 15, 20, 25, and 30 gr/ft. Expanding tubes with 15, 20, and 25 gr/ft were freely expanded without failure. In contrast, the 30 gr/ft expanding tube failed at both ends of the cylinder, as shown in Figure 4. The dimensions of each expanding tube were measured, and these measurements were averaged. These results are used to validate the numerical model, which will be discussed in Section 3.

It can be deduced from the ballistic test results that the threshold explosive load of the tested samples must lie between 25 gr/ft and 30 gr/ft. Ballistic tests are a good approach to determine a proper explosive load for expanding tubes, as well as a better approximation of actual conditions. However, this experimental approach has several disadvantages, in which ballistic tests typically require many expanding tube samples and connected structures, which are also damaged during the test and are nonreusable. The experimental method is also not flexible for design change and is expensive and time consuming. Moreover, it is difficult to explain the physical phenomena of structure and detonation interactions. Therefore, to mitigate this problem, the ballistic test should be the final confirmation test of the expanding tube development procedure, after replacing the numerous case samples with a reliable numerical model.

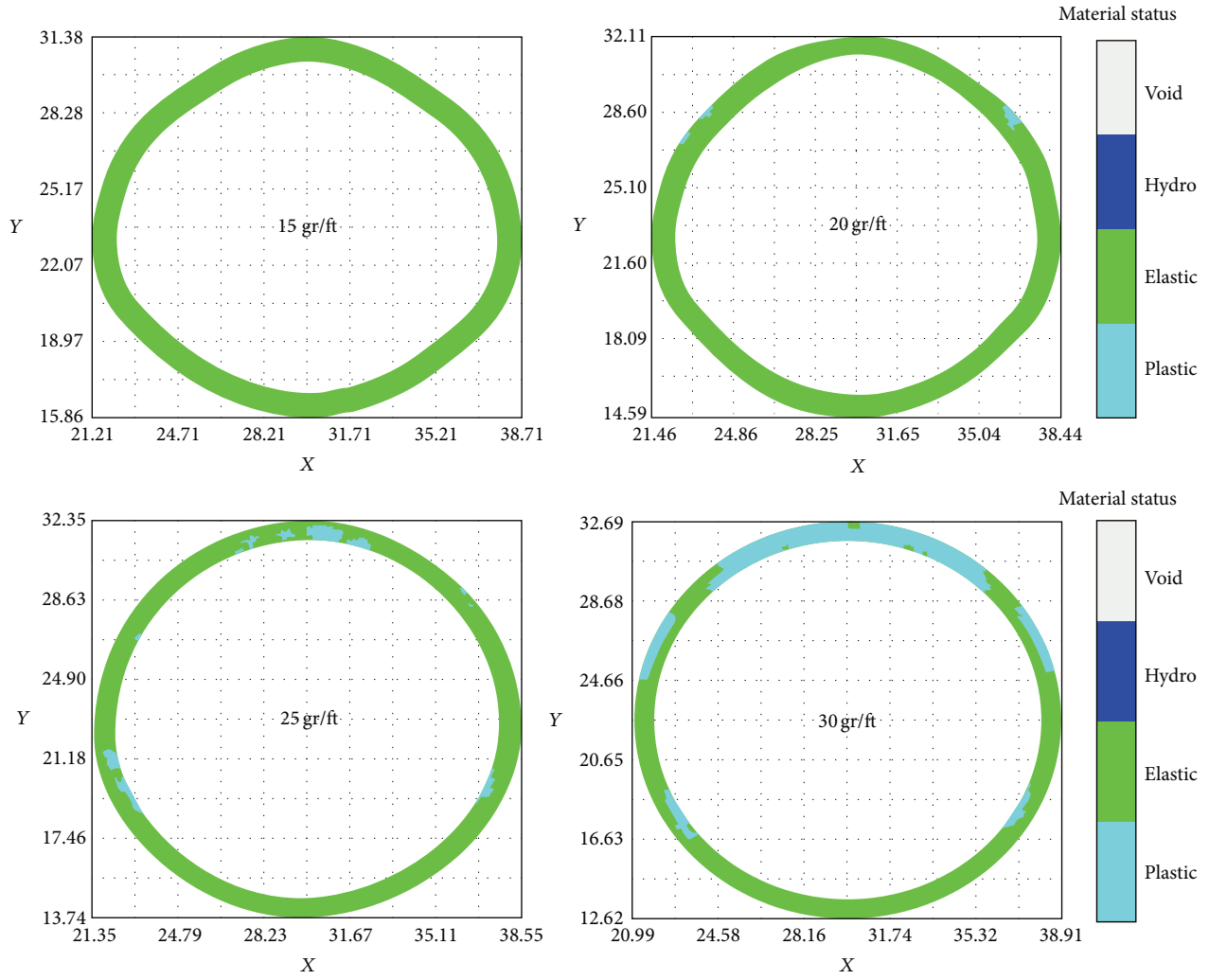

Figure 8: Material status of expanded steel tube.

3. Numerical Modeling

3.1. Numerical Model. Numerical simulations were performed for all the experiments using hydrocode in AUTODYN 2D, examining the experimental expanding behavior and numerical stresses. The two-dimensional model was made of a steel tube, support, MDF, and surrounding air, as shown in Figure 5. The surrounding air was modeled as an ideal gas, and the area was 400 mm × 400 mm. Since the material of the support layer was Teflon and it did not affect tube expansion significantly, it was assumed as air. The explosive material was HNS 1.65, where 1.65 indicates the density of HNS which is 1.65 g/cm^3. The explosive loads for all cases ranged from 15 to 30 gr/ft. The explosive propagation velocity for HNS 1.65 was approximately 7,030 m/s, and the detonation point was set to the center of the MDF.

3.2. Material Description and Boundary Conditions. Both the reacted solid and reacted gaseous products of HNS 1.65 explosive were characterized with the Jones-Wilkins-Lee

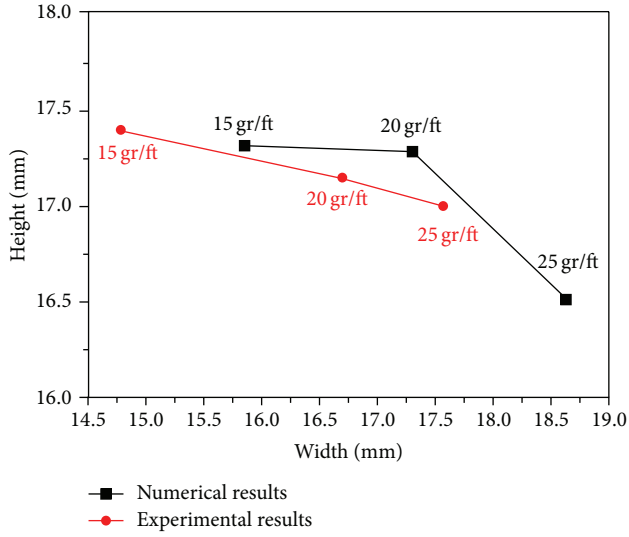

Figure 9: Comparison between the experimental and calculational results.

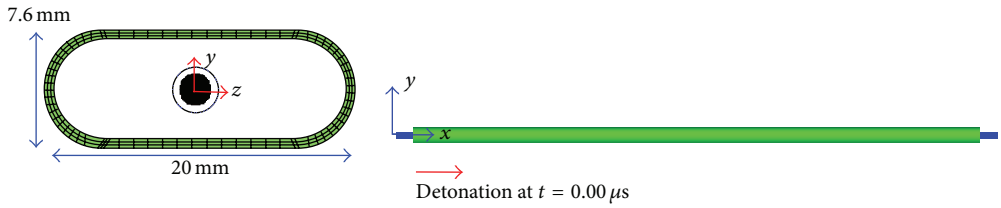

Figure 10: Three-dimensional expanding tube.

Table 1: Material coefficients in Jones-Wilkins-Lee (JWL) equation for HNS 1.65.

Parameter	Value	Unit
A	4.65×10^8	kPa
B	8.87×10^6	kPa
R_1	4.55	—
R_2	1.35	—
ω	0.35	—

equation of state (JWL EOS, [16]). The pressure in either phase is defined in terms of volume and internal energy independent of temperature as

$$p = A\left(1 - \frac{\omega}{R_1 V}\right)e^{-R_1 V} + B\left(1 - \frac{\omega}{R_2 V}\right)e^{-R_2 V} + \frac{\omega e}{V}, \quad (1)$$

where $V = \rho/\rho_o$ is the relative volume, e is the internal energy, and A, B, R_1, R_2, and ω are empirically determined constants that depend on the kind of the explosive. Table 1 lists the JWL EOS coefficients used for this analysis of the HNS with a density of 1.65 g/cm^3.

The ideal gas EOS for air is shown as follows:

$$p = (\gamma - 1)\rho e, \quad (2)$$

where γ is the ideal gas constant and ρ and e are the density and internal energy of the air. The internal energy of air at room temperature and ambient pressure is 2.068×10^5 kJ.

Both the tube and sheath were modeled as SS304 steel and AL6061. With the high pressure resulting from explosive detonation, both the tube and sheath undergoing high strain rates were modeled using the shock equation of state [17] and Steinberg-Guinan strength model [18]. Both the von Mises yield strength (Y) and the shear modulus (G) of the Steinberg-Guinan model are assumed to be described as a function of pressure (P), density (ρ), and temperature (T), and, in the case of yield strength, the effective plastic strain as well (ε):

$$G = G_0\left(1 + \left(\frac{G_0'}{G_0}\right)\frac{p}{\eta^{1/3}} + \left(\frac{G_T'}{G_0}\right)(T - 300)\right),$$

$$Y = Y_0\{1 + \beta(\varepsilon + \varepsilon_i)\}^n \quad (3)$$

$$\times\left(1 + \left(\frac{Y_p'}{Y_0}\right)\frac{p}{\eta^{1/3}} + \left(\frac{Y_T'}{Y_0}\right)(T - 300)\right),$$

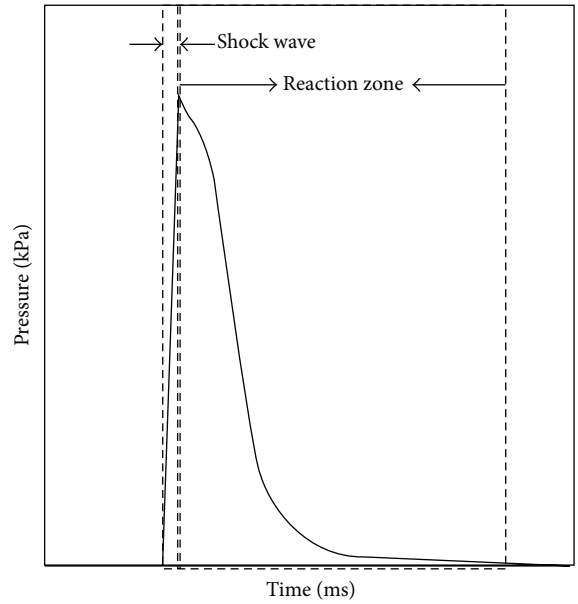

Figure 11: Pressure loading profile.

where β is the hardening constant and n is the hardening exponent. The subscript 0 refers to the reference state (T = 300 K, P = 0, ε = 0). The primed parameters with the subscripts P and T indicate the derivatives of the parameters with respect to pressure or temperature at the reference state. Table 2 summarizes the Steinberg-Guinan strength parameters used for the numerical model for the SS304 steel and AL6061 used in the present analysis.

A flow-out condition was applied to all boundaries of the Euler grid. This allowed the material to freely leave the grid and also prevented relief waves from being generated off the lateral boundaries of the solid, which would reduce the overall strength of the compressive shock and rarefaction waves.

3.3. Failure Model. Spallation (spall-fracture) is a kind of fracture that occurs as planar separation of material parallel to the incident plane wave fronts as a result of dynamic tensile stress components perpendicular to this plane [19]. The spall strength for tensile stress generated when a rarefaction wave travels through material is 2.1 GPa for the steel tube. If the tensile stress of the tube exceeds the predefined spall strength,

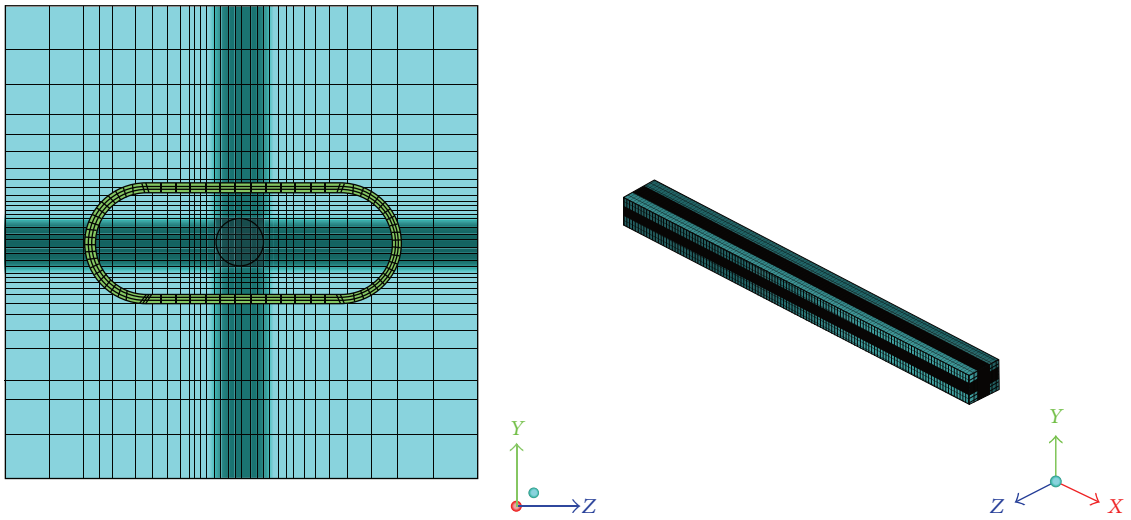

(a) (b)

Figure 12: Three-dimensional model of expanding tube (front view (a) and isotropic view (b)).

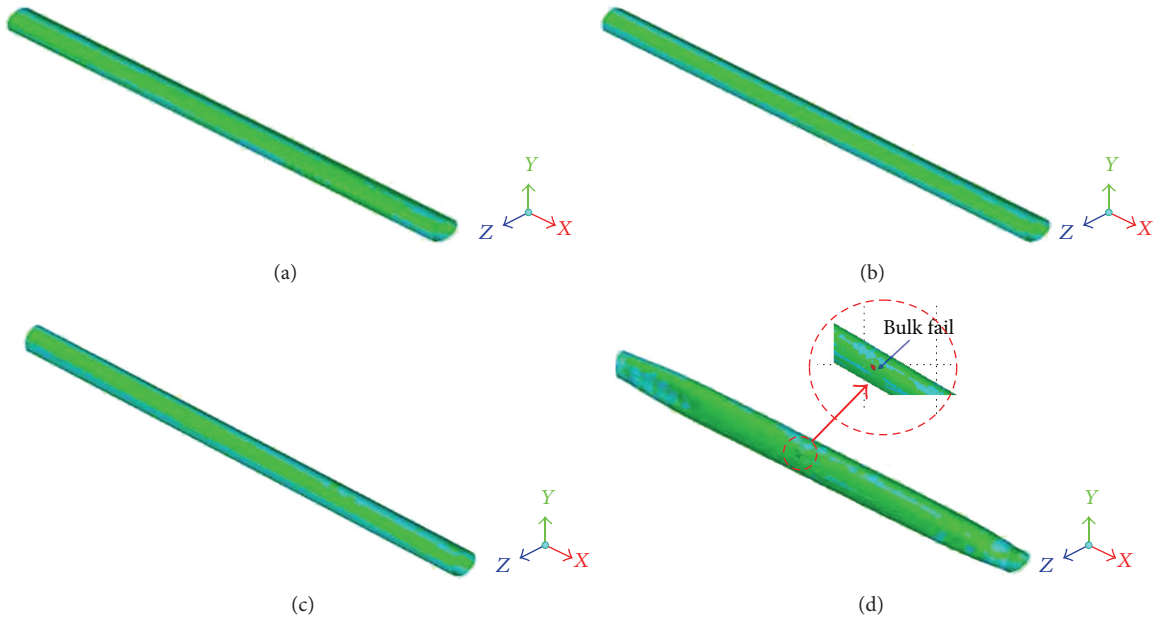

(a) (b) (c) (d)

Figure 13: Material status of one-sided detonation expanding tube ((a): 15 gr/ft, (b): 20 gr/ft, (c): 25 gr/ft, and (d): 30 gr/ft).

the material is considered to have "failed." The tensile stress produced by a rarefaction wave is often shown as a negative pressure [14].

3.4. Solvers. AUTODYN provides various solvers for nonlinear problems [11, 20, 21]. Lagrange and Euler solvers were adopted in these FSI (fluid-structure interaction) simulations. The Lagrangian representation keeps material in its initial element, and the numerical mesh moves and deforms with the material. The Lagrange method is most appropriate for the description of solid-like structures. Eulerian representation allows materials to flow from cell to cell, while the mesh is spatially fixed. The Eulerian method is typically well suited for representing fluids and gases [20–23]. In this study, the steel tube and sheath were modeled using a Lagrange solver, while HNS and air were modeled using an Euler solver. The Euler and Lagrange interaction was also implemented to take into account the interaction between fluid (explosive and air) and structures (tube and sheath). This coupling technique allows complex fluid-structure interaction problems that

Table 2: Steinberg-Guinan strength parameters.

Parameter	SS304	AL6061	Unit
G	7.7×10^8	2.97×10^7	kPa
Y	3.4×10^5	5×10^4	kPa
β	43	28	—
n	0.35	0.8	—
dG/dP	1.74	1.4	
dG/dT	-3.5×10^4	-1.29×10^4	kPa/K
dY/dP	7.68×10^{-3}	2.35×10^{-3}	—
Melting temperature	2380	1604	K

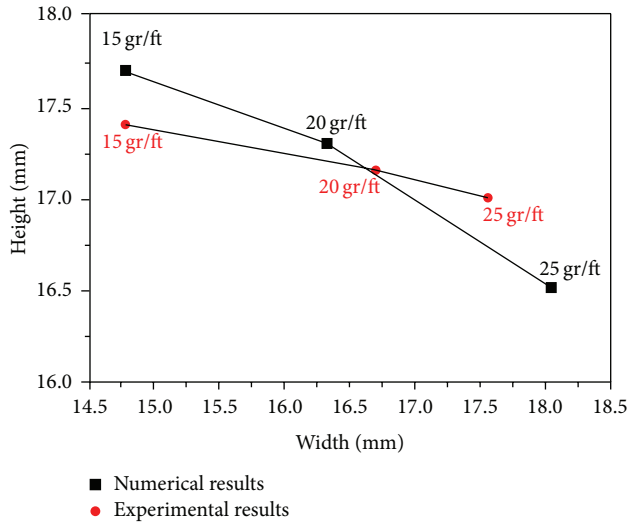

Figure 14: Comparison between the experimental and calculational results.

include large deformation of the structure to be solved in a single numerical analysis.

4. Results and Discussion

4.1. Two-Dimensional Numerical Results. Figure 6 shows the two-dimensional numerical model of an expanding tube explosion. The cell width was approximately 0.16 mm. The number of elements in the tube model was 1,404, and the whole model had 161,504 elements. A description of the numerical model is shown in Table 3.

To illustrate the expansion process of the steel tube over time, the deformed configurations of a 15 gr/ft expanding tube are depicted in Figure 7 at $t = 0$ ms, 0.02 ms, 0.07 ms, and 0.1 ms. The calculation was started at time $t = 0.0$ ms and finished at $t = 0.1$ ms, when it could be assumed that detonation had been completed. It is clearly seen that the tube is expanded outward radially from the detonation point. At $t = 0.02$ ms, early in the detonation, the minor axis of the tube started to be expanded, and the length of the major axis was becoming shorter over time. At a later time, the shape of the tube section was deformed from elliptical to circular, such that the shape change might separate a joint.

Table 3: Description of numerical model of 2D expanding tube.

Part	Materials	Number of mesh	Solver
Tube	SS304	1,404	Lagrangian
Sheath	AL6061	100	
Air	Air	160,000	Eulerian
High explosive	HNS 1.65		

A series of computations was performed by varying explosive loads to compute the material response of the tube, and the deformations are presented in Figure 8. It is apparent that the tube expansion increases as the explosive load increases. For a pressure tube in the plastic deformation regime, catastrophic failure is associated with ductile tearing or plastic instability [19, 24, 25]. Rapidly expanding regions (the minor axis of the tube) are accompanied by rapid loss of stress-carrying capability and intense heating due to the dissipation of plastic work, and present risks of rupture [26]. As shown in Figure 8, the plastic region and computed stress were increased proportionally to the explosive load. As a result, the 30 gr/ft expanding tube shows the largest plastic region, and the greatest stress is on the minor axis due to energy absorption. However, the 30 gr/ft expanding tube expanded without spallation in the 2D simulation, which differs distinctly from the experimental results, because this FE analysis accounts for only radial expansion. This suggests that the tube expansion due to the detonation wave propagation should be considered to develop a more reliable numerical model.

Figure 9 compares the changes of width and height of the tube in the FE analysis and experimental results for three cases, with 15, 20, and 25 gr/ft. Although the calculation results slightly overestimated the experimental results of each core load, the overall error of both width (minor axis) and height (major axis) prediction was less than 10%.

4.2. Three-Dimensional Numerical Results. Figure 10 illustrates a three-dimensional expanding tube and detonation direction. The open-ended steel tube was 300 mm long, and MDF of a 320 mm length of MDF was inserted into the central bore. Its cross section was the same as in the 2D case. Detonation was assumed to be started from the left end of the tube at $t = 0.0$ ms, identically to the experimental conditions. To describe the 3D detonation propagation, a cylindrical blast wave was generated and then remapped in the air. The pressure profile of the detonation wave propagation into the tube is presented in Figure 11, and its structure consists of a shock wave and reaction zone, where the explosive is changed into gaseous products at high temperature. These reaction products act as a piston that allows the shock wave to propagate at a constant velocity [27]. Figure 12 shows the numerical model of the 3D expanding tube. A graded grid was applied to the air and HNS 1.65 to save computation time. Table 4 summarizes the description of the 3D numerical model.

Figure 13 displays the expansion behaviors and material status of each expanding tube. Similar to the 2D results,

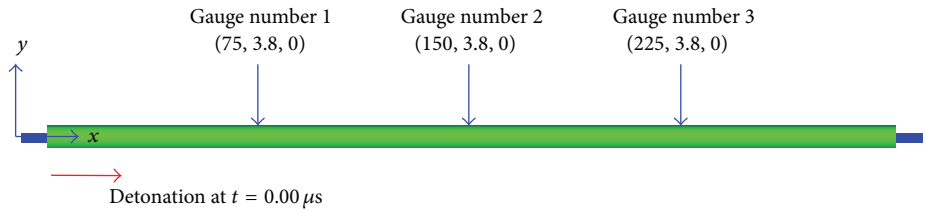

Figure 15: Gauges position.

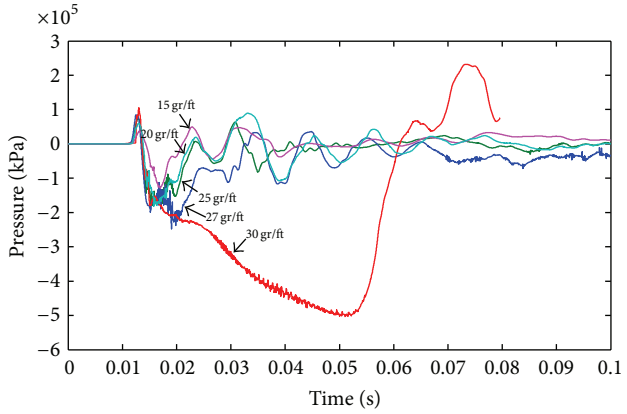

Figure 16: Pressure histories from gauge number 1.

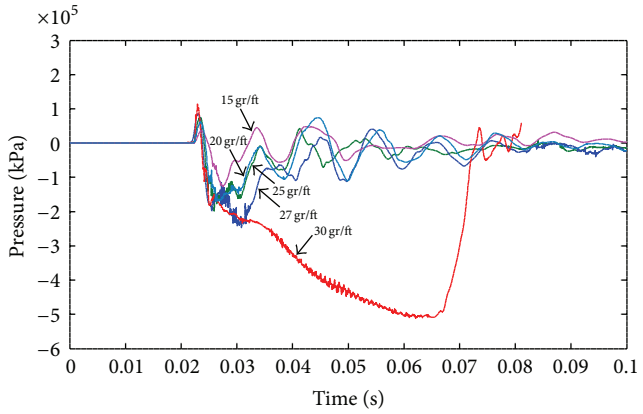

Figure 17: Pressure histories from gauge number 2.

Table 4: Description of 3D expanding tube numerical model.

Part	Materials	Number of mesh	Solver
Tube	SS304	64,800	Lagrangian
Sheath	AL6061	13,360	
Air	Air	203,125	Eulerian
High explosive	HNS 1.65		

the tubes with explosive loads of 15–25 gr/ft freely expanded, but the 30 gr/ft tube failed due to plastic deformation. As shown in Figure 13, there was spallation at 130 mm from the side of the 30 gr/ft expanding tube at around $t = 0.07$ ms. This ductile fracture was caused by the significant amount

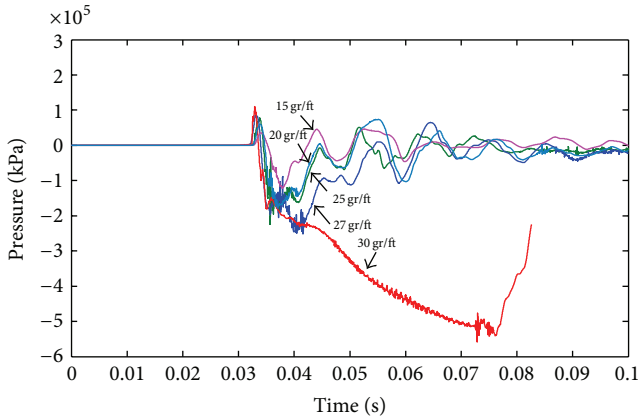

Figure 18: Pressure histories from gauge number 3.

of plastic deformation during tube expansion. This failure behavior in FE analysis was somewhat different from the experimental failure behavior. In experiments, two failures occurred on the left and right sides of the steel tube, while one bulk failure was found in the numerical simulation. Even if the first spallation could be predicted, it might be inappropriate to simulate a successive multiple-spallation generation mechanism.

Figure 14 compares between the numerical simulation and experimental results of each expanding tube deformation. The overall error was less than 3%, and the agreement was improved by considering the tube expansion due to detonation wave propagation.

To compute a proper core load, the internal pressure of the expanding wall of the steel tube was numerically calculated for explosive loads of 15, 20, 25, 27, and 30 gr/ft. The three points indicated in Figure 15 represent the placement of a gauge for measuring the internal pressure. Figures 16, 17, and 18 plot the time histories of pressure observed by gauges in the middle of the steel tube thickness over time. The first peak was due to the initial shock wave traveling through the tube. The rarefaction wave generated due to free surface interaction is often shown as negative pressure following the first peak, and it produces tensile stress on the tube. The maximum pressure of the respective gauges ranged from −130 to −520 MPa for the various explosive loads. The pressure histories of expanding tubes with loads of 15–25 gr/ft fluctuated and became stable over time. In the FE analysis, the 27 gr/ft expanding tube was able to expand freely without failure, and its maximum pressure was

1.25 times higher than that of the 25 gr/ft expanding tube, which was found to have a proper explosive load in the ballistic test using expanding tube samples. Therefore, we can conclude that the proper explosive load in the experiments was underestimated according to the numerical results. For an explosive load of 30 gr/ft, the internal pressure increased dramatically and reached a value of −520 MPa. The maximum pressure on the steel tube with the 30 gr/ft load was about 2.7 and 2 times higher than those with the 25 gr/ft and 27 gr/ft loads, respectively. This means that, since the explosive load of 30 gr/ft was greater than the failure threshold, spallation occurred in the actual expanding tube.

5. Conclusions

The development of a numerical model has been presented for the free expansion of expanding tubes by MDF detonation in pyro-separation systems using AUTODYN 2D and 3D hydrocode. Numerical simulations were performed for four expanding tube explosive load cases as a verification set for the numerical model, and additional simulation was done to suggest a more effective explosive load.

In the 2D model, since the detonation wave propagation could not be considered, the results slightly overestimated the shape of the expanded tube. To improve the accuracy of the results, the 3D model was developed, which allowed for tube expansion due to detonation wave propagation. The developed model was verified with explosive test results and showed less than 3% overall error. From the results of 3D numerical simulation, where the Steinberg model was applied for the failure criteria of the steel tube, 27 gr/ft was the proper explosive load, and the 30 gr/ft explosive load exceeded the threshold of expanding tube failure. Since the numerical model verified with ballistic test results allows for various design changes, the development cost and time can be greatly reduced by minimizing the number of experimental tests required. Therefore, it is suggested to add a numerical model development step using 3D hydrocode to the overall procedure of expanding tube development for pyrotechnic separation systems.

Conflict of Interests

The authors declare that there is no conflict of interests regarding the publication of this paper.

Acknowledgments

This research was supported by the Leading Foreign Research Institute Recruitment Program (2011-0030065) and the Basic Science Research Program (2011-0010489) through the National Research Foundation of Korea, funded by the Ministry of Education, Science, and Technology. This study was also financially supported by the University Collaboration Enhancement Project of the Korea Aerospace Research Institute.

References

[1] K. Y. Chang and D. L. Kern, Super∗Zip (linear separation) shock characteristics, 1986, http://ntrs.nasa.gov/archive/nasa/casi.ntrs.nasa.gov/19870011172_1987011172.pdf.

[2] L. J. Bement and M. L. Schimmel, "A manual for pyrotechnic design, development and qualification," NASA Technical Memerandum 110172, 1995.

[3] J. R. Lee, C. C. Chia, and C. W. Kong, "Review of pyroshock wave measurement and simulation for space systems," *Measurement: Journal of the International Measurement Confederation*, vol. 45, no. 4, pp. 631–642, 2012.

[4] K. Y. Chang, "Pyrotechnic devices, shock levels, and their applications," in *Proceedings of the Pyroshock Seminar, ICSV9*, 2002.

[5] NASA, "Pyroshock test criteria," NASA-STD-7003A, 2011.

[6] L. H. Richards, J. K. Vision, and D. J. Schorr, "Thrusting separation system," US Patent, US5372071, 1993.

[7] W. C. Hoffman III, "Age life evaluation of space shuttle crew escape system pyrotechnic components loaded with hexanitrostilbene (HNS), NASA," Technical Paper 3650, 1996.

[8] L. J. Bement and M. L. Schimmel, "Investigation of Super∗Zip separation joint," NASA Technical Memorandum 4031, 1988.

[9] M. Miyazawa and Y. Fukushima, "Development status of Japan's new launch vehicle: H-II rocekt," in *Proceedings of the 40th Congress of the International Astronautical Federation*, 1989.

[10] M. Quidot, "Some examples of energetic material modeling with LSDYNA," in *Proceedings of the 3rd European LS-DYNA Conference*, 2001.

[11] G. E. Fairlie, "The numerical simulation of high explosives using AUTODYN-2D & 3D," in *Proceedings of the Institute of Explosive Engineers 4th Biannual Symposium (Explo '98)*, 1998.

[12] J. K. Chen, H. Ching, and F. A. Allahdadi, "Shock-induced detonation of high explosives by high velocity impact," *Journal of Mechanics of Materials and Structures*, vol. 2, no. 9, pp. 1701–1721, 2007.

[13] S. M. Muramatsu, "Numerical and experimental study of a pyroshock test set up for small spacecraft component," Project Report, UPNA, 2010.

[14] J. Danyluk, *Spall fracture of multi-material plates under explosive loading [M.S. thesis]*, Rensselaser Polytechnic Institute at Hartford, Hartford, Conn, USA, 2010.

[15] R. H. B. Bouma, A. E. D. M. van der Heijden, T. D. Sewell, and D. L. Thompson, "Chapter2. Simulations of deformation processes in energetic materials," in *Numerical Simulations of Physical and Engineering Processes*, 2011.

[16] E. L. Lee, H. C. Hornig, and J. W. Kury, "Adiabatic expansion of high explosive detonation products," Technical Report UCRL-50422, Lawrence Radiation Laboratory, University of California Livermore, Berkeley, Calif, USA, 1968.

[17] M. A. Meyers, *Dynamic Behavior of Materials*, Wiley, New York, NY, USA, 1994.

[18] D. J. Steinberg, S. G. Cochran, and M. W. Guinan, "A constitutive model for metals applicable at high-strain rate," *Journal of Applied Physics*, vol. 51, no. 3, pp. 1498–1504, 1980.

[19] J. N. Johnson, "Dynamic fracture and spallation in ductile solids," *Journal of Applied Physics*, vol. 52, no. 4, pp. 2812–2825, 1981.

[20] ANSYS, *Workshop 7. Ship Blast, ANSYS Training Manual*, ANSYS, Cecil Township, Pa, USA, 2010.

[21] ANSYS, *Chapter 1. Introduction to AUTODYN, AUTODYN Training Manual*, ANSYS, Cecil Township, Pa, USA, 2010.

[22] X. Quan, N. K. Birnbaum, M. S. Cowler, B. I. Gerber, R. A. Clegg, and C. J. Hayhurst, "Numerical simulation of structural deformation under shock and impact loads using a coupled multi-solver approach," in *Proceedings of the 5th Asia-Pacific Conference on Shock and Impact Loads on Structures*, 2003.

[23] Century Dynamics, *AUTODYN Theory Manual*, Century Dynamics, Concord, Calif, USA, 2003.

[24] J. E. Shepherd, "Structural response of piping to internal gas detonation," *Journal of Pressure Vessel Technology, Transactions of the ASME*, vol. 131, no. 3, pp. 0312041–03120413, 2009.

[25] J. Kanesky, J. Damazo, K. Chow-Yee, A. Rusinek, and J. E. Shepherd, "Plastic deformation due to reflected detonation," *International Journal of Solids and Structures*, vol. 50, no. 1, pp. 97–110, 2013.

[26] A. J. Rosakis and G. Ravichandran, "Dynamic failure mechanics," *International Journal of Solids and Structures*, vol. 37, no. 1-2, pp. 331–348, 2000.

[27] S. Fordham, *High Explosives and Propellants*, Pergamon Press, Elmsford, NY, USA, 2nd edition, 1980.

Hindawi Publishing Corporation
Shock and Vibration
Volume 2014, Article ID 296426, 10 pages
http://dx.doi.org/10.1155/2014/296426

Research Article

Laser Ultrasonic System for Surface Crack Visualization in Dissimilar Welds of Control Rod Drive Mechanism Assembly of Nuclear Power Plant

Yun-Shil Choi, Hyomi Jeong, and Jung-Ryul Lee

Department of Aerospace Engineering and LANL-CBNU Engineering Institute Korea, Chonbuk National University, 664-14 Deokjin-dong, Deokjin-gu, Jeonju, Jeollabuk-do 561-756, Republic of Korea

Correspondence should be addressed to Jung-Ryul Lee; leejrr@jbnu.ac.kr

Received 25 December 2012; Accepted 4 March 2013; Published 17 March 2014

Academic Editor: Gyuhae Park

Copyright © 2014 Yun-Shil Choi et al. This is an open access article distributed under the Creative Commons Attribution License, which permits unrestricted use, distribution, and reproduction in any medium, provided the original work is properly cited.

In this paper, we propose a J-groove dissimilar weld crack visualization system based on ultrasonic propagation imaging (UPI) technology. A full-scale control rod drive mechanism (CRDM) assembly specimen was fabricated to verify the proposed system. An ultrasonic sensor was contacted at one point of the inner surface of the reactor vessel head part of the CRDM assembly. Q-switched laser beams were scanned to generate ultrasonic waves around the weld bead. The localization and sizing of the crack were possible by ultrasonic wave propagation imaging. Furthermore, ultrasonic spectral imaging unveiled frequency components of damage-induced waves, while wavelet-transformed ultrasonic propagation imaging enhanced damage visibility by generating a wave propagation video focused on the frequency component of the damage-induced waves. Dual-directional anomalous wave propagation imaging with adjacent wave subtraction was also developed to enhance the crack visibility regardless of crack orientation and wave propagation direction. In conclusion, the full-scale specimen test demonstrated that the multiple damage visualization tools are very effective in the visualization of J-groove dissimilar weld cracks.

1. Introduction

Control rod drive mechanism (CRDM) assembly includes a reactor vessel head (RVH) and many penetration nozzles made of carbon steel and alloy 690, respectively, as shown in Figure 1(a). The two dissimilar metal parts, namely, the RVH and penetration nozzle, are coupled with welding as shown in the unit structure of the CRDM assembly in Figure 1(b). The inner surface of the RVH, which is in direct contact with the primary coolant, is covered with cladding to prevent any reaction between the carbon steel ingredient in the RVH and the boric ingredient in the coolant. During a nuclear power plant (NPP) operation period, thermal and pressure loadings are concentrated on the penetration nozzles and dissimilar metal welding, which are comparatively fragile spots. As the operation period of nuclear plants has increased, there has been an increase in the growth of primary water stress corrosion (PWSCC) on the welds of dissimilar metals or penetration nozzles by cyclic stress. As shown in Figure 2(a), these PWSCCs ultimately grow into surface cracks and become the path of primary water leakage. While the boric acid ingredient in the coolant not only accumulates on the outer surface of the reactor vessel as boric acid deposits, but it also creates a cavity by reacting with the carbon steel ingredient of the RVH, as shown in Figure 2(b) [1]. Practically, corrosions of RVH by boric acid deposits have been demonstrated by Davis-Besse 2002 [2], and a leak of primary coolant water through the inner surface cracks was noticed at the Ohi NPP in Japan, 2004 [3].

In order to detect small amounts of PWSCC in the reactor, an inspection needs to be carried out using an automatic inspection system capable of rapid testing and analyzing because the CRDM assembly has minimal human accessibility. Furthermore, even though PWSCCs grow into surface cracks, they are difficult to detect because they are not open cracks and thus not easily distinguishable with the naked eye. If these kinds of damage were neglected, serious accidents could occur such as fracture of penetration nozzles due to the growth of PWSCC around the welds. If the tests take too long to complete, extreme economic loss ensues

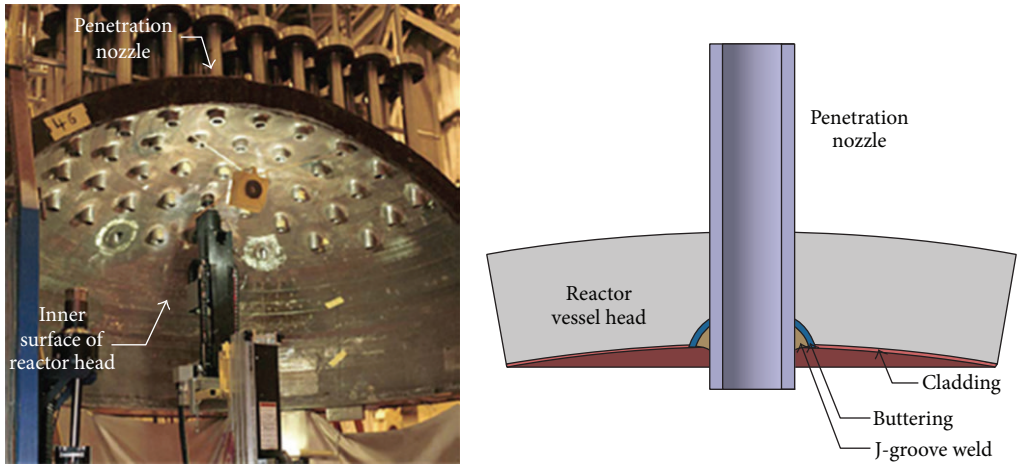

Figure 1: (a) Real photo of control rod drive mechanism (CRDM) assembly [10] and (b) schematic diagram of CRDM assembly.

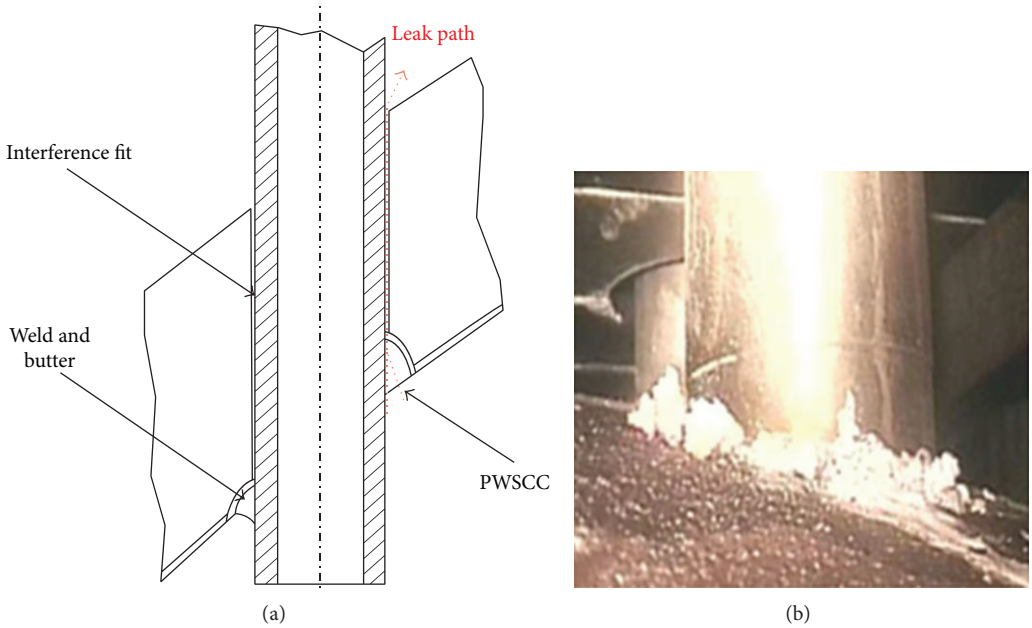

Figure 2: (a) Leak path of primary coolant by PWSCC, (b) Boric acid deposits [1].

because most of the testing then needs to be completed during an out-of-service period.

Various NDT methods are currently being used to detect PWSCC in CRDM assembly such as ultrasonic technique (UT), Eddy current technique (ET), visual technique (VT), and penetrant technique (PT). Cumblidge et al. [4] have presented a PWSCC detecting method based on ET for RVH, J-groove weld, and penetration nozzle, and so forth in a removed-from-service CRDM assembly. However, problems arise from the ET methods such as long inspection time for a small area because of the narrow contact surface of the probe and low reliability caused by a variation of the contacted area between the target surface and the probing area in each probing. For the UT, a PWSCC detecting method using a pulse/echo mode has been presented by Kerr and Alers [5]. The method showed superior penetration depth and serviceability over the ET-based method but it required point-by-point scanning by directly contacting the UT probe. Therefore, fulfilling the testing in a complex welding part and curved RHV is difficult and time consuming. Thus, advanced nondestructive evaluation (ANDE) techniques capable of faster and more reliable scanning should be developed for the CRDM assembly.

In this paper, we design a dissimilar weld crack visualization system for the CRDM assembly. The system can perform noncontact scanning generation of ultrasonic waves on the inner surface of the RVH by impinging the laser pulses Q-switched at 200 Hz. The system can also acquire

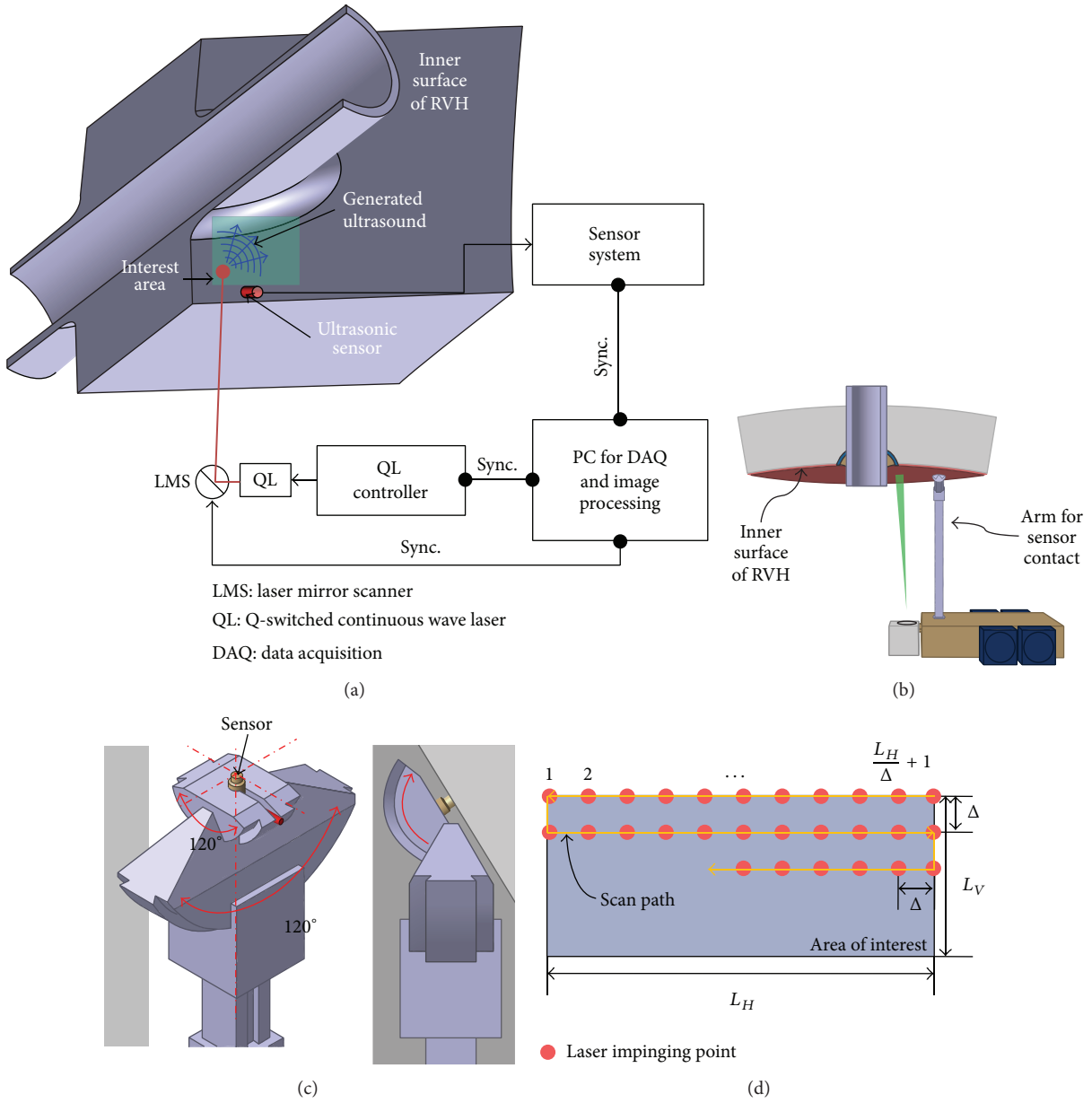

FIGURE 3: (a) Schematic diagram of ultrasonic propagation imaging (UPI) system for CRDM assembly inspection, (b) schematic diagram for real-world application of the developed system, (c) sensor contact mechanism, and (d) scan path on the area of interest.

ultrasonic waves using an ultrasonic sensor contacted at one position without reception scanning. The system is designed to automatically visualize the surface cracks when cracks inside the dissimilar metal welding of the RVH have reached the welding surface. This system is based on laser ultrasonic propagation imaging technology [6] and is newly equipped with an advanced platform of multiple damage visualization processing for surface crack visualization. To present a proof-of-concept for the field overhaul application, a full-scale mockup was fabricated and its structural dimensions pertain to the signal-to-noise ratio of the proposed laser ultrasonic technique. Finally, the proposed system is tested for surface crack detection in the dissimilar metal welding of the mockup.

2. System Configuration

2.1. Configuration of Dissimilar Weld Crack Visualization System and Experimental Setup. Figure 3(a) shows the system configuration developed in this research for crack detection in CRDM assemblies. Due to the nature of the nuclear reactor vessel, automation of the system is essential to avoid a human directive approach. The RVH head is lifted during the overhaul process of the NPP. During this period, the proposed system shown in Figure 3(b) is inserted below the opened RVH head and makes contact with the ultrasonic sensor on the inner surface of the RVH using its robot arm. High speed laser scanning is then applied around the dissimilar weld using a laser mirror scanner (LMS).

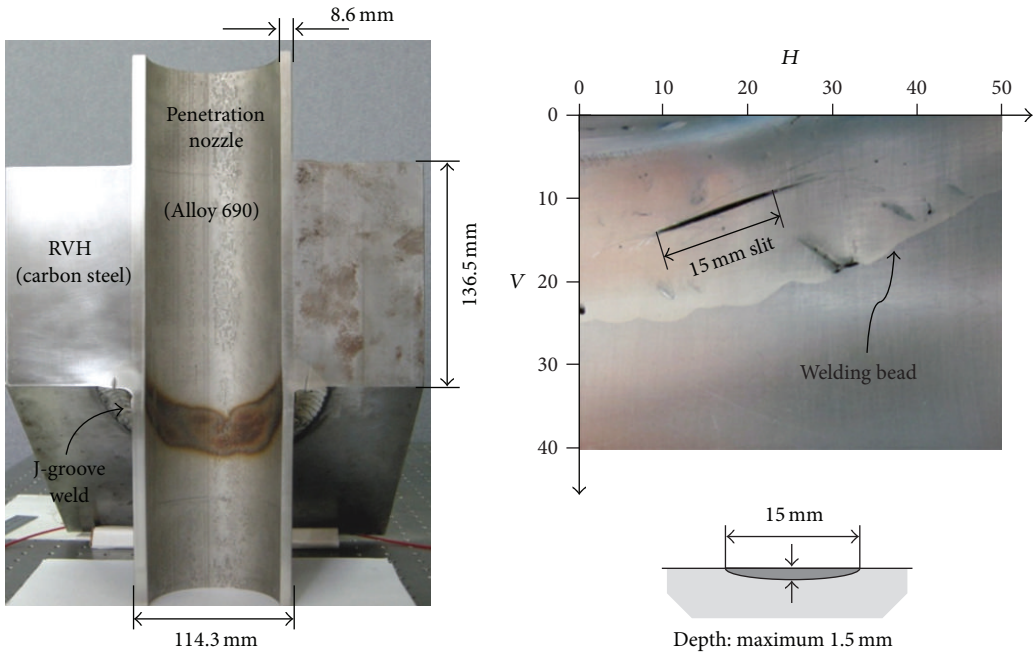

Figure 4: (a) Full-scale mockup of the CRDM assembly and (b) the artificial crack on the dissimilar welding bead.

The Q-switched solid state diode pumped laser (QL) with a wavelength of 532 nm was used to generate a laser beam pulse with a duration of 8 ns and the laser mirror scanner (LMS) was used to impinge the laser beam with the same interval on the inner surface of RVH. Impinging of the laser beam in each scanning grid point generated an ultrasonic wave. The LMS was equipped with a pair of laser mirrors for the 532 nm operating wavelength and the mirrors were fixed on two orthogonal galvanomotors which had 75 rad/s for maximum angular velocity. Each mirror was able to rotate by ±20 degrees from top to bottom or from left to right. The laser pulse was impinged once on each grid point by synchronizing the pulse repetition frequency (PRF) of QL and the movement of galvanomotors. Figure 3(c) shows a sensor contact mechanism installed at the end of a robot arm. An amplifier-integrated PZT sensor with a diameter of 4 mm and a central frequency of 350 kHz was used. Gel couplant was used on the wear plate of the sensor to increase ultrasonic transmissibility. As shown in Figure 3(d), a laser beam was impinged on each point along the scan path in the area having a width L_H and length L_V with constant interval Δ. Laser-induced ultrasonic waves were generated on points stimulated by the laser, while the generated ultrasonic waves were detected by the sensor contacted on the target via an in-line band-pass filter and saved in the PC for image processing.

Multiple damage visualization algorithms were integrated in this system, such as ultrasonic wave propagation imaging (UWPI) [6], ultrasonic spectral imaging (USI) [6], wavelet transformed ultrasonic propagation imaging (WUPI) [7], and anomalous wave propagation imaging with adjacent wave subtraction (AWPI with AWS, refer as AWS) [8] for damage visualization and localization.

Validation of the proposed system was carried out using the full-scale mockup of the CRDM assembly shown in Figure 4(a). For the carbon steel part for the real RVH with a 136.5 mm thickness, the alloy 690 pipe for the real penetration nozzle with a 114.3 mm diameter and an 8.6 mm thickness was used. A crack with an arc-shaped depth was generated with a length of 15 mm and maximum depth and width of 1.5 mm and 0.7 mm, respectively, in the middle on dissimilar metal welds as shown in Figure 4(b). Scanning was fulfilled at a standoff distance of 1 m for the scan area with $L_H = 50$ mm, $L_V = 40$ mm, and $\Delta = 0.1$ mm. The diameter of the impinging beam was 2 mm. The PRF of QL is equal to the number of impinged points per second. In this study, 200 Hz PRF was used and thus 200 pulses of laser beam were impinged on 200 points in one second. The scanning time for the interested area was 17 minutes and the damage visualization image processing time was almost in real time. During the experiments, band-pass filtering in a 130 kHz~150 kHz range was used for narrowband waveform acquisition with high signal to noise ratios, the energy density of QL was 91.45 mJ/cm, and the ultrasonic sensor was placed on (40, 65) mm against the origin of the scanning area.

2.2. Basic Ultrasonic Propagation Image Processing. The UWPI method rearranges 1D time-domain signals in the 3D data structure. As shown in Figure 5(a), one time-domain wave signal is expressed with N sampling points, and $L_v/\Delta+1$ signals on one vertical line are saved in one spreadsheet. A 2D array $N \times (L_v/\Delta + 1)$ is created by arranging the signals as shown in Figure 5(d). After generating spreadsheets for every horizontal path of $L_H/\Delta + 1$, these spreadsheets are

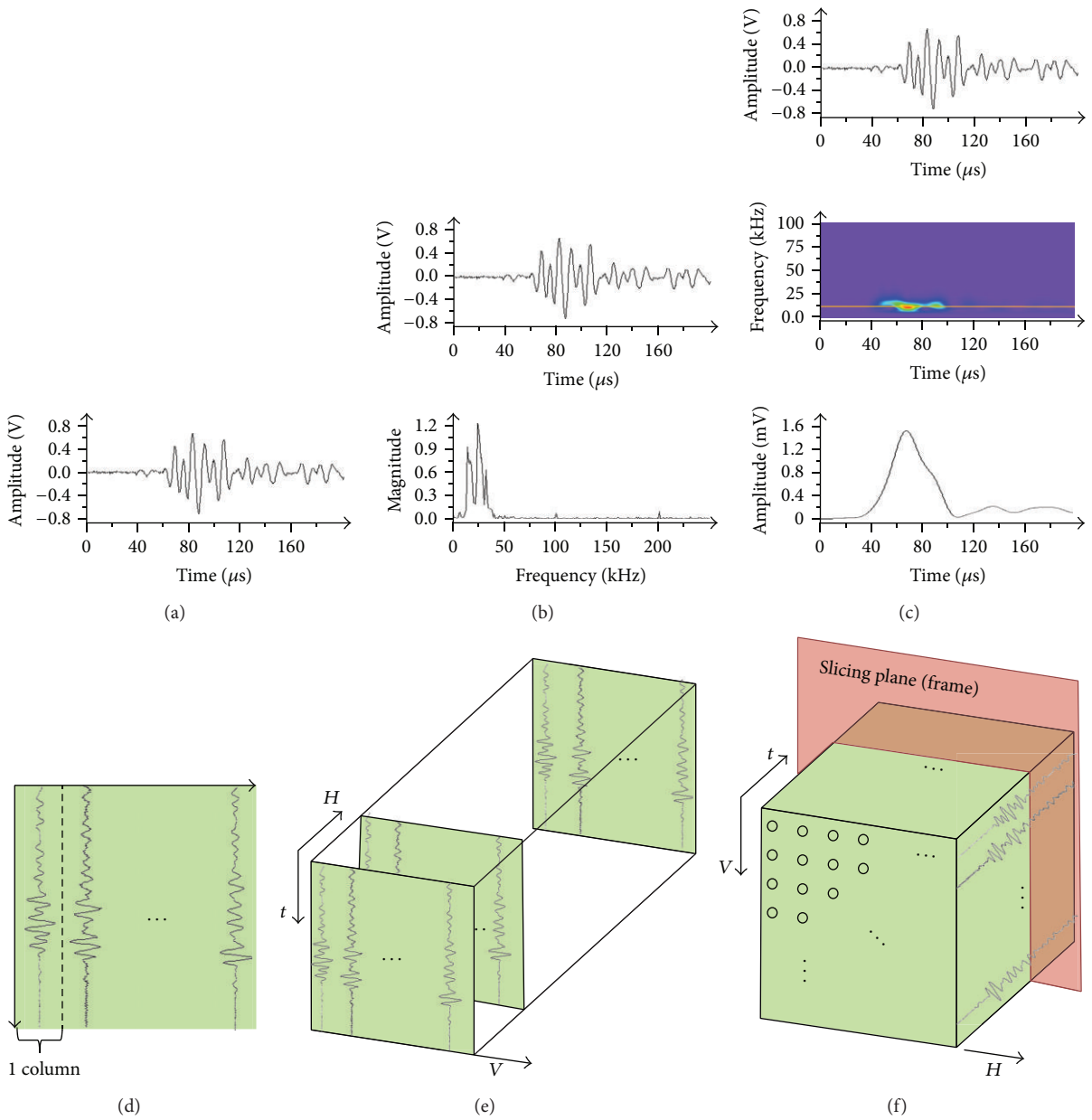

FIGURE 5: (a) 1D time-domain signal acquired at one of the scanning points, (b) fast Fourier transformed 1D frequency domain signal for USI, (c) wavelet transformed 1D time-domain signal for WUPI, (d) arranged signals along one vertical scan path in one spreadsheet (2D array), (e) arranged spreadsheets along horizontal scan path (3D array), and (f) sliced plane along time axis.

rearranged in a 3D data array structure of $N \times (L_v/\Delta + 1) \times (L_H/\Delta + 1)$ as shown in Figure 5(e). The intensity maps expressing the amplitude of signal for each point by color scale are generated by slicing the rotated 3D array along the time axis as shown in Figure 5(f). The intensity maps of N take the role of freeze frames of N in generating the video of wave propagation.

Figure 5(b) shows a 1D frequency-domain signal transformed from the 1D time-domain signal by applying fast Fourier transform (FFT). In the USI method, these transformed signals are used to generate an ultrasonic spectral video. These signals are arranged in the same way as the UWPI. Each frame of the USI video expresses the spatial distribution of spectral amplitude with color scale. Here, since the local structural area with damage-induced wave frequency change can be identified in the frame sliced at each frequency, the damaged area is effectively visualized. Also, the frequency component found in the USI that pertains to damage can be utilized in the WUPI. When the wavelet-transformed 1D time-domain signal is selected from the wavelet scalogram as presented in Figure 5(c), both the central frequency and the damage-related frequency found can be selected to visualize propagations of dominant wave and damage-related wave, respectively.

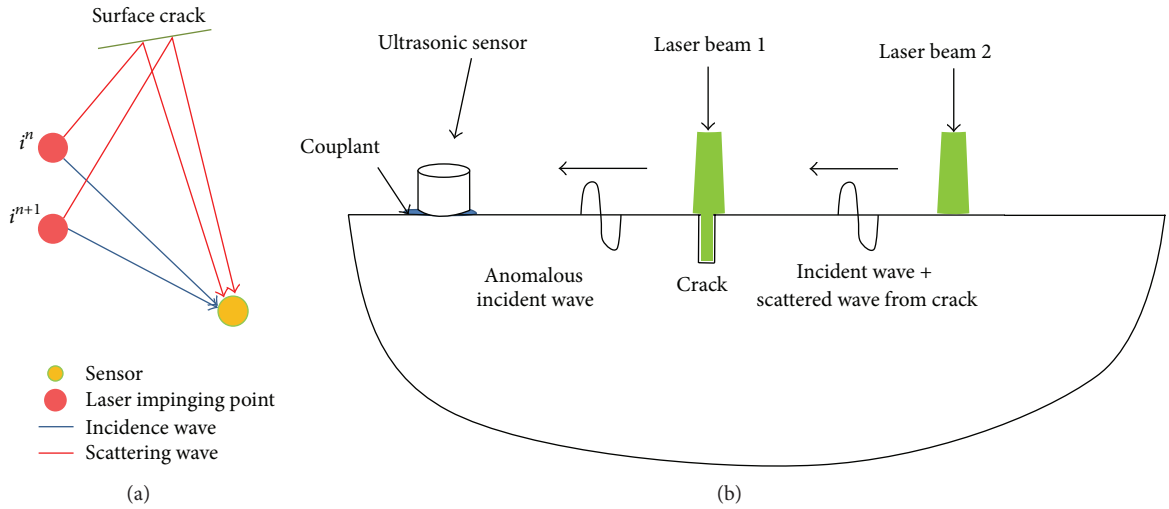

FIGURE 6: (a) Scattering wave generation mechanism of the beam impingement near the surface crack and (b) anomalous wave generation mechanism of the beam impingement within the surface crack.

The WUPI method generates a wavelet-transformed ultrasonic propagation video by rearranging 1D wavelet-transformed signals with a selected frequency in the same way as that of the UWPI, as presented in Figures 5(d)–5(f).

2.3. Novel Dual-Directional Anomalous Wave Propagation Imaging and Crack Orientation. The system developed in this study was equipped with the advanced AWS method developed to be a suitable crack visualization method by modifying the conventional AWS [8] developed for area type damage evaluation. In the case of area type damage such as delamination or debonding, when an ultrasonic wave is generated by a laser beam impinged within the damage area, the confining wave (which is a type of 2D standing wave which stays in the damaged area) occurs as well as the scattering wave by laser beams impinged around the area damage.

As shown in Figure 6(a), when an ultrasonic wave was generated by a laser beam impinged around the crack (i_n or i_{n+1}), partial ultrasonic wave components bounced off the crack and became scattering waves. In this paper, for the crack as the target which has reached the surface such as the PWSCCs, waves generated near and within the crack as represented in Figure 6(b) should show considerable difference. In general, a wave generated by a laser beam impinged within the damage would have higher amplitude due to the boundary impinging effect and deeper excitation.

Figure 7(a) shows horizontally adjacent signals acquired at (40.0, 34.2), (40.1, 34.2), and (40.2, 34.2) in an intact region. Similarly, Figure 7(b) shows vertically adjacent signals acquired at (40.0, 34.2), (40.0, 34.3), and (40.0, 34.4). The horizontally or vertically adjacent signals generated on the intact surface show strong similarity to each other, regardless of direction. Figure 7(c) shows signals acquired on the three horizontally adjacent points, (14.0, 12.3), (14.1, 12.3), and (14.2, 12.3), which are placed on a position close to the artificial crack. These adjacent signals still have strong similarities. Since the 2 mm laser beam scanned the surface crack almost along its orientation, the interactions between the laser beam and crack did not considerably differ and the adjacently generated signals thus had strong similarities. On the other hand, the vertically adjacent signals shown in Figure 7(d) differ considerably despite the small interval of 0.1 mm because the laser beam scanned the surface crack almost perpendicular to its orientation.

As a result, the conventional AWS algorithm, which does not consider the directivity of the crack in selecting the two adjacent signals, might fail to visualize the crack that has an orientation parallel to the processing. Therefore, dual-directional adjacent wave subtraction (DAWS) which processes both directional adjacent signals is proposed in this paper.

The AWS algorithm includes a signal processing step which allows the matching of two signals that have different arrival times. Arrival time matching is accomplished by shifting the time axis of the second signal in scanning the two signals, while the number of sampling points to be shifted is determined when the subtracted signal, $s(N)_i - s(N \pm l)_{i+1}$, has minimum root mean square (RMS) value

$$s_{\mathrm{RMS}} = \sqrt{\frac{\sum_{k+l_{\max}}^{N-l_{\max}} \left[s(N)_i - s(N \pm l)_{i+1} \right]}{N - 2l_{\max}}}, \quad (\text{where } k = 0,\ l_{\max} > 0), \tag{1}$$

where l is the amount of the shifting, and T and N denote the sampling interval and the number of data points during the signal acquisition, respectively. The shifted time could be expressed as $l(T/N)$(sec.). The first signal $s(N)_i$ and second signal $s(N)_{i+1}$ are considered to be matched when the calculated s_{RMS} in $l_{\max}(T/N) < t < T - l_{\max}(T/N)$ is minimum. Therefore, the two adjacent waves obtained in an intact area are similar, even before the time point adjustment is made to minimize their difference; however, two adjacent

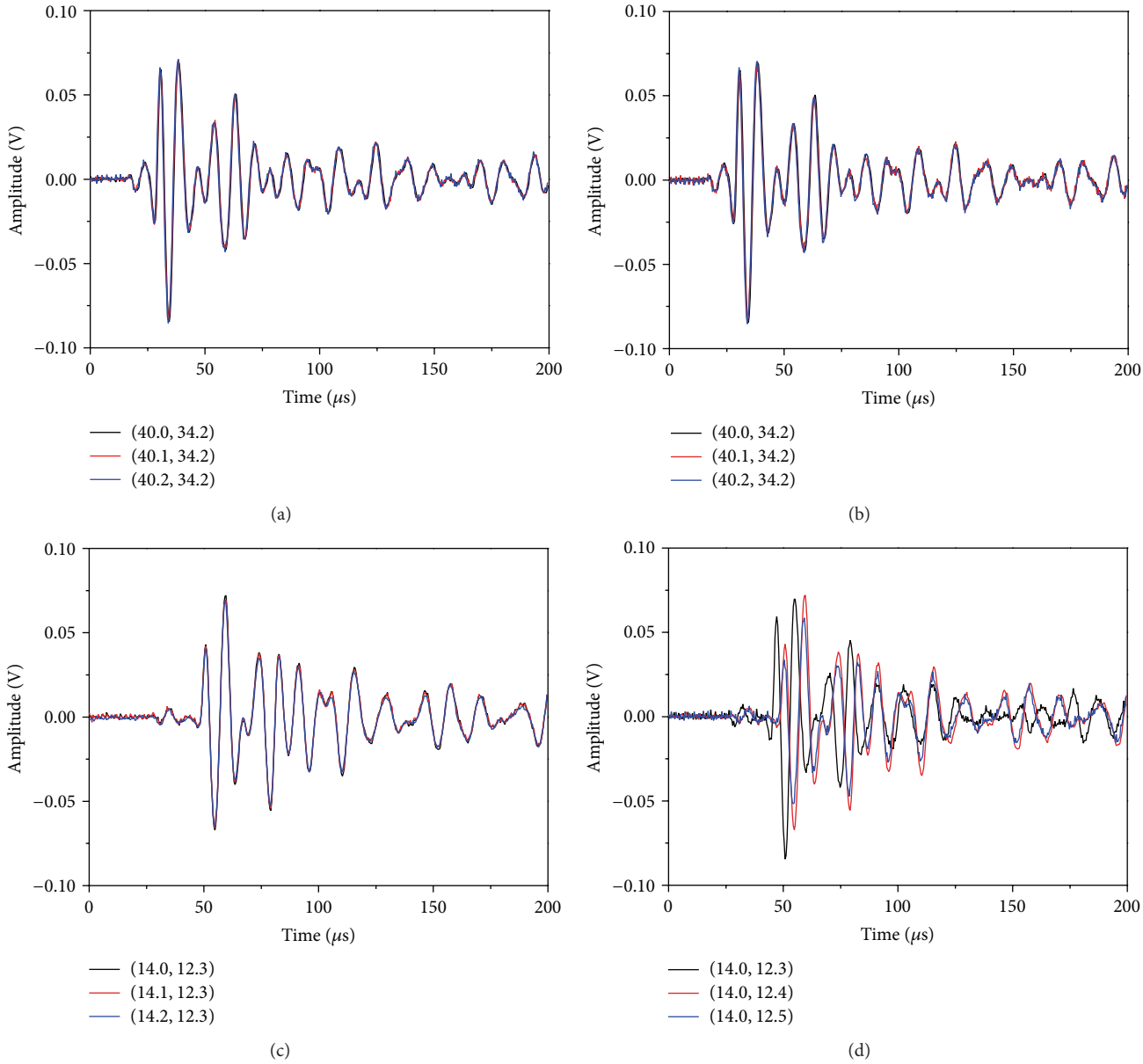

FIGURE 7: Similarities of three adjacent signals along (a) H-axis, (b) V-axis at an intact surface position, (c) H-axis, and (d) V-axis at the surface crack position.

waves obtained in a damaged area differ even after the time point adjustment and thus the subtracted signal still contains a visible residual component. The nature of the residual wave is dependent on the damage types which can cause a residual of incidence wave, scattering wave, and/or confining wave.

Figure 8(a) shows the result of horizontally adjacent wave subtraction using the first signal at (14.0, 12.3) and second signal at (14.1, 12.3) on the surface crack. The subtracted signal shows low residual of incidence wave because of the high similarity of the horizontally adjacent waves and the parallel crack orientation. Thus, the AWS with horizontally adjacent wave subtractions failed to increase visibility of anomalous wave components, which can be clarified in Figure 9(d). On the other hand, Figure 8(b) shows the result of vertically adjacent wave subtraction using the first signal at (14.0, 12.3) and second signal at (14.0, 12.4), where it shows high residual of incidence wave with high amplitude even though the signals have the same interval as that of the signals of Figure 8(a). The result of vertically adjacent wave subtraction shown in Figure 8(c) was calculated by using signals at (40.0, 34.2) and (40.0, 34.3), which are independent of the surface crack position. Even if it was also processed with vertically adjacent waves such as shown in Figure 8(b), the residual was completely removed by the time point adjustment and subtraction. Consequently, the crack orientation is unknown in real-world applications; DAWS thus needs to be used to not overlook the random directional cracks.

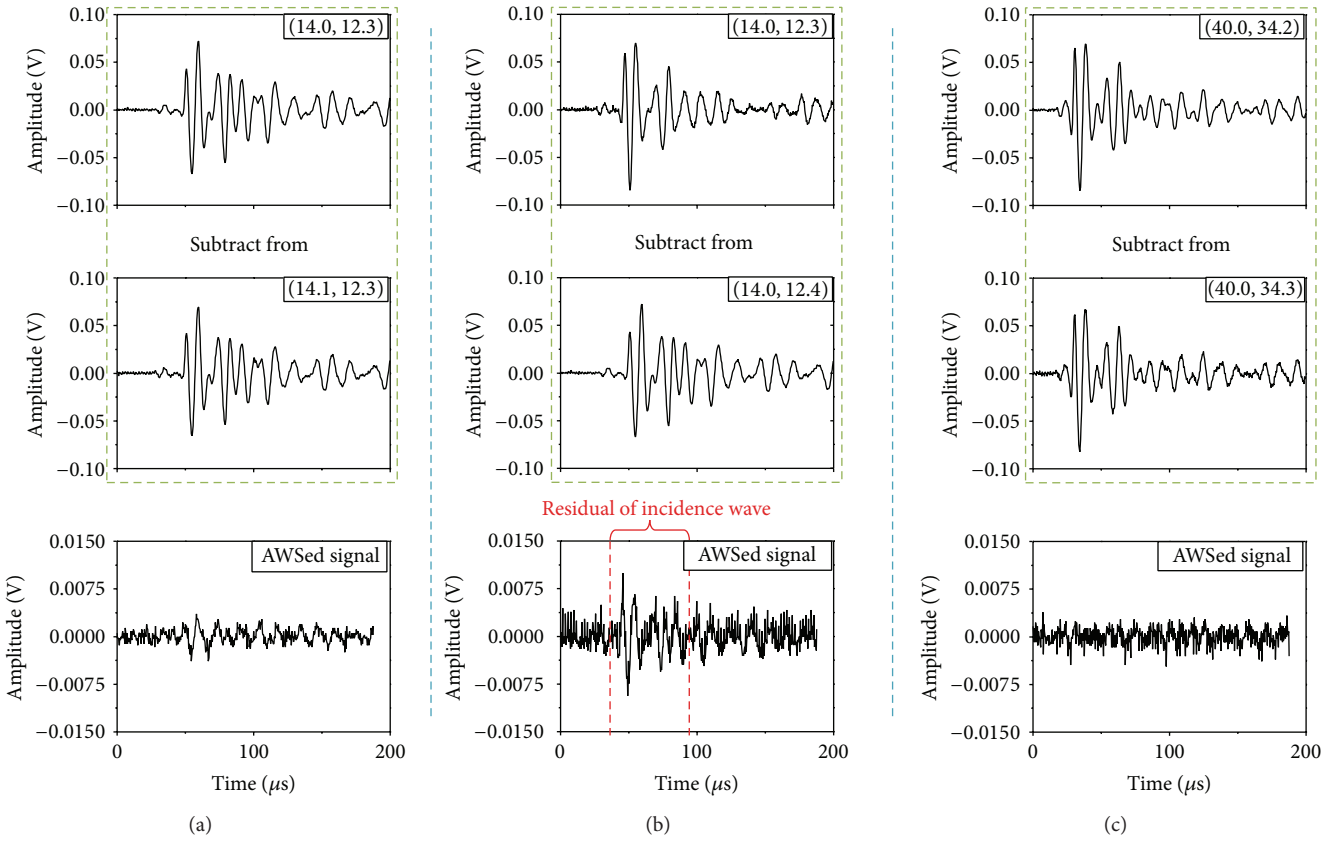

FIGURE 8: Adjacent wave subtraction process using signals obtained at (a) (14.0, 12.3) and (14.1, 12.3), horizontal AWS; (b) (14.0, 12.3), (14.0, 12.4), and vertical AWS on the surface crack; and (c) (40.0, 34.2), (40.0, 34.3), and vertical AWS on the intact area.

3. Experimental Results

Figure 9(a) shows the freeze frame at 29.4 μs of the UWPI video result, which is the moment when the propagating wave interacts with the crack as presented in Figure 4(b). Since the thickness of the CRDM assembly is at the limit for still being considered a semi-infinite structure, the Rayleigh surface wave [9] is dominative the longitudinal waves and the Rayleigh waves are observed in the UWPI movie. The position and shape of the crack were able to be detected from the length of the collapsed wave front and the length of the high amplitude pattern along the surface crack line. The main frequency component induced by damage could be distinguished by the USI. As shown in Figure 9(b), the freeze frame at 140 kHz clearly isolates the shape and location of the surface crack on the dissimilar weld. The same frequency component was also used to generate the WUPI video result as shown in Figure 9(c). The freeze frame of the WUPI video presents an ultrasonic wave component corresponding to only the narrowband of 140 kHz. In the case of UWPI, since all frequency components are mixed in one signal, a very complex propagation pattern is shown. On the other hand, WUPI shows a simpler propagation pattern because it uses only one selected frequency component; thus, it can extract a signal component related to damage with greater visibility. However, a number of steps are required to find the changed frequency components and if the damage did not cause any change in the frequency components, WUPI might fail to visualize this damage.

The DAWS algorithm described in Section 2.3 was applied and the freeze frame for the horizontally processed AWS video result is shown in Figure 9(d). The damage could not be visualized in the horizontal direction because the directivity of the surface crack is also approximately horizontal. A small difference was induced between the two adjacent signals; thus considerably less residual incidence waves remained on the subtracted signals. On the other hand, as shown in Figure 9(e), the vertically processed AWS video result visualized the artificial crack exclusively with high contrast. It provided much better visibility of the crack by suppressing most incidence waves not related to the damage and was also able to visualize the complex welding bead in the CRDM assembly.

The crack lengths estimated in the respective imaging methods are indicated in the freeze frames and show good agreement with the real crack length of 15 mm. Since this multiple image processing platform cross-checks the damaged or nondamaged area from the random noisy area, inspectors can make more reliable decisions about the damage.

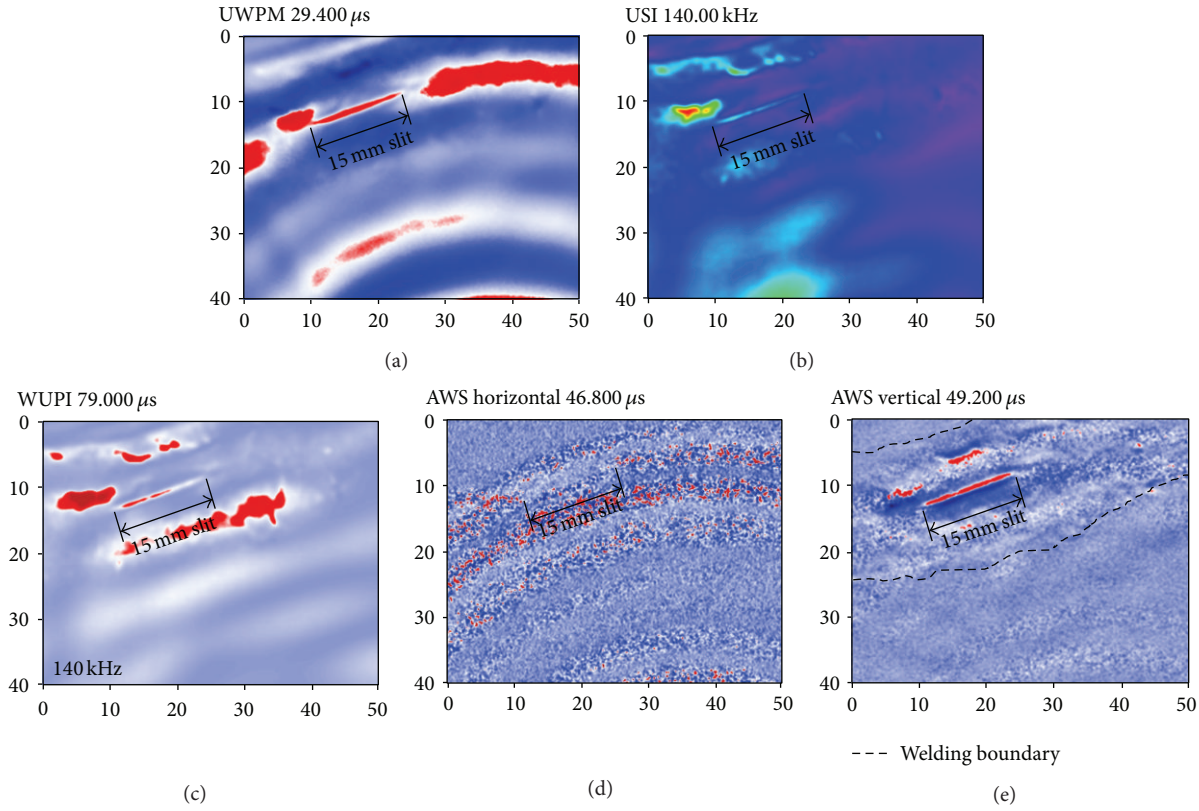

FIGURE 9: Multiple damage visualization results for a 15 mm surface crack in the welding, freeze frames at (a) 29.4 μs of the UWPI video, (b) 140 kHz of the USI video, (c) 79 μs and 140 kHz of the WUPI video, (d) 46.8 μs of the horizontal AWS video, and (e) 49.2 μs of the vertical AWS video.

4. Conclusion

A novel laser ultrasonic crack visualization system was designed and fabricated to detect and evaluate PWSCCs on dissimilar welds between penetration nozzles and an RVH of a CRDM assembly based on the ultrasonic propagation imaging technology. A multiple-damage visualization platform consisting of the four algorithms, UWPI, USI, WUPI, and DAWS, was equipped in the proposed system.

The RVH is lifted during the regular overhaul process of the NPP. During this period, the proposed system is operated and its robot arm contacts the ultrasonic sensor on the inner surface of the RVH and high speed laser scanning is performed around the dissimilar weld. For the proof-of-concept, a full-scale mockup for the CRDM assembly was fabricated and a 15 mm artificial surface crack was generated in the welding bead. The system feasibility has been proved by visualizing the crack length exactly. In particular, the newly developed DAWS was able to visualize any crack regardless of its orientation.

The dense scanning grid with 0.1 mm scanning interval was realized for exhaustive inspection of the complex welding area of 40 mm × 50 mm. The scanning time was only 17 minutes and damage visualization image processing was completed in real time, thereby minimizing the economic loss induced by the interruption of plant operation.

Conflict of Interests

The authors declare that there is no conflict of interests regarding the publication of this paper.

Acknowledgments

This research was supported by the Basic Science Research Program (2011-0010489) and the Leading Foreign Research Institute Recruitment Program through the National Research Foundation of Korea funded by the Ministry of Education, Science and Technology (2011-0030065).

References

[1] Nuclear Regulatory Commission, *Davis-Besse Reactor Pressure Vessel Head Degradation: Overview, Lessons Learned, and NRC Actions Based on Lessons Learned (NUREG/BR-0353, Revision 1)*, 2008.

[2] R. Schrauder, "Lessons learned-reactor pressure vessel degradation: material degradation and related managerial issues at nuclear power plants," in *Proceedings of the Technical Meeting*, pp. 33–38, International Atomic Energy Agency, Vienna, Austria, 2005.

[3] H. Ito and M. Kameyama, "Trend of PWSCC in nuclear reactor vessel head penetrations," *E-Journal of Advanced Maintenance*, vol. 1, no. 1, pp. 1–7, 2009.

[4] S. E. Cumblidge, S. R. Doctor, G. J. Schuster et al., "NDE and DE of PWSCC found in the j-groove weld of a removed-from-service control rod drive mechanism," in *Proceedings of the 6th International Conference on NDE in Relation to Structural Integrity for Nuclear and Pressurized Components*, pp. 723–733, Budapest, Hungary, 2007.

[5] D. S. Kerr and R. B. Alers, "Method and system for nondestructive inspection of components," Tech. Rep. U.S. Patent No. 2004/0091076 A1, 2004.

[6] J.-R. Lee, H. Jeong, C. C. Ciang, D.-J. Yoon, and S.-S. Lee, "Application of ultrasonic wave propagation imaging method to automatic damage visualization of nuclear power plant pipeline," *Nuclear Engineering and Design*, vol. 240, no. 10, pp. 3513–3520, 2010.

[7] J.-R. Lee, C. C. Chia, H. J. Shin, C.-Y. Park, and D. J. Yoon, "Laser ultrasonic propagation imaging method in the frequency domain based on wavelet transformation," *Optics and Lasers in Engineering*, vol. 49, no. 1, pp. 167–175, 2011.

[8] J.-R. Lee, C. C. Chia, C.-Y. Park, and H. Jeong, "Laser ultrasonic anomalous wave propagation imaging method with adjacent wave subtraction: algorithm," *Optics and Laser Technology*, vol. 44, no. 5, pp. 1507–1515, 2012.

[9] J. L. Rose, *Ultrasonic Waves in Solid Media*, Cambridge University Press, New York, NY, USA, 1999.

[10] D. Schlader, "The evolution of inspection and repair approaches for reactor vessel head penetrations," in *Proceedings of the Conference on Vessel Penetration Inspection, Crack Growth and Repair*, vol. 1, pp. 81–148, Gaithersburg, Md, USA, 2003.

Hindawi Publishing Corporation
Shock and Vibration
Volume 2014, Article ID 571017, 8 pages
http://dx.doi.org/10.1155/2014/571017

Research Article

High Temperature Endurable Fiber Optic Accelerometer

Yeon-Gwan Lee,[1] Jin-Hyuk Kim,[2] and Chun-Gon Kim[2]

[1] *The 1st R and D Institute 2, Agency for Defense Development, P.O. Box 35, Yuseong, Daejeon 305-600, Republic of Korea*
[2] *Department of Aerospace Engineering, Korea Advanced Institute of Science and Technology, 291 Daehak-ro, Yuseong-gu, Daejeon 305-701, Republic of Korea*

Correspondence should be addressed to Chun-Gon Kim; cgkim@kaist.ac.kr

Received 25 January 2013; Accepted 27 April 2013; Published 12 March 2014

Academic Editor: Gyuhae Park

Copyright © 2014 Yeon-Gwan Lee et al. This is an open access article distributed under the Creative Commons Attribution License, which permits unrestricted use, distribution, and reproduction in any medium, provided the original work is properly cited.

This paper presents a low frequency fiber optic accelerometer for application in high temperature environments of civil engineering structures. The reflection-based extrinsic fiber optic accelerometer developed in this study consists of a transmissive grating panel, reflective mirror, and two optical fiber collimators as the transceiver whose function can be maintained up to 130°C. The dynamic characteristics of the sensor probe were investigated and the correlation between the natural frequency of the sensor probe and temperature variation was described and discussed. Furthermore, high temperature simulation equipment was designed for the verification test setup of the developed accelerometer for high temperature. This study was limited to consideration of 130°C applied temperature to the proposed fiber optic accelerometer due to an operational temperature limitation of commercial optical fiber collimator. The sinusoidal low frequency accelerations measured from the developed fiber optic accelerometer at 130°C demonstrated good agreement with that of an MEMS accelerometer measured at room temperature. The developed fiber optic accelerometer can be used in frequency ranges below 5.1 Hz up to 130°C with a margin of error that is less than 10% and a high sensitivity of 0.18 (m/s^2)/rad.

1. Introduction

Over the past three decades, many types of fiber optic accelerometers (FOAs) have been developed because optical fibers (OFs) allow structural health monitoring within highly electromagnetic environments [1].Furthermore, optical fiber with fused silica is useful in a wide temperature range up to about 1000°C [2] although it depends on the optical fiber material such as fused silica and sapphire (Al_2O_3, single crystal alumina) [3, 4].

While most intensity-based fiber optic sensor systems are relatively low cost, fiber Bragg grating (FBG) sensor systems are rather higher cost wavelength shift interrogation equipment for high speed sampling frequency rates. Alternatively, intensity modulation techniques have been conducted on grating-based extrinsic type fiber optic sensors (FOSs) [5–7] because the grating-based sensors [8, 9] possess significant advantages [10]: simple mechanical structure and good reliability, among others.

Therefore, research on grating-based fiber optic sensors has been conducted based on the shutter effect [9, 11] or the Moiré phenomenon techniques [7], which require four optical fiber lines and two grating panels. However, these transmission type FOSs [6, 7, 9, 11], including the Moiré fringe-based FOA, depending on the transmitted light between the separated optical fibers, require the placement of optical fibers (OFs) on both sides of the prototype [6–9, 11]. Consequently, this leads to significant limitations during corner installations due to the geometric conditions. When the FOAs are used to monitor large structures using multipoint sensors in hazardous locations, the issues of complex cabling are further intensified.

Nowadays, in order to resolve these problems, reflection-based techniques using grating panel have been developed [12, 13]. This resolved the difficulties in corner installations and complex cabling problems in multipoint sensing due to the 50% simplified cabling by employing collimated optical fibers as transceivers, which allows the fibers to be placed on only one side of the sensor case. However, this FOA was reported to withstand temperatures up to only 65°C due to the use of epoxy for assembly. Thus, most reported FOAs have been limited to handling temperatures up to

60°C although many kinds of civil engineering structures are exposed to high temperature environments. For instance, for ambient vibration monitoring of a pipe in nuclear power plant structures where hot water after cooling flows through, high temperature resistant and temperature independent materials must be used for sensor fabrication. Except for various kinds of fiber-based temperature sensors, which are able to operate beyond 1000°C [3, 4], and pressure sensors [14] for high temperature environments, there are almost no low frequency FOAs available for use in high temperature environments in civil engineering structures. This is because sensor structure assemblies usually involve numerous materials including silicon, glass with a low softening point, polymer, and epoxy as an adhesive. As a result, the thermal expansion mismatch among these materials can lead to stability degradation of the sensors' accuracy, resolution, and repeatability [15].

Therefore, as a fundamental study, this paper presents an FOA that uses a reflection-based technique using a grating panel for application to high temperature environments in civil engineering structures such as a plumbing pipe, in which hot water flows through, of nuclear power plant structures. The targeted operating temperature is 130°C due to the operational temperature limitation of the commercial optical fiber collimator. The fiber optic accelerometer that can endure 130°C was fabricated using mostly the following materials: invar, ceramic adhesive, and 130°C endurable collimated optical fiber for dimensional stability in high temperature environments. Furthermore, a high temperature adjustable chamber was developed and installed with a shaker for the accelerometer performance test. The dynamic characteristics of the sensor probe were investigated after a prototype was fabricated. The correlation between the natural frequency of the sensor probe and temperature variation was empirically investigated. Then a performance test of the 130°C endurable FOA was implemented through a comparison with a commercial low frequency accelerometer.

2. Working Principles

In this study, the foundational quantification principle of acceleration states, in which the change in acceleration is proportional to the change in the relative displacement of a seismic mass, was considered. Moreover, the acceleration can be calculated using the measured relative displacement of the seismic mass through

$$\ddot{u}_0 = u(t) \cdot \sqrt{\left(1 - r^2\right)^2 + \left(2\zeta r\right)^2} \cdot \omega_n^2, \tag{1}$$

where $r = (\omega/\omega_n)$, ζ is the damping ratio, ω_n is the natural frequency of the integrated mass-spring system, and $\ddot{u}_0$ is the acceleration imparted on the seismic mass.

In order to convert the relative displacement into acceleration, the natural frequency and damping ratio of the sensor probe need to be identified. The sensor head as a single degree of freedom structure consists of a single transmissive grating panel (TGP), a reflective mirror, and two transceiver OFs that are separated by a distance of a quarter of the grating pitch l to have a phase difference of 90° between the two received signals [12, 13], as shown in Figure 1, in order to obtain the relative displacement of the seismic mass. The variable u_1 refers to the seismic mass displacement and the variable u_0 refers to the sensor case displacement. If the periodic sine wave signals are obtained in quadrature, the relative displacement u, defined as the difference of u_1 and u_0, can be inferred by unwrapping the two normalized received signals and can be expressed using sine and cosine functions, as follows [16]:

$$u(t) = \frac{l}{2\pi} \cdot \text{unwrap}\left[\tan^{-1}\left\{\frac{(\sin(2\pi \cdot u(t)/l))}{(\cos(2\pi \cdot u(t)/l))}\right\}\right]. \tag{2}$$

The TGP consists of multiple opaque gratings with evenly spaced transparent spacings. The opaque grating width (l_1) and transparent spacing (l_2) are smaller than the optical beam width. The grating pitch of l is the additive sum of l_1 and l_2. The OFs and reflective mirror, placed on the back of the TGP and perfectly aligned to the end surfaces of the OFs, are fixed to the sensor case in order to produce stable reflectivity.

When the excited acceleration is assumed to be defined as $\ddot{u}_0 = A_{\text{exc}} \cdot e^{i\omega t}$ where ω is the excited frequency, the steady state response should be the relative displacement of the mass defined as $u = B_{\text{res}} \cdot e^{i\omega t}$. A_{exc} refers to the acceleration measured through the reference accelerometer and B_{res} refers to the seismic mass measured displacement in the FOA. Therefore, through the deformation response factor R, the acceleration can be obtained theoretically, which is expressed using the relationship between the excited acceleration and relative displacement, as defined by the following equation:

$$R = \left|\frac{B_{\text{res}}}{A_{\text{exc}}}\right| \cdot \omega_n^2 = \frac{1}{\sqrt{\left(1 - r^2\right)^2 + \left(2\zeta r\right)^2}}, \tag{3}$$

where $r = \omega/\omega_n$, ζ is the damping ratio, and ω_n is the natural frequency of the integrated mass-spring system. The quantification of the parameters such as the relative displacement and acceleration was accomplished using this mechanism.

3. Fabrication of a Prototype for High Temperature Environments

In order to develop the 130°C endurable FOA, the basic material of the prototype for dimensional stability, the adhesive for the assembly of the sensor components, and the fiber optic collimator that has to maintain its function as a collimator at 130°C were considered.

3.1. Fabrication of Sensor Probe. In order to realize the sensor principles at high temperature, the parallel alignment between the reflective surface of the mirror and the end surface of the collimated optical fiber should be maintained during operation at the targeted high temperature. To comply with this requirement, the dimensional stability and consistent functionality of the sensor components such as the collimator and TGP were important consideration factors. Basically, the sensor probe was designed and fabricated based on the researched stable sensor probe without miniscule

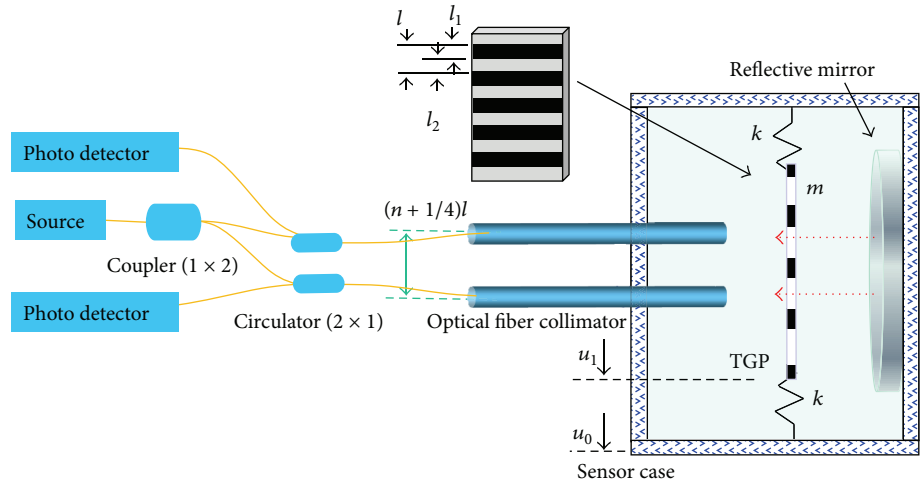

Figure 1: Schematic diagram of the transmissive grating-reflective mirror based FOA sensor system [12].

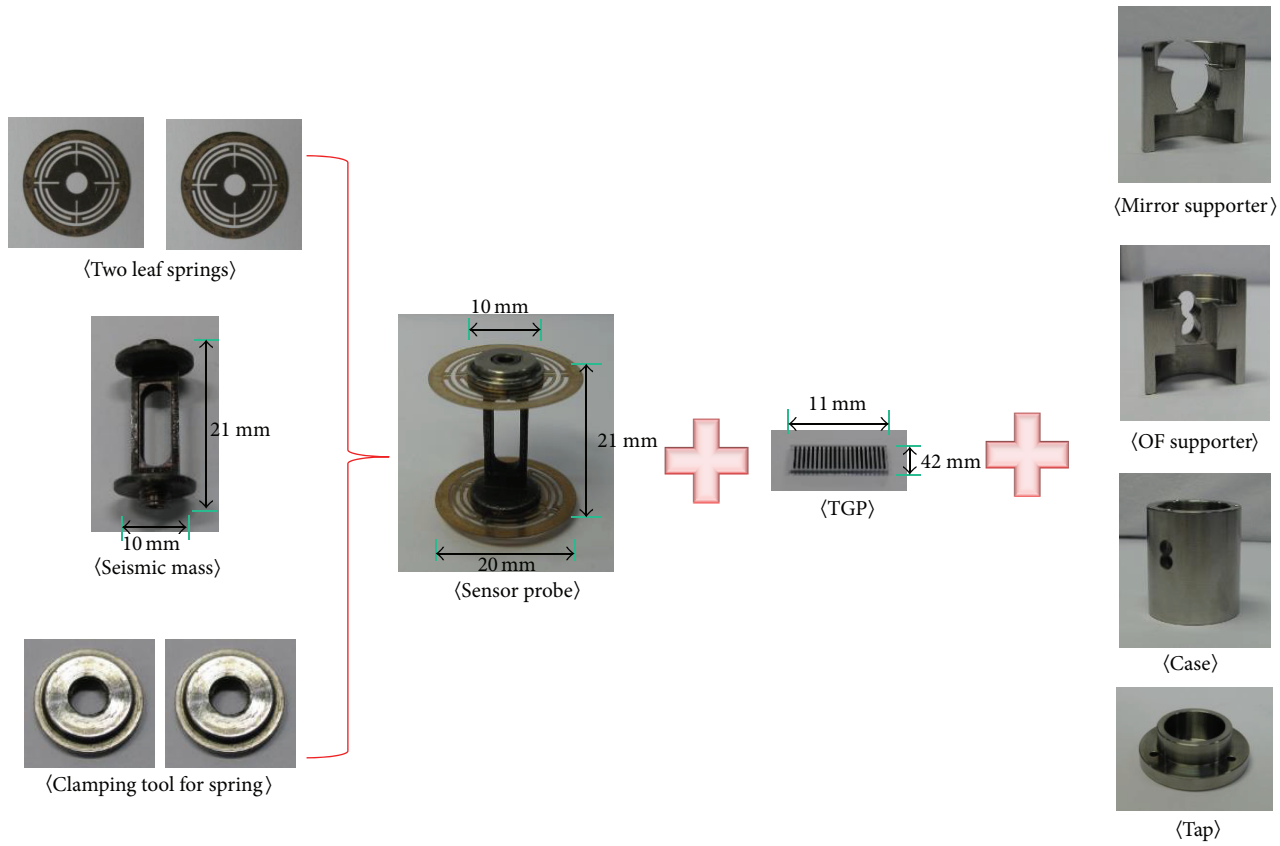

Figure 2: Key components for a 130°C endurable FOA with an invar base.

rotation and lateral motion of the seismic mass [17]. For seismic motion, a leaf plate with a pattern was employed as a spring. The leaf spring is composed of phosphor bronze with a thickness of 60 μm. These are placed on both the top and bottom of the sensor probe with horizontal symmetry, as shown in Figure 2. The circular clamping tools were used to fix the leaf spring on the seismic mass. First of all, clamping tools, which have the possibility of causing distortion of the leaf springs at an elevated temperature, were made of invar material due to its low coefficient of thermal expansion (CTE, 1.2×10^{-6}/K). Furthermore, in order to prevent distortion of the TGP due to CTE difference between the TGP, whose base material is quartz, and the seismic mass, the seismic mass was made using invar material because the TGP has to be attached to the seismic mass. The sensor probe, which plays a pivotal role in the accelerometer, was constructed by

assembling two fabricated leaf springs and clamping tools. In addition, the mirror supporter, OF supporter, and sensor case were also fabricated using invar material because the optical fiber collimators and mirror have to be supported and fixed by them. Therefore, in order to keep their alignment at high temperature, dimensional stability among them must be guaranteed. Consequently, all sensor components were made with an invar base. The sensor probe had a size of 20 (outer diameter of spring) × 21 (height) mm^2. The TGP (thickness: 700 μm), which has a size of 11.0 × 4.2 mm^2, was employed to be attached to the center of the fabricated seismic mass. Furthermore, a ceramic adhesive (940LE, Cotronics Co., USA), whose strength can be maintained up to 1357°C, was used for the assembly of all the optical components for dimensional stability and high adhesive strength.

3.2. FOA Prototype. In this research, a pigtail-type fiber optic collimator is used to minimize the emitted light dispersion at the end surface of the OF and maximize the reflected light receiving rate from the reflective mirror. Most commercial pigtail-type collimators, which employ ferrule and grin lenses, are not designed to withstand high temperatures in terms of dimensional stability and adhesive strength of the bonding material used and the polymer jacket, which was used to avoid damage of the optical fiber line. The dimensional instability may cause difficulties in holding the alignment between the end of the optical fiber and the lens at elevated temperatures. Therefore, commercial fiber optic collimators were customized in order to withstand temperatures up to 130°C by OZ Optics Corporation. Two customized single mode optical fibers combined with the collimator (LPC-06-1550-9/125-S-0.5-2.61CL-40-3S-1-5-HT-SP, OZ Optics Co., Canada) were bonded to the sensor case using ceramic adhesive, as shown in Figure 3. The TGP, which has an l of 280 μm, l_1 (Cr material) of 140 μm, and l_2 of 140 μm, was also attached to the center of the sensor probe using ceramic adhesive. The reflective aluminum mirror (PF05-03-G01, Thorlabs, Inc., USA) was also fixed to the sensor case on the opposite side of the optical fiber. The FOA prototype was assembled and it had dimensions of 30 (outer diameter) × 26 (height) mm^2 and a total weight of 95.7 g. Although it is relatively large in comparison to the MEMS type low frequency accelerometer, the FOA prototype was manufactured to be similar in size to the PZT-based or servo type low frequency accelerometers.

4. 130°C Endurable Fiber Optic Accelerometer

4.1. Dynamic Characteristics of the Sensor Probe according to the Temperature Variations. The mechanical properties of most materials are affected by temperature variations. Young's modulus of phosphor bronze, which was used for the leaf springs, decreases as the applied temperature increases [18]. This indicates that the spring coefficient of the *m-k* structure leads to a change in the natural frequency of the sensor probe at elevated temperatures. To verify the sensor performance regarding the effect of temperature, the natural frequency variations of the sensor were investigated. When the sensor

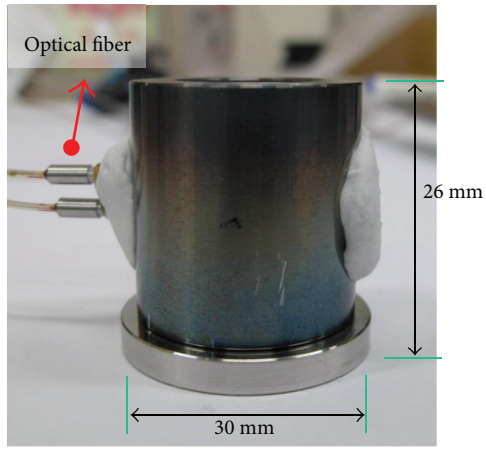

Figure 3: Prototype of 130°C endurable FOA.

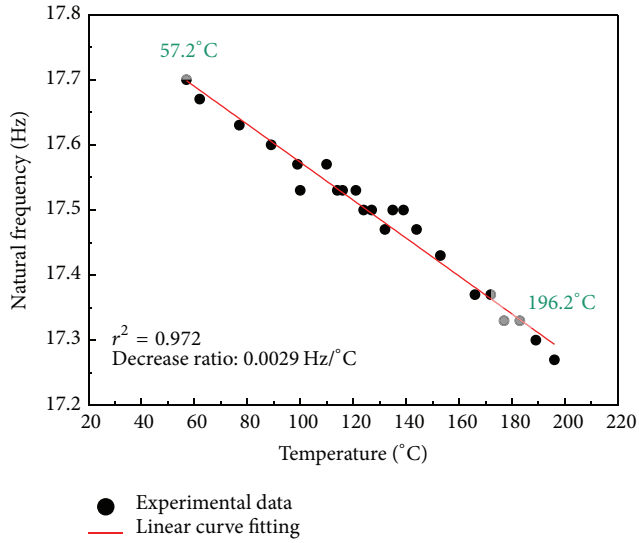

Figure 4: 1st natural frequency variations of the sensor probe according to the surrounding temperature variations.

was used at the equilibrium state of the elevated temperature, the measurable frequency range was found to be affected by the temperature variation. At this equilibrium state, the natural frequencies of the sensor obtained experimentally are plotted according to the corresponding equilibrium temperatures, and, therefore, the measurable frequency range of the FOA can be estimated according to the change in temperature, as shown in Figure 4.

The sensor probe without the TGP and bonding material was excited by an impact hammer, and then the impulse response function was measured by the laser displacement sensor (LK-H050, Keyence Co., Japan). A natural frequency of 17.77 Hz at 28°C and a damping ratio of 0.00073 were empirically achieved from the free vibration test. The weight of the sensor probe with seismic mass, two leaf springs, and two clamping tools was measured to be 4.27 g.

The natural frequency of the sensor probe is an important performance factor because the measurable frequency range of the FOA depends on the natural frequency of

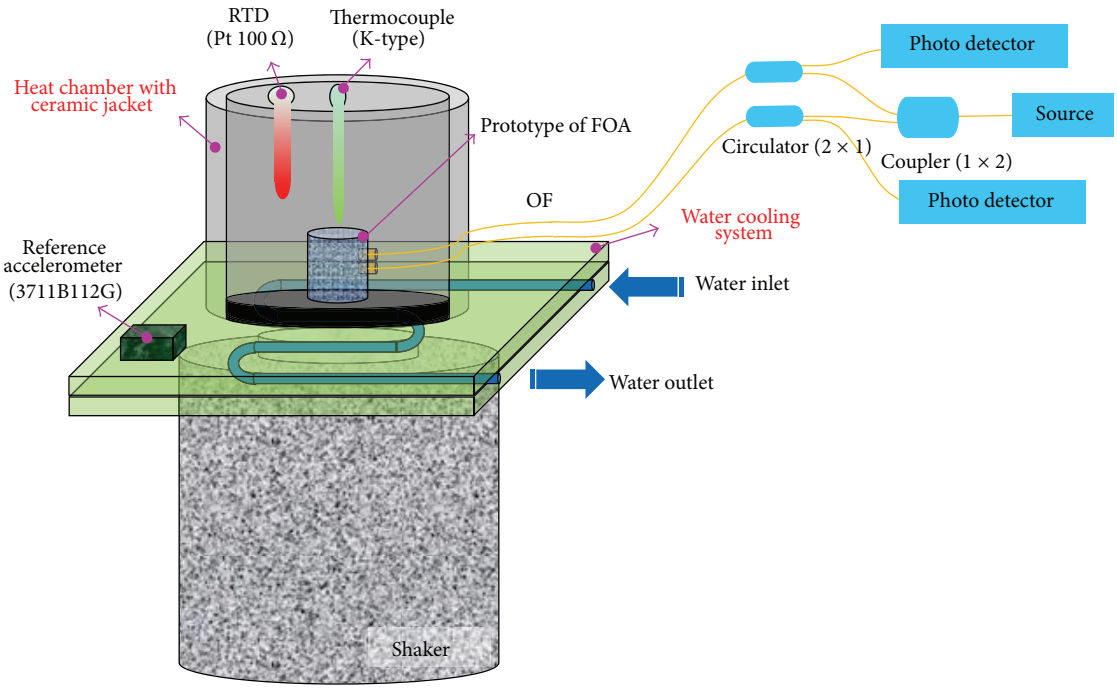

Figure 5: Experimental setup for the performance test of the FOA.

the embedded sensor probe. Most accelerometers can be used below one-third of the natural frequency. In the temperature-equilibrium state, the correlation between the natural frequency of the sensor probe and temperature variation was investigated, as shown in Figure 4. The sensor performance regarding sensitivity and the measurable acceleration range among others also depends on the spring coefficient. Therefore, the experiment for the temperature effect on the sensor was limited to the consideration of the natural frequency variation of the sensor.

The temperatures applied to the sensor were set to vary from 57.2°C to 196.2°C. In the linear regression analysis below the temperature of 196.2°C, the R-square value between the natural frequency and temperature was 0.972 while the decrease ratio of the natural frequency was approximately 0.0029 Hz/°C. This indicates that the natural frequency of the sensor linearly decreased with an increase in the sensor temperature. The decrease ratio can be altered by the level of the maximum experienced temperature because the mechanical property variation of the phosphor bronze depends on the maximum experienced temperature. Thus, due to a small decrease in natural frequency, the fabricated sensor probe is expected to measure acceleration without large variation of the measurable frequency range.

The result of natural frequency reduction with an increase in temperature indicates that the spring coefficient may be reduced due to a decrease in Young's modulus of the phosphor bronze (spring material). In addition, after annealing at a nonexperienced temperature, the natural frequency can be changed at room temperature due to the mechanical property change of the leaf spring.

4.2. Experimental Setup. In order to verify the performance of the fabricated FOA according to temperature variations, the use of an exciter that is stabilized against temperature variations and a large temperature chamber that the exciter can be placed inside is necessary. However, it may be practically difficult to set up a temperature variable acceleration test system because it would require all components, accessories, and equipment, such as the shaker and reference accelerometer, to satisfy a certain temperature resistance (dimensional stability) necessary for the validity of the test. In addition, a large temperature chamber may also be required. Therefore, a simple and new installation for verification was fabricated, as shown in Figure 5. A K-type thermocouple was employed to control the temperature of the chamber. Accurate temperature of the chamber inside can be measured using a resistance temperature detector (RTD) with a platinum 100 Ω. The fabricated FOA was placed inside the chamber where the environmental temperature can be controlled by a ceramic jacket. Consequently, the FOA prototype and the microelectromechanical system (MEMS) reference sensor (3711B112G, PCB Piezotronics, Inc., USA), which has a high sensitivity of 101.9 mV/(m/s^2) at low frequency acceleration, were fixed to the shaker. The reference accelerometer and the fabricated 130°C endurable FOA were placed on the shaker (PM50A, MB Dynamics Co., OH, USA), whose motion was controlled using a sine function generator. However, the commercial accelerometer and the shaker have to be protected from heat transfer because they are not guaranteed for use at high temperature. Therefore, a water cooling system in plate form was installed between the heat chamber and the shaker. While heat was applied to the chamber inside by the ceramic jacket, cold running water was used as a

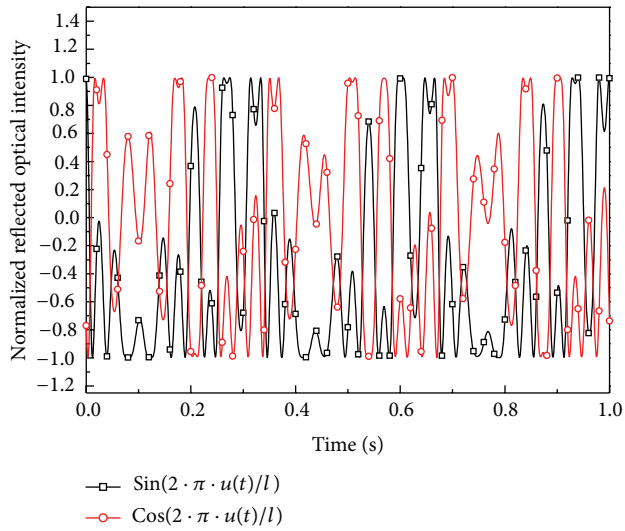

(a) Two normalized reflected optical signals in quadrature at 3.0 Hz excitation.

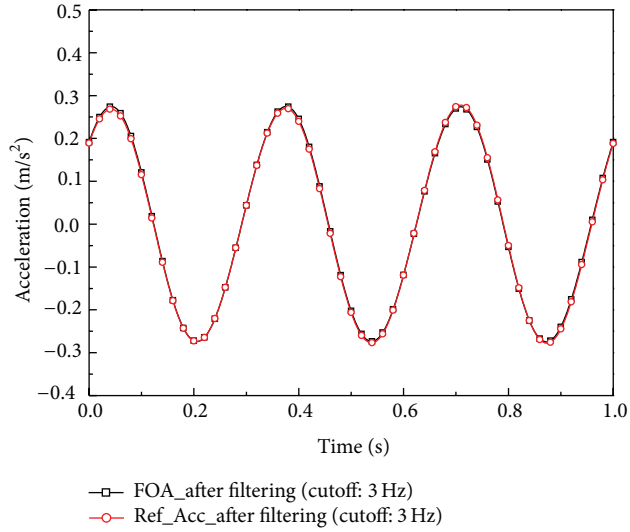

(b) Comparison of the acceleration measured using the proposed FOS (130°C) and a commercial reference accelerometer (24°C) at 3.0 Hz excitation with low pass filtering of 3.0 Hz.

Figure 6: Measured normalized optical signals and acceleration at 130°C.

coolant. Furthermore, the reference accelerometer was placed on the edge of the water cooling plate where the heat cannot be transferred. During the experiment, the temperature was maintained at room temperature without heat transfer to the reference sensor. Therefore, the reference acceleration data was obtained at room temperature where the acquired data was reliable.

An erbium doped fiber amplifier (EDFA; 1530–1565 nm, JDS Uniphase Co., USA) was used as the light source. As the plate that was fixed to the shaker was excited, the received lights of the 130°C endurable FOA were stored in the data acquisition (DAQ) system at sampling rates of 1 kHz through the two circulators (PICT-1550-S, Oyokoden Lab., Tokyo, Japan) and photo detectors (v2011, New Focus, Inc., USA).

4.3. Performance of the Fiber Optic Accelerometer. In the fabricated prototype, the weight of the sensor probe increased after bonding the TGP with ceramic adhesive. The initial natural frequency before annealing was 17.27 Hz with a standard deviation of 0.03. The natural frequency after annealing at 130°C was 17.09 Hz with a standard deviation of 0.06 at 24.6°C due to mechanical property change. The natural frequency of 16.91 Hz at 130°C was experimentally determined. 1.04% of the initial natural frequency decreased until an elevated equilibrium temperature of 130°C was reached. The natural frequency of the sensor probe changed because of the increased weight of 0.25 g due to the added TGP and ceramic bonding material used between the TGP and seismic mass. As the shaker vibrated the base plate, the reflected signals at the two observation points were periodic sine wave functions of the relative displacement l with a phase difference of 90° with respect to each other. The raw reflected signals of these two points can be expressed as a DC component. The two normalized reflected signals were plotted after normalization to a sinusoidal function, which has an amplitude of 1 and a mean magnitude of 0, as shown in Figure 6(a). This figure describes the normalized reflected optical signals of fiber optic collimator 1 (OF1) and fiber optic collimator 2 (OF2) at the 3.0 Hz excitation. Figure 6(b) shows the comparison of the acceleration measured using the proposed FOA and a commercial reference accelerometer at 3.0 Hz excitation with low pass filtering of 3.0 Hz. The measured acceleration data of the developed FOA and reference accelerometer were tracked at 130°C and 24°C, respectively. The measured root mean square (RMS) values of the vibrated acceleration were approximately 0.195 m/s^2 at 3.0 Hz. At 3.0 Hz excitation, the acceleration measured by the proposed FOA agrees very well with that of Ref_Acc after filtering. This indicates that the fabricated FOA including the OF line with a jacket operates well at 130°C.

The measured relative displacement of the seismic mass was 49.37 μm (peak-to-peak magnitude). The acquired voltage from the normalization signal processing was 1.11 rad because the acquired period of the sinusoidal signal was 0.18 periods. The average sensitivity was 5.68 rad/(m/s^2) based on the RMS acceleration value criterion because the magnitude of the measured RMS acceleration value was 0.20 m/s^2 (peak-to-peak magnitude) after low pass filtering. This indicates that the proposed FOA has a higher sensitivity of 55.69 rad/[G] (gravitational acceleration G). The minimum measurable acceleration of the fabricated prototype was 0.0016 m/s^2 based on the RMS acceleration value criterion because of a minimum measurable displacement of 0.41 μm of the sensor probe.

The frequency response curve of the FOA was experimentally obtained as the shaker was excited by the sine signals at selected frequencies covering a usable area. The frequency response curve in the form of a deformation

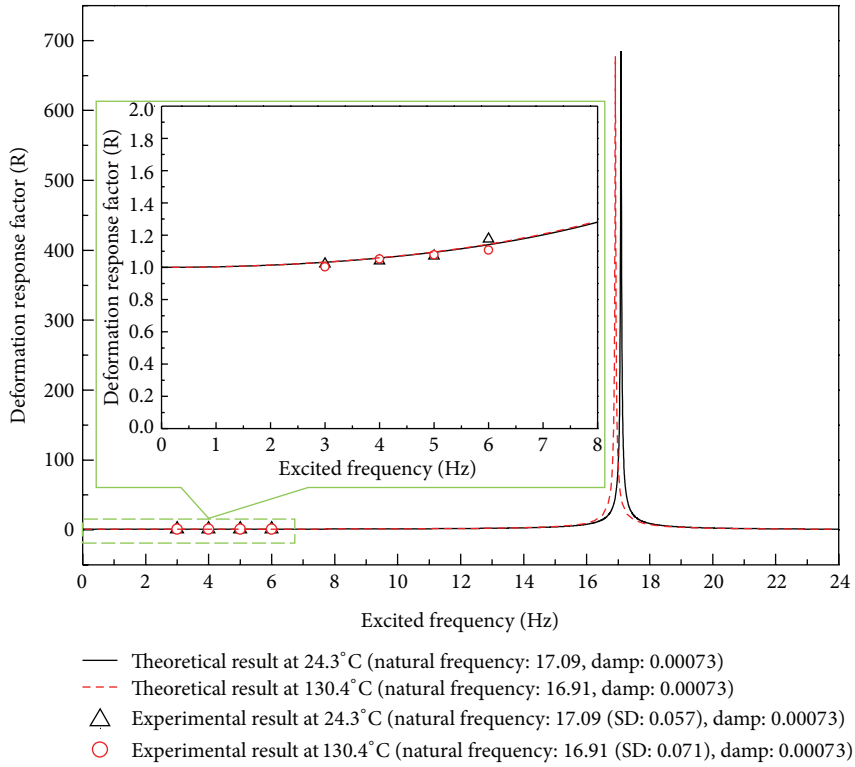

Figure 7: Comparison between the measured and theoretical deformation response factor (R).

response factor (R) was plotted as a function of the excited frequencies, as shown in Figure 7. The frequencies of the excitation signals selected were 3.0 Hz, 4.0 Hz, 5.0 Hz, and 6.0 Hz in order to determine the measurable frequency range. The experimental points, which were calculated using displacements and acceleration measured by the FOA and MEMS accelerometer, respectively, were compared with the theoretical result, which was plotted using (3). The theoretical curves were plotted at 24.3°C and 130.4°C, respectively, based on the assumption of negligible variation of the damping ratio at 130°C. These theoretical curves agree very well with the experimental points measured at 24.3°C and 130.4°C. The deformation response factor of the developed FOA was almost 1 in the frequency ranges below 5.1 Hz. This implies that the designed and fabricated FOA can be used in the frequency ranges below 5.1 Hz within a 10% error margin in order to measure the low frequency acceleration of civil engineering structures.

5. Conclusion

The high temperature endurable fiber optic accelerometer was fabricated using invar, ceramic adhesive, and a 130°C endurable fiber optic collimator. A simple performance test setup of the accelerometer at high temperature was proposed. The developed fiber optic accelerometer measured low frequency acceleration below 5.1 Hz within a 10% error margin in a surrounding high temperature of 130°C. Furthermore, the proposed fiber optic accelerometer has a very high sensitivity of 0.18 (m/s^2)/rad at 130°C. The fabricated sensor probe can be used for the 130°C endurable fiber optic accelerometer in equilibrium temperature states although the fabricated sensor in our paper may not be appropriate for steadily increasing temperature environments like most accelerometers due to sensitivity variation. For use in high temperature environments, the natural frequency change rate should be considered at the targeted temperature due to natural frequency reduction that occurs with an increase in temperature. If a leaf spring with high stiffness is used, the maximum measurable frequency range can be extended at a higher temperature. However, although the measurable frequency range would increase with greater stiffness of the leaf spring, the sensor sensitivity decreases. Therefore, it is desirable to design for a spring stiffness value appropriate for the target temperature range taking into consideration the tradeoff between sensitivity and maximum measurable frequency range. In addition, if the operating temperature limitation of the commercially available fiber optic collimator is overcome or the aimed temperature endurable fiber optic collimator with a lensed tip is developed, the developed fiber optic accelerometer can be applied to higher temperature although this research was limited to developing a 130°C endurable fiber optic accelerometer.

Conflict of Interests

The authors declare that there is no conflict of interests regarding the publication of this paper.

Acknowledgments

This research was supported by the Leading Foreign Research Institute Recruitment Program (Grant no. 2011-0030065) through the National Research Foundation of Korea funded by the Ministry of Education, Science and Technology.

References

[1] B. Lee, "Review of the present status of optical fiber sensors," *Optical Fiber Technology*, vol. 9, no. 2, pp. 57–79, 2003.

[2] A. Wang, S. Gollapudi, K. A. Murphey, R. G. May, and R. O. Claus, "Sapphire-fiber-based intrinsic Fabry-Perot interferometer," *Optics Letters*, vol. 17, pp. 1021–1223, 1992.

[3] L. Tong, Y. Shen, L. Ye, and Z. Ding, "A zirconia single-crystal fibre-optic sensor for contact measurement of temperatures above 2000°C," *Measurement Science and Technology*, vol. 10, no. 7, pp. 607–611, 1999.

[4] J. L. Kenndey and N. Djeu, "Operation of Yb:YAG fiber-optic temperature sensor up to 1600°C," *Sensors Actuators A*, vol. 100, no. 2–3, pp. 187–191, 2002.

[5] S. Zhao, J. Zhang, C. Hou, J. Bai, and G. Yang, "Optical tilt sensor with direct intensity-modulated scheme," *Optical Engineering*, vol. 50, no. 11, Article ID 114405, 2011.

[6] Y. N. Kulchin, O. B. Vitrik, and A. V. Dyshlyuk, "Fiber-optic inclinometer for structural health monitoring," in *Proceedings of SPIE*, vol. 6662, 2007, 66620H.

[7] D. H. Kim, "A fiber-optic tiltmeter system based on the moiré-fringe effect," *Measurement Science and Technology*, vol. 20, no. 2, Article ID 025203, 2009.

[8] M. Q. Feng and D. H. Kim, "Novel fiber optic accelerometer system using geometric moiré fringe," *Sensors and Actuators A*, vol. 128, no. 1, pp. 37–42, 2006.

[9] W. B. Spillman Jr., "Multimode fiber-optic hydrophone based on a schlieren technique," *Applied Optics*, vol. 20, no. 3, pp. 465–470, 1981.

[10] S. Zhao, C. Hou, J. Bai, G. Yang, and F. Tian, "Nanometer-scale displacement sensor based on phase-sensitive diffraction grating," *Applied Optics*, vol. 50, no. 10, pp. 1413–1416, 2011.

[11] E. Udd and P. M. Turek, "single mode fiber optic vibration sensor," in *Proceedings of SPIE*, vol. 566, pp. 135–140, 1985.

[12] Y. G. Lee, D. H. Kim, and C. G. Kim, "Transmissive grating-reflective mirror based fiber optic accelerometer for stable signal acquisition in industrial applications," *Optical Engineering*, vol. 51, no. 5, Article ID 054402, 2012.

[13] Y. G. Lee, D. H. Kim, and C. G. Kim, "Performance of a single reflective grating-based fiber optic accelerometer," *Measurement Science and Technology*, vol. 23, no. 4, Article ID 045101, 2012.

[14] W. Pulliam, P. Russler, R. Mlcak, K. Murphy, and C. Kozikowski, "Micromachined, SiC fiber optic pressure sensors for high-temperature aerospace applications," in *Proceedings of SPIE Industrial Sensing Systems*, pp. 21–30, 2000.

[15] Y. Zhu, *Miniature Fiber-Optic Sensors for High-Temperature Harsh Environments [Ph.D. thesis]*, Virginia Polytechnic Institute and State University, 2007.

[16] Y. G. Lee, Y. Y. Kim, and C. G. Kim, "Fiber optic displacement sensor with a large extendable measurement range while maintaining equally high sensitivity, linearity, and accuracy," *Review of Scientific Instruments*, vol. 83, no. 4, Article ID 045002, 2012.

[17] Y. G. Lee, D. H. Kim, and C. G. Kim, "Design of patterned leaf spring for sensor-probe with stable reflectivity and high sensitivity," *Sensors and Actuators A*, vol. 176, pp. 19–26, 2012.

[18] J. P. Andrews, "The variation of Young's Modulus at high temperatures," *Proceedings of the Physical Society of London*, vol. 37, no. 1, pp. 169–177, 1924.

Hindawi Publishing Corporation
Shock and Vibration
Volume 2014, Article ID 702404, 5 pages
http://dx.doi.org/10.1155/2014/702404

Research Article

Measurement of Microvibration by Using Dual-Cavity Fiber Fabry-Perot Interferometer for Structural Health Monitoring

Dae-Hyun Kim,[1] Jin-Hyuk Lee,[2] and Byung-Jun Ahn[3]

[1] *Department of Mechanical and Automotive Engineering, Seoul National University of Science and Technology, 172 Gongneung 2-dong, Nowon-gu, Seoul 139-743, Republic of Korea*
[2] *Graduate School of Energy & Environment, Seoul National University of Science and Technology, 172 Gongneung 2-dong, Nowon-gu, Seoul 139-743, Republic of Korea*
[3] *Graduate School of NID Fusion Technology, Seoul National University of Science and Technology, 172 Gongneung 2-dong, Nowon-gu, Seoul 139-743, Republic of Korea*

Correspondence should be addressed to Dae-Hyun Kim; dkim@seoultech.ac.kr

Received 4 December 2012; Accepted 14 March 2013; Published 3 March 2014

Academic Editor: Gyuhae Park

Copyright © 2014 Dae-Hyun Kim et al. This is an open access article distributed under the Creative Commons Attribution License, which permits unrestricted use, distribution, and reproduction in any medium, provided the original work is properly cited.

Extensive researches have recently been performed to study structural integrity using structural vibration data measured by in-structure sensors. A fiber optic sensor is one of candidates for the in-structure sensors because it is low in cost, light in weight, small in size, resistant to EM interference, long in service life, and so forth. Especially, an interferometric fiber optic sensor is very useful to measure vibrations with high resolution and accuracy. In this paper, a dual-cavity fiber Fabry-Perot interferometer was proposed with a phase-compensating algorithm for measuring micro-vibration. The interferometer has structurally two arbitrary cavities; therefore the initial phase difference between two sinusoidal signals induced from the interferometer was also arbitrary. In order to do signal processing including an arc-tangent method, a random value of the initial phase difference is automatically adjusted to the exact 90 degrees in the phase-compensating algorithm part. For the verification of the performance of the interferometer, a simple vibration-test was performed to measure micro-vibration caused by piezoelectric transducer (PZT). As an experimental result, the interferometer attached on the PZT successfully measured the 50 Hz-vibration of which the absolute displacement oscillated between −424 nm and +424 nm.

1. Introduction

Advanced sensor and structural monitoring technology can play an important role in prioritizing repair and rehabilitation process, improving the cost effectiveness of inspection and maintenance, and ultimately enhancing the longevity and safety of large-scale mechanical systems. Extensive researches have recently been performed to study structural integrity using structural vibration data measured by in-structure sensors [1, 2]. One of the major obstacles preventing sensor-based monitoring is however the unavailability of reliable, easy-to-install, and cost-effective sensors. In particular, civil engineering structures place unique demands on sensors. Besides accuracy, sensors and their cables are expected to be reliable, low in cost, light in weight, small in size, resistant to EM interference, and long in service life. They are required to withstand harsh environments, be moisture-, explosion-, and lightning-proof, and corrosion-resistant. Furthermore, civil structures are usually very large, demanding easy cabling of the sensors. It is very difficult, if not impossible, for the currently available electric-type sensors to satisfy these demanding requirements.

Emerging fiber optic sensor technologies have shown great potential to overcome the difficulties associated with the conventional sensors. They are immune to EM noise and electric shock and thus can be used in explosion-prone areas. Several kinds of fiber optic sensors have been developed over the last two decades to take advantage of these merits [3–6]. There have also been many field applications of fiber optic

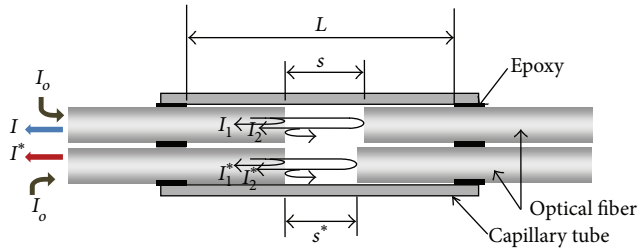

Figure 1: Schematic diagram of dual-cavity Fabry-Perot Interferometer.

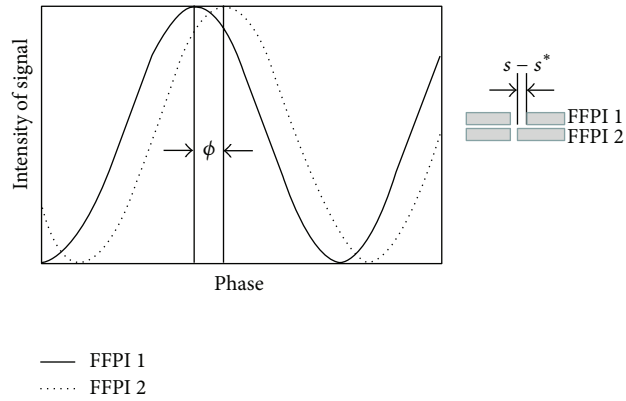

Figure 2: Characteristics of signals of dual-cavity Fabry-Perot Interferometer.

sensors for health monitoring of engineering structures [7–9]. Among them, an interferometric fiber optic sensor is very useful to measure vibrations with high resolution and accuracy.

In this paper, a dual-cavity fiber Fabry-Perot interferometer was proposed with a phase-compensating algorithm. The sensor is structurally similar to a quadrature-phase-shifted fiber Fabry-Perot interferometer (QPS-FFPI); however, mechanical adjustment of two cavities is not needed because of the phase-compensating algorithm. Basically, the mechanical adjustment of two cavities is required in the QPS-FFPI in order to take two sinusoidal signals which have an initial phase difference of exact 90 degrees [10, 11]. However, the mechanical adjustment is very difficult, sometimes impossible. In the phase-compensating algorithm, a random value of the initial phase difference can be automatically adjusted to the exact 90 degrees. As a result, we can exactly measure the phase of the sinusoidal signal induced from the dual-cavity fiber Fabry-Perot interferometer by using an arctangent method. For the verification of the performance of the interferometer, a simple vibration test was performed to detect microvibration caused by piezoelectric transducer (PZT). As a result, it showed that the dual-cavity fiber Fabry-Perot interferometer successfully measured the microvibration with the assistance of the phase-compensating algorithm.

2. Dual-Cavity Fiber Fabry-Perot Interferometer

Theoretically, an interferometric fiber optic sensor generates a sinusoidal signal of which phase is changed periodically by the variation of external environment. A fiber Fabry-Perot interferometer is also one of interferometric fiber optic sensors and it can measure microvibration precisely because of its high sensitivity and accuracy. In this paper, two fiber Fabry-Perot interferometers are used as one sensor called a dual-cavity fiber Fabry-Perot interferometer. Figure 1 shows a sensor head of the dual-cavity fiber Fabry-Perot interferometer. As shown in Figure 1, two pairs of optical fibers in the sensor generate two sinusoidal signals because of optical interference. An initial phase difference between the output signals of I and I^* should be 90 degrees for using an arctangent method. So, the initial phase difference is adjusted to the exact 90 degrees in the case of QPS-FFPI by the mechanical adjustment of the cavities of s and s^*. However, the dual-cavity fiber Fabry-Perot interferometer has arbitrary values of s and s^*; therefore, the output signals have an initial phase difference (ϕ) as a random value as shown in Figure 2. This condition is a major difference between the dual-cavity fiber Fabry-Perot interferometer and the conventional QPS-FFPI.

3. Signal Processing with Phase-Compensating Algorithm

As mentioned in the previous section, the dual cavity fiber Fabry-Perot interferometer has an arbitrary value of the initial phase difference between two output sinusoidal signals. Therefore, it is needed for the measurement of displacement that the initial phase difference is forcibly adjusted to the exact 90 degrees. In this section, a signal processing part is introduced with a phase-compensating algorithm in which the initial phase difference is automatically changed to the exact 90 degrees. A detailed explanation is following. Firstly, the intensity signals of the two pairs of optical fibers with an arbitrary initial phase difference (ϕ) can be expressed in (1) and (2) as follows. Secondly, these two sinusoidal signals are needed to be normalized as shown in (3) and (4). Consider

$$I_1(t) = C_1 \sin\left(2\frac{2\pi}{\lambda}s(t)\right) + C_2, \tag{1}$$

$$I_2(t) = C_3 \sin\left(2\frac{2\pi}{\lambda}s(t) + \phi\right) + C_4, \tag{2}$$

$$\bar{I}_1(t) = \frac{I_1(t) - C_2}{C_1} = \sin\left(2\frac{2\pi}{\lambda}s(t)\right), \tag{3}$$

$$\bar{I}_2(t) = \frac{I_2(t) - C_4}{C_3} = \sin\left(2\frac{2\pi}{\lambda}s(t) + \phi\right), \tag{4}$$

where C_1 and C_3 are amplitudes of sinusoidal signals and C_2 and C_4 are values of offsets. $s(t)$ is a cavity between two optical fibers of the interferometer as shown in Figure 1. Thirdly, the normalized signals $(\bar{I}_1, \bar{I}_2)$ and ϕ are used for generating a new sinusoidal signal of which wavelength is the same as the

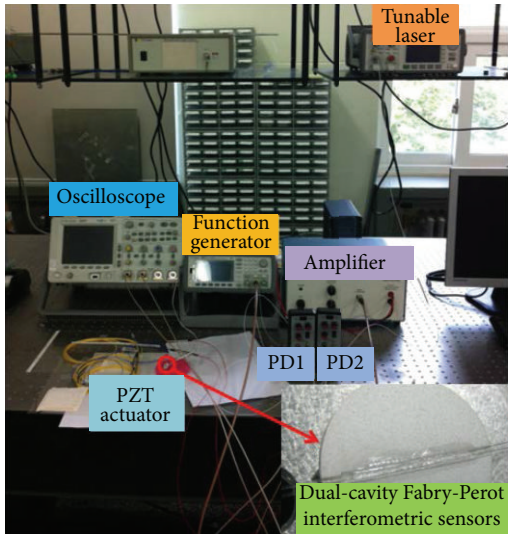

Figure 3: Experimental setup for measuring microvibration by using a dual-cavity fiber Fabry-Perot interferometer.

normalized signal of $\bar{I}_1$. The phase difference between the new sinusoidal signal ($\bar{I}_3$) and $\bar{I}_1$ is exactly 90 degrees. The new sinusoidal signal ($\bar{I}_3$) is expressed in

$$\bar{I}_3 = f\left(\bar{I}_1, \bar{I}_2, \phi\right) = \sin\left(2\frac{2\pi}{\lambda}s(t) + \frac{\pi}{2}\right) = \cos\left(2\frac{2\pi}{\lambda}s(t)\right). \tag{5}$$

The equations for calculating the displacement of $\Delta s(t)$ can be expressed as follows:

$$s(t) = \frac{\lambda}{4\pi}\text{unwrap}\left(\tan^{-1}\left(\frac{\bar{I}_1}{\bar{I}_3}\right)\right)$$
$$\Delta s(t) = \frac{\lambda}{4\pi}\Delta\left[\text{unwrap}\left(\tan^{-1}\left(\frac{\bar{I}_1}{\bar{I}_3}\right)\right)\right]. \tag{6}$$

As a result, the displacement can be successfully measured by calculating the phase-shifting.

4. Measurement of Microvibration

4.1. Experimental Setup and Procedures. Figure 3 shows an experimental setup to measure microvibration by using the dual-cavity fiber Fabry-Perot interferometer with the phase-compensating algorithm. An actuating system is composed of a linear amplifier (PIEZO, EPA-104-230), a function waveform generator (AGILENT, 33522A), and PZT (FUJI CERAMICS, C82). A sensing system is also composed of a tunable laser (AGILENT, 81949A) as a laser source, two photodetectors (NEWFOCUS, 2117) as laser receivers, and a dual-cavity fiber Fabry-Perot interferometer (gauge length = 10.2 mm) which is attached on the surface of the PZT as shown in Figure 3.

In detail, these optical components are combined by using one coupler and two circulators as shown in Figure 4. Two photodetectors are connected to an oscilloscope (AGILENT, DSO6034A) to observe and save the output signals induced from the dual-cavity fiber Fabry-Perot interferometer.

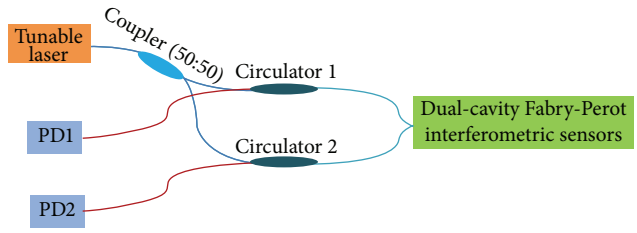

Figure 4: Experimental setup for driving optical devices of dual-cavity fiber Fabry-Perot interferometer.

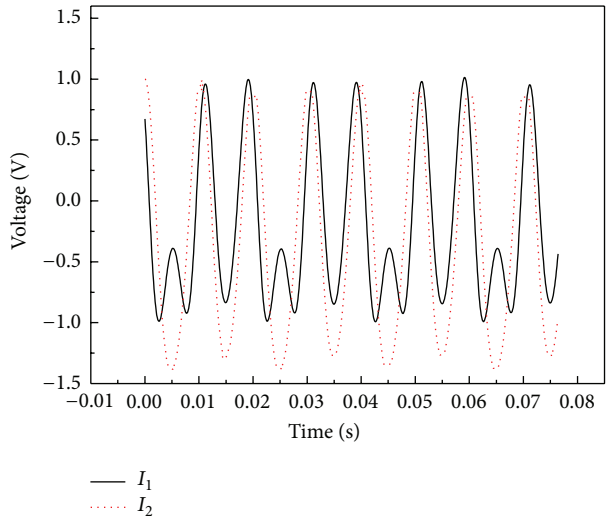

Figure 5: Two sinusoidal signals induced from a dual-cavity fiber Fabry-Perot interferometer.

Experimental procedures are the following. Firstly, the wavelength of the tunable laser is set as 1542 nm, and a 50 Hz-sinusoidal signal is generated from the function waveform generator. Secondly, the amplitude of the sinusoidal signal is forced to be gradually increased by controlling the gain value of the linear amplifier. Thirdly, two output signals induced from the dual-cavity fiber Fabry-Perot interferometer are measured by the oscilloscope. Finally, the absolute value and variation of the displacement are calculated in a signal processing software including the phase-compensating algorithm explained in the previous section.

4.2. Experimental Results. Figure 5 shows two sinusoidal signals induced from the dual-cavity fiber Fabry-Perot interferometer. A low pass filter of which the cut-off frequency was 190 Hz was applied to the signals for noise reduction. The first step of the signal processing was to normalize these two sinusoidal signals by using minimum and maximum values of the sinusoidal signals. The second step was to generate a new sinusoidal signal by using these two normalized sinusoidal signals and the initial phase difference (ϕ).

Figure 6 shows the normalized sinusoidal signals ($\bar{I}_1, \bar{I}_2$) and the newly generated sinusoidal signal ($\bar{I}_3$). It was also

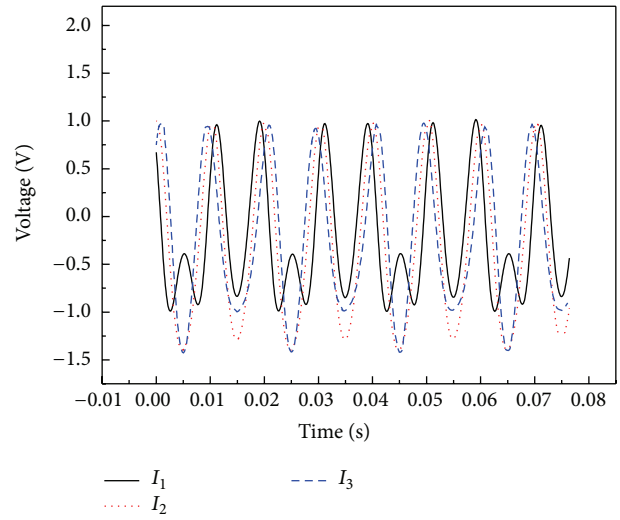

Figure 6: Two normalized sinusoidal signals and one newly generated signal for the signal processing.

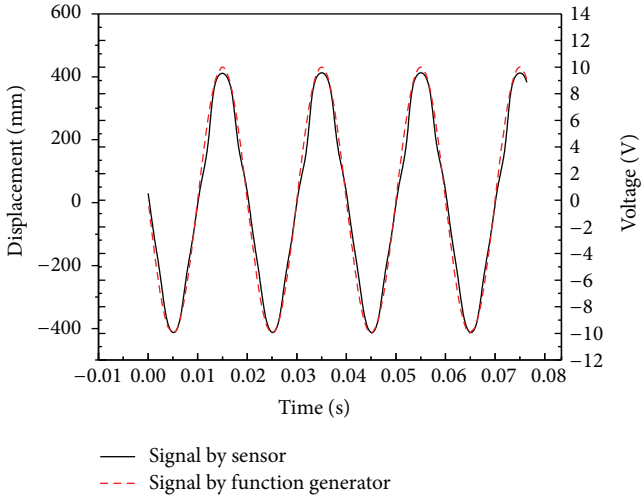

Figure 7: Absolute value of displacement induced by vibration-excitation.

checked out that the phase difference between $\bar{I}_1$ and $\bar{I}_3$ was exactly 90 degrees. The phase of $\bar{I}_1$ or $\bar{I}_2$ and the absolute value of the displacement were calculated by using (6) as explained in Section 3. Figure 7 shows the calculated displacement which oscillates between −424 nm and +424 nm. The frequency of the oscillating displacement was also checked by a spectrum analysis. Figure 8 shows the result of the spectrum analysis that the frequency is the same as the excitation frequency of 50 Hz. From the experiment, it is verified that the dual-cavity fiber Fabry-Perot interferometer can successfully measure the microvibration by using the phase-compensating algorithm.

5. Conclusions

In this paper, a dual-cavity fiber Fabry-Perot interferometer was proposed with a phase-compensating algorithm. The

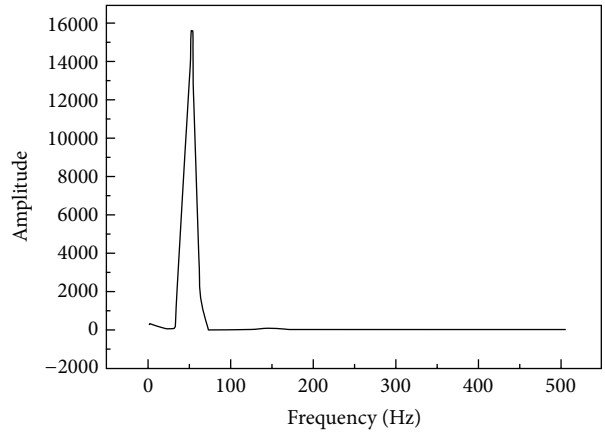

Figure 8: Spectrum analysis of the oscillating displacement.

dual-cavity fiber Fabry-Perot interferometer generates two sinusoidal signals of which initial phase difference was a random value. In the phase-compensating algorithm, the random value of the initial phase difference can be automatically adjusted to the exact 90 degrees. As a result, we can exactly measure the phase of the sinusoidal signal induced from the dual cavity fiber Fabry-Perot interferometer by using an arc-tangent method. For the verification of the performance of the interferometer, an experimental test was performed. In the experiment, a dual-cavity fiber Fabry-Perot interferometer was fabricated and attached on the surface of the PZT. The interferometer was excited by the PZT and two output sinusoidal signals were processed with the phase-compensating algorithm to measure the displacement of the PZT. As a result, the interferometer successfully measured the displacement induced by the PZT. In detail, the PZT led to 50 Hz mechanical vibration and the interferometer attached on the PZT successfully measured the same vibration of which the absolute displacement oscillated between −424 nm and +424 nm. Furthermore, it is expected that the dual-cavity fiber Fabry-Perot interferometer can be applied to more precise and accurate vibration measurement with the phase-compensating algorithm.

Conflict of Interests

The authors declare that there is no conflict of interests regarding the publication of this paper.

Acknowledgments

This research was supported by Basic Science Research Program through the National Research Foundation of Korea (NRF) funded by the Ministry of Education, Science and Technology (2010-0004312) and Basic Science Research Program through the National Research Foundation of Korea (NRF) funded by the Ministry of Education (2013R1A1A2007061).

References

[1] M. Q. Feng, J.-M. Kim, and H. Xue, "Identification of a dynamic system using ambient vibration measurements," *Journal of Applied Mechanics*, vol. 65, no. 4, pp. 1010–1021, 1998.

[2] M. Q. Feng and D.-H. Kim, "Novel fiber optic accelerometer system using geometric moiré fringe," *Sensors and Actuators A: Physical*, vol. 128, no. 1, pp. 37–42, 2006.

[3] E. Udd, *Fiber Optic Smart Structures*, John Wiley & Sons, New York, NY, USA, 1995.

[4] B. Lee, "Review of the present status of optical fiber sensors," *Optical Fiber Technology*, vol. 9, no. 2, pp. 57–79, 2003.

[5] D. H. Kim and M. Q. Feng, "Real-time structural health monitoring using a novel fiber optic accelerometer system," *IEEE Sensors Journal*, vol. 7, no. 4, pp. 536–543, 2007.

[6] J. Im, M. Kim, K. S. Choi, T. K. Hwang, and I. B. Kwon, "FBG sensor probes with silver epoxy for tracing the maximum strain of structures," *Journal of KNST*, vol. 33, no. 5, pp. 459–464, 2013.

[7] H.-N. Li, D.-S. Li, and G.-B. Song, "Recent applications of fiber optic sensors to health monitoring in civil engineering," *Engineering Structures*, vol. 26, no. 11, pp. 1647–1657, 2004.

[8] F. Ansari, "Fiber optic health monitoring of civil structures using long gage and acoustic sensors," *Smart Materials and Structures*, vol. 14, no. 3, pp. S1–S7, 2005.

[9] W. Moorman, L. Taerwe, W. De Waele, J. Degrieck, and J. Himpe, "Measuring ground anchor forces of a quay wall with Bragg sensors," *Journal of Structural Engineering*, vol. 131, no. 2, pp. 322–328, 2005.

[10] D. A. Jackson and J. D. C. Jones, "Interferometers optical fiber sensors," *Optical Fiber Sensors: Systems and Applications*, vol. 12, no. 4, pp. 277–281, 2001.

[11] K. A. Murphy, M. F. Gunther, A. M. Vengsarkar, and R. O. Claus, "Quadrature phase-shifted, extricsic fabry-perot optical fiber sensors," *Optics Letters*, vol. 16, no. 4, pp. 273–275, 1991.